

THE UNIVERSITY OF CALGARY

AN EXPERIMENTAL STUDY OF THE MIXING BEHAVIOUR
OF AN ACOUSTICALLY PULSED AIR JET
WITH A CONFINED CROSSFLOW

BY

CHING-FATT CHIN

A THESIS

SUBMITTED TO THE FACULTY OF GRADUATE STUDIES
IN PARTIAL FULFILLMENT OF THE REQUIREMENTS FOR THE
DEGREE OF MASTER OF SCIENCE

DEPARTMENT OF MECHANICAL ENGINEERING

CALGARY, ALBERTA

DECEMBER, 1987

© Ching-Fatt Chin, 1987

Permission has been granted to the National Library of Canada to microfilm this thesis and to lend or sell copies of the film.

The author (copyright owner) has reserved other publication rights, and neither the thesis nor extensive extracts from it may be printed or otherwise reproduced without his/her written permission.

L'autorisation a été accordée à la Bibliothèque nationale du Canada de microfilmer cette thèse et de prêter ou de vendre des exemplaires du film.

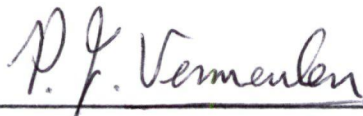
L'auteur (titulaire du droit d'auteur) se réserve les autres droits de publication; ni la thèse ni de longs extraits de celle-ci ne doivent être imprimés ou autrement reproduits sans son autorisation écrite.

ISBN 0-315-42480-X

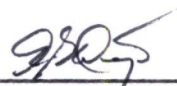
THE UNIVERSITY OF CALGARY

FACULTY OF GRADUATE STUDIES

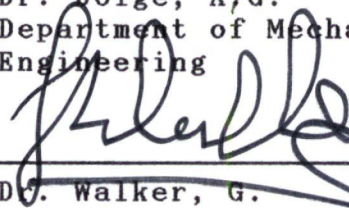
The undersigned certify that they have read, and recommend to the Faculty of Graduate Studies for acceptance, a thesis entitled "An experimental study of the mixing behaviour of an acoustically pulsed air jet with a confined crossflow" submitted by Ching-Fatt Chin in partial fulfillment of the requirements for the degree of Master of Science in Mechanical Engineering.



Dr. Vermeulen, P.J.
Chairman & Supervisor
Department of Mechanical
Engineering



Dr. Doige, A.G.
Department of Mechanical
Engineering



Dr. Walker, G.
Department of Mechanical
Engineering



Dr. Moore, R.G.
Department of Chemical and
Petroleum Engineering

Date: December 21, 1987

ABSTRACT

Previous work by Vermeulen, et. al. on the mixing of a free jet clearly showed that the entrainment, and therefore the mixing of the jet, was significantly increased by acoustically pulsing the jet. Since jet flow mixing is of fundamental importance to the performance of a gas turbine combustor, an experimental investigation into the mixing behaviour of an acoustically pulsed air jet with a confined uniform crossflow has therefore been undertaken. Such a study will elucidate the basic nature of the process and therefore provide the fundamental understanding for possible applications.

The experimental apparatus as developed by Yu (3) was modified such that maximum jet and crossflow velocities are now 110 m/s and 40 m/s respectively. This has allowed mixing to be assessed, by mean velocity and turbulence profile measurements, over a jet velocity/ crossflow velocity ratio of 1.31 to 4.56, for a jet orifice size of 19.93 mm diameter.

The Strouhal number range of the tests was from 0.09 to 0.31. The driving system was calibrated, for strength of the velocity pulsation imparted to the jet flow, over a greater power range than that of previous work, and

indicated that pulsation strength may have an upper limit which so far has not been reached.

Acoustic excitation was shown to produce strong changes in the mean velocity and turbulence profiles, and indicated considerable improvement in the entrainment and mixing by the jet. The mixing length was significantly shortened. The effects increase with power, and overall it may be concluded that the jet mixing processes are significantly improved, in a controllable fashion, by pulsating the jet flow.

The acoustic drive increased the jet penetration by as much as 67%, measured at three diameters downstream of the jet orifice. The pressure drop across the jet orifice to achieve a particular trajectory was also beneficially affected by acoustic excitation.

The effect of Strouhal number, deduced from jet penetration and turbulence data, was found to be optimum at about $St = 0.22$.

Overall a good understanding of the mixing behaviour of an acoustically excited jet with a confined crossflow has been obtained. The effects are beneficial, controllable, and application of the technique will contribute to the development of improved combustors.

ACKNOWLEDGMENTS

The author is greatly indebted to his supervisor Dr. P.J. Vermeulen who initiated and supervised this research. His continued interest, discussions and suggestions, guidance, support and encouragement are gratefully acknowledged.

Acknowledgements are also due to the support staff of the Mechanical Engineering workshop, particularly to Mr. R. Bechtold (Machine Shop Supervisor) and Mr. P. Halkett (Technician) who assisted in modifying the experimental test rig, Mr. W. A. Anson (Technical Supervisor) for the help in employing the M.E.D.A.S. (Mechanical Engineering Data Acquisition System) throughout the whole process of the experiment, and to Mr. R. W. Gustafson (Technician) for assistance with flow calibration problems.

The financial assistance and support provided by the Department of Mechanical Engineering of the University of Calgary, and the Natural Sciences and Engineering Research Council of Canada (NSERC), under Research Grant No. A7801, are also gratefully acknowledged.

TABLE OF CONTENTS

	PAGE
THE APPROVAL PAGE	ii
ABSTRACT	iii
ACKNOWLEDGMENTS	v
TABLE OF CONTENTS	vi
LIST OF FIGURES	viii
NOMENCLATURE	xv
CHAPTER 1 INTRODUCTION	1
1.1 Prologue	1
1.2 Origin of the Present Work	2
1.3 Scope of the Thesis	4
CHAPTER 2 LITERATURE STUDIES	8
2.1 Physical Description of the Jet in a Crossflow	8
2.2 General Information in Literature	11
CHAPTER 3 EXPERIMENTAL APPARATUS	23
3.1 Description of Apparatus	23
3.2 Description of Test Section	27
3.3 The Modulating Apparatus and Hot-Film Anemometer	28

3.4	Data Acquisition System	29
CHAPTER 4	EXPERIMENTAL PROCEDURES	45
4.1	Initial Operation Conditions	45
4.2	Calibration of the Apparatus	46
4.3	Frequency Response of the Mechanical System of Driver, Driver Tube, Jet Flow Tube	49
4.4	Main Experimental Techniques and Procedures	51
CHAPTER 5	EXPERIMENTAL RESULTS AND DISCUSSIONS	80
5.1	Velocity Pulsation Strength	80
5.2	Velocity Profiles	80
5.2.1	Blockage Effect	81
5.2.2	Velocity Profiles "Without Acoustic Excitation"	82
5.2.3	Velocity Profiles "With Acoustic Excitation"	86
5.3	Jet Trajectory, Strouhal Number Effect and Other Parameters	94
CHAPTER 6	CONCLUSIONS AND RECOMMENDATIONS	162
REFERENCES		166
APPENDIX		174

LIST OF FIGURES

<u>FIGURE</u>	<u>TITLE</u>	<u>PAGE</u>
1.1	Cross Section of Typical Tubular Combustion Chamber Showing the Air Distributuion.	6
1.2	Schema of Final Apparatus for Acoustic Control of Dilution Mixing Processes.	7
2.1	The Sketch of Flow Description of Jet in Crossflow.	19
2.2	The Configuration of the Flow in the Plane of Symmetry.	20
2.3	The Delineation of Jet Boundaries in Crossflow for (a) $X/D = 1.0$, $Z/D = 0.0$, and, (b) $X/D = 2.0$, $Z/D = 0.0$.	21
3.1	Schematic Diagram of the Test Rig.	31
3.2	View Looking Upstream from the Main Settling Chamber.	32
3.3	Sketch of a Rake of Pitot Tubes for Flow Metering, installed on 20.3 cm Dia. Main line.	33
3.4	(a) Position of Ref. Velocity Measurement, and (b) Sketch of Pitot-Static Tubes.	34
3.5	Test Section Crossflow Calibration in terms of the Product of Test Section Density and Ref. Velocity versus the Crossflow Mass Flow Rate.	35
3.6	The Performance Curve of a 56 KW Air Blower with a 20.3 cm. Diameter Pipe Line.	36
3.7	View Looking Upstream from the Test Section.	37
3.8	View Looking Downstream from the Test Section with Loudspeaker Drivers coupled to the Pipe-Jet Flow Tubes.	37
3.9	View of Single Loudspeaker with a Jet set-up for Bottom Bypass Line.	38

3.10	View of Jet Orifice Bolted in the Test Section (with side wall window removed).	38
3.11	Sketch of Cross Section through Orifice.	39
3.12	Plan of the Measurement Stations in the Test Section Ceiling.	40
3.13	X-Y-Z Traverse Mechanism Mounted on Top of the Test Section.	41
3.14	Instrumentation Setup for Frequency Response Measurement.	42
3.15	Instrumentation Setup for Jet Flow Mixing with Crossflow Experiment.	43
3.16	The Data Acquisition System (M.E.D.A.S.).	44
4.1	Schematic Diagram of Test Rig from Ref. (3).	58
4.2	The Calibration Results of Mass Flow Rate for (i) Top and (ii) Bottom Orifice Plate Flowmeters.	59
4.3	Mean Velocity Profiles across Entrance, Middle, Exit Planes for $U_{\infty} = 15.11$ m/s.	63
4.4	U_{rms} Profiles across Entrance, Middle, Exit Planes for $U_{\infty} = 15.11$ m/s.	65
4.5	Mean Velocity Profiles across Entrance, Middle, Exit Planes for $U_{\infty} = 75.45$ m/s.	67
4.6	U_{rms} Profiles across Entrance, Middle, Exit Planes for $U_{\infty} = 75.45$ m/s.	69
4.7	Frequency Response of the Mechanical System with No Air Flow for 1.75 m. long, 20.00 mm. Diameter Bore Connecting Tube.	71
4.8	Frequency Response of the Mechanical System with No Air Flow for 0.14 m. long, 20.00 mm. Diameter Bore Connecting Tube.	72

4.9	Frequency Response of Mechanical System for Constant Input Current (2.0 Amp.) with Air Flow From $U_j = 10.65 - 42.70$ m/s.	73
4.10	Typical Anemometer Signals of Velocity Wave Forms on Centre-Line in the Jet Exit Orifice Plane, $U_j = 19.0$ m/s, 250 Hz, 9.53 mm Dia.	76
4.11	Dimensionless Pulsation Strength versus Dimensionless Driving Power for 19.93 mm. Diameter Jet Orifice, 208 Hz.	77
4.12	Pulsation Strength versus Acoustic Driving Power with Air Flow, $U_j = 10.65 - 42.70$ m/s, $D = 19.93$ mm., 208 Hz.	78
4.13	Pulsation Strength versus Acoustic Driving Power with Air Flow, $U_j = 10.65$ m/s, and $U_\infty = 6.69$ m/s, for 208 Hz and 1072 Hz.	79
5.1	Mean Velocity Profiles across Entrance Plane at $X/D = -1.5$ for $U_j = 10.37$ m/s and $U_\infty = 10.32$ m/s.	101
5.2	U_{rms} Turbulence Profiles across Entrance Plane at $X/D = -1.5$ for $U_j = 10.37$ m/s and $U_\infty = 10.32$ m/s.	102
5.3	Mean Velocity Profiles across Entrance Plane at $X/D = -1.5$ for $U_j = 42.04$ m/s and $U_\infty = 10.32$ m/s.	103
5.4	U_{rms} Turbulence Profiles across Entrance Plane at $X/D = -1.5$ for $U_j = 42.04$ m/s and $U_\infty = 10.32$ m/s.	104
5.5	The Blockage Effect Comparison of Mean Velocity Profiles across Entrance Plane, $X/D = -1.5$ for $U_j = 10.37$ m/s, $U_\infty = 10.32$ m/s and $U_j = 42.04$ m/s, $U_\infty = 10.32$ m/s.	105

5.6	Structure of Jet Contour Constructed from Actual Velocity Profiles.	106
5.7	Mean Velocity Profiles on Centre Plane for $U_j = 13.20$ m/s, $U_\infty = 10.06$ m/s, 208 Hz, $W = 52.80$ Watts, $St = 0.31$, $U_e = 22.00$ m/s.	107
5.8	Mean Velocity Profiles on Centre Plane for $U_j = 23.27$ m/s, $U_\infty = 10.27$ m/s, 208 Hz, $W = 52.80$ Watts, $St = 0.18$, $U_e = 20.00$ m/s.	108
5.9	Mean Velocity Profiles on Centre Plane for $U_j = 34.30$ m/s, $U_\infty = 10.27$ m/s, 208 Hz, $W = 52.00$ Watts, $St = 0.12$, $U_e = 18.50$ m/s.	109
5.10	Mean Velocity Profiles on Centre Plane for $U_j = 46.22$ m/s, $U_\infty = 10.13$ m/s, 208 Hz, $W = 51.20$ Watts, $St = 0.09$, $U_e = 14.00$ m/s.	110
5.11	U_{rms} Turbulence Profiles on Centre Plane for $U_j = 13.20$ m/s, $U_\infty = 10.06$ m/s, 208 Hz, $W = 52.80$ Watts, $St = 0.31$, $U_e = 22.00$ m/s.	111
5.12	U_{rms} Turbulence Profiles on Centre Plane for $U_j = 23.27$ m/s, $U_\infty = 10.27$ m/s, 208 Hz, $W = 52.80$ Watts, $St = 0.18$, $U_e = 20.00$ m/s.	112
5.13	U_{rms} Turbulence Profiles on Centre Plane for $U_j = 34.30$ m/s, $U_\infty = 10.27$ m/s, 208 Hz, $W = 52.00$ Watts, $St = 0.12$, $U_e = 18.50$ m/s.	113
5.14	U_{rms} Turbulence Profiles on Centre Plane for $U_j = 46.22$ m/s, $U_\infty = 10.13$ m/s, 208 Hz, $W = 51.20$ Watts, $St = 0.09$, $U_e = 14.00$ m/s.	114
5.15	Peak Value of Turbulence versus Relative Pulsation Strength at Jet Centre in the Orifice Exit Plane, $X/D = 0.0$, $Y/D = 0.2$.	115

- 5.16 Lateral Mean Velocity and U_{rms} Turbulence Profiles Showing Symmetry at $X/D = 3.0$,
 $U_j = 25.27$ m/s, $U_\infty = 9.74$ m/s, 208 Hz,
 $W = 51.20$ Watts, $St = 0.16$, $U_e = 15.50$ m/s. 116
- 5.17 Lateral Mean Velocity and U_{rms} Turbulence Profiles Showing Symmetry at $X/D = 3.0$,
 $U_j = 37.60$ m/s, $U_\infty = 9.73$ m/s, 208 Hz,
 $W = 50.40$ Watts, $St = 0.11$, $U_e = 14.00$ m/s. 118
- 5.18 Lateral Mean Velocity Profiles, $U_j = 13.20$ m/s,
 $U_\infty = 10.06$ m/s, at $X/D = 1.5, 3.0, 6.0$.
(Refer Fig. 5.7 for Operating Conditions). 120
- 5.19 Lateral Mean Velocity Profiles, $U_j = 23.27$ m/s,
 $U_\infty = 10.27$ m/s, at $X/D = 1.5, 3.0, 6.0$.
(Refer Fig. 5.8 for Operating Conditions). 121
- 5.20 Lateral Mean Velocity Profiles, $U_j = 34.30$ m/s,
 $U_\infty = 10.27$ m/s, at $X/D = 1.5, 3.0, 6.0$.
(Refer Fig. 5.9 for Operating Conditions). 122
- 5.21 Lateral Mean Velocity Profiles, $U_j = 46.22$ m/s,
 $U_\infty = 10.13$ m/s, at $X/D = 1.5, 3.0, 6.0$.
(Refer Fig. 5.10 for Operating Conditions). 123
- 5.22 Lateral U_{rms} Profiles, $U_j = 13.20$ m/s,
 $U_\infty = 10.06$ m/s, at $X/D = 1.5, 3.0, 6.0$.
(Refer Fig. 5.7 for Operating Conditions). 124
- 5.23 Lateral U_{rms} Profiles, $U_j = 23.27$ m/s,
 $U_\infty = 10.27$ m/s, at $X/D = 1.5, 3.0, 6.0$.
(Refer Fig. 5.8 for Operating Conditions). 125
- 5.24 Lateral U_{rms} Profiles, $U_j = 34.30$ m/s,
 $U_\infty = 10.27$ m/s, at $X/D = 1.5, 3.0, 6.0$.
(Refer Fig. 5.9 for Operating Conditions). 126

- 5.25 Lateral U_{rms} Profiles, $U_j = 46.22$ m/s,
 $U_\infty = 10.13$ m/s, at $X/D = 1.5, 3.0, 6.0$,
(Refer Fig. 5.10 for Operating Conditions). 127
- 5.26 Jet Boundary Contour for Various Velocity
Ratios for (i) "No-Drive" and (ii) "With-
Drive" cases. 128
- 5.27 Mean Velocity Profiles on Centre Plane at
Constant Strouhal Number for $U_j = 18.99$ m/s,
 $U_\infty = 9.82$ m/s, $U_e/U_j = 0.00 - 1.53$, 208 Hz,
 $St = 0.22$. 130
- 5.28 U_{rms} Turbulence Profiles on Centre Plane at
Constant Strouhal Number for $U_j = 18.99$ m/s,
 $U_\infty = 9.82$ m/s, $U_e/U_j = 0.00 - 1.53$, 208 Hz,
 $St = 0.22$. 138
- 5.29 Comparative Centre Plane Velocity-Axis Trajec-
tory for Steady Jets in a Confined Crossflow,
for $U_j = 13.20, 23.27, 34.30, 46.22$ m/s,
and $U_\infty = 10.06, 10.27, 10.27, 10.13$ m/s. 146
- 5.30 Comparative Centre Plane Velocity Trajectory
for Steady Jet versus Unsteady Jet for same
Acoustic Driving Power of 50.00 watts,
for $U_j = 13.20, 23.27, 34.30, 46.22$ m/s,
and $U_\infty = 10.06, 10.27, 10.27, 10.13$ m/s. 147
- 5.31 Penetration Trajectory for Different Driving
Power Conditions on Centre Plane at Constant
Strouhal Number for $U_j = 18.99$ m/s and
 $U_\infty = 9.82$ m/s, 208 Hz, $U_e/U_j = 0.00 - 1.53$,
 $St = 0.22$. 151
- 5.32 Centre Plane Penetration Trajectory versus
Relative Pulsation Strength at Constant
Strouhal Number for $U_j = 18.99$ m/s and
 $U_\infty = 9.82$ m/s, 208 Hz, $U_e/U_j = 0.00 - 1.53$,
 $St = 0.22$. 152

5.33	The Variation of Jet Penetration with Relative Pulsation Strength at Different Downstream Locations, Showing Strouhal Number Effect.	153
5.34	Jet Penetration versus Pressure Dropped across Jet Orifice at Constant Strouhal Number.	154
5.35	Overall Turbulence (U°_{rms}) for Steady Jet at Different Downstream Locations for the Velocity Ratios of 1.31, 2.26, 3.34, 4.56.	155
5.36	Overall Change in Turbulence at Different Downstream Locations for the Velocity Ratios of 1.31, 2.26, 3.34, 4.56, with Driving Power of 50 Watts.	156
5.37	Overall Change in Turbulence at Different Downstream Locations at Constant Strouhal Number for $U_j = 18.99$ m/s, $U_{\infty} = 9.82$ m/s, $St = 0.22$, $U_e/U_j = 0.00 - 1.53$, 208 Hz.	157
5.38	Overall Change in Turbulence with Relative Pulsation Strength at $X/D = 3.0$, Showing Strouhal Number Effect.	158
5.39	Velocity Traverse Quality at Different Downstream Locations for Velocity Ratios of 1.31, 2.26, 3.34, 4.56, with Driving Power of 50 Watts.	159
5.40	Velocity Traverse Quality at Different Downstream Locations at Constant Strouhal Number for $U_j = 18.99$ m/s, $U_{\infty} = 9.82$ m/s, $St = 0.22$, $U_e/U_j = 0.00 - 1.53$, 208 Hz.	161

NOMENCLATURE

A	=	Current
D_∞	=	Test section hydraulic diameter
D, D_j	=	Jet diameter
f	=	Driving frequency
H	=	Tunnel height
m_a	=	Air mass flow rate
\hat{P}	=	Sound pressure level
P_d	=	Blower discharge pressure
P_{oj}	=	Stagnation pressure of the jet
P_s	=	Static pressure in Test Section
$\Delta P_j = P_{oj} - P_s$	=	Pressure dropped across jet nozzle
Q_u	=	Velocity Traverse Quality
Re_j	=	Reynolds number of jet, $\rho_j U_j D_j / \mu_j$
Re_∞	=	Reynolds number of crossflow, $\rho_\infty U_\infty D_\infty / \mu_\infty$
St	=	Strouhal number, $f D_j / U_j$
U_e	=	Centre-line jet velocity excitation pulsation amplitude or pulsation strength at the orifice exit plane (unsteady flow)
U_j	=	Centre-line unexcited steady jet velocity at orifice exit plane
U_∞	=	Average crossflow velocity in the X-axis direction at $X/D = -1.5$ plane
U_{rms}	=	Local r.m.s. value of fluctuating velocity in X-axis direction

U_{rms}°	= Overall r.m.s. fluctuating velocity in X direction for each X/D plane
ΔU_{rms}°	= Change in overall r.m.s. value ("no-drive" and "with-drive")
U	= Local velocity in X direction
U_{ref}	= Reference velocity from pitot-static tubes in Test Section
\dot{W}	= Input power to the loudspeaker driver
X	= Axial distance downstream from orifice exit plane
X, Y, Z	= Space coordinates
Y_0	= Initial jet penetration without acoustic drive
ΔY	= Change in jet penetration ("no-drive" and "with-drive")
ρ_{∞}	= Test section or crossflow density
ρ_j	= Jet density
μ_{∞}	= Crossflow viscosity
μ_j	= Jet viscosity

CHAPTER 1

INTRODUCTION

1.1 Prologue

The phenomenon of a turbulent jet of fluid injected perpendicularly into a uniform crossflow occurs in numerous situations. Recent investigations of this phenomenon have been motivated by a variety of possible engineering applications, namely :

- (a) smoke plumes issuing from tall chimney stacks on a windy day;
- (b) flares from the safety system of a petroleum plant;
- (c) impingment cooling schemes for turbine blades;
- (d) discharge of an effluent into a waterway;
- (e) aerodynamic characteristics of V/STOL aircraft in transition flight configurations;
- (f) processes of cooling and mixing combustion gases in a gas turbine combustion chamber.

In fact, it is the last item mentioned above which has motivated this research study.

It is well-known that mixing processes are of great interest and importance to combustion engineers, especially in the design of a gas turbine combustion chamber. Jet mixing processes play a

vital role in achieving satisfactory combustor performance. In the primary zone, good mixing can promote efficient combustion for a high burning rate and minimum soot and nitric oxide pollutant formation. In the intermediate zone, rapid mixing of the injected air with the hot gas from the primary zone is needed to accelerate soot oxidation and to convert any dissociated species into normal products of combustion. Finally, in the dilution zone, the attainment of a satisfactory temperature pattern factor at the combustion chamber exit (ie, temperature profile distribution at the entrance of the 1st turbine stage) is dependent on the proper mixing of air and combustion products.

1.2 Origin of The Present Work

There have already been many research studies on experimental investigations and theoretical modelling of the penetration and mixing characteristics of a single jet or multiple jets of cooling air directed normally into a crossflow (heated or unheated), in a constant area duct. The studies were motivated by the considerations of dilution zone mixing in gas turbine combustion chambers. This rapid mixing of the diluent fluid with hot combustor gases leaving the primary zone was desired to (a) provide a suitable temperature distribution at the turbine inlet, (b) provide a rapid quench for any continuing chemical reaction, and (c) reduce the length of the combustion chamber. However, none of these studies had considered the possible improvements in

mixing which might ensue from the externally controlled modulated jets interacting with a crossflow.

The results from Vermeulen et al. (1,2,9,15,26,37) clearly showed that acoustically pulsating a jet flow into the surroundings had strong effects on the mixing behaviour and the entrainment rate. This evidence suggested that the application of acoustic mixing as a stirring technique to the dilution air flow would be beneficial to the mixing effectiveness with the hot main combustion gases. Beneficial changes in the combustion chamber exit plane temperature distribution caused by the acoustic control of the diluent air jets were clearly observed. Figure 1.1 illustrates the cross section of a typical tubular combustion chamber showing the air distribution. Figure 1.2 shows the schematic diagram of the apparatus used for the acoustic control of dilution mixing processes.

In addition to Vermeulen's work, numerous studies have been carried out into the acoustic excitation of jets, boundary layers, and separated flows, as reported by Refs. (5,10,17,18,20,22,25,32,42,46,51). However, apparently no work has been conducted on the mixing behaviour of an acoustically excited jet with a crossflow. Therefore, the main objective of the present study is to carry out extensive experimental work in order to understand the mixing behaviour of an acoustically excited jet with a confined crossflow, so that, the previous work by investigators (9,15,26) may be better interpreted and the future potential of the

technique assessed.

1.3 Scope of The Thesis

The objective of this thesis is to study experimentally the mixing characteristics of an acoustically modulated jet with a confined uniform crossflow. The experimental investigations included the detailed measurements of velocity and turbulence level profiles.

The work was divided into the following sections :-

- (1) to optimise the existing 56 kW blower - pipe operating range, so that a suitable range of velocity ratios (jet/crossflow) for experimental investigation could be easily achieved;
- (2) to carry out detailed measurements of mean axial velocity and its corresponding fluctuating velocity for values of jet-to-crossflow velocity ratio of 1.31, 2.26, 3.34, 4.56 for "no-drive", and "with-drive" at the system optimum response frequency of 208.0 Hz;
- (3) to investigate the effects of changing driving power from 0 to 160 Watts at a jet velocity that has an optimum Strouhal number of 0.22, as stated in Refs (1,2). The velocity ratio of jet-to-crossflow was about 1.93.

Chapter (2) provides a literature review of previous studies on steady and non-steady jets interacting with a uniform crossflow.

Chapters (3) and (4) present information about the

experimental rig and some results due to necessary modifications.

Chapter (5) presents and discusses the detailed results of the experimental investigations on the externally controlled acoustically pulsed jet flow injected vertically into a two dimensional crossflow.

Chapter (6) presents the conclusions from this research study.

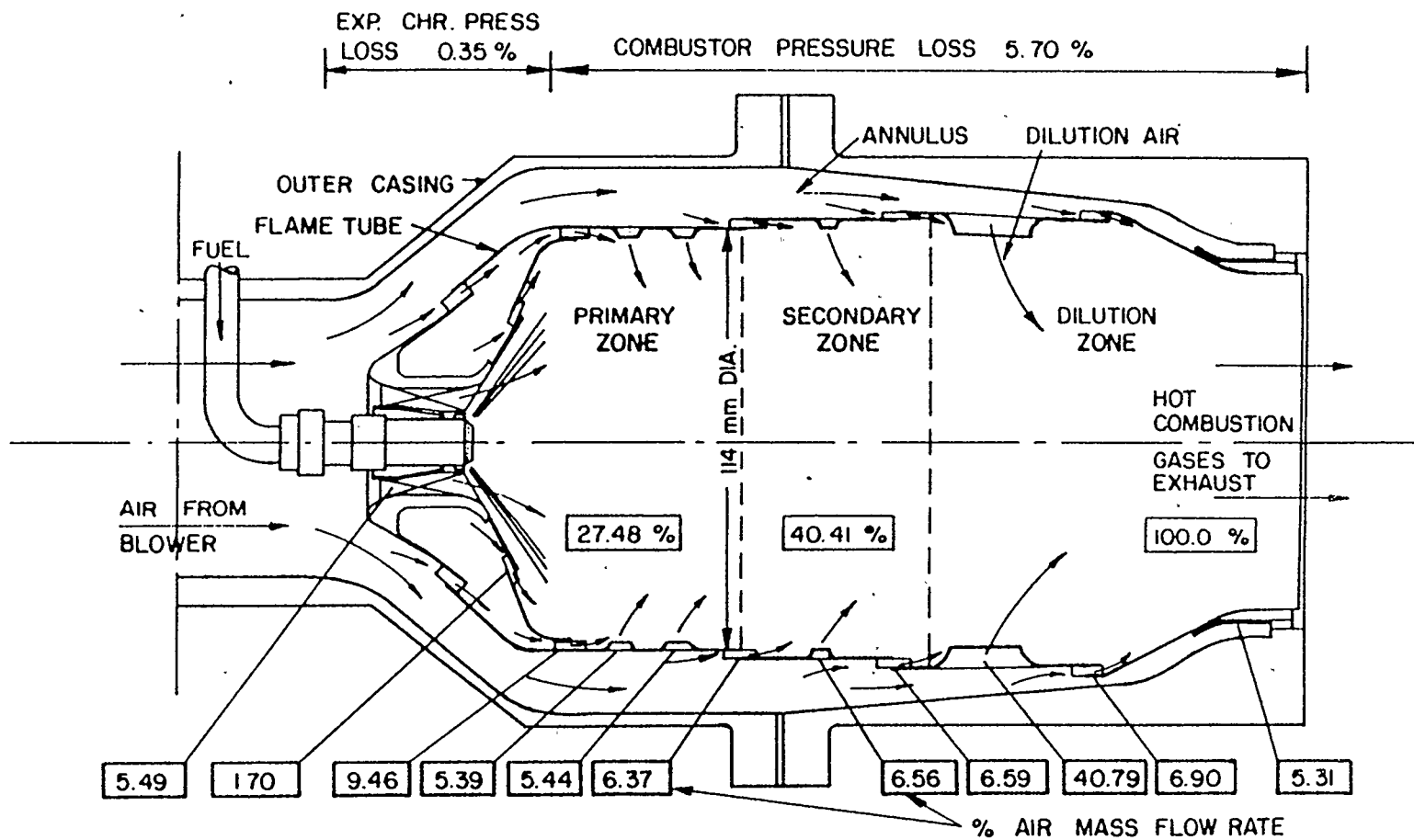


FIGURE 1.1 CROSS SECTION OF TYPICAL TUBULAR COMBUSTION CHAMBER SHOWING THE AIR DISTRIBUTION, TAKEN FROM REF. (15).

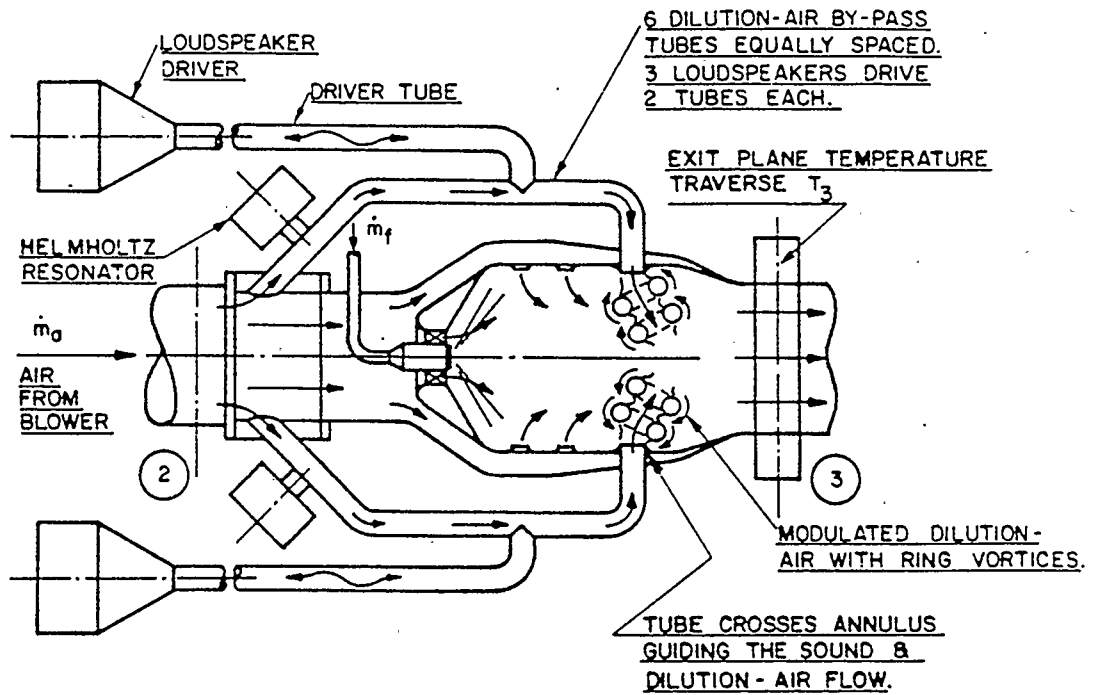


FIGURE 1.2 SCHEMA OF FINAL APPARATUS FOR ACOUSTIC CONTROL OF DILUTION MIXING PROCESSES, TAKEN FROM REF. (9).

CHAPTER 2

LITERATURE STUDIES

2.1 Physical Description of The Jet in a Crossflow

Figure 2.1 and Figure 2.2, taken separately from Refs. (31) and (40), schematically illustrate the representation of a jet in a uniform crossflow.

Starting at the jet exit plane at which the vertical velocity profile of the jet is relatively uniform, depending on the jet-to-crossflow velocity ratio, and the turbulence intensity is low as compared with what is consequently generated downstream. Immediately, upon entering the crossflow, the edges of the jet are subjected to intense shear stresses resulting from the velocity gradient between the jet and the crossflow, which eventually causes the jet to bend over. In the case of the free jet, where the external flow velocity is zero, uniform entrainment of the surrounding fluid occurs. The entrained fluid is accelerated as the jet spreads and the jet fluid is correspondingly decelerated. However, in the presence of the crossflow, the fluid entrainment is complicated by the potential flow field surrounding the jet.

The uniform crossflow decelerates as it approaches the jet boundary as if its passage is blocked by a rigid obstacle, and

creates a positive pressure region contributing to jet deflection, the crossflow bends around the jet column boundary surface (refer Figure 2.1) undergoing partial mixing with the jet flow.

The sides of the jet, which possess less momentum than the center of the jet, are subjected to a lateral shearing stress or lateral mixing processes and therefore are displaced towards the rear forming bound vortices as shown in Figure 2.1. Separation of the crossflow occurs at the rear and gives rise to a negative pressure region or wake, bending the jet. A similar phenomena exists for a circular cylinder in crossflow, but with the jet, the return flow in the center of the wake is carried downstream by the crossflow, and the entrained fluid into the jet moves rapidly along the jet direction. As a result, the interface of the two flows rolls up into periodically shed vorticity regions similar to those in the Von Karman-Bernard Street. Behind the jet column, the crossflow stream lines become roughly parallel again, but a large scale turbulent wake persists as with the solid cylinder at a comparable Reynolds number. The effect of the pressure forces and the lateral shear eventually alter the shape of the cross section of the jet from circular at the outlet to a characteristic kidney shape at the region of similarity of the velocity profile, Figure 2.2.

Chassaing et al. (40) state that, as in the case of the free jet, three zones can be distinguished in the evolution of a jet in the presence of a crossflow, as shown in Figure 2.2, namely :-

- (i) zone of residual inlet velocity,
- (ii) zone of accommodation,
- (iii) zone of velocity profile similarity.

In zone (i), the external fluid starts to be entrained by the jet, which as a consequence spreads, slows down and becomes curved. The characteristics of this zone are that only the outer circumferential part of the jet takes part in the mixing, the remainder forming the potential core, where the axial velocity remains at a constant magnitude.

In zone (ii), the maximum axial velocity begins to decrease due to the complete penetration of turbulent mixing on the jet. The velocity profile changes under the mixing action towards a fully developed state, and the curvature of the jet increases.

In zone (iii), the velocity profile is fully developed and a velocity profile similarity law has become established.

Figures 2.3 (a) and (b) present the delineation of the jet boundary in a crossflow. These figures, taken separately from Refs. (31) and (27), show the experimental results of mean velocity distributions and its corresponding turbulent levels on the plane of symmetry $Y/D = 0.0$ for $X/D = 1.0$, $Z/D = 0.0$, and $X/D = 2.0$, $Z/D = 0.0$ respectively. These schematic diagrams clearly depict various regions in the entire flow field, namely: the free stream region, the deflected jet region, the wake and vortex region. It is important to understand them, so that a better interpretation on experimental results can be clearly resolved.

2.2 General Information from the Literature

The flow field established by jet injection from a single hole into a mainstream has already received considerable attention, mainly due to the variety of possible engineering applications. As a result, the general flow characteristics of a single jet discharged at right angles to a crossflow are well-known, and hence, there is available considerable information from experimental investigations and theoretical predictions by many researchers.

To study the physical characteristics of a jet flowing into a crossflow, some researchers have selected a flow visualization method as the measuring technique, whilst others have chosen a tedious and time consuming direct flow measurement method by means of velocity and fluctuating turbulence profiles using a hot wire anemometer, or temperature profiles. These experimental data provide understanding and interpretation of the physical phenomenon; determine the jet structure and envelope, the vortexlike structure and strength, the entrainment rate and mixing, and the jet penetration and trajectory. Grabb et al. (21) provide a table summarising the results of experimental studies in terms of parameters such as jet diameter, incident angle, jet velocity, crossflow velocity, and velocity ratios. These parameters are the important factors in practice which influence the rate of mixing, as mentioned in Lefebvre's recent book (14).

The experimental approaches of studying the physical and

structural characteristics of the flow conditions for isothermal mixing of a jet and crossflow of the same fluid have been carried out by many researchers. Andreopoulos (4), Andreopoulos and Rodi (11), Moussa et al. (31), Chassaing et al. (40), McMahon et al. (49), Keffer and Baines (52) and Abramovich (54) present a qualitative description and detailed explanation of the mechanics of the mixing interaction and the shape of the flow field developed.

It seems to indicate that the study around the near-field region, which defined as the region of the flow from the jet exit to a distance of a few diameter downstream of the exit, of a jet discharge normal to a crossflow should be mentioned here, mainly because it includes a lot of vital information about the complex flow phenomenon, and provides useful knowledge for better understanding about the significant effect. McMahon et al. (49) provided quantitative evidence that there was vortex shedding behind a turbulent jet in a crossflow. These shed vortices travelled in a downstream direction along the floor rather than in the same direction as the jet. Ramsey and Goldstein (45) stated that as the jet entered, the crossflow was drawn from the side to fill the low pressure region immediately downstream of the jet. This interface indeed quickly generated a wake region behind the jet with periodically shed vortices which was similar to Von Kerman-Benard Street from a solid circular cylinder.

Moussa et al. (31) stated that a considerable amount of

dynamical adjustment took place in this near-field region. This near-field region characterised the subsequent behaviour and development of the jet, its wake, and the crossflow in the vicinity of this mixing region. The existence of the rapid evolution of the flow gave rise to a pair of counter-rotating bound vortices attached to the lee side of the jet boundary, to fast development of the turbulent and mean vorticity, to a vortex shedding system and to the large rates of entrainment of crossflow into the jet have been found experimentally and investigated by many workers, (4), (11), (35), (39), (44), (52). These bound vortices caused internal circulation and large scale motion that mixed within the jet and entrained the external crossflow fluid by the lateral shearing action. Keffer and Baines (52) stated that the total mass flow entrained into the outside jet boundary for a jet in crossflow was much greater than by a free jet into a stagnant surrounding fluid. Kamotani and Greber (44) extended Keffer and Baines's work (52) to farther downstream regions, and included a detail investigation of the circulating flow in the cross planes. This circulating flow was a vortex-like structure, which was dominant feature of the downstream jet. Their detailed experimental results from velocity and temperature distributions revealed that the jet spread and decay rate were faster for a jet in crossflow than a free jet case, and further concluded higher entrainment rate than a free jet.

Fearn and Weston (39) carried out experimental study by means

of extensive velocity field measurements at downstream distances. They correlated the velocity field with a model to investigate the physical properties of the vortices in term of its core size, vortex strength, vortex spacing and diffuseness associated with a jet in crossflow.

Bergeles et al. (35) conducted detailed investigation in the vicinity of the injection hole and upstream from the hole and found that even at a low injection rate of 0.046, there was still a clearly identifiable reverse flow region springing from the downstream side of the hole. Andreopoulos et al. (11) confirmed further that the reverse flow did occur at very near the wall in his study. Andreopoulos (4) investigated the area where the initial jet layer interacted with the oncoming crossflow boundary layer, detected experimentally the annular mixing layer rolling up and toroidal vortices were formed. He also concluded that the flow in the interaction region 'time shared' between four possible zones, namely irrotational crossflow, irrotational pipe flow, turbulent boundary layer, and turbulent pipe flow.

The interference effect on the jet outlet profile due to the presence of the crossflow seems to be quite limited. However, the data for the measured velocity distribution by Bergeles et al. (35) showed that for low velocity ratios, the velocity profile across the exit plane of the jet could be considerably non-uniform. A more complete survey on mean flow velocity profiles, in three-dimensions, was further carried out by workers

(4), (11), (21). Grabb et al (21) also found the existence of non-uniform velocity profile in the plane of the jet exit. Andreopoulos et al. (11) stated that for a low velocity ratio, there was a strong interaction between jet and crossflow right at the exit region, which caused a non-uniform exit velocity profile and a sharp bending over the jet which started already inside the discharge pipe. He also concluded that the bending of the jet column and the extent of wake region were mainly dependent on the jet-to-crossflow velocity ratio, and at higher velocity ratios, the bound vortex motion was stronger and persisted longer in the downstream direction. This kind of flow phenomenon was also reported by workers, (44), (45), (52). Andreopoulos (4) stated that in cases for high velocity ratios, the near field of the jet in crossflow was largely controlled by the complex inviscid dynamics, so that the influence of turbulence on the flow was rather limited. However, he also said that the flow further downstream was always influenced by turbulence and at small velocity ratios, even the near field was turbulence dominated. Very few measurements of turbulence quantities have been reported so far. Furthermore, Andreopoulos (19) conducted a study in order to investigate the significant impact effect due to the presence of crossflow, and found that non-uniformities of the velocity profiles inside the supply pipe could be detected as far as 3 pipe-diameters upstream of the exit plane for a small velocity ratio, but at high velocity ratios, the pipe flow was very weakly

affected by the crossflow.

The study of jet penetration and jet center-line trajectory has been the subject of several experimental investigations by various workers (38), (44), (45). Based on their experimental results, they tried to correlate the data in order to develop an empirical equation. Odgers and Wojcikowski (38) stated that their results were good for low values of jet penetration (about 38 mm or less) because for high velocity ratios, the wall effect was quite significant. Kamotani and Greber (44) claimed that the jet velocity trajectory was mainly determined by the jet-to-crossflow momentum ratio and stated that the jet structure was clearly dominated by a vortex wake which formed behind the jet. A visualization technique was also being employed by these workers in all their experimental studies.

Analytical investigations for the prediction of the jet penetration and trajectory have been carried out by several researchers with various degree of success. The analytical approaches have been based on one of the following assumptions : 1-Dimensional Flow (41), 2-Dimensional Flow (27,34), or 3-Dimensional Flow (28,29,33). In general, the mathematical model formulations were based on the mass continuity, the momentum equation, the turbulence stress, the length of the potential core, and the bound vortex circulation. Bojic and Eskinazi (27) claimed that it was the first time that the influence of the bound vortex had been taken into account in this kind of analytical modelling.

All of the analytical results were compared with the available experimental data. They respectively claimed that their results showed a good agreement for the velocity ratios of 2 to 12. However, their results were not applicable to the current experimental study, mainly because all of their studies considered a jet issuing into a infinite uniform velocity crossflow, rather than a confined crossflow. Although Stoy and Ben-Haim (41) seemed to carry out similar experimental setup, yet the ratio value of tunnel height to jet diameter was about 3.05 which was lower than the current investigation, 5.75. Therefore, it is quite difficult to compare the results versus each other, due to the presence of the wall effect.

So far, the work just reviewed was largely involved with steady jets interacting with a crossflow. On the other hand, a pulsating jet flow mixing with a crossflow is a new research subject. There is very limited information on this particular topic. However, there seems to be an increasing number of publications about the pulsating free jet. Stone and Mckinzie (10) have carried out an extensive review of this area including the acoustic excitation of wakes, boundary layers, and separated flows. They concluded that acoustic excitation was a promising new means of controlling shear layers and examined some potential applications of practical aerospace systems. Using acoustic excitation as a technique to pulse the jet flow has been considered by many researchers. They studied and investigated the

interaction behaviour of the pulsed jet in a similar manner as for a free jet in term of mean flow structure (5,8,13,46,47,48,50), jet spread and widening (7,8,13,18), jet noise production and suppression (5,6,24,36), vortex evolution (12,16,23,55,56,57), shear layer instability (7,20,32,46), jet entrainment rate and mixing (1,2,3,9,15,17,18,42). They documented the experimental results and compared the results for differences and attempted to establish a simple fundamental flow mechanism involved, in order to understand and interpret the flow behaviour, so that an analytical technique or modelling might be applied to acoustic streaming phenomenon. Vermeulen et al. (9,15) sucessfully pioneered the application of the acoustically pulsed air jet to the dilution zone mixing of a gas turbine combustion chamber.

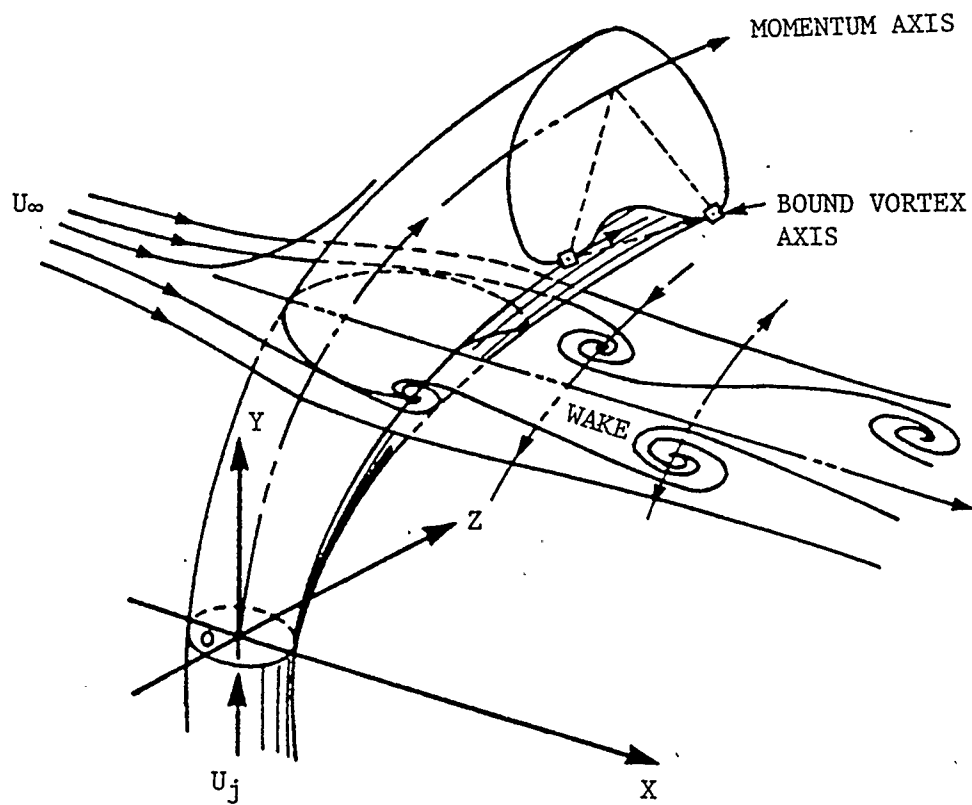


FIGURE 2.1 THE SKETCH OF FLOW DESCRIPTION OF JET IN CROSSFLOW, TAKEN FROM REF. (31).

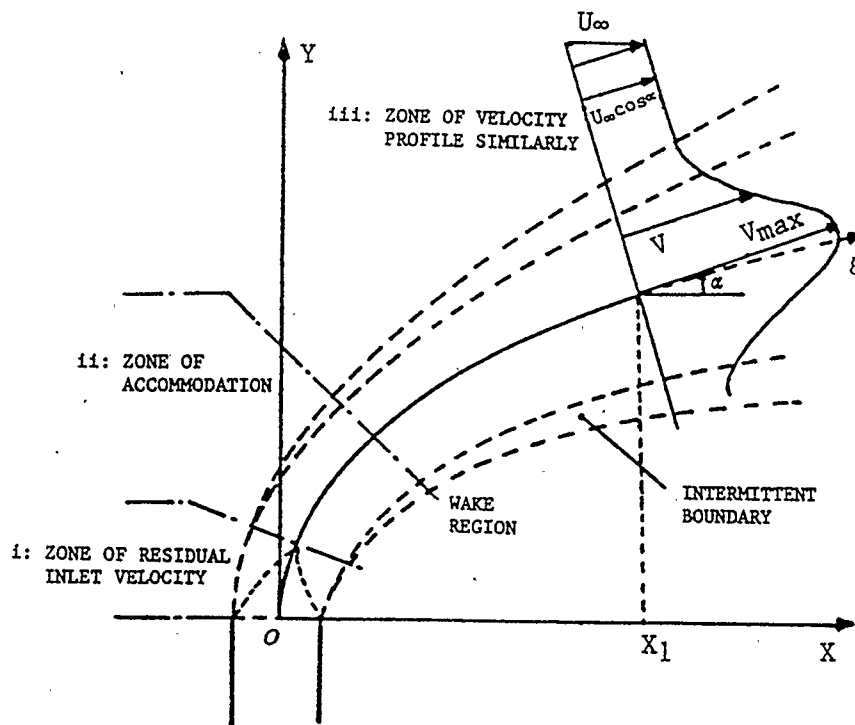


FIGURE 2.2 THE CONFIGURATION OF THE FLOW IN THE PLANE OF SYMMETRY, TAKEN FROM REF. (40).

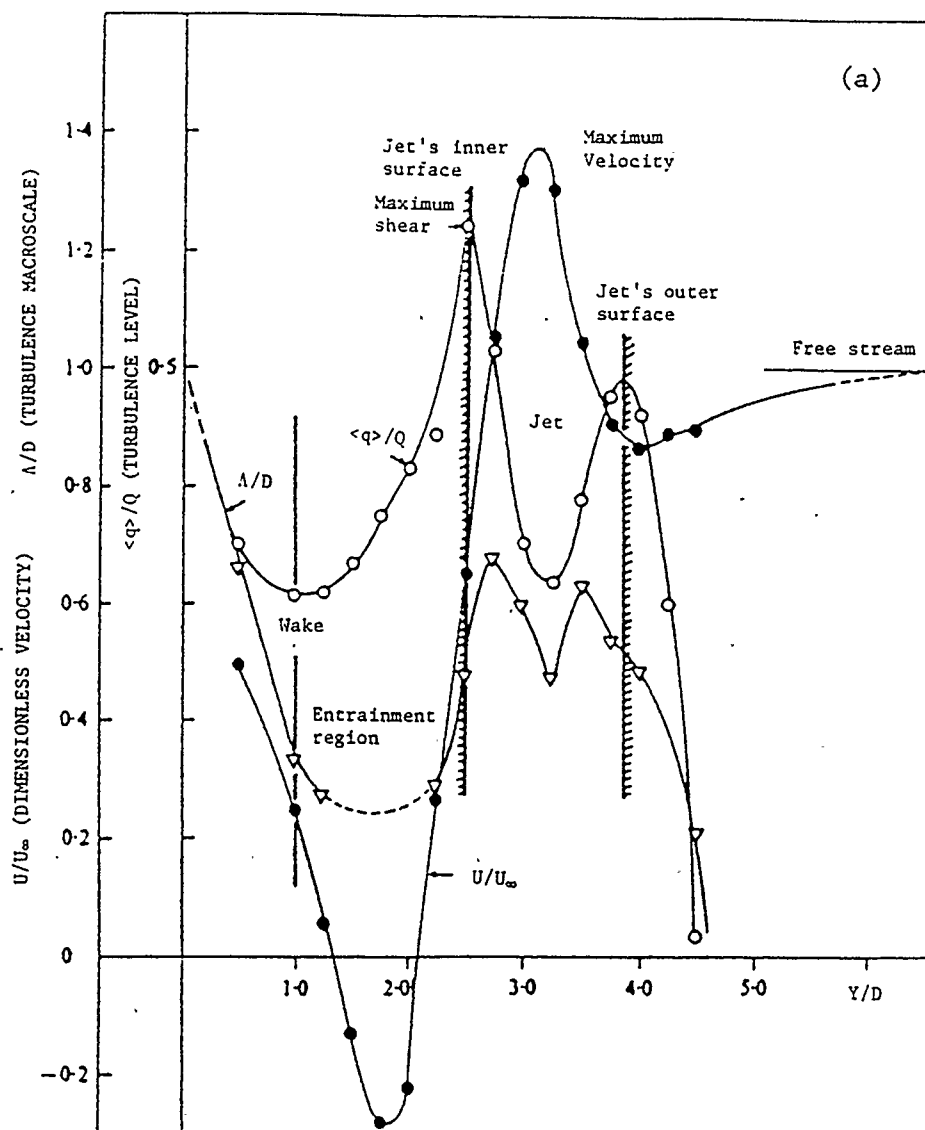


FIGURE 2.3 THE DELINEATION OF JET BOUNDARIES IN CROSSFLOW FOR $X/D = 1.0$, $Z/D = 0.0$, TAKEN FROM REF. (31).

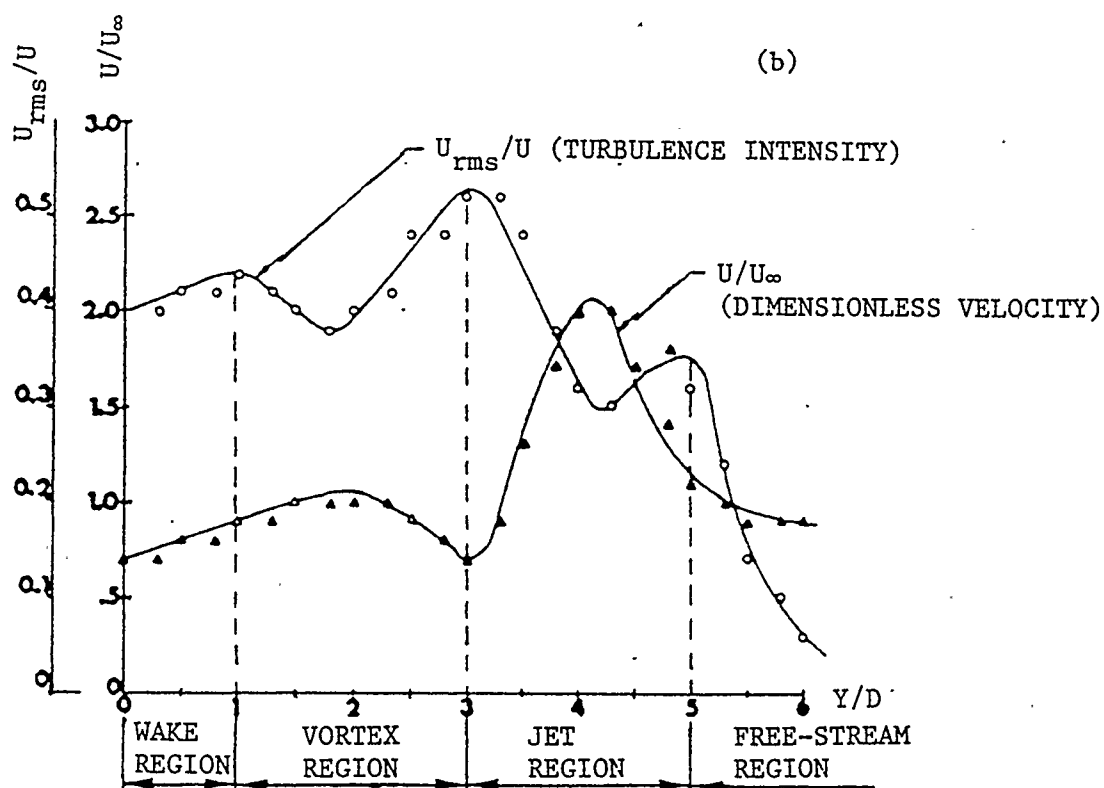


FIGURE 2.3 CONTINUED. (FOR $X/D = 2.0$, $Z/D = 0.0$, TAKEN FROM REF. (27))

CHAPTER 3

EXPERIMENTAL APPARATUS

3.1 Description of Apparatus

A schematic diagram of the test rig is shown in Figure 3.1. The overall test rig was about 12 metres long, and was an open circuit type of wind tunnel which could be used for carrying out either cold or hot crossflow studies, depending on the need.

The inlet of the test rig was connected to a moderate sized centrifugal blower, with a delivery rate of about 2.0 kg/s at sea level, which was driven by a 56 kW induction motor at a speed of 3560 rpm. The compressed air was delivered to the 20.3 cm. diameter inlet pipe via a short transition element, bend and a throttle valve, as shown in Figures 3.1 and 3.2. The pipe delivered air to the apparatus which consisted of three flow streams, namely one main stream or crossflow and two identical top and bottom bypass diluent air flows which later emerged together with the crossflow in the test section.

The inlet flow meter section was made from two diametral rakes of pitot tubes, as shown in Figure 3.3 and was installed in the 20.3 cm. diameter inlet line at about 1 pipe-diameter upstream of the Y branch fitting. This flow meter was designed and built

by Mr. P. Grabinski, a fellow student, as part of his research project. The mass flow rate delivered by the blower was measured by this flow meter using the ten-point log-linear pitot method as mentioned in Ower and Pankhurst (30) with the bypass lines (or the diluent airflow lines) closed. This mass flow rate was also referenced to the velocity measured by pitot-static tubes at a particular reference position in the test section, as shown in Figure 3.4. This calibration established a very convenient method for measuring the crossflow mass flow rate. The temperature and pressure at the entrance to the flow meter during the tests were in the range of 315.75 - 324.25 °K and 92.24 - 104.37 kPa respectively. The result of the mass flow versus reference velocity calibration is shown in Figure 3.5 and the performance curve for the blower is shown in Figure 3.6. The total mass flow rate is the sum of the crossflow from the reference velocity calibration plus the two bypass diluent air streams measured by orifice meters in the bypass lines. Each orifice meter was designed by Yu (3), to British Standard B.S.:1042 (53), with a throat to pipe area ratio of 0.3818.

The test rig was modified to a 20.3 cm. diameter inlet pipe size from the former 7.6 cm. diameter inlet pipe size, as part of this project, in order to improve performance and was mainly due to the following reasons :-

- (i) excessive pressure drop of the design system,
- (ii) greater mass flow rate demanded for current and

future experimental purposes.

Figure 3.6 shows the improvement in performance achieved.

A previously employed combustion chamber from Vermeulen et al. (26) was replaced in this particular experimental set up since a cold flow study only was required, however, it was feasible to reinstall it for a future hot crossflow experimental study with some minor mounting modifications.

The main plenum chamber had a 61 cm. by 34 cm. rectangular cross section and was about 92 cm. long, all of stainless steel. Three equally spaced, 16 mesh screens (pitch = 1.59 mm., and wire diameter = 0.41 mm.) were employed to eliminate the swirl and the large scale turbulence in the main crossflow. The air was then led into a two-dimensional nozzle with a contraction area ratio of 5.3 before entering the test section.

As shown by Figure 3.1 the inlet air mass flow was divided at the Y branch fitting to form top and bottom diluent air bypass streams, each of 50 mm. I.D. pipe and branching off at 45° from the main stream. Adjustable throttle valves plus orifice meters facilitated accurate flow control and mass flow rate measurement within the diluent air ducts. The delivered diluent air entered a diffuser and small settling chamber (45.7 cm. by 30.5 cm. by 15.6 cm.) and finally through a contraction unit, with a contraction area ratio of 8.0, at the end of which was a two-dimensional slot (30.5 cm. by 1.4 cm.). Two 16 mesh screens were installed equally spaced in the small settling chamber to smooth out the swirl and

the large turbulences as shown in Figure 3.1. Figure 3.7 shows the bypass air settling chambers supported by the main plenum chamber.

Ten opposed jets emerging from the roof and floor in the test section were designed by Yu (3) with the jet center spacing at 61.75 mm., which corresponds to the diluent jet center spacing in the typical combustion chamber as used by Vermeulen et al. (15). The flow to each of the jets is designed to be delivered by a straight 20 mm. I.D. tube and a 90° elbow from the end plate of the two-dimensional slot at the diluent air plenum chamber.

Connected at right angles to the jet tube was another tube of the same size, coupling to a cone speaker driver of about 400 Watts power rating. Thus, two acoustic drivers mounted on supporting stands, provided the excitation sources for the pulsating jet study, as shown in Figure 3.8. However, only a single jet with an orifice size of 19.93 mm. diameter from the bottom bypass line was eventually used for the present study, as shown in Figure 3.9. The other discharge holes were completely blocked off, Figure 3.10.

The pitot tubes, static tube, orifice plates were designed to be a flow metering device in accordance with N.P.L. Standard as in Ref. (30) and the British Standard B.S.:1042 as in Ref. (53). The pitot and static tubes were made of 3.175 mm. O.D. stainless tubing, with 0.7938 mm. I.D.. There were seven static side holes for static pressure reading, and they were located at 6 diameters

downstream from the tip. The distance from the tip to the stem was about 14 diameters as from Ref. (30).

The orifice plates were made of aluminum with a thickness of 3.18 mm. and the flow devices employed D and $D/2$ (D = pipe dia.) pressure tappings for measuring the flow rate. The pressure signals of the flow device were measured either with an oil micromanometer, an inclined water manometer or a calibrated electrical pressure transducer. A standard chromel alumel thermocouple was located upstream of the flow meter and was used for measuring the fluid temperature without interference with the flow device measurement.

3.2 Description of Test Section

Air jet injection and mixing took place in the test section which was a straight rectangular cross section duct (88.9 cm. by 34.2 cm. by 11.4 cm.). The size of this unit was similar to the one used by Walker and Kors (43), except that the height of the current test section was a duplication of the diameter of the flame tube at the dilution zone of the typical combustion chamber used in Ref. (15).

The injection plane, where jets discharged at right angles to the crossflow, was located at mid-length of the test section. Mild steel was primarily used for the construction of the test section in which two side wall windows and portions of the top and bottom tunnel sides were made of plexiglass to give provision for

future visualization experiments.

Interchangeable nozzles can be housed in the tunnel floor and ceiling to form a discharge configuration with the crossflow. This arrangement allows a range of nozzle sizes, up to an open pipe orifice, to be investigated. For the present investigation a 19.93 mm. dia. pipe orifice was used. Figure 3.10 shows the 19.93 mm. dia. open pipe orifice, duplicating the same exit geometry as that of the flame tube holes of the diluent air jets in the typical combustion chamber (15), positioned in the test section. Figure 3.11 illustrates the dimensions of the jet orifice.

A pattern of access holes in the tunnel ceiling was designed in order to allow vertical transversing of instruments across the test section, as shown in Figure 3.12. An X-Y-Z traversing mechanism was mounted on top of the test section as shown in Figure 3.13. This mechanism provided rigid support and accurate positioning for the measurement probe (hot-film anemometer probe) in the test section.

It should be noted, as mentioned by Yu (3), that the test rig could be changed into a free jet apparatus in the absence of the crossflow and the removal of the tunnel ceiling.

3.3 The Modulating Apparatus and Hot-Film Anemometer

The hot film anemometer was selected for test section measurements in the present work mainly because of (i) its wide use in research work for measuring time variation velocity and

turbulence data, (ii) only a cold flow study was to be carried out, and (iii) its fast response characteristics. The measured analogue signals were monitored by a digital storage oscilloscope and stored in a computer data acquisition system for eventual analysis.

A loudspeaker driver of about 400 Watts power rating was used to excite the jet. The instrumentation setups for frequency response measurement by B & K 2032 dual-channel FFT analyser and jet flow mixing with crossflow are illustrated in Figures 3.14 and 3.15 respectively. The sinusoidal signal was generated by the function generator and amplified by the 200 Watts amplifier to allow the excitation sources to be driven over a wide range of frequencies and powers. The input power to the driver speaker was measured by a voltmeter and ammeter, ignoring the phase change. The selected driving frequency could be easily and accurately identified by using the dual-channel FFT analyser.

3.4 Data Acquisition System

As mentioned in the above section, the analogue signals from the hot film sensor were not only monitored by a digital storage oscilloscope, but also stored in a computer data acquisition system from which the experimental data may be retrieved for analysis.

The data acquisition system consisted of : (i) HP 21MX E-Series computer, (ii) multiple purpose voltmeter, (iii) memory

address unit with analog amplifier output control, (iv) HP 7970E digital magnetic tape recorder, and (v) HP 2648A graphic terminal. Figure 3.16 illustrates the data acquisition system.

The maximum voltage to be monitored by the computer was set at 10 volts, therefore, it was very important not to overload the incoming signals from the hot-film anemometer and the true rms meter through the analog amplifier output control unit. The sampling size was set to be 6000 samples for a total time of 2.4 seconds. (ie. at a rate of 400 micro seconds per sample) for this study.

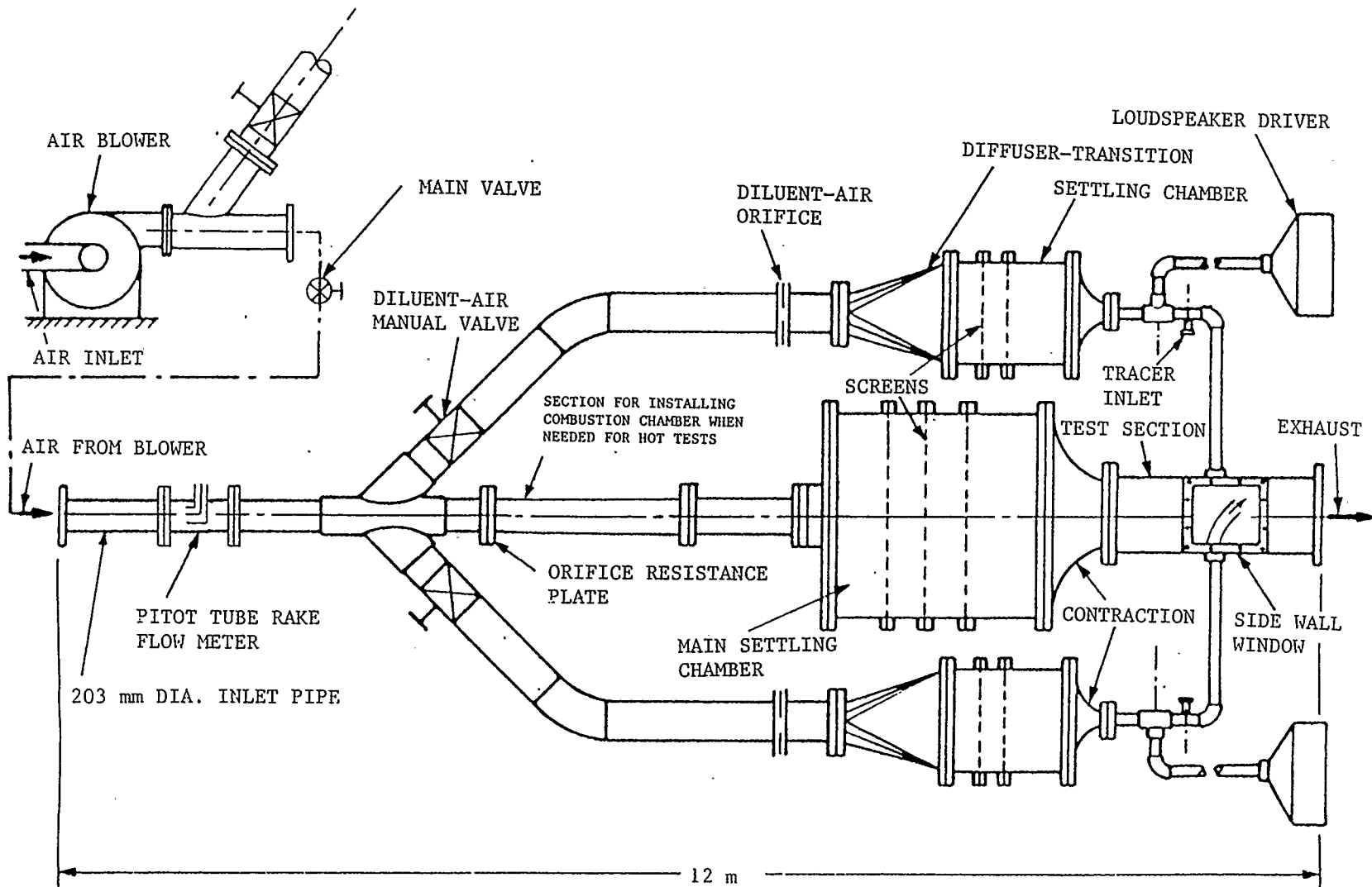


FIGURE 3.1 SCHEMATIC DIAGRAM OF THE TEST RIG.

(NOT TO SCALE)

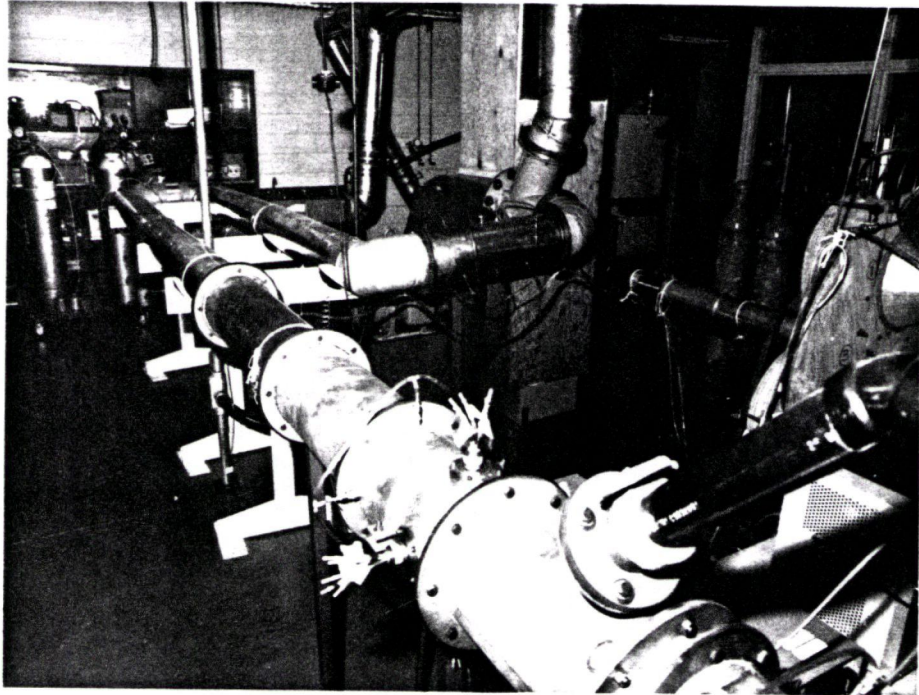


FIGURE 3.2 VIEW LOOKING UPSTREAM FROM THE MAIN SETTLING CHAMBER.

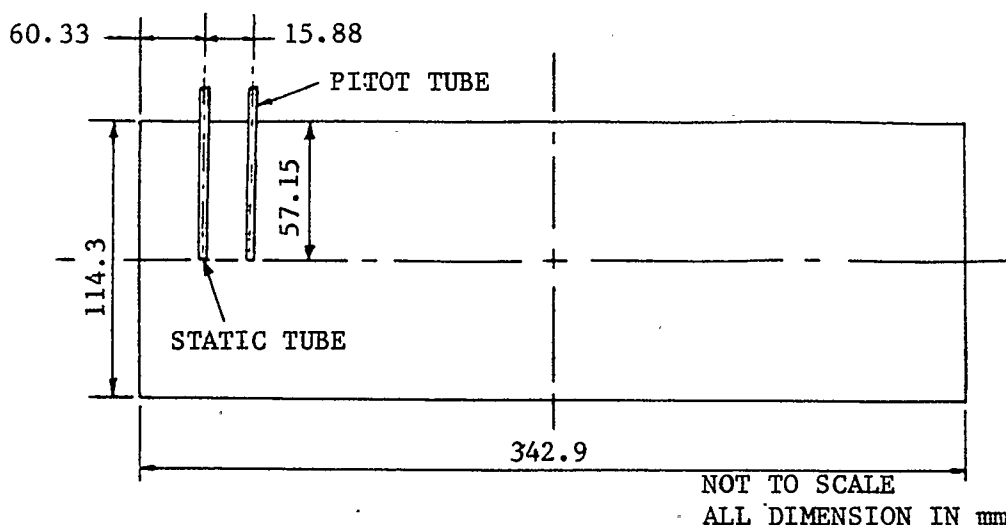


FIGURE 3.4 (a) POSITION OF REF. VELOCITY MEASUREMENT. VIEW LOOKING UPSTREAM IN TEST SECTION WITH PITOT STATIC INSTRUMENT.

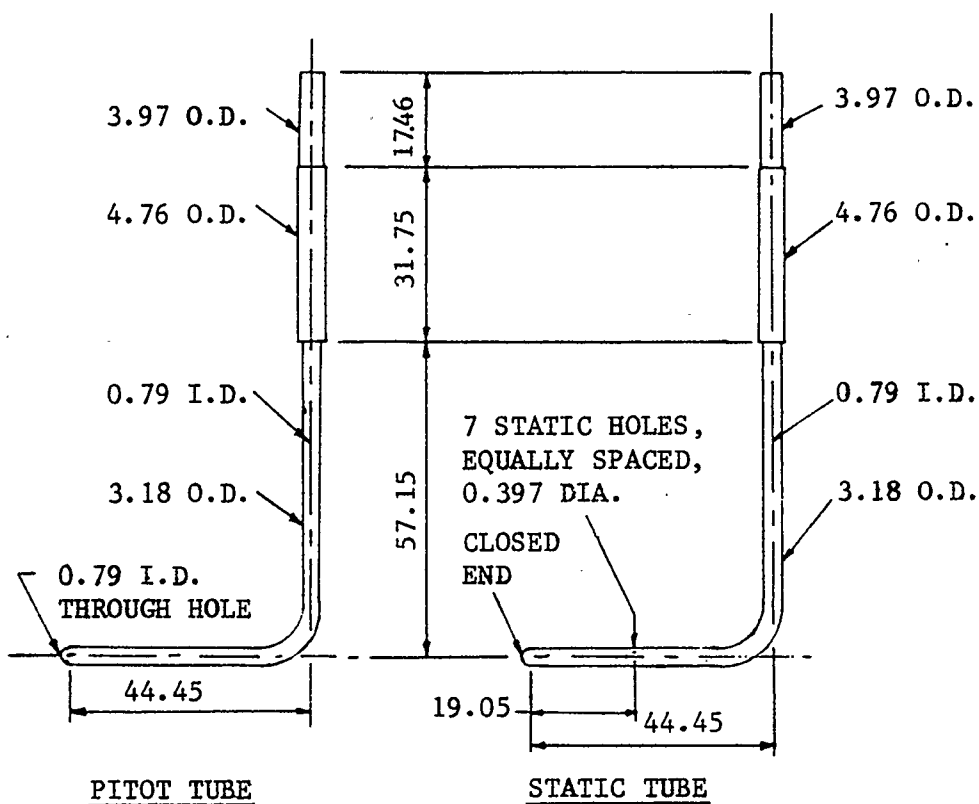


FIGURE 3.4 (b) SKETCH OF PITOT-STATIC TUBES FOR MEASURING REF. VELOCITY.

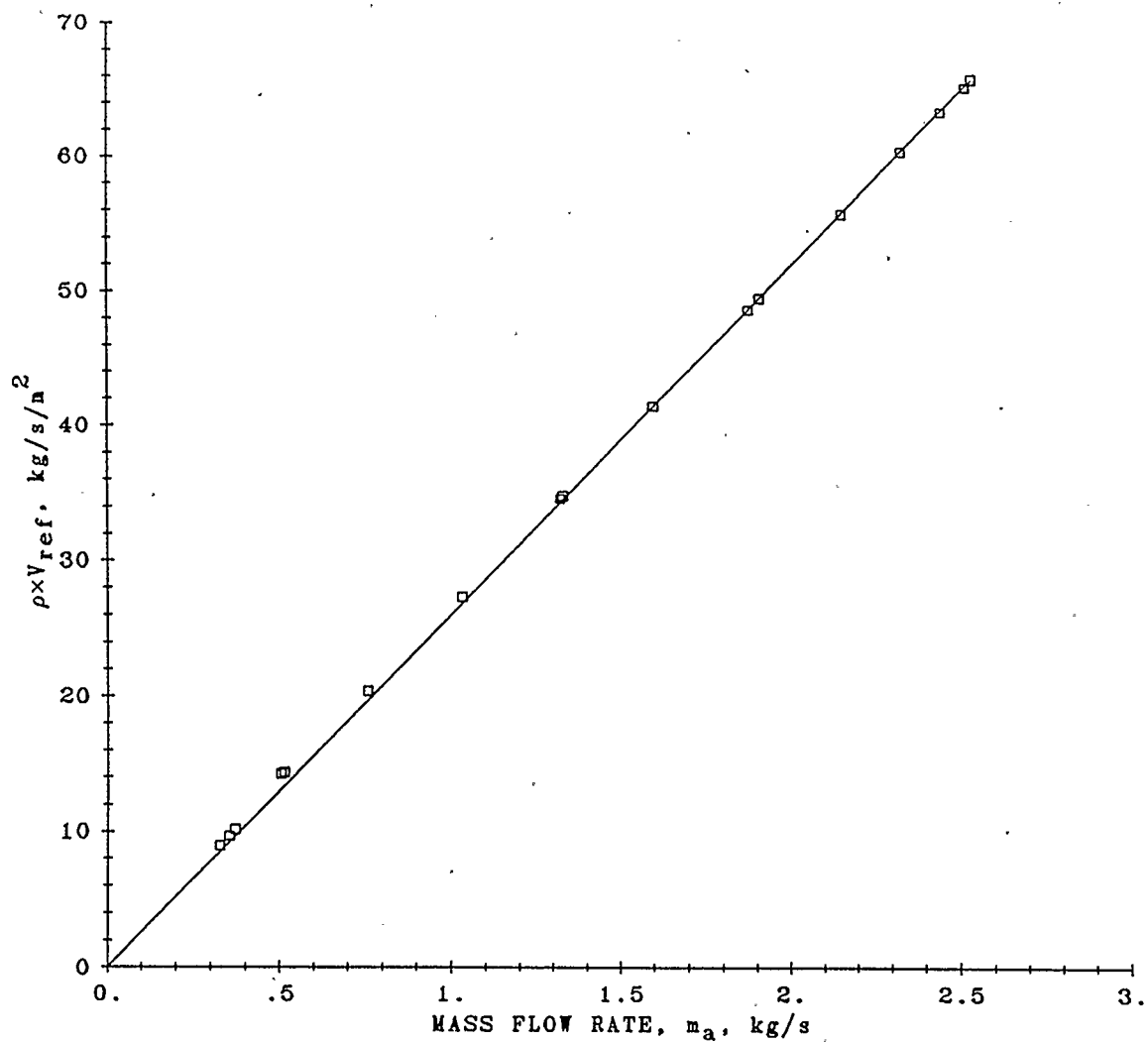


FIGURE 3.5 TEST SECTION CROSSFLOW CALIBRATION IN TERMS OF THE PRODUCT OF TEST SECTION DENSITY AND REF. VELOCITY VERSUS THE CROSSFLOW MASS FLOW RATE.

TEMP. RANGE : 315.85 - 322.30 (K)

Re. RANGE : 7.3546×10^4 - 5.7962×10^5

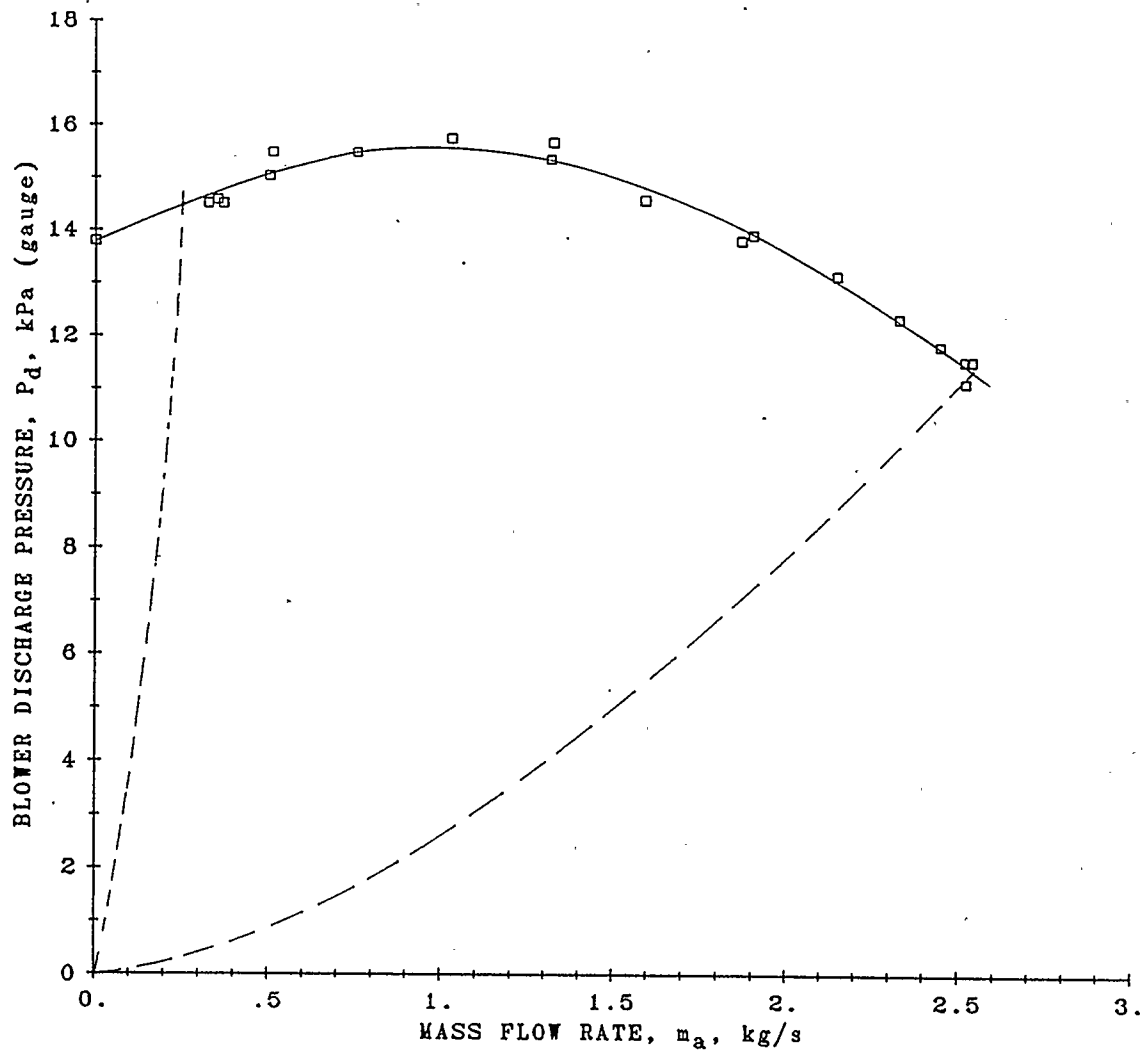


FIGURE 3.6 THE PERFORMANCE CURVE OF A 56 KW AIR BLOWER WITH A 20.3 cm. DIAMETER PIPE LINE.

BLOWER DISCHARGE TEMP. : 315.85 - 326.20 (K)

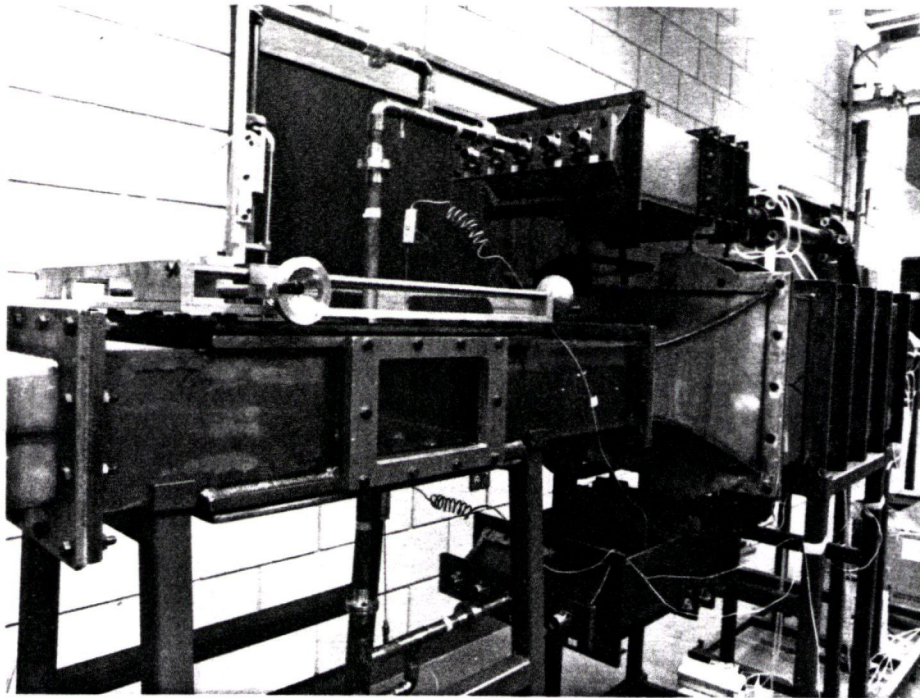


FIGURE 3.7 VIEW LOOKING UPSTREAM FROM THE TEST SECTION.

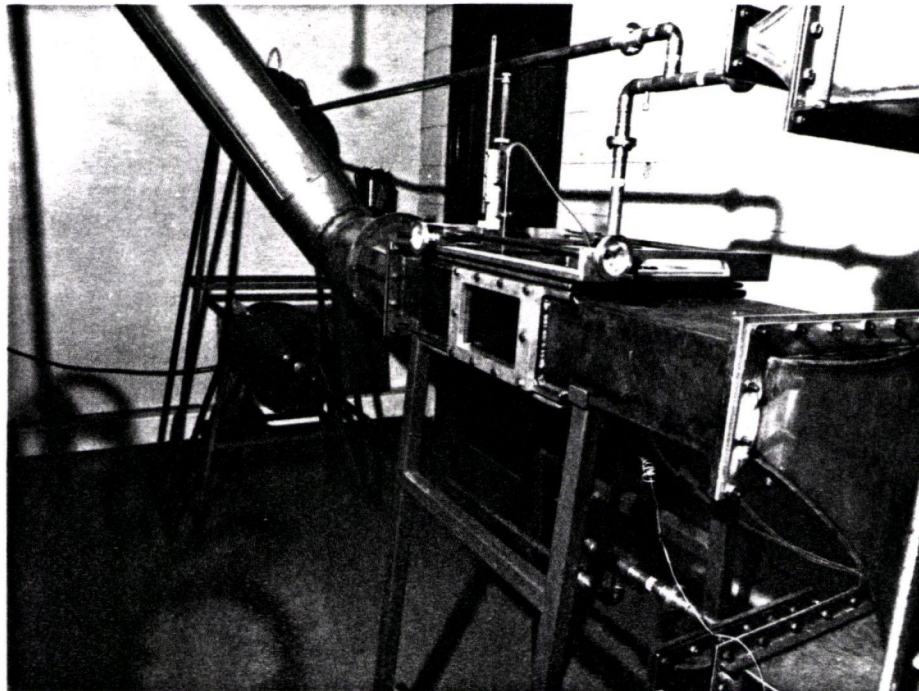


FIGURE 3.8 VIEW LOOKING DOWNSTREAM FROM THE TEST SECTION WITH LOUSPEAKER DRIVERS COUPLED TO PIPE-JET TUBES.

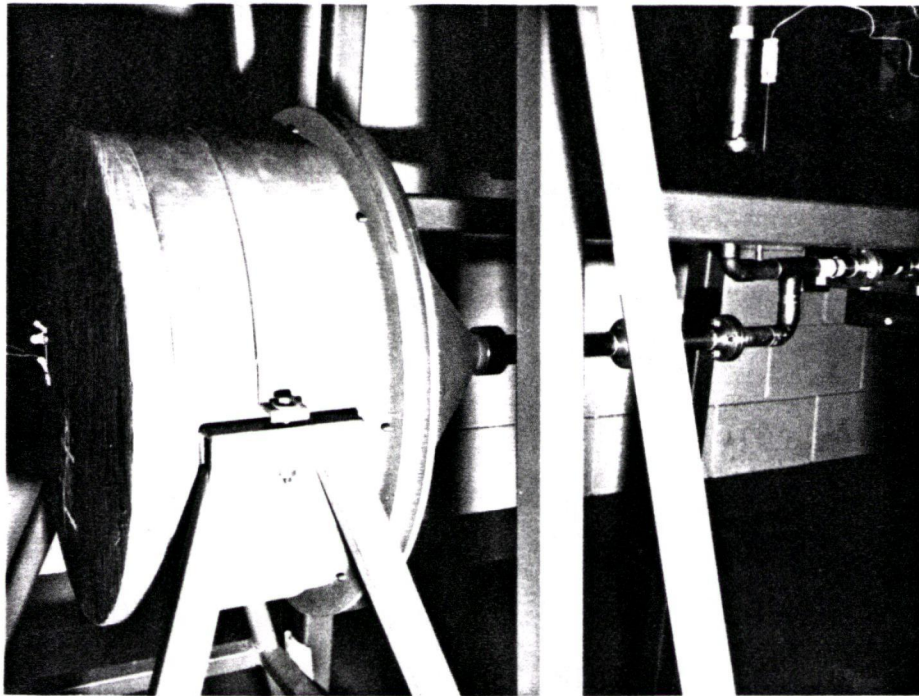


FIGURE 3.9 VIEW OF SINGLE LOUDSPEAKER WITH JET SETUP FOR BOTTOM BYPASS LINE.

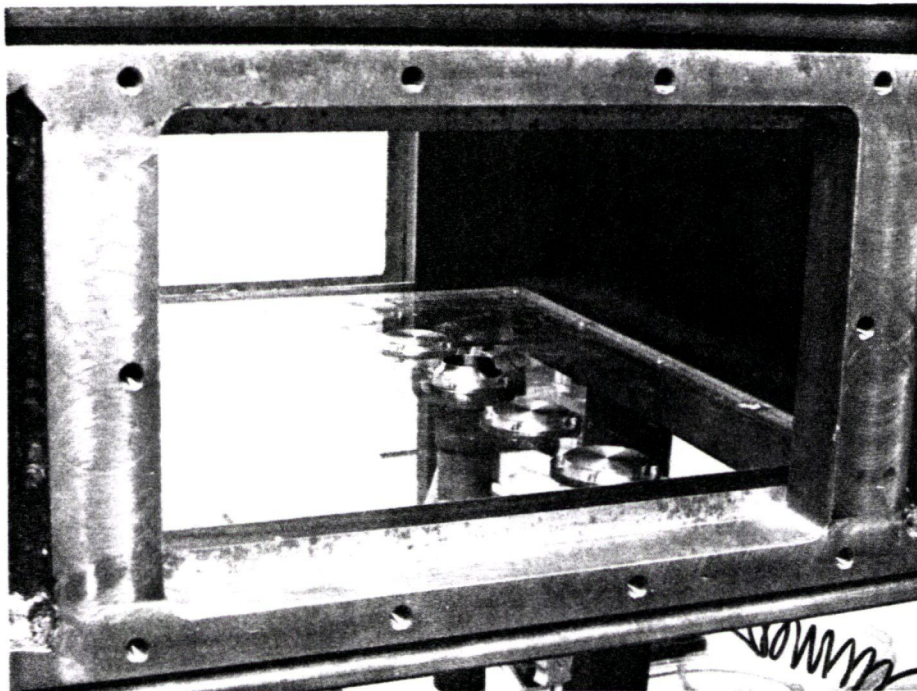
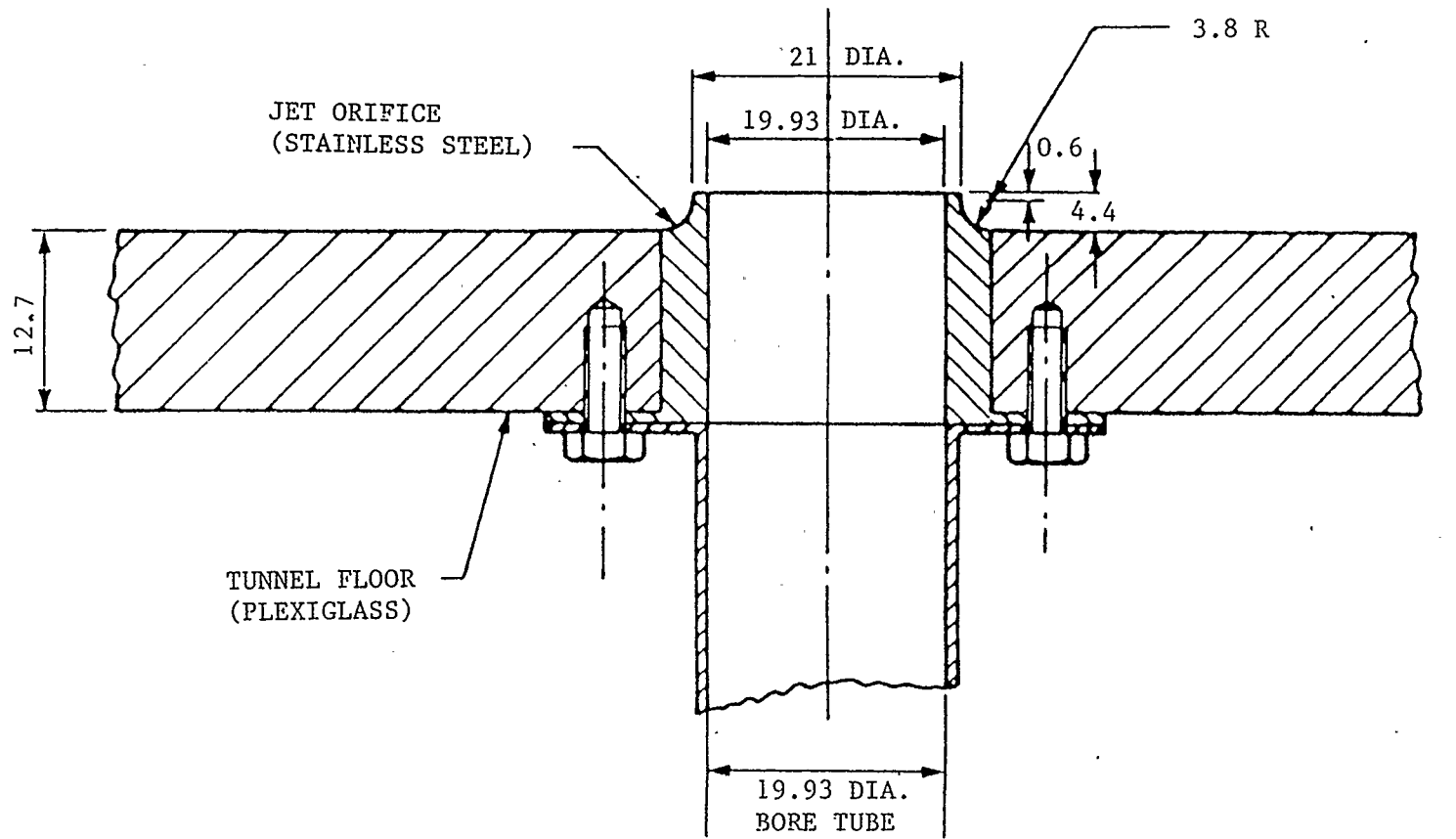


FIGURE 3.10 VIEW OF JET ORIFICE BOLTED IN THE TEST SECTION (WITH SIDE WALL WINDOW REMOVED).



ALL DIMENSIONS ARE IN mm
 (NOT TO SCALE)

FIGURE 3.11 SKETCH OF CROSS SECTION THROUGH JET ORIFICE.

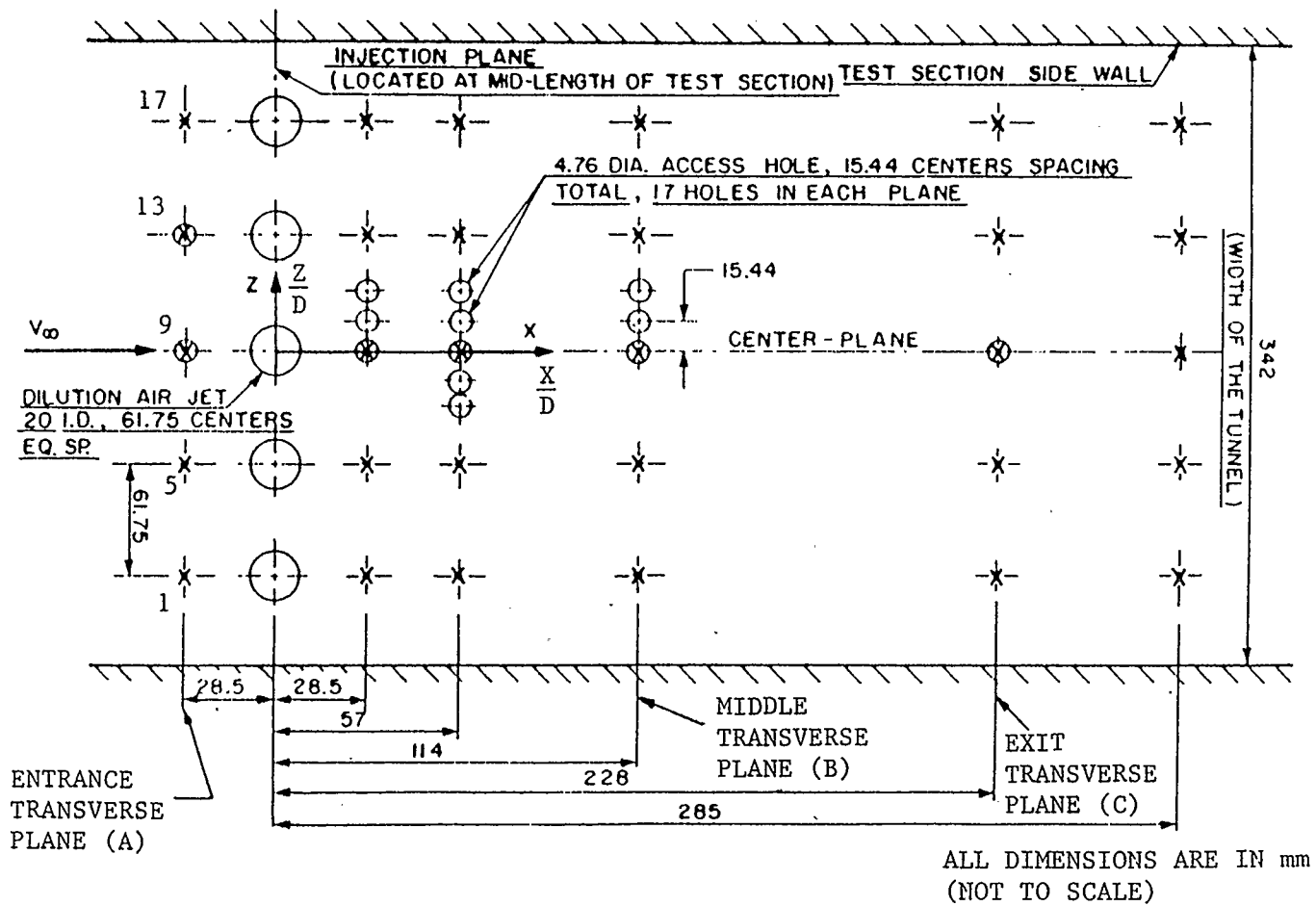


FIGURE 3.12 PLAN OF THE MEASUREMENT STATIONS IN THE TEST SECTION CEILING.

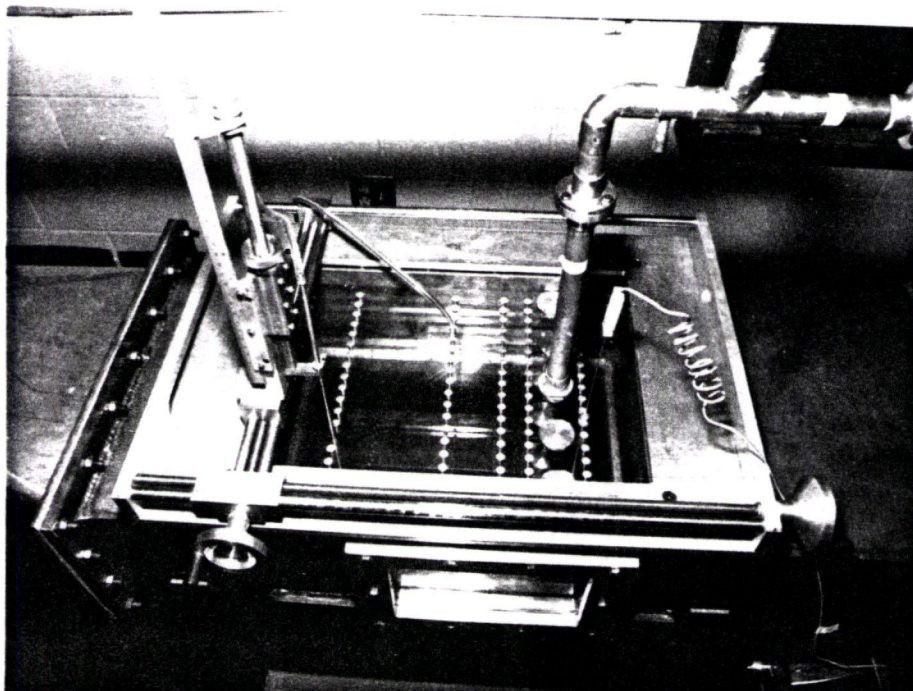


FIGURE 3.13 X-Y-Z TRAVERSE MECHANISM MOUNTED ON TOP OF THE TEST SECTION.

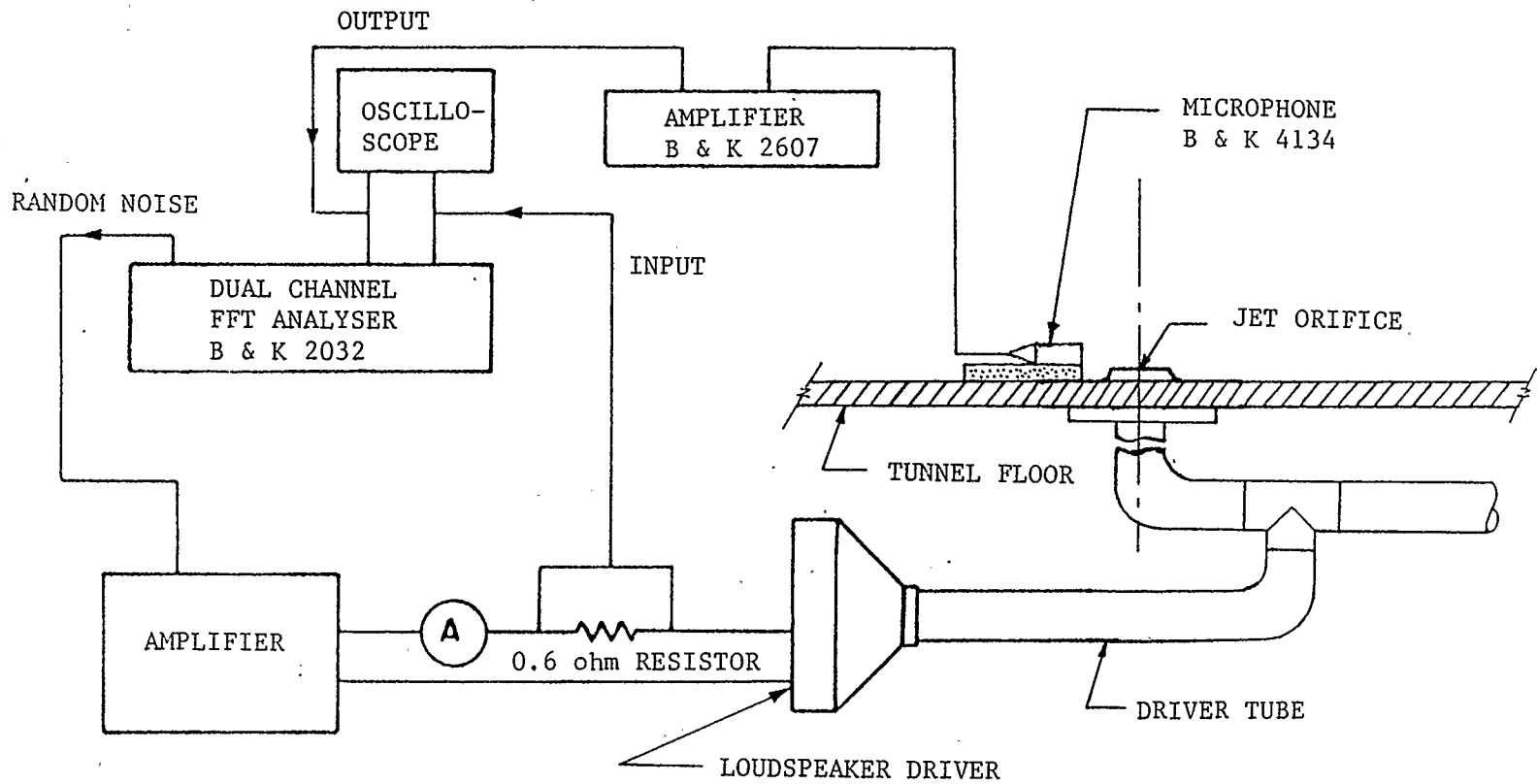


FIGURE 3.14 INSTRUMENTATION SETUP FOR FREQUENCY RESPONSE MEASUREMENT BY A DUAL CHANNEL FFT ANALYSER (B & K 2032).

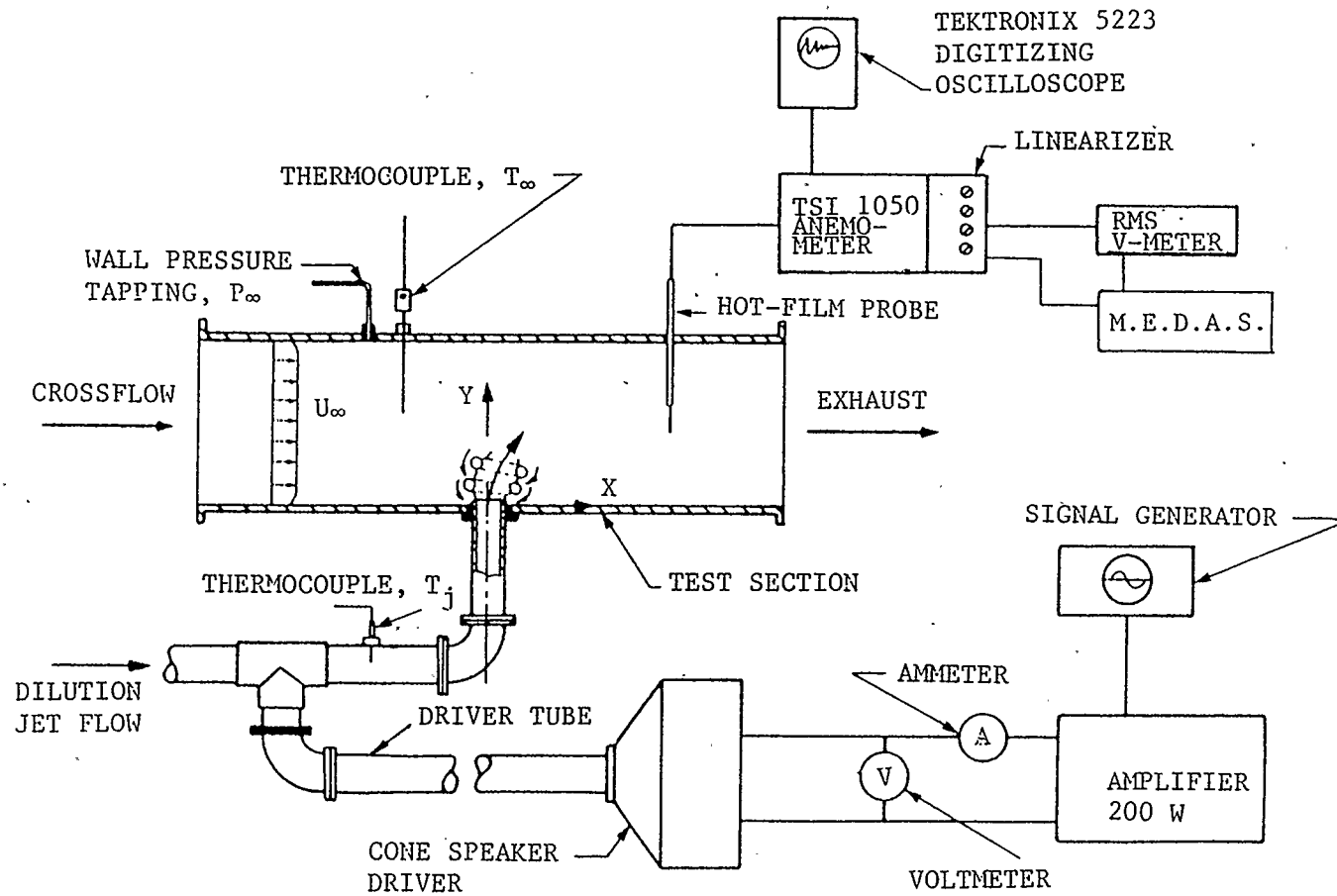


FIGURE 3.15 INSTRUMENTATION SETUP FOR JET FLOW MIXING WITH CROSSFLOW EXPERIMENT.

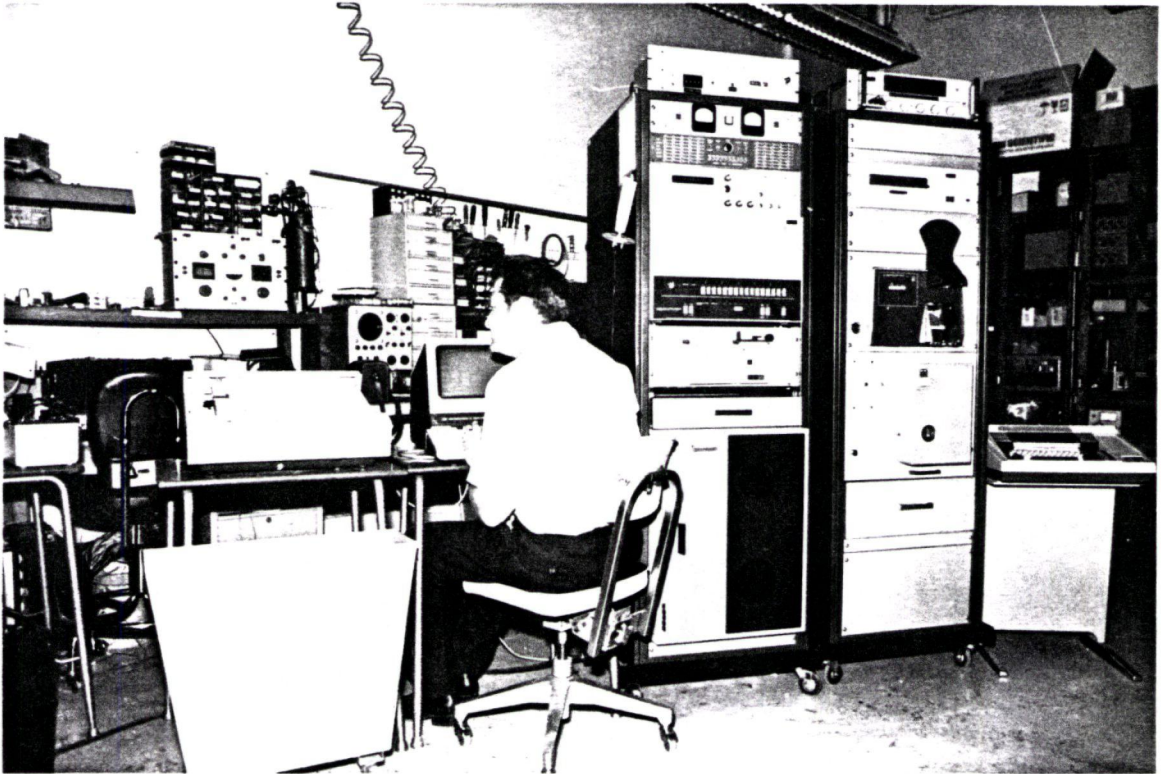


FIGURE 3.16 THE DATA ACQUISITION SYSTEM (M.E.D.A.S.)

CHAPTER 4

EXPERIMENTAL PROCEDURES

4.1 Initial Operation Conditions

Yu (3) pointed out that the blower was not delivering enough mass flow mainly because of the excessive pressure loss of the complicated test rig structure (refer to Figures 3.6 and 4.1). A substantial investigation was therefore carried out to identify the major sources of pressure loss in Yu's (3) system. An initial test was conducted by removing the existing 44.53 mm. I.D. orifice plate installed in the 76.20 mm. diameter main line, and it was found that the mass flow rate was significantly increased from about 0.26 kg/s to 0.48 kg/s. Further tests were carried out, including pressure measurements at strategic points, which revealed that (i) a very unusual high frequency noise was generated at full open position of the throttle valve, after the orifice plate was removed, (ii) the mass flow rate was still not sufficient for the current and future experimental studies, (iii) the desired jet-to-crossflow velocity ratio could not be achieved, (iv) the throttling effect of the transition element for the 76.20 mm. diameter outlet significantly reduced the mass flow rate, and (v) the jet breaker also reduced the mass flow rate. Therefore,

it was decided to enlarge the pipe size from 76.20 mm. diameter to the current 203.20 mm. diameter, which was equivalent to the blower discharge outlet size, to replace the orifice meter with the pitot tube rake flow meter because of its lower pressure loss, and to remove the jet breaker.

After the construction was completed, a series of test runs were carried out, and it was confirmed that the modifications had greatly improved the blower-pipe system performance and consequently the mass flow rate as well, as shown in Figure 3.6. The mass flow rate for the current blower-pipe system could range up to 2.55 kg/s, as compared with Yu's (3) system for about 0.22-0.26 kg/s with the orifice meter installed in the 76.20 mm diameter main line and its corresponding maximum crossflow velocity was about 5.0 m/s (considered not enough for future use). The mass flow rate for the current setup could be easily adjusted either by means of the main line throttle valve, or by employing an orifice resistance plate inserted just downstream of the Y branch fitting, which resulted in a maximum jet velocity approaching 100.0 m/s, depending on the size of the orifice resistance plate employed and the opening of the main throttle valve, as compared with maximum jet velocity of about 30.0 m/s from Yu's (3) system.

4.2 Calibration of The Apparatus

The mass flow rate delivered by the blower through the test

section was calibrated over the full range of operating conditions by the pitot tube rake flow meter using the ten-point log-linear pitot method according to B.S.:1042 Part 2A (53), and referred to the reference velocity measured by pitot-static tubes installed in the test section. The experimental results are shown in Figure 3.5.

The orifice plate flow meters were also calibrated against the Mechanical Engineering Department Flow-Prover. This was necessary because the range of jet velocities for the current experimental studies resulted in orifice velocities that were beyond the lowest permissible limit of Reynolds number of 20000 as specified by British Standard B.S.:1042. Figures 4.2.1 and 4.2.2 respectively show the calibration results of the mass flow rate for the top and bottom orifice plates for the full Reynolds number range. The experimental results showed good agreement to each other. Figures 4.2.3 and 4.2.4 present the results of mass flow rate for Reynolds number less than 20000 at an enlarged scale.

Several velocity and turbulence level profiles in the test section were conducted at 1/4 and 1/1 of the full range of the mass flow rate for the transverse entry, middle, and exit planes, in the absence of the jet flows, by using a vertically traversed hot film sensor probe. Prior to this, the tunnel walls had been rendered flush with covering plugs after all nozzles had been removed from the test section. A hot film sensor, TSI Model No. 1210-20, was used for measuring the mean axial flow velocity, and

its fluctuating level, distributions in the test section.

A systematic pattern of positions for measuring the velocity and turbulence level distributions within the test section was decided upon, and is shown in Figure 3.12. The cross marks (x) indicate the point of measurement of vertical profiles of velocity and its fluctuating level by the hot film sensor.

Thirteen data points for velocity and turbulence level profiles were measured for each vertical plane, which included regions close to the side walls of the test section. Figures 4.3 and 4.5 present typical flat velocity distributions, and Figures 4.4 and 4.6 show the fluctuating level profiles at the three representative transverse measurement planes in the test section as mentioned earlier. All measured profiles were considered to be adequately flat and behaved stably, indicating no adverse flow conditions occurred. The turbulence level was about 2.78 % and 1.65 %, measured at the centre point of the test section at the ninth hole of the entrance plane, for the values of crossflow velocity of about 15.11 m/s and 75.45 m/s respectively. Hence, it was concluded that the flow conditions within the test section were satisfactory and pertinent experimental work could be carried out. The discrepancy of velocity profiles on the measuring planes was mainly due to the fact that the tests were not carried out on the same day and the operating setting was simply slightly different.

4.3 Frequency Response of The Mechanical System of Driver, Driver Tube, Jet Flow Tube

The frequency response of the driver, driver tube and jet flow tube had to be investigated in order to determine at which particular frequency the jet flow could be most powerfully driven by the 400 Watts loudspeaker.

Two experimental approaches were carried out for this investigation. In the first method, the frequency response without air jet flow was determined by using a B & K 2032 dual-channel FFT analyser, as shown in Figure 3.14. The acoustic output signal from the jet orifice was detected by using a B & K 4134 1/2-inch condenser microphone. The signal from the microphone was amplified and then fed as the system output signal to the B & K 2032 dual-channel FFT analyser. The random noise input signal to the acoustic driver was picked up as a voltage across a dummy resistor of 0.6 ohm in one of the supply power leads to act as the system input signal to the B & K 2032 dual-channel FFT analyser. The system input and output signals were also monitored by a dual beam oscilloscope.

In the second method, the frequency response with air jet flow was established by means of the hot film anemometer, which measured the velocity pulsation amplitude (defined in section 4.4) on the jet center-line at the orifice mouth ($X/D = 0.0$), by manually sweeping the frequency of the signal from the function generator from about 50 Hz to 1.2 kHz whilst keeping the driver

input current constant at 2.0 Amp. The corresponding output voltage was recorded. The measurements were made over a range of jet velocities of about 10 to 40 m/s, which is about that expected to be encountered during the main study. A small crossflow velocity was maintained to ensure that the jet did not strike the tunnel ceiling, and also to simulate typical test conditions. This crossflow velocity was sufficiently small such that the jet flow at the orifice exit plane was essentially flowing parallel to the orifice axis. Figure 3.15 shows the set-up for the instrumentation.

Figure 4.9 shows the experimental results obtained and clearly demonstrates a strong resonance mode at 208 Hz and a minor mode at about 1072 Hz irrespective of the jet velocity. This accurately corresponds with the results obtained for the mechanical system with no air jet flow, Figure 4.8. According to Yu (3) the position of the microphone near the orifice exit plane does not alter the measured frequency response, therefore, the microphone was positioned in the manner as shown in Figure 3.14 for convenience.

The driver tubes as designed by Yu (3) were 1.75 m. long and had a frequency response, without air flow, as shown in Figure 4.7. Assuming an "open" tube (58) the frequencies of the first fourteen harmonics are 98.4, 196.7, 295.1, 393.5, 491.9, 590.2, 688.6, 787.0, 885.3, 983.7, 1082.1, 1180.5, 1278.8, 1377.2 Hz for air at 22° C. Comparison with Figure 4.7 shows the first harmonic

to be conspicuously absent and only the 2nd, 4th, 5th, 10th and 14th harmonics (underlined) apparently present. Likewise for a "closed" tube (58) only the 3rd and 9th harmonics (underlined) are present in the first fifteen harmonics (odd series: 49.2, 147.6, 245.9, 344.3, 442.7, 541.0, 639.4, 737.8 Hz). This suggests that the resonance modes of the driver tube do not dominate the system and that the strongest mode at 208 Hz may be stronger for a shorter tube. The tube was therefore drastically shortened to 0.14 m. long to produce the response shown in Figure 4.8. This resulted in some gain in amplitude at 208 Hz with essentially the same harmonic content as for the 1.75 m. long tube. Based on this evidence it was decided to use the short driver tubes throughout the study on the assumption that the amplitude of the velocity pulsation of the jet (pulsation strength, defined in section 4.4) would be optimum for a given driver power at 208 Hz. Of course it would be interesting to undertake a detailed analysis of the acoustics of the driver system, but this was considered to be beyond the scope of this investigation, somewhat secondary in nature, and therefore not pursued.

4.4 Main Experimental Techniques and Procedures

The single jet flow in a uniform crossflow was the main subject of this experimental study. The objectives, and economy of effort, decided that two experimental categories were investigated: (i) with a constant crossflow velocity and an input

driving power of about 50 Watts, a series of tests were carried out for jet-to-crossflow velocity ratios from 1.31 to 4.56, (ii) with the same crossflow velocity as in (i), a series of tests were carried out for a single jet velocity with a good Strouhal number response of 0.22 (1,2) over a power range from 0 to 160 Watts. The jet orifice size was fixed at 19.93 mm. diameter, and the velocity for the crossflow was chosen to be about 10.0 m/s. This velocity corresponds to the Mach number at the lower end of the combustion chamber range of 0.03 to 0.07, thereby ensuring that the maximum jet velocity was not too great to be effectively pulsed by the driver power available.

As mentioned earlier, the experimental technique employed in this phase of the work was mainly the well established method of using a hot film sensor, operated by a constant temperature anemometer, in order to measure velocity and turbulence profiles. For all measurements the hot film sensor was aligned in a direction perpendicular to the main crossflow. The overall instrumentation set up is shown in Figure 3.15.

Prior to proceeding with the detailed experimental study, a thorough investigation of the overall frequency response of the mechanical system was conducted (section 4.3) followed by calibration of the jet pulsation strength. From the frequency response results shown in Figures 4.8 and 4.9, the strongest resonance mode for the system was clearly identified to be at a frequency of 208 Hz. At this frequency (0.14 m. driver tube), a

series of measurements of pulsation strength were carried out over a range of jet flow velocities from about 10.0 m/s to 80.0 m/s and with a crossflow velocity of about 5.0 m/s, and with respect to various input driving powers. Also pulsation strength measurements were made for a series of jet velocities and crossflow velocities that would be close to those actually used in the main experiments. In both cases the crossflow velocity was small enough so as not to significantly interfere with jet flow at the orifice exit plane.

The air jet velocity was measured by positioning the hot film sensor normal to the jet flow, in the orifice exit plane, and on the jet centre-line. The anemometer voltage was displayed on the digital oscilloscope giving jet velocity - time data. In this manner the steady jet velocity and the excited jet velocity could be measured. For low excitation powers the jet velocity - time distribution closely followed the sinusoidal driving signal, and it was relatively easy to measure the centre-line jet velocity excitation pulsation amplitude U_e or pulsation strength. This velocity pulsation, of course, was the means whereby the dynamic behaviour of the jet column could be excited. At higher driving powers, in relation to the unexcited steady jet velocity U_j , the orifice exit plane flow reverses from jet flow to sink flow, with separation at the orifice lip, Disselhorst and Wijngaarden (23). The inflow will be associated with increased losses, and this with the sink type flow results in the measured centre-line velocity

being not truly representative of the flow. This causes the negative velocity amplitude to be somewhat smaller than the positive velocity amplitude, and therefore taking the average velocity amplitude to characterise the pulsation strength may lead to some underestimation at the highest driver powers. Since the hot film sensor is ambiguous to flow direction, then during the inflow at the orifice, the displayed signal takes on the appearance of a rectified voltage wave, which complicates somewhat the measurement of pulsation strength U_e . At larger jet velocities the reverse flow may not take place because of insufficient driver power. Figure 4.10 shows a sketch of typical anemometer signals. This behaviour has been previously observed and discussed by Vermeulen and Yu (2) and (3), and Vermeulen and Odgers (26). Traversing the hot film sensor vertically upwards revealed the typical velocity distribution of a toroidal vortex, as was reported previously by Yu (3).

Since the crossflow velocity has been purposely kept to minor size in relation to the jet velocity, the jet behaviour close to the orifice exit plane should essentially be that of a free jet, and the dimensional analysis of Vermeulen et. al. (1) should apply, ie.,

$$\left[\frac{U_e}{U_j} \right]^2 = \left[\frac{k \dot{W}}{\rho_j D_j^2 U_j^3} \right] \quad (1), \text{ where } k \text{ is a constant.}$$

plotting the data in this fashion, Figure 4.11, indeed shows a good correlation, but the relationship is not linear as was the

case for Ref. (1) and therefore is more properly written as,

$$\left[\frac{U_e}{U_j} \right]^2 = F \left[\frac{\dot{W}}{\rho_j D_j^2 U_j^3} \right] \quad (2), \text{ where } F \text{ is a function.}$$

The apparent linearity was simply the outcome of using data of a

restricted range in terms of the power number, $\frac{\dot{W}}{\rho_j D_j^2 U_j^3}$. In

contrast the data of Figure 4.11 has a factor of 10 greater range.

The Reynolds number range of the data is from 11076 to 86394 and

perhaps therefore has little effect. The Strouhal number range is

large, from about 0.049 to 0.389, and thus the slight deviation of

the low jet velocity data is presumed not to be a Strouhal number

effect (nor indeed a Reynolds number effect) but perhaps due to

the influence of the crossflow velocity. The "flat topping" of

some of the data is the result of over driving the speaker cone

onto its amplitude stops.

The data in Figure 4.11 provide a calibration for finding the pulsation strength of a particular free jet flow excited by a particular driver power at 208 Hz. Unfortunately it is not truly universal, since changing the driver will no doubt affect the calibration, and it is restricted to a particular mechanical system geometry, including that of the orifice, which if it was replaced by a smaller bore nozzle would no doubt affect the calibration. The effect of changing the driving frequency to about 1072 Hz (the next most powerful resonance mode) was explored, and Figure 4.11 definitely shows this to be a much

weaker mode than that at 208 Hz, which is therefore the preferred driving frequency.

Figure 4.12 presents pulsation strength versus power for jet velocities approximately the same as those used in the main tests. This data has also been used in Figure 4.11. The data shows that pulsation strength is approximately proportional to $\sqrt{\dot{W}}$ and decreases with increase of U_j , in agreement with Refs. (2) and (3). This follows, of course, from Equation (1) where for a linear characteristic,

$$\left[\frac{U_e}{U_j} \right] = \left[\frac{k_1 \sqrt{\dot{W}}}{U_j \sqrt{m_j}} \right] \quad \text{--- (3), where } m_j = \frac{\pi}{4} \rho_j U_j D_j^2,$$

$$k_1 = \text{constant.}$$

or

$$U_e = \frac{k_1 \sqrt{\dot{W}}}{\sqrt{m_j}} \quad \text{--- (4)}$$

Figure 4.13 repeats the data for $U_j = 10.65$ m/s, $f = 208$ Hz, and also plots data for corresponding similar jet velocity but for a frequency of 1072 Hz (included in Figure 4.11 also). The system response is definitely weaker at 1072 Hz, however, excitation at this frequency may be useful if a good Strouhal number (≈ 0.25) is required at a high jet velocity. Both figures show "flat topping" of the data taking place at about 160 Watts.

The main experimental results will be reported in the following ways: (i) velocity and turbulence level profiles for the

center plane position and lateral plane position, (ii) jet path trajectories and penetrations; in terms of different velocity ratios of jet-to-crossflow and at different acoustic driving power conditions.

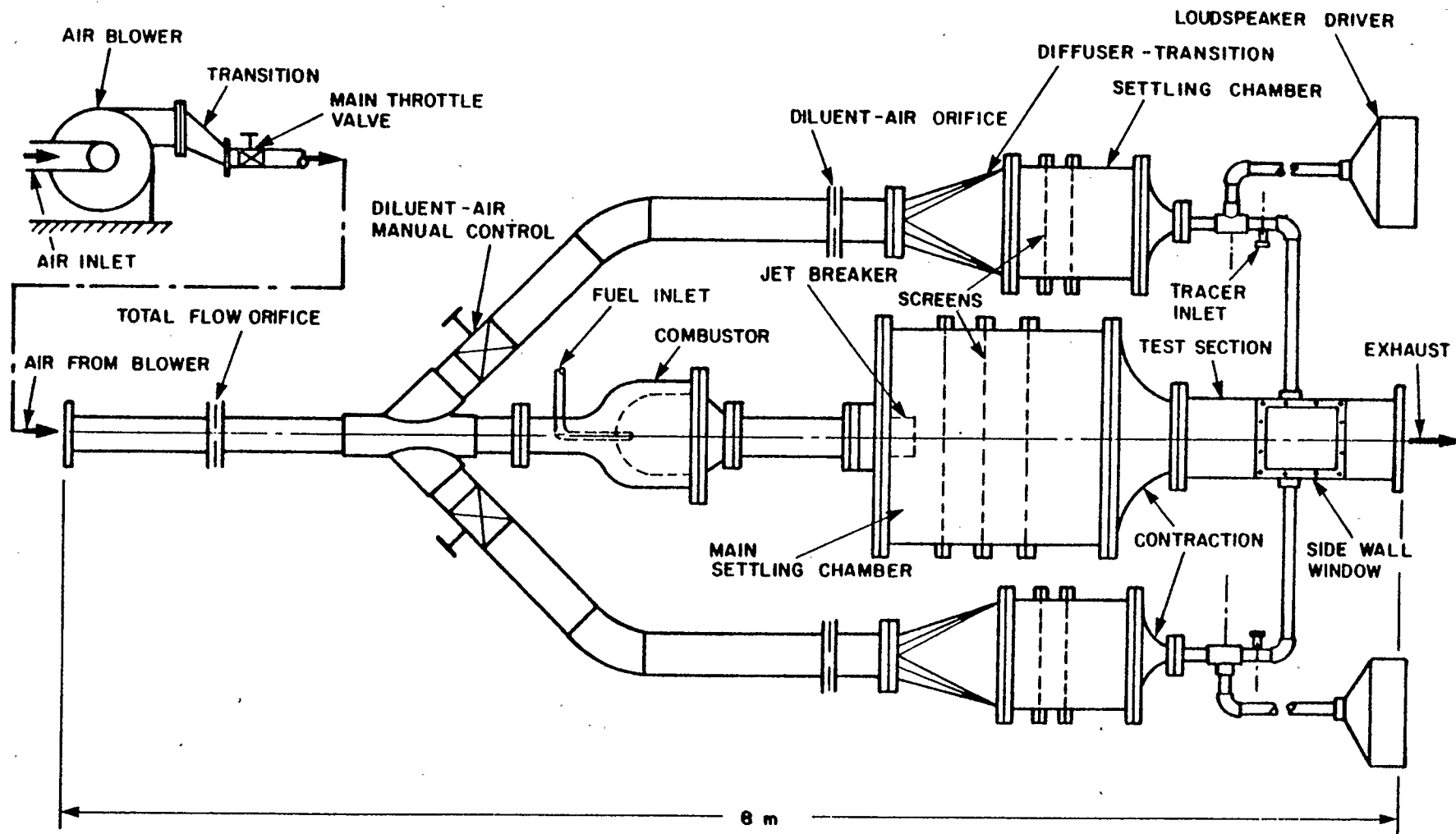


FIGURE 4.1 SCHEMATIC DIAGRAM OF TEST RIG, TAKEN FROM REF. (3).

NOT TO SCALE

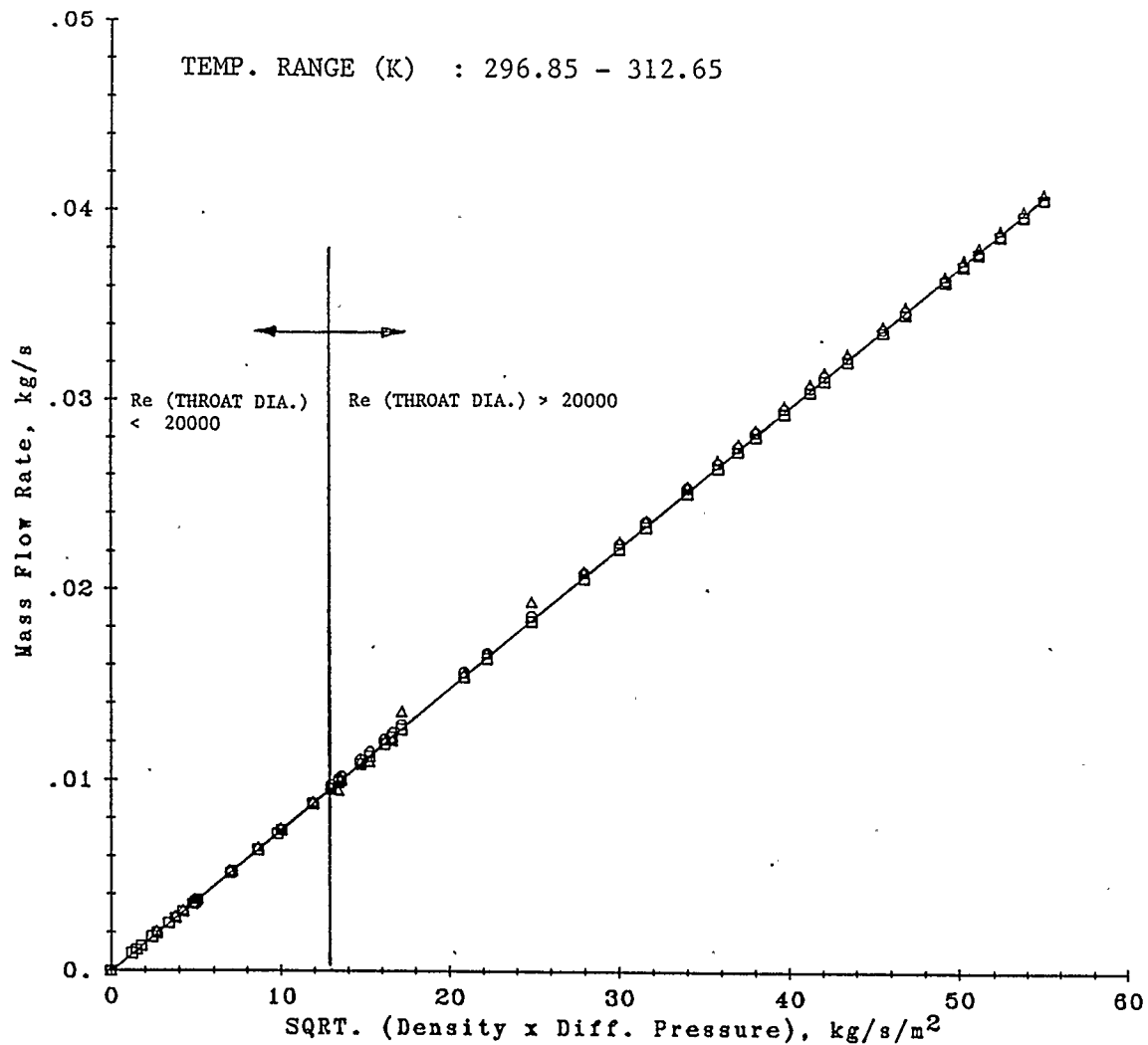


FIGURE 4.2.1 CALIBRATION RESULT OF MASS FLOW RATE FOR TOP ORIFICE PLATE FLOWMETER.

THROAT DIA. = 31.73 mm

PIPE DIA. = 51.38 mm

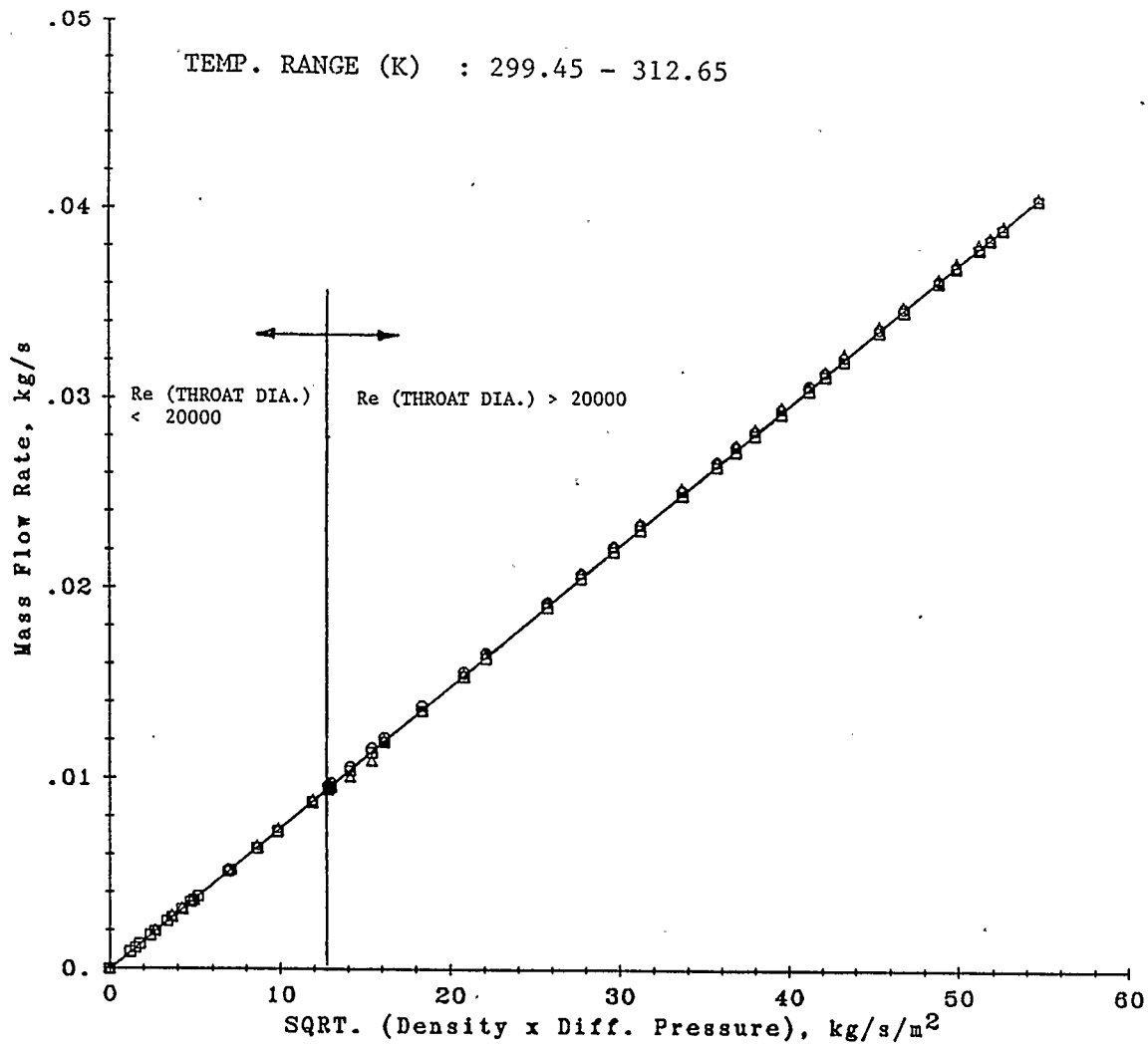


FIGURE 4.2.2 CALIBRATION RESULT OF MASS FLOW RATE FOR
 BOTTOM ORIFICE PLATE FLOWMETER.
 THROAT DIA. = 31.73 mm
 PIPE DIA. = 51.38 mm

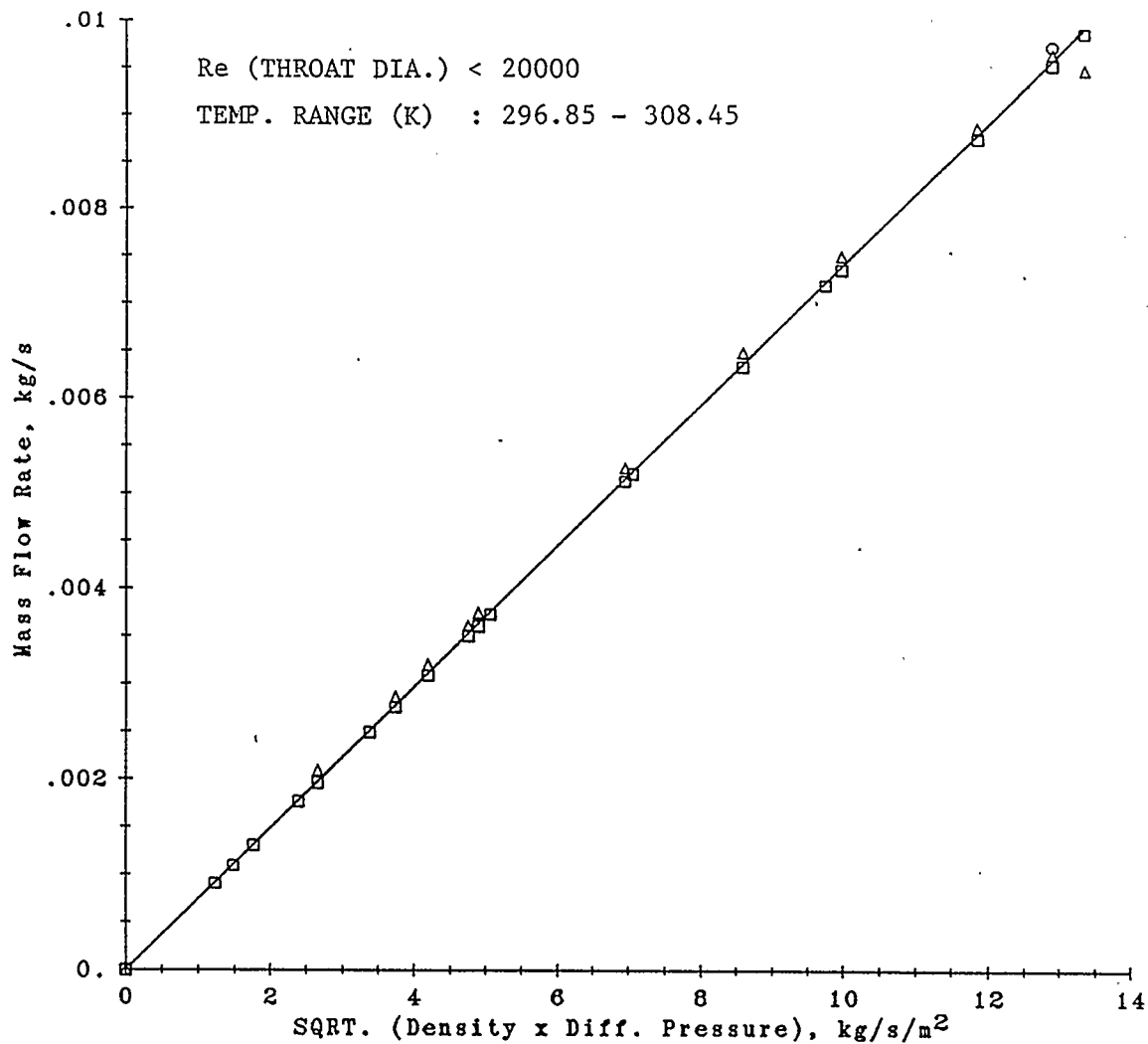


FIGURE 4.2.3 CALIBRATION RESULT OF MASS FLOW RATE FOR
TOP ORIFICE PLATE FLOWMETER.
THROAT DIA. = 31.73 mm
PIPE DIA. = 51.38 mm

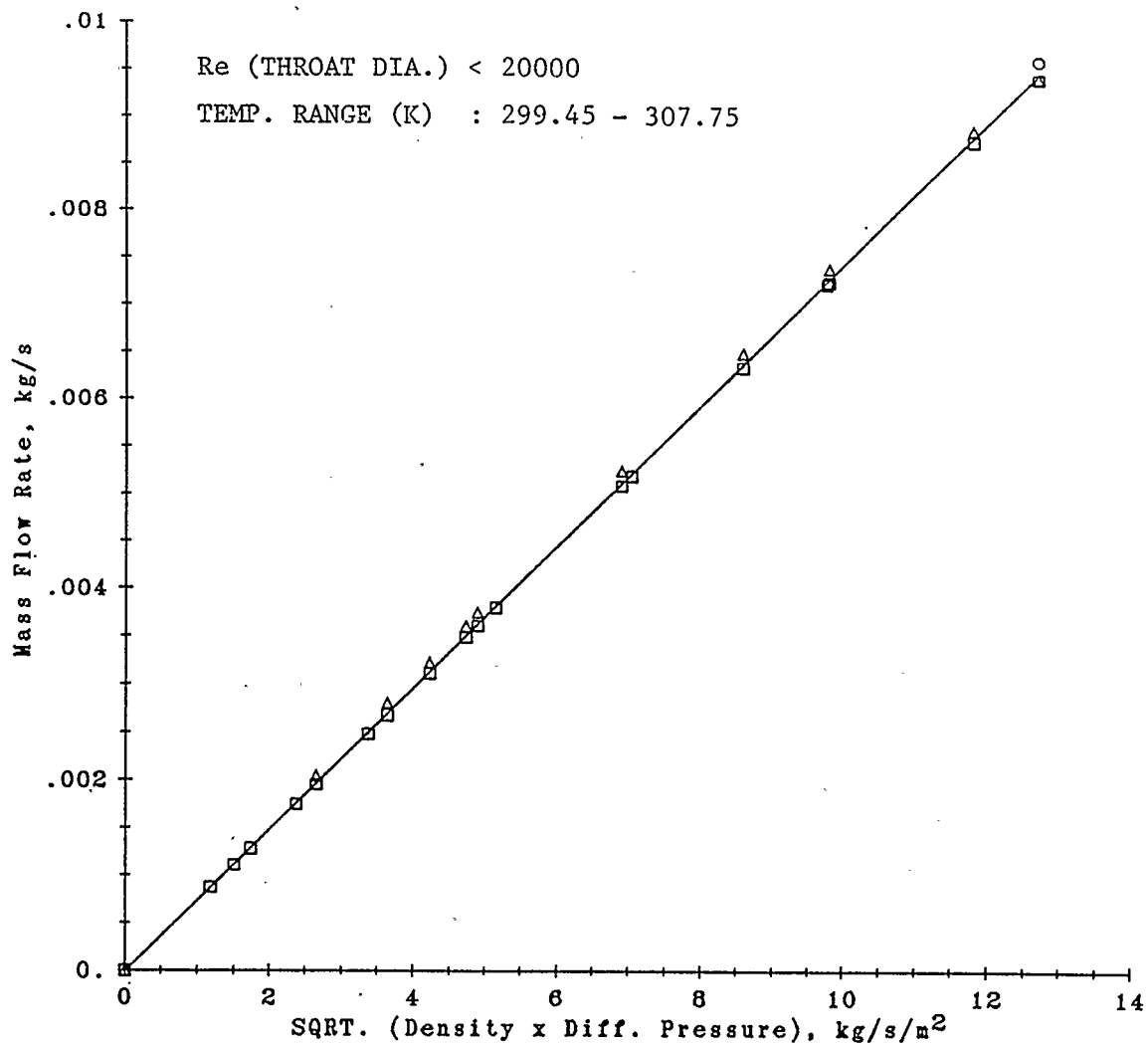


FIGURE 4.2.4 CALIBRATION RESULT OF MASS FLOW RATE FOR
BOTTOM ORIFICE PLATE FLOWMETER.
THROAT DIA. = 31.73 mm
PIPE DIA. = 51.38 mm

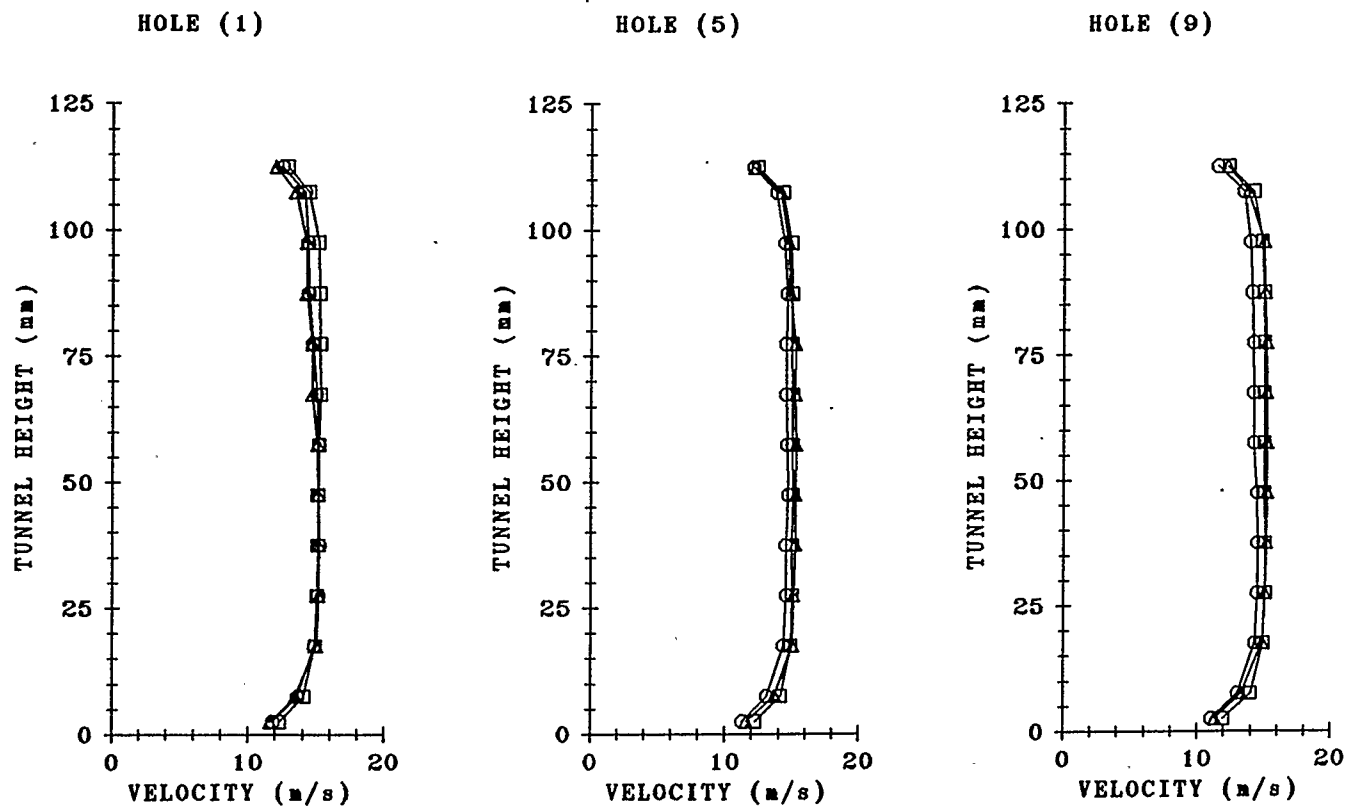


FIGURE 4.3

MEAN AXIAL VELOCITY PROFILE ACROSS DIFFERENT VERTICAL PLANES (REFER FIGURE 3.12).

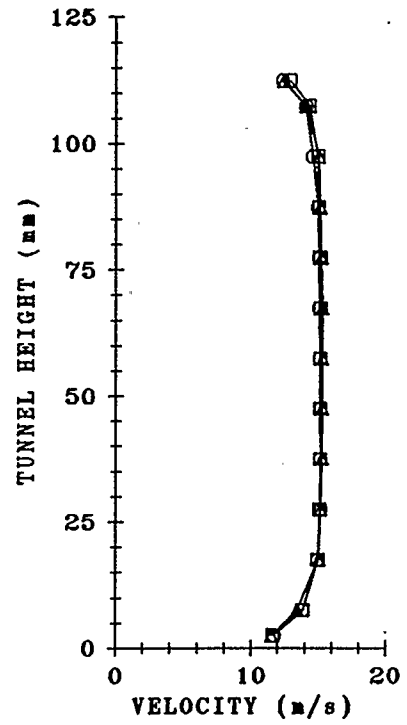
$$U_{\infty} = 15.11 \text{ m/s}, \quad \rho_{\infty} = 0.9817 \text{ kg/m}^3$$

WHERE : \square - ENTRANCE TRANSVERSE PLANE

\circ - MIDDLE TRANSVERSE PLANE

\triangle - EXIT TRANSVERSE PLANE

HOLE (13)



HOLE (17)

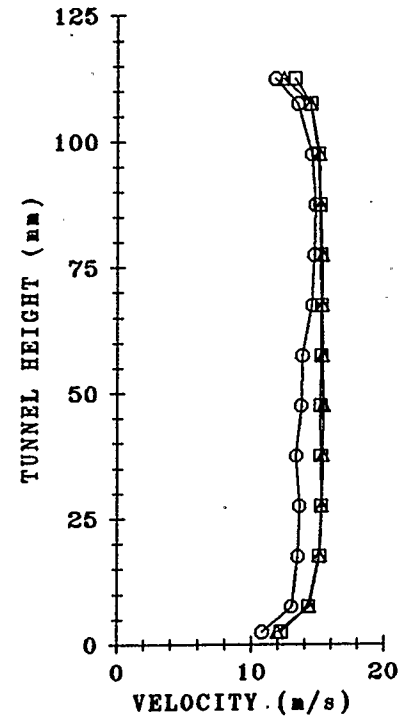


FIGURE 4.3 CONTINUED.

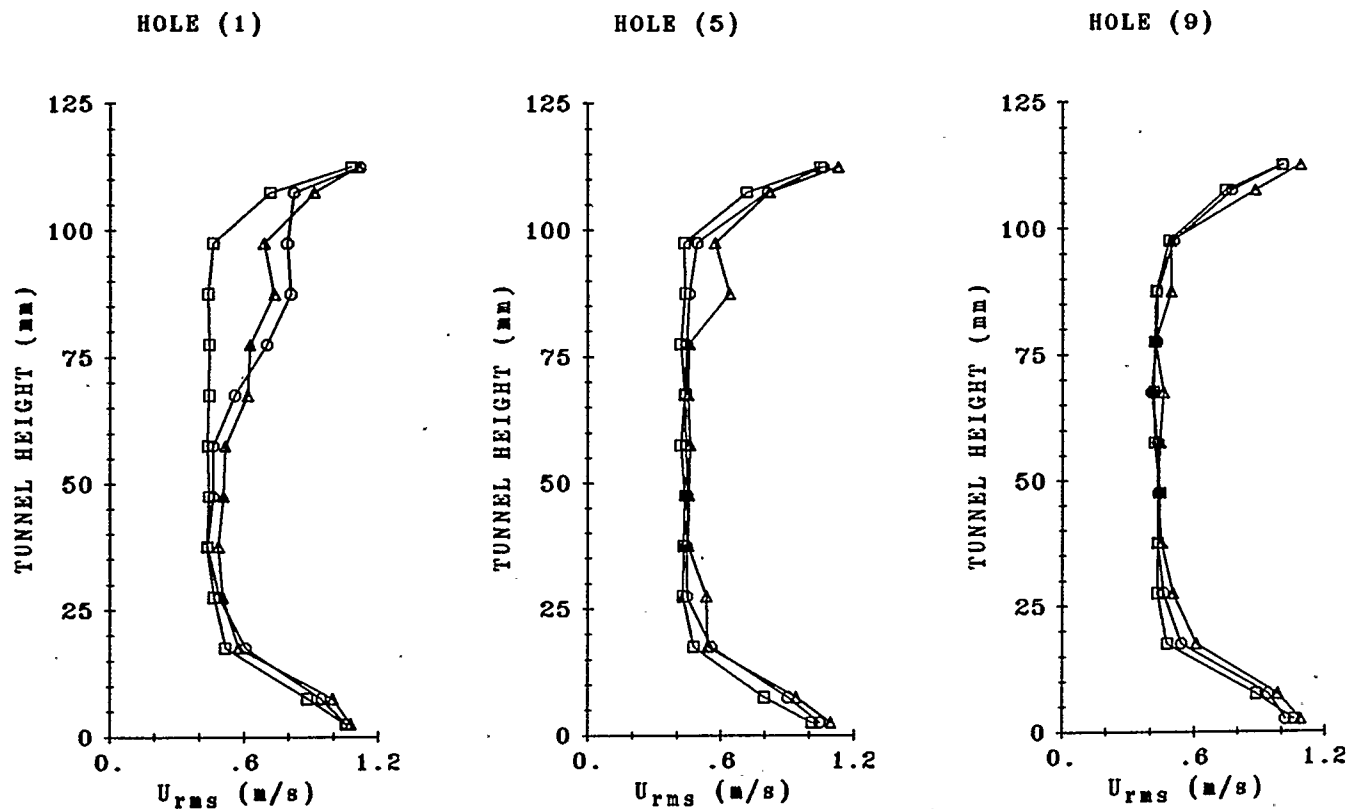


FIGURE 4.4 MEAN AXIAL RMS VELOCITY PROFILE ACROSS DIFFERENT VERTICAL PLANES (REFER FIGURE 3.12).

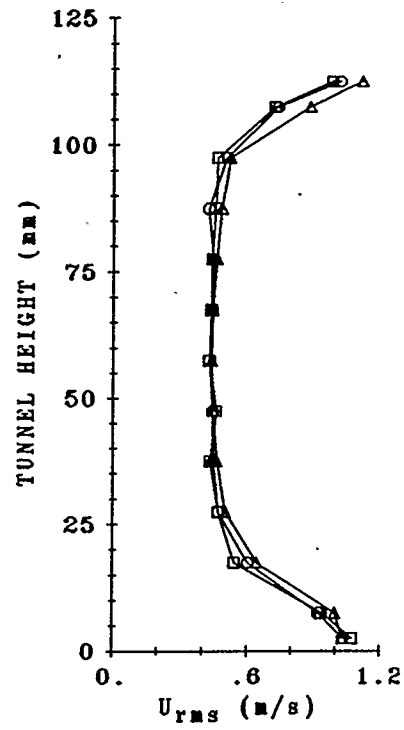
$U_{\infty} = 15.11 \text{ m/s}, \quad \rho_{\infty} = 0.9817 \text{ kg/m}^3$

WHERE : \square - ENTRANCE TRANSVERSE PLANE

\circ - MIDDLE TRANSVERSE PLANE

\triangle - EXIT TRANSVERSE PLANE

HOLE (13)



HOLE (17)

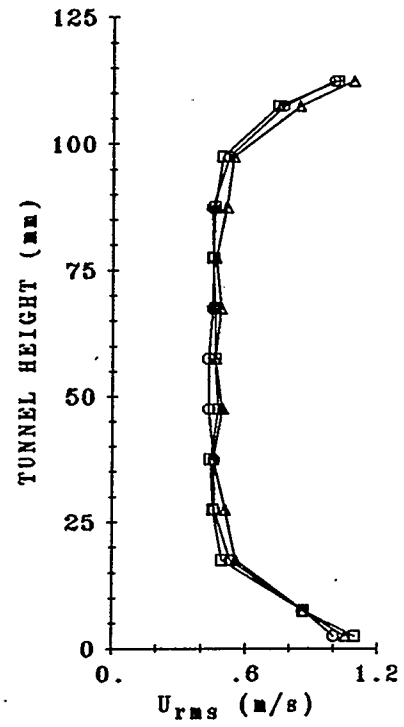


FIGURE 4.4 CONTINUED.

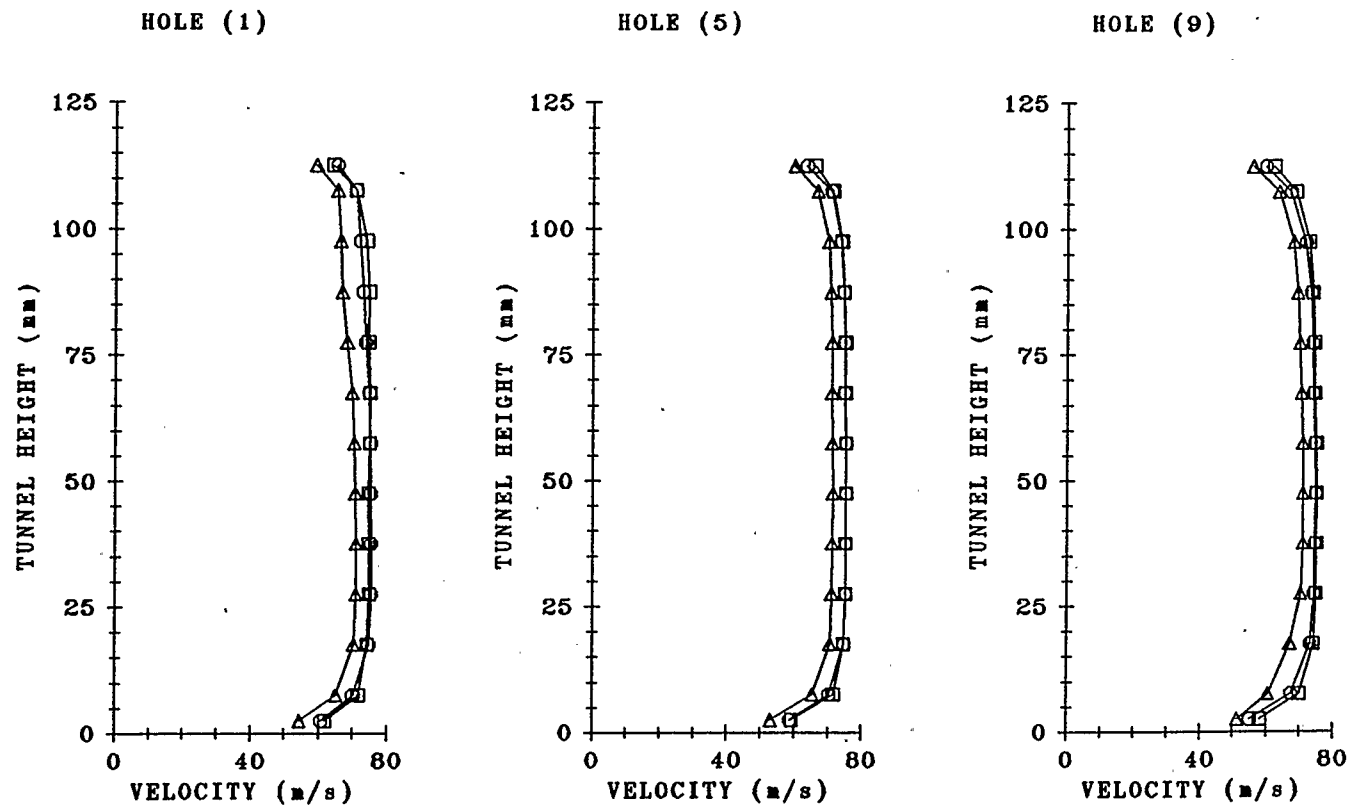


FIGURE 4.5 MEAN AXIAL VELOCITY PROFILE ACROSS DIFFERENT VERTICAL PLANES (REFER FIGURE 3.12).

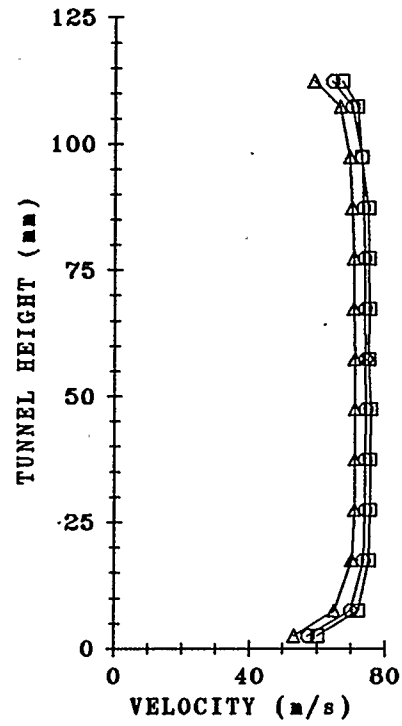
$$U_{\infty} = 75.45 \text{ m/s}, \quad \rho_{\infty} = 1.0205 \text{ kg/m}^3$$

WHERE : \square - ENTRANCE TRANSVERSE PLANE.

\circ - MIDDLE TRANSVERSE PLANE

\triangle - EXIT TRANSVERSE PLANE

HOLE (13)



HOLE (17)

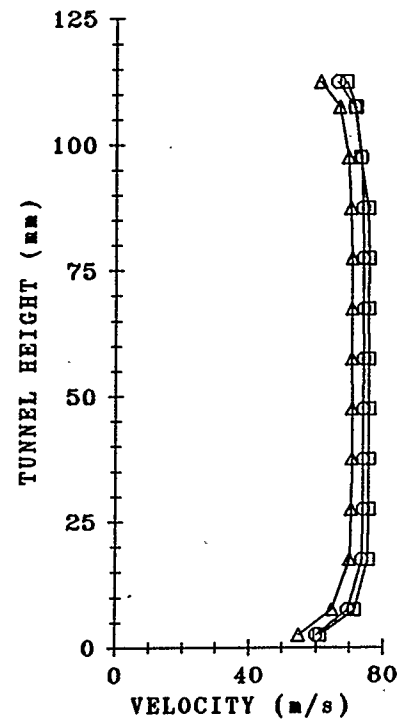


FIGURE 4.5 CONTINUED.

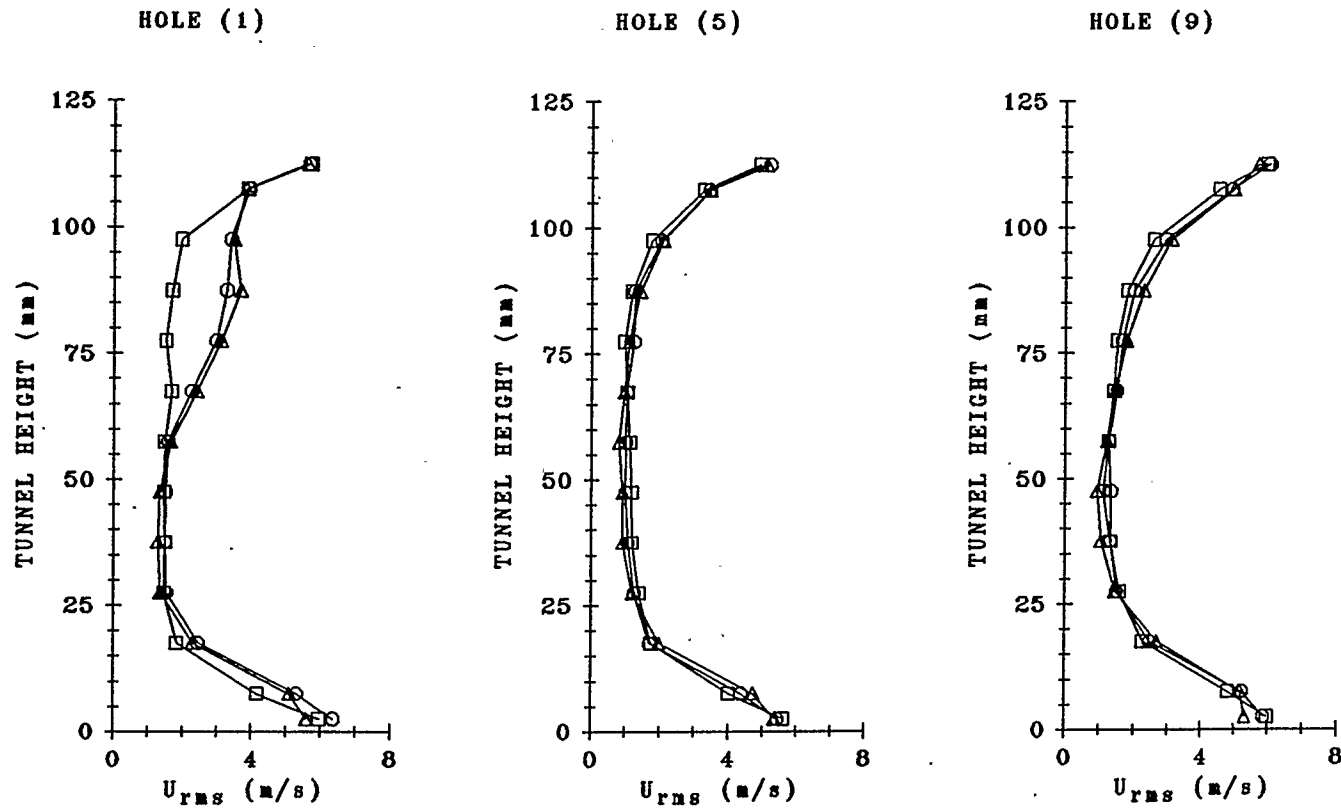


FIGURE 4.6 MEAN AXIAL RMS VELOCITY PROFILE ACROSS DIFFERENT VERTICAL PLANES (REFER FIGURE 3.12).

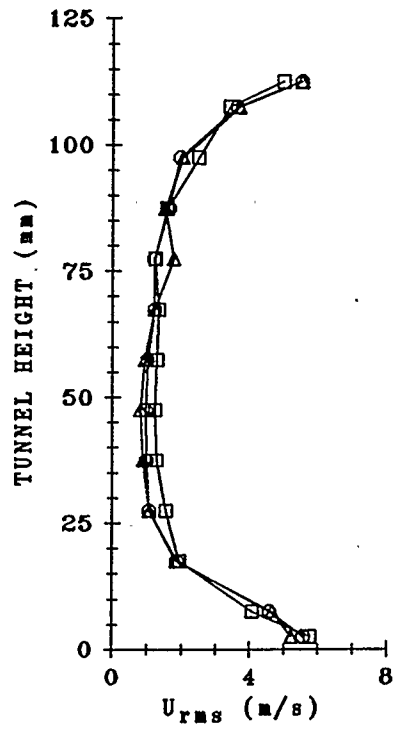
$U_{\infty} = 75.45 \text{ m/s}, \quad \rho_{\infty} = 1.0205 \text{ kg/m}^3$

WHERE : \square - ENTRANCE TRANSVERSE PLANE

\circ - MIDDLE TRANSVERSE PLANE

\triangle - EXIT TRANSVERSE PLANE

HOLE (13)



HOLE (17)

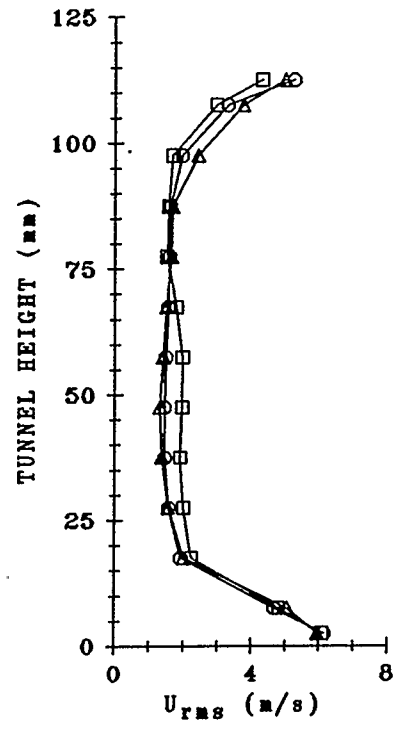


FIGURE 4.6 CONTINUED.

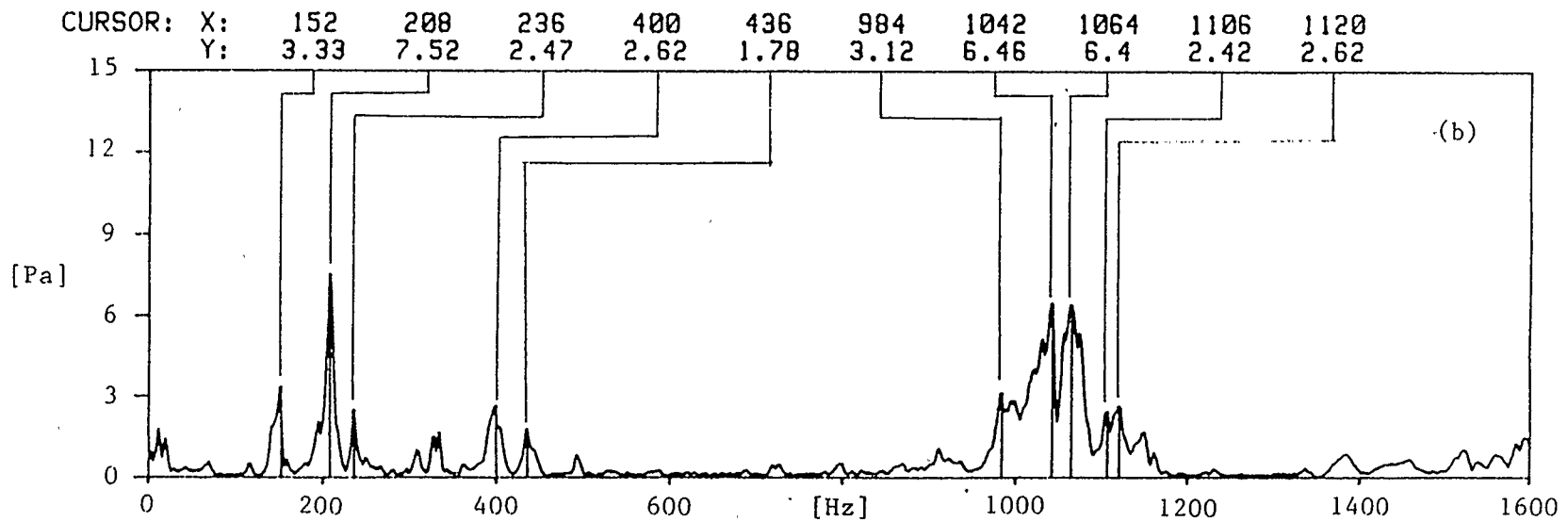
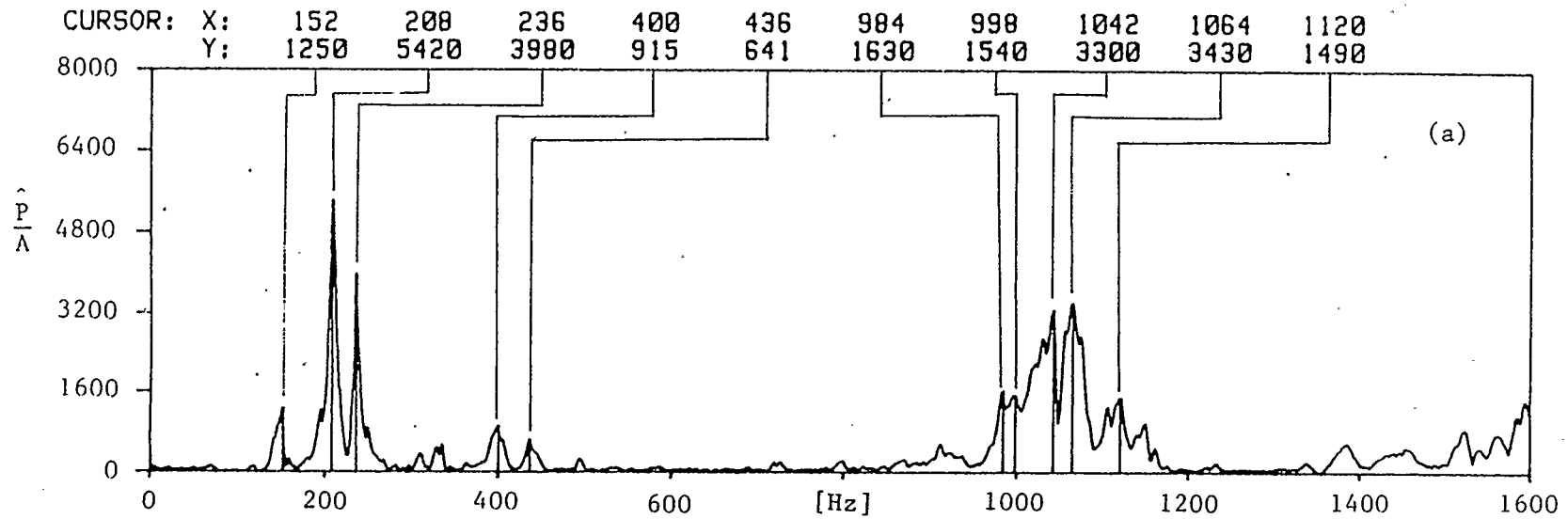


FIGURE 4.7 (a) FREQUENCY RESPONSE AND (b) MICROPHONE PICK-UP OF THE MECHANICAL SYSTEM WITH NO AIR FLOW (FOR 1.75 m. LONG, TUBE CONNECTING LOUDSPEAKER-JET).

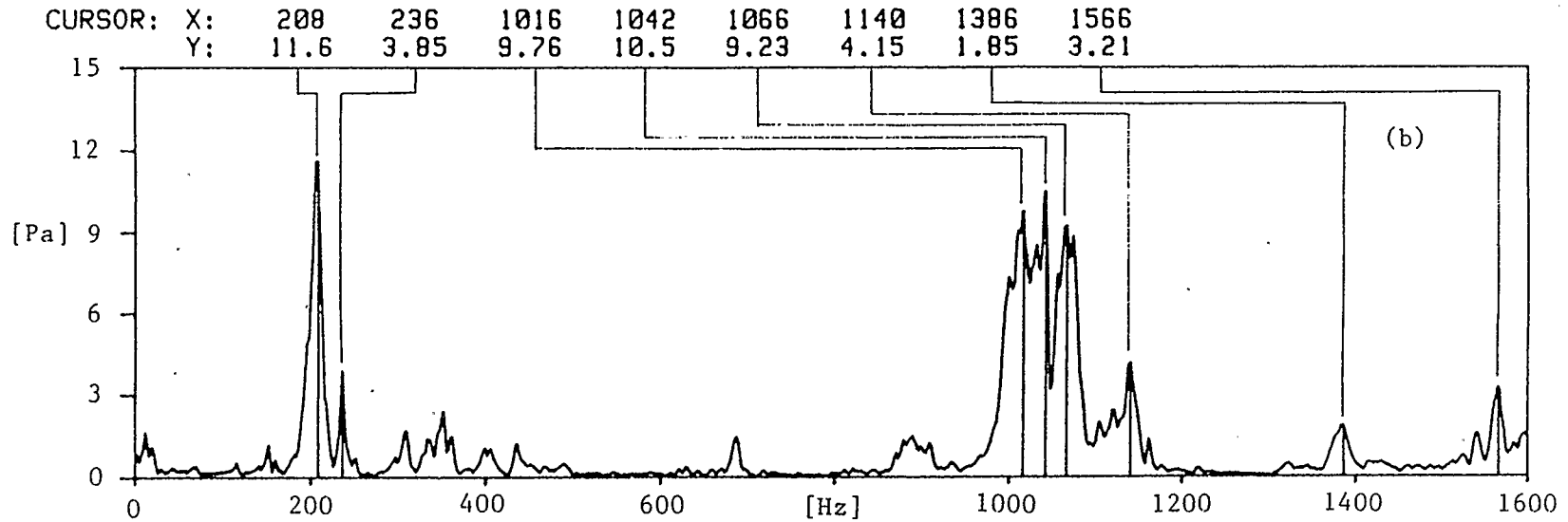
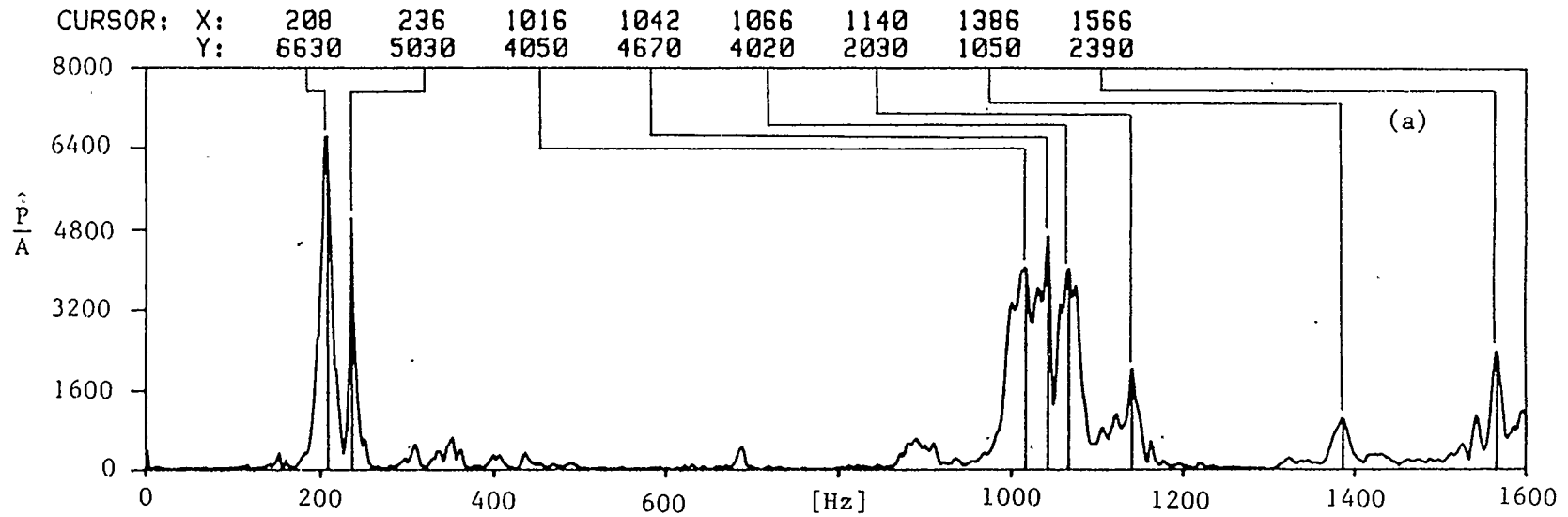


FIGURE 4.8 (a) FREQUENCY RESPONSE AND (b) MICROPHONE PICK-UP OF THE MECHANICAL SYSTEM WITH NO AIR FLOW (FOR 0.14 m. LONG, TUBE CONNECTING LOUDSPEAKER-JET).

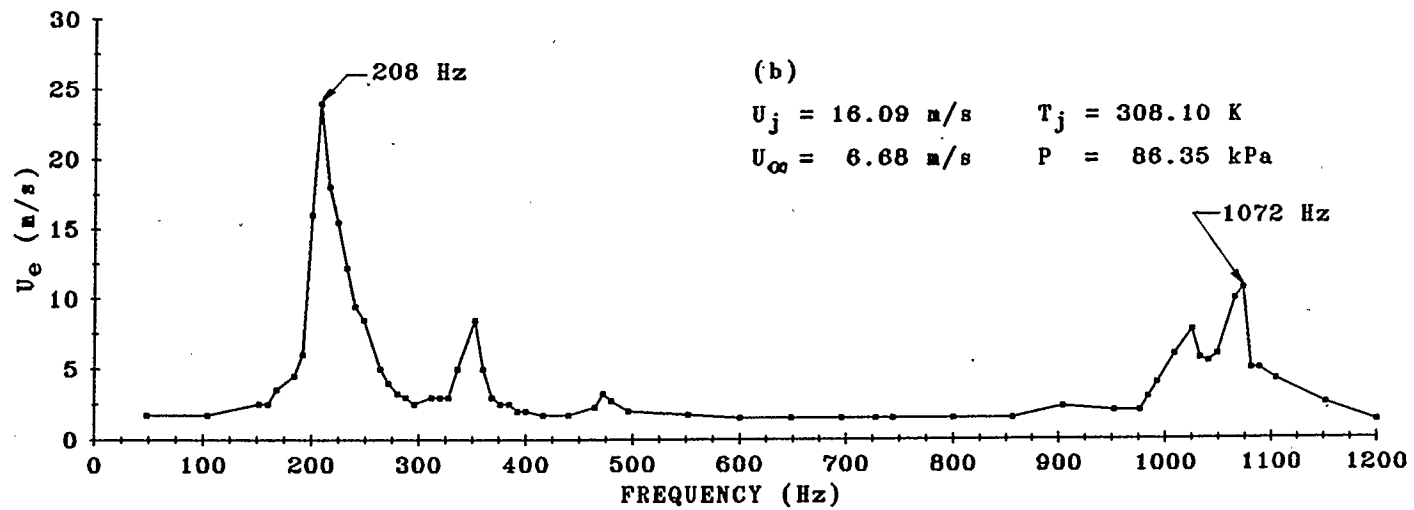
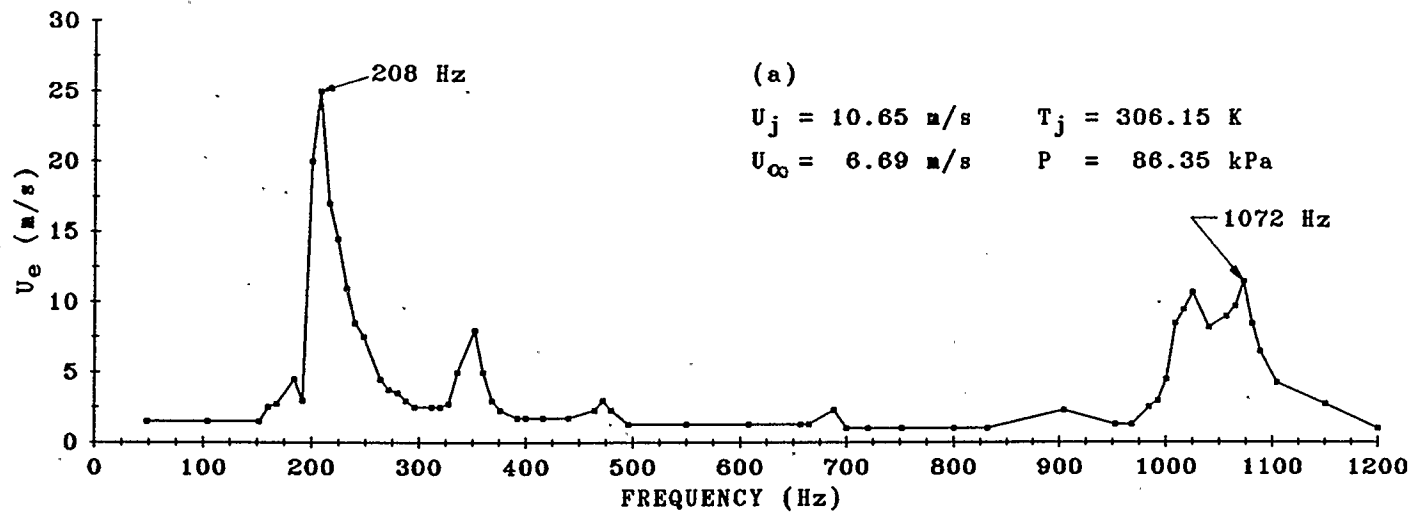


FIGURE 4.9 FREQUENCY RESPONSE OF MECHANICAL SYSTEM FOR CONSTANT INPUT CURRENT (2.0 Amp.) WITH AIR FLOW FOR ORIFICE 19.93 mm. DIA., 0.14 m. LONG DRIVER TUBE.

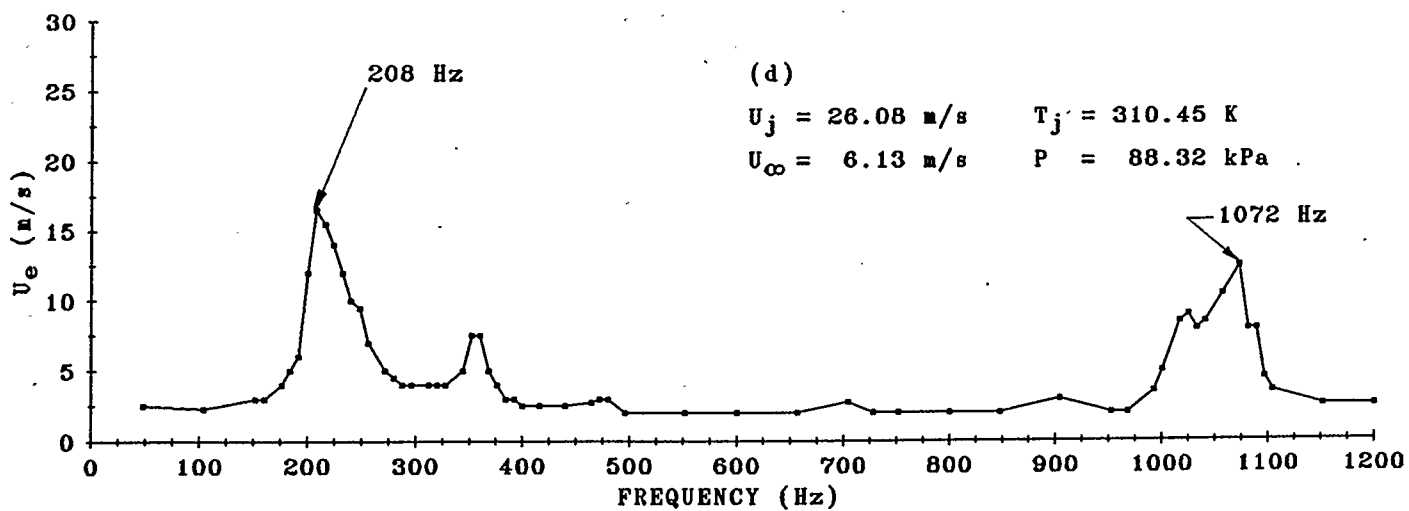
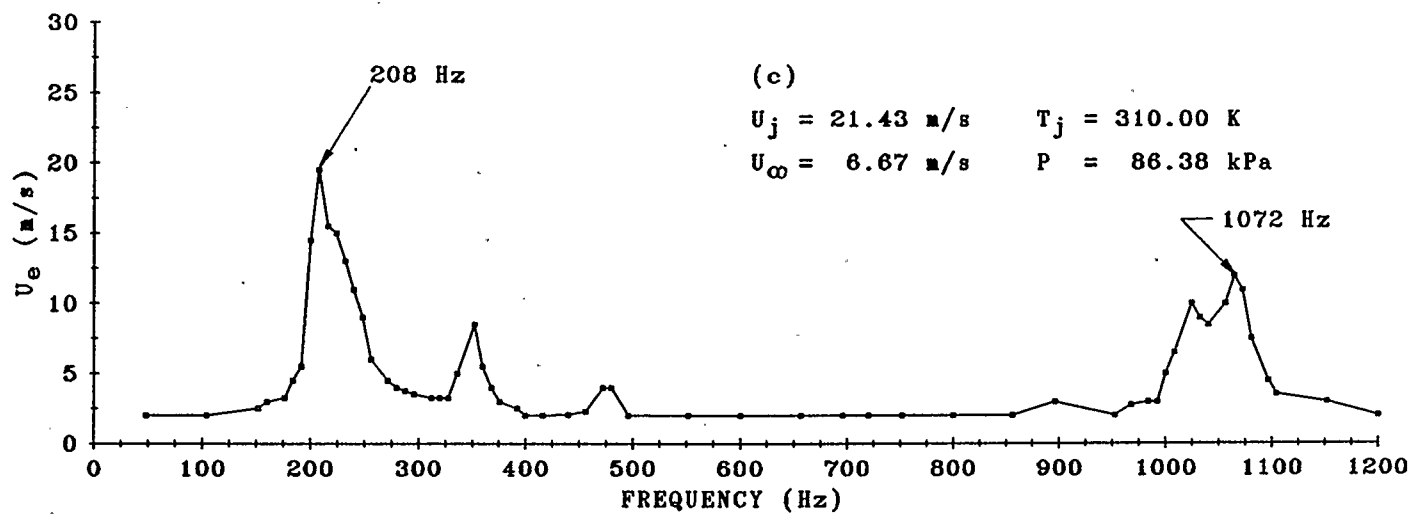


FIGURE 4.9 CONTINUED.

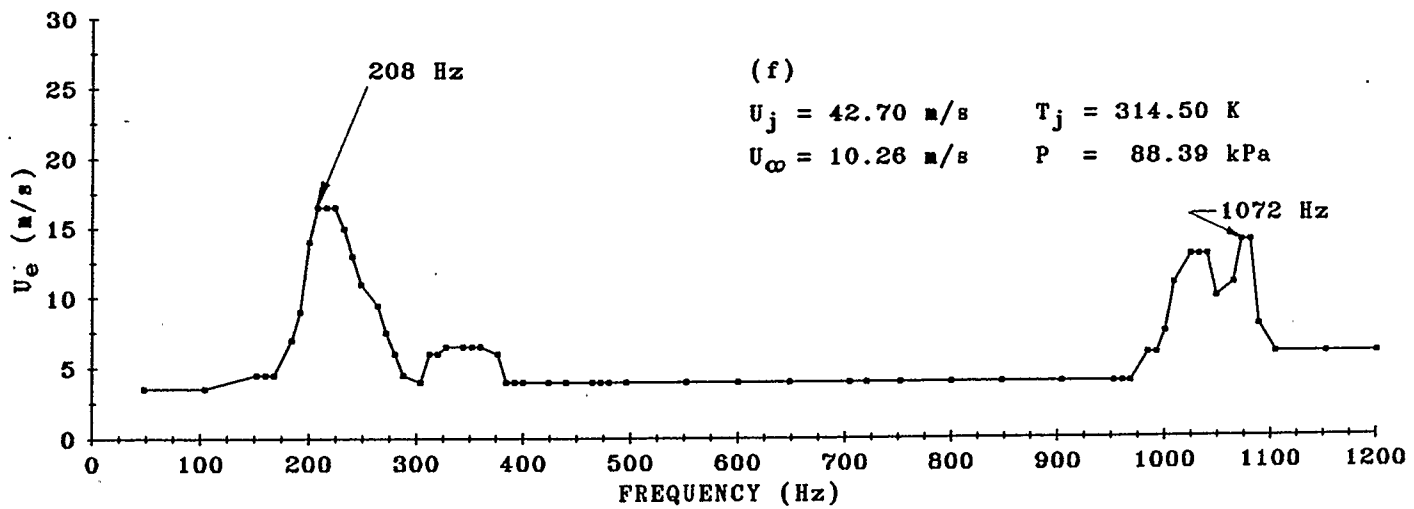
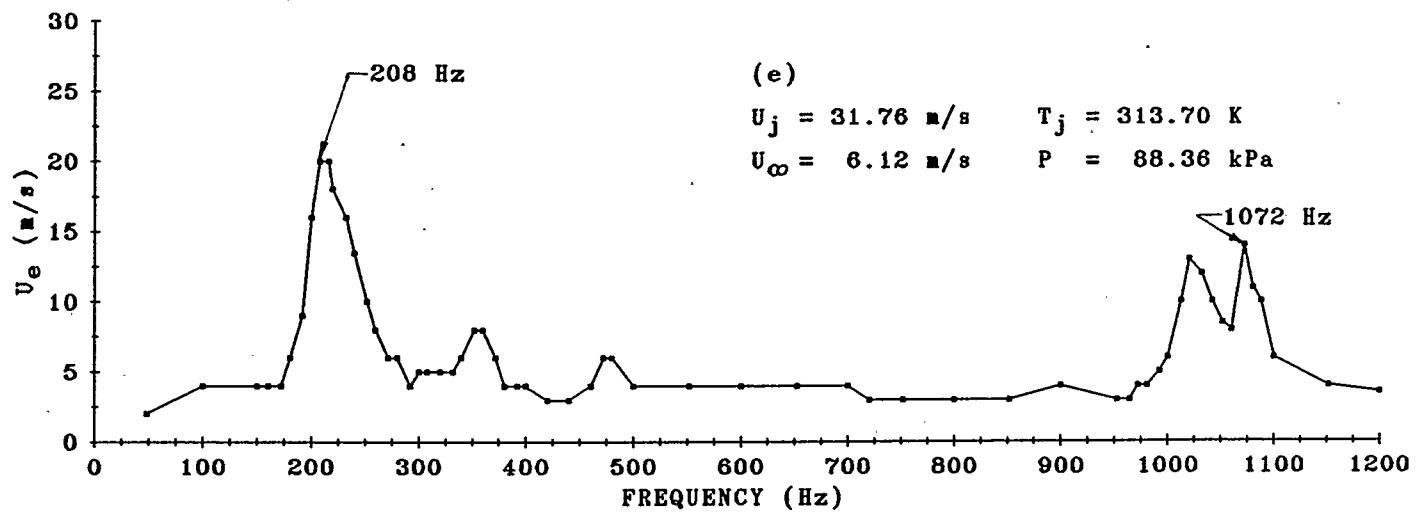


FIGURE 4.9 CONTINUED.

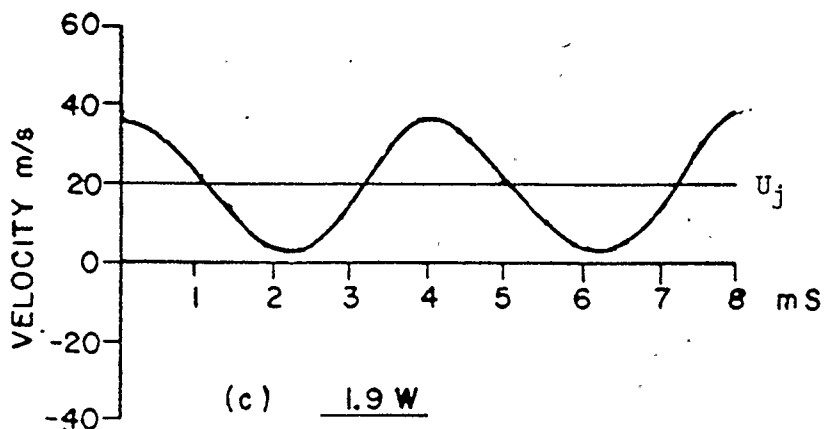
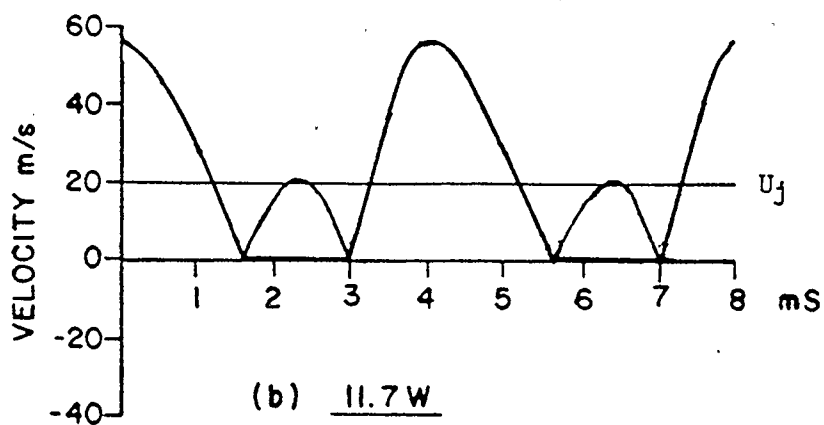
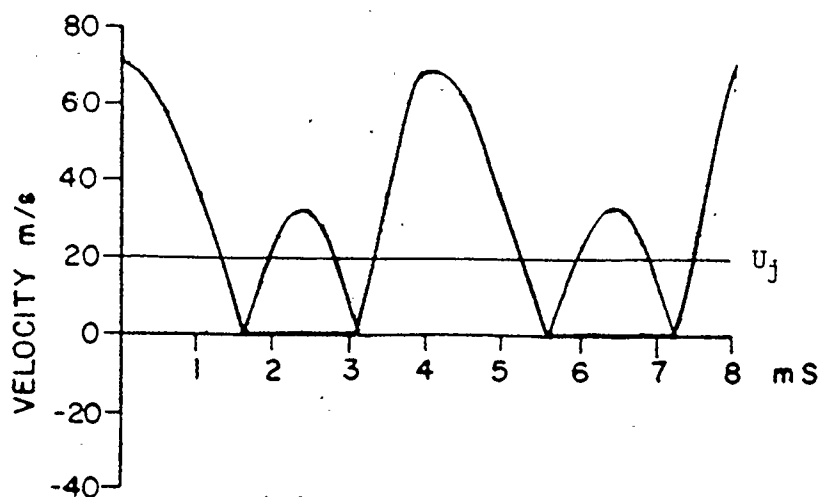


FIGURE 4.10 TYPICAL ANEMOMETER SIGNALS OF VELOCITY WAVE FORMS ON THE CENTRE-LINE IN THE JET ORIFICE EXIT PLANE WITH $U_j = 19$ m/s, $f = 250$ Hz, $D = 9.53$ mm DIA., TAKEN FROM REF. (3).

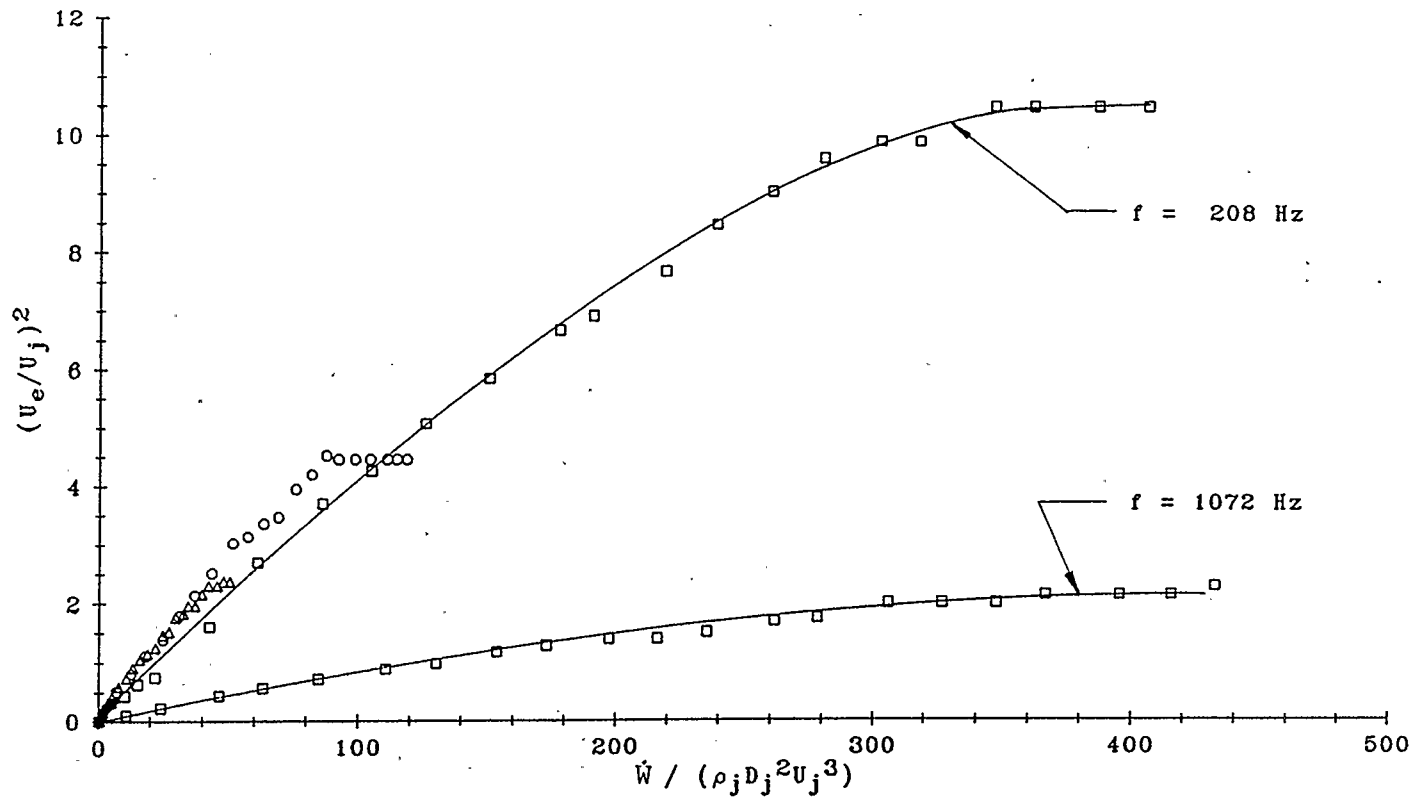


FIGURE 4.11 DIMENSIONLESS PULSATION STRENGTH VERSUS DIMENSIONLESS DRIVING POWER FOR 19.93 mm DIA. ORIFICE.

Re RANGE : 11076 - 86394
 St RANGE : 0.049 - 0.389 (f= 208 Hz)
 2.014 (f=1072 Hz)

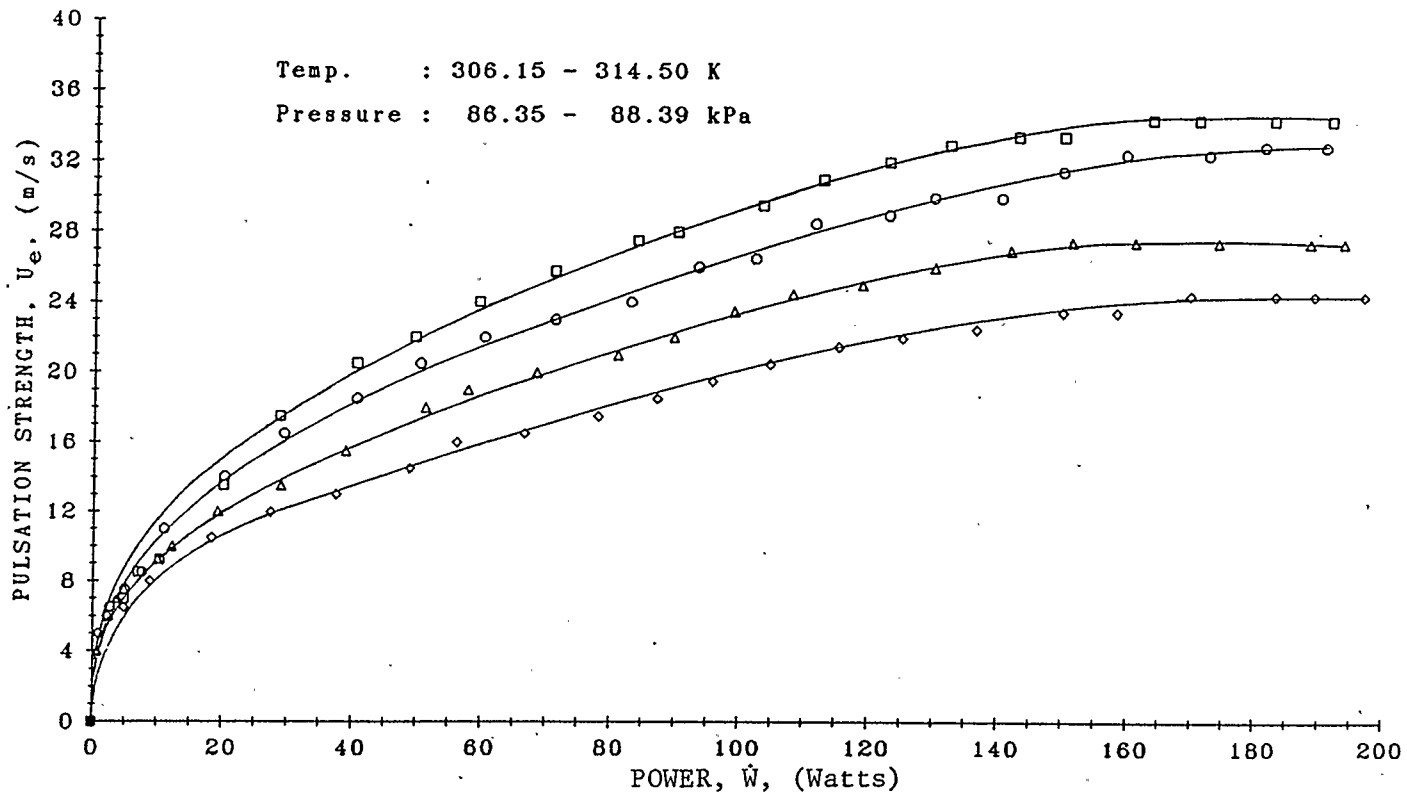


FIGURE 4.12 PULSATION STRENGTH VERSUS ACOUSTIC DRIVING POWER FOR TYPICAL VELOCITY CONDITIONS.

	$f = 280.0 \text{ Hz}$,	$D_j = 19.93 \text{ mm}$		
□ :	$U_j = 10.65 \text{ m/s}$,	$U_\infty = 6.69 \text{ m/s}$,	$St = 0.389$,	$Re = 11123$
○ :	$U_j = 21.43 \text{ m/s}$,	$U_\infty = 6.67 \text{ m/s}$,	$St = 0.193$,	$Re = 21898$
△ :	$U_j = 31.76 \text{ m/s}$,	$U_\infty = 6.12 \text{ m/s}$,	$St = 0.131$,	$Re = 32504$
◇ :	$U_j = 42.70 \text{ m/s}$,	$U_\infty = 10.26 \text{ m/s}$,	$St = 0.097$,	$Re = 43518$

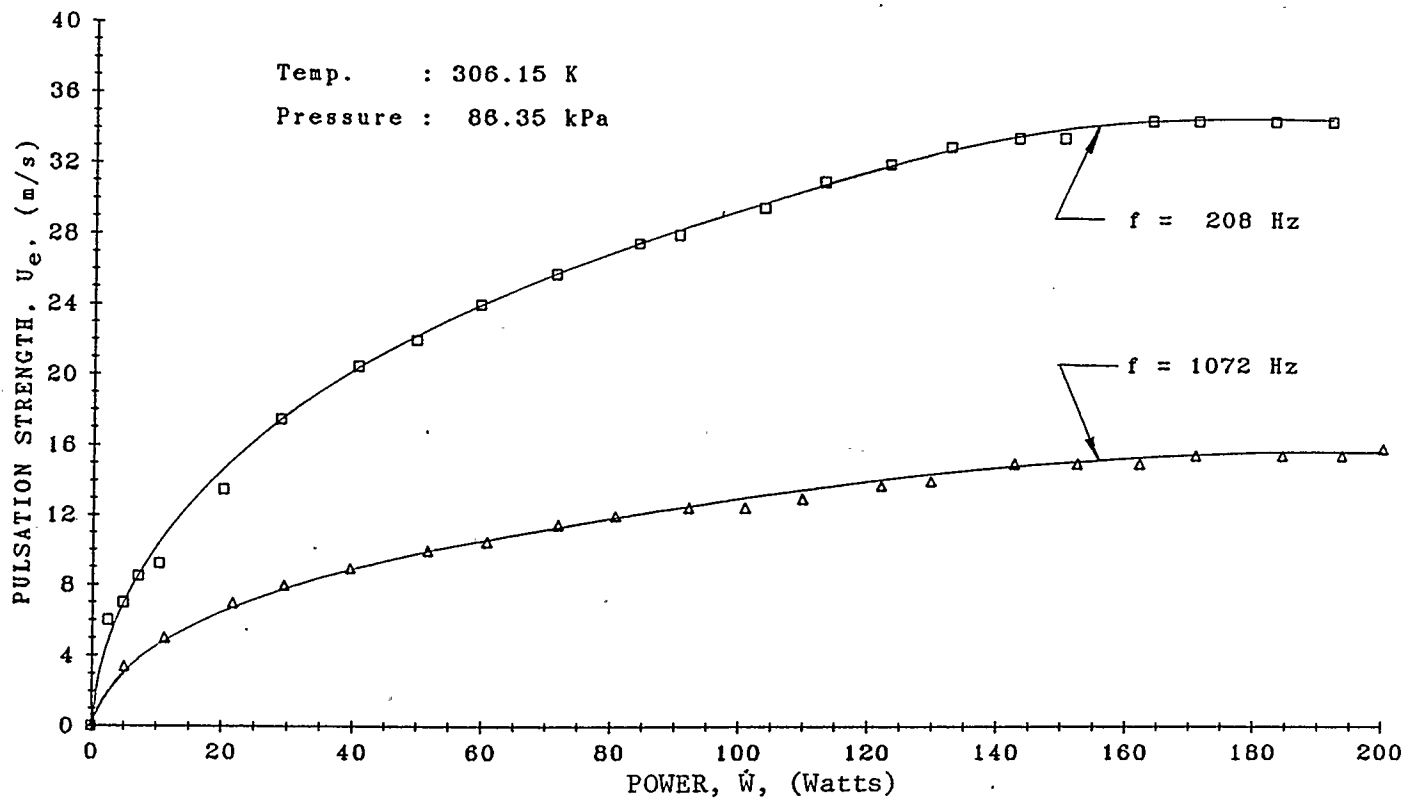


FIGURE 4.13 PULSATION STRENGTH VERSUS ACOUSTIC DRIVING POWER FOR DIFFERENT FREQUENCY CONDITIONS, 19.93 mm DIA., ORIFICE.

□ : $U_j = 10.65$ m/s, $U_\infty = 6.69$ m/s, $St = 0.389$, $Re = 11123$

△ : $U_j = 10.61$ m/s, $U_\infty = 6.69$ m/s, $St = 2.014$, $Re = 11076$

CHAPTER 5

EXPERIMENTAL RESULTS AND DISCUSSION

5.1 Velocity Pulsation Strength

The data of Figure 4.11 shows a unique relationship between pulsation strength, U_e and dimensionless power for the particular system of these experiments. The usefulness of simply measuring voltage and current for power is clearly shown, since rough comparisons between different driving situations may be easily made, allowing easy experimental control which would be difficult via pulsation strength. The non-linearity of the relationship is not clearly understood but, no doubt, it is influenced by the efficiency of energy transmission through the system to the jet flow. This problem is currently under active investigation by Vermeulen and Ramesh, but it is presenting severe experimental difficulties and to date no definite results are available. It should be noticed that care was taken to avoid amplifier distortion during the experiments for this thesis and therefore this factor was eliminated.

5.2 Velocity Profiles

This section presents the main experimental results in

terms of velocity and turbulence level profiles for situations with and without acoustic excitation.

5.2.1 Blockage Effect

The main experimental investigations covered a wide range of velocity ratios of jet-to-crossflow from 1.31 to 4.56, and since the reference pitot tube was being used to measure the crossflow mass flow rate it was important to assess any jet blockage effects. Therefore, a study of the influence of the jet column blockage was carried out. This study considered only two extreme cases for comparisons: (i) the case of the lowest velocity ratio of about 1.00, where two tests were involved, one for "no-drive", and the other for a 160 Watts "with-drive" condition; (ii) the case of a high velocity ratio of about 4.07 for "no-drive" condition. All the data were measured at the location of $X/D = -1.5$ (upstream from the orifice exit plane, refer to Figure 3.12) and notice that hole (9) was located directly ahead of the jet orifice.

Figures 5.1 and 5.2 present the experimental results for the case of the lowest velocity ratio for mean velocity profiles and turbulence level profiles respectively. The velocity profiles show a slight effect for "with-drive", and there is a definite increase in turbulence level at hole (9). The turbulence change will perhaps propagate to the plane of U_{ref} , $X/D = -3.66$, but the effect on the velocity profiles should be negligible. Figures 5.3

and 5.4 show the results of the case for high velocity ratio for "no-drive". There has been a slight decrease in velocity at hole (9) in comparison with the profiles at holes (5) and (13). This is clearly shown by Figure 5.5 where the profiles for the two jet velocity cases are compared. Again, it is not expected that significant change will take place in the velocity profiles in the plane of U_{ref} at $X/D = -3.66$. There was negligible effect on the turbulence profiles. Since a jet of this velocity cannot be strongly excited by the driver power available, acoustic excitation is not expected to produce significant changes in these results. Therefore, overall, it may be concluded that blockage effects on the velocity profiles in the plane of U_{ref} may be ignored and therefore the test section crossflow calibration in terms of U_{ref} is not changed by jet flows, and even when excited.

5.2.2 Velocity Profiles "Without Acoustic Excitation"

The experimental data of mean velocity profiles and fluctuating velocity profiles, U_{rms} , are presented in Figures 5.7 to 5.10, and 5.11 to 5.14 for a range of velocity ratios of jet to crossflow from 1.31 to 4.56 respectively.

To define the boundaries of the jet and crossflow, it is necessary to interpret the results of the mean velocity profiles and U_{rms} profiles simultaneously. It should be borne in mind that even though the hot film sensor is aligned such that its axis is parallel to the Z direction it will measure fluid velocities in

the X-Y plane irrespective of direction. It will also measure velocity components in this plane of fluid velocities which are not alligned in the X-Y plane. This, of course, greatly complicates any interpretation of the measured velocity profiles. Referring to the sets of profiles for a velocity ratio of about 2.26 in Figures 5.8 and 5.12. It was found that at the orifice exit plane, $X/D = 0.0$, $Y/D = 0.2$ (orifice lip 4.4 mm. high), the mean velocity was a maximum and the turbulence was a minimum. This is a typical pattern for the jet because the measuring location is on the centre line of a fully developed pipe flow. As the measuring probe is traversed vertically from the orifice, ie., in the Y direction, the mean velocity decreases according to the fully developed profile, to reach a minimum value with the crossflow, whilst the turbulence reaches a maximum value. The jet center axis is bent by the crossflow forces depending on the magnitude of the jet to crossflow velocity ratio, and only half the jet flow is traversed. However, a peak value of turbulence is reached (point su) which defines the jet upper boundary, the position of maximum shear. The velocity distributions are not symmetrical as they would be for the free jet, because the jet is now interferred with and distorted by the presence of the crossflow ($X/D = 3.0$ & 6.0).

A better position for describing the typical features of a complete jet in crossflow is shown by the profiles at the location of $X/D = 1.5$. From Figures 5.8 and 5.12, the region of the wake

was estimated to be from $Y = 0$ to about $Y = 17$ mm, and the region of influence of the jet bound vortices is from about $Y = 17$ to 40 mm (see Figure 2.1). This vortex-wake fluid then becomes entrained by the jet, as shown by the increasing velocity from $Y = 30$ mm. The jet zone is assumed to be defined by the maximum region in the turbulence profile, between points jj, with U_{rms} maximum (point sl), associated with the region of maximum shear, at about $Y = 40$ mm, resulting from the jet lower surface. As the measuring probe reaches about $Y = 45$ mm the velocity attains a maximum value (point a) whilst the turbulence reduces to a plateau. The point of maximum velocity, a, is taken to be the axis of the jet. At about $Y = 48$ mm, point su, the turbulence starts to decrease again indicating that the shear at the upper jet boundary has been masked by the increasing turbulence due to mixing and entrainment. The turbulence from points sl to su represents the last vestiges of the jets initial distribution now masked by increasing turbulence due to mixing and entrainment, and the absence of a maximum is due to the reduction in shear since the crossflow now reduces the relative velocity between jet flow and surrounding fluid. Similar features are shown by the other figures and are consistent with published work (3,11,21,27,31,35, 45).

By comparing the mean velocity profiles at different downstream locations, it was found that the peak jet velocity, corresponding to the axis of the jet, decreased in magnitude

indicating the whole jet stream had taken part in turbulent mixing and entrainment processes with the crossflow fluid. The jet trajectory, defined by the peak jet velocity, was clearly shown and the jet penetration increased with velocity ratio. The depth of the jet increased as the jet moved downstream and the dip in the velocity profile associated with the vortex-wake region gradually leveled off as mixing proceeded. The turbulence profiles showed similar behaviour in that the peak turbulence decreased, the jet depth increased, and the turbulence became more uniform as mixing proceeded. Both mean velocity and turbulence profiles were quite uniform by $X/D = 12.0$ indicating that mixing was substantially completed. As for the mean velocity profiles, the turbulence profiles define the jet trajectory and showed that jet penetration increased with velocity ratio. Figure 5.6 shows the structure of a typical jet-crossflow situation constructed from actual mean velocity profile measurements.

Figures 5.16 and 5.17 show the experimental details for velocity profile measurements on both sides of the jet. The results showed profiles of good symmetry, that the mixing processes were the same on both sides of the jet, and the jet axis coincided with the centre plane. Hence, there was no need to repeat the data for Figures 5.18 to 5.25 at lateral positions of negative value of Z/D .

There were eight lateral positions selected to measure the mean velocity profiles and turbulence profiles (refer to Figure

3.12 , $Z/D > 0.0$). Figures 5.18 to 5.21 and 5.22 to 5.25 present the experimental results for similar flow conditions as were used in Figures 5.7 to 5.10 and 5.11 to 5.14. Data in Figures 5.18 and 5.21 showed that the measurements were made on the verge of the jet stream, mostly revealing crossflow information. However, it was shown that as the velocity ratio of jet to crossflow was increased, the effect of jet spreading was found to be greater. This is conveniently summarised by Figure 5.26.1, which shows the jet mean velocity contours for "no-drive". All the lateral profiles showed the same features of a jet in crossflow as that of the center plane profiles, except that magnitudes were lower.

5.2.3 Velocity Profiles "With Acoustic Excitation"

It was mentioned earlier in section 4.4 that two kinds of major experimental tests were utilised for studying the affects of acoustic drive. Firstly, for a constant acoustic driver power of about 50 Watts, tests were conducted for a range of velocity ratios of jet-to-crossflow from 1.31 to 4.56, by only changing the jet velocity. Figures 5.7 to 5.10 and Figures 5.11 to 5.14 present the relevant experimental data. It should be pointed out that this set of tests is in the nature of a survey from which the overall behaviour may be deduced, since even though the driving power is kept constant the pulsation strength gradually varies, because of the changing jet velocity, which in turn causes the Strouhal number to vary. Thus the effects of the major variables

should be observable for a reasonable economy of effort. Secondly, keeping the crossflow velocity unchanged, the acoustic driving power was varied from 0 to 160 Watts for a constant jet velocity of 18.99 m/s that enabled the tests to take place at the optimum Strouhal number of 0.22. This ensured that a full range of data at optimum conditions was obtained in order to indicate the potential of the technique. Figures 5.27 and 5.28 present the experimental results for mean velocity and turbulence measurements of the tests.

Consider first the centre plane mean velocity distributions shown in Figures 5.7 to 5.10. For the lowest velocity ratio of 1.31, Figure 5.7, at the location $X/D = 0.0$, $Y/D = 0.2$, it will be seen that a significant increase in mean velocity was detected. This is considered to be due to the large pulsation strength causing reversed flow and hence a rectified signal, as sketched in Figure 4.10, which is then averaged by the anemometer-lineariser output to give an apparent increase in velocity. Of course, this is an ambiguous situation, although because the inflow and outflow events at the orifice are unsymmetrical, and the bypass system is unchoked, it is possible that the mass flow rate is increased by the acoustic drive and hence the average velocity may also be increased. Experiments to test this hypothesis were considered to be beyond the scope of this thesis. Furthermore, as illustrated by Figures 5.7 to 5.10 this apparent increase in velocity has disappeared since $U_e < U_j$, i.e., there is now no reverse flow. Of

course, U_e decreased as U_j was increased since W was kept constant.

The acoustic drive increases jet penetration, as shown by the displacement of point a, the axis of the jet, in Figures 5.7 at $X/D = 1.5$ and 3.0 and in Figures 5.8 to 5.10. This is also reflected in the displacement of the jet zone, points jj. Thus as the sensor is traversed vertically away from the orifice (Figure 5.7), the pulsating jet is measured in regions closer to the displaced jet zone boundary, Figure 5.6, until point su is reached, the position of maximum shear deduced from Figure 5.11. The region from su to v-v is most likely to be associated with the toroidal vortex mixing, v-v core region, and may represent a true increase in mean velocity. From v-v to j, in the jet outer zone, the velocity increase probably represents increased entrained flow due to the action of the toroidal vortices, compare Figures 5.7 and 5.8 with Figures 5.11 and 5.12. Beyond j the crossflow becomes dominant. Because of the ambiguity in mean velocity measurement (particularly near the orifice), the entire jet zone jj is perhaps best thought of as a zone of agitation and mixing.

The data shows acoustic excitation produces significant changes in the velocity profiles (increasing with pulsation strength), in particular the jet zone jj has greater depth than for the "no-drive" case, Figure 5.6. There is some indication that the velocity profile changes faster with distance downstream for the excited case in comparison with the "no-drive" case, and a

more uniformly mixed state is reached sooner. It should be realised that from $X/D = 1.5$ and onwards there was no experimental evidence of reverse flow, and hence data interpretation is not complicated by such considerations. Particularly at $X/D = 1.5$, the velocity profiles "with-drive" are more uniform than for "no-drive" indicating increased mixing with acoustic excitation.

Examining next the centre plane turbulence profiles of Figures 5.11 to 5.14, strong changes produced by the acoustic excitation are immediately obvious. Comparing the data at $X/D = 0.0$, and observing the effect of increasing U_e/U_j from 0.30 to 1.67, it will be seen that the turbulence profile is progressively changed from at first being simply amplified to becoming greatly altered in the jet core. For instance, Figures 5.11 and 5.12 show the core turbulence greatly increased at $Y/D = 0.2$ (point c), however, this is not considered to be true turbulence but the rms value of the pulsation velocity as shown by Figure 5.15, which plots U_e/U_j and $\sqrt{2}U_{rms}/U_j$ versus U_e/U_j . Data from Figures 5.28.1 to 5.28.8 are also plotted. Clearly for $U_e/U_j < 1.0$, $\sqrt{2}U_{rms}/U_j$ is closely the same as U_e/U_j , as it should be for a sinusoidal pulsation of amplitude U_e . For $U_e/U_j > 1.0$, the pulsation velocity is less sinusoidal (2), and rectification of the signal takes place by the hot film sensor, thus $\sqrt{2}U_{rms}/U_j$ deviates more and more from U_e/U_j . Figure 5.11 ($X/D = 0.0$) shows U_{rms} to be constant up to $Y/D \approx 0.8$ whereas Figure 5.12 ($X/D = 0.0$) shows

U_{rms} to decrease. This behaviour is presumed to be due to the presence or absence of signal rectification and the fact that as Y increases the probe is effectively making measurements off the jet axis and further downstream from the orifice. The whole jet zone, c-su-v-v-j, is best thought of as pseudo-turbulence, or agitation, being largely composed of pulsating flow in the core region, and induced pulsating flow due to travelling toroidal vortices in the outer region su-v-v-j. Figures 5.27.2 and 5.28.2 clearly shows the vortex core region v-v. A rough comparison (since the geometry is somewhat different) with the results of Ref. (1) indicates that for Figure 5.11 the fully developed entrainment is increased by about 50% by acoustic drive. Thus the much enlarged jet zone c-su-v-v-j, $X/D = 0.0$, indicates increased entrainment and mixing is taking place. The zone is considerably more vigorous than for the "no-drive" condition.

As Figures 5.11, $X/D = 1.5$ and $X/D = 3.0$, show there is rapid decay of the velocity pulsations and perhaps toroidal vortices. In fact the typical velocity structure of the vortex core could not be detected at $X/D = 3.0$. The more rapid decay of the toroidal vortices here, than for the pulsating free jet (2), is presumed to be due to the shearing action of the crossflow fluid, which opposes the rotation of the toroidal vortices. Thus from $X/D = 1.5$ onwards U_{rms} is a better indication of true turbulence, however the vortices still remain but are degenerating into large scale turbulence structures beyond this station.

Entrainment by the jet is taking place from the crossflow, augmented by the acoustic drive (1), therefore the increased turbulence profile, both in extent and magnitude, indicates that acoustic excitation has considerably improved the entrainment and mixing by the jet at $X/D \geq 1.5$. Temperature profiles for cold steady jets in a hot crossflow (59) show that in the wake region beneath the jet, from $Y = 0.0$ to j , $X/D = 1.5$ and 3.0 , some jet fluid and crossflow fluid mix. It is assumed that this continues for a pulsed jet and therefore that the much increased and modified wake region at $X/D = 1.5$ and 3.0 represents a vigorous mixing zone of some jet and crossflow fluid. Thus the acoustically increased zone of jet and wake represents a much improved mixing of jet and crossflow fluid than for the "no-drive" situation. By $X/D = 3.0$ the acoustically stimulated region affects some 90% of the tunnel flow height whereas the unexcited jet only affects 46%. By $X/D = 6.0$ the turbulence has decayed considerably but, now the acoustically excited jet affects 100% of the tunnel flow height and only 53% by the steady jet. By $X/D = 12.0$ the excited jet appears to be well mixed but the steady jet still has only affected 60% of the tunnel height. Acoustic drive has therefore shortened the mixing length. Figures 5.12 to 5.14 tell much the same story except that the acoustic drive is weaker as U_j is increased (W constant) and effects are smaller and more localised. In particular for Figure 5.10 and 5.14, at $X/D = 1.5$, the jet region is broadened as if the action of the toroidal

vortices is localised in the jet shear layer. Thus the shear peaks sl and su have become clearly resolved, and the maximum velocity has been reduced by the broadening. Also the effect of a weak acoustic drive has been further weakened by the poor Strouhal number condition.

The effect of acoustic excitation on the lateral mean velocity profiles is shown by Figures 5.16 to 5.17 and Figures 5.18 to 5.21. The former figures demonstrate that there is good symmetry about the centre plane for typical jet velocities of 25.27 m/s, $U_j/U_\infty = 2.59$ and 37.60 m/s, $U_j/U_\infty = 3.86$. Hence attention may be focused on the profiles on one side of the centre plane, Figures 5.18 to 5.21, for discussion purposes. As for the "no-drive" case the width of the jet has increased with increase of jet velocity, which is conveniently demonstrated by the contour plots of Figure 5.26.1. However, acoustic drive appears to have produced little additional change in jet width, although there has been a significant increase in jet depth and hence cross-sectional area. Excitation appears to have flattened the kidney type shape of the "no-drive" case suggesting, perhaps, flow field modification and therefore a flow visualisation study may prove interesting. Obviously jet penetration has significantly increased. The changes with downstream distance are consistent with those shown by the centre plane results, except that magnitudes are reduced because of being off the centre plane of the jet.

The lateral turbulence profiles in Figures 5.22 to 5.25 present data which is similar to those at the centre plane except for reduced magnitudes because of being off the centre plane of the jet. Similar information would be obtained from contour plots as for the mean velocity contours, Figures 5.26.1 and 5.26.2, and therefore it was felt unnecessary to produce these plots.

Figures 5.27.1 to 5.27.8 and Figures 5.28.1 to 5.28.8 present centre plane mean velocity and turbulence profiles at $St = 0.22$, the optimum Strouhal number, for increasing pulsation strength U_e/U_j . Making comparisons with the data of Figures 5.7 to 5.10 and Figures 5.11 to 5.14, at comparable values of U_e/U_j , reveals similar behaviour except for changes in magnitudes due to jet velocity and Strouhal number. Comparing Figures 5.27.1 and 5.28.1 with Figures 5.9 and 5.13 ($X/D = 1.5$ and 3.0) reveals similar patterns, except for penetration since the different U_j 's have not been normalised, for the same $U_e/U_j \approx 0.6$. The effect of the Strouhal number is not marked. At stronger excitation ($U_e/U_j = 1.53$ and 1.67) Figures 5.27.8 and 5.28.8 compared with Figures 5.7 and 5.11 ($X/D = 1.5$ and 3.0) clearly show that $St = 0.22$ optimises the response, also for all tests there has been a strong change in the wake zone, and for $St = 0.22$ there is a significant increase in the value of the velocity peak. The jet zone is distinctly broader, and with the strongly changed wake, by $X/D = 3.0$ the velocity profile is taking on the appearance of that of a free-jet (2). Following the development in the velocity profiles,

Figures 5.27.1 to 5.27.8 ($X/D = 1.5$ and 3.0), it will be observed that the velocity peak is less than that for "no-drive" at low U_e/U_j , the difference decreasing somewhat by $X/D = 3.0$, also shown by Figure 5.9. However, as U_e/U_j gets stronger the "with-drive" velocity peak soon surpasses that of the "no-drive" condition, with the difference at $X/D = 3.0$ being greater. The influence of X/D indicates that the flow is still developing. It is presumed that at low U_e/U_j , Figure 5.9, the reduced velocity peak "with-drive" is the result of increased jet flow area as shown by the contour plots of Figure 5.26.2. Conversely the increased jet flow area and velocity magnitude at large U_e/U_j implies a substantial increase in entrainment. Overall the data establishes typical optimum results and provides an optimum boundary for derived results, showing Strouhal number effect, as discussed in section 5.3.

5.3 Jet Trajectory, Strouhal Number Effect, and Other Parameters

It is common practice to define the centre plane jet trajectory as the locus of the maximum velocity of the velocity profiles. Thus the trajectory data from Figures 5.7 to 5.10, for steady jet conditions, has been plotted in Figure 5.29. Obviously the jet penetration has been substantially increased with increase of velocity ratio U_j/U_∞ (1.31 to 4.56) or momentum ratio $(U_j/U_\infty)^2$ (1.72 to 20.8). This appears to be normal behaviour when compared

with the results of other authors (38,41,44,52). A brief attempt was made to correlate the data, along the lines of Lefebvre for an unconfined crossflow (14), with only partial success. The lack of success is presumed to be due to the confining effect of the tunnel walls and further effort was abandoned for the purposes of this thesis. The suppression of penetration by the tunnel ceiling is obviously apparent by $U_j/U_\infty = 3.34$, and is marked by $U_j/U_\infty = 4.56$ where the jet strikes the tunnel ceiling at $X/D \approx 3.0$.

The effect on penetration by acoustic excitation is presented in Figures 5.30.1 to 5.30.4 which demonstrate that penetration is significantly increased with increase of excitation U_e/U_j . This data is complicated by the fact that Strouhal number and U_j/U_∞ are variables, hence Figure 5.31, for constant Strouhal number St and U_j/U_∞ , gives a clearer picture of the affect of acoustic drive. The suppression of penetration by the tunnel ceiling is an obvious feature. The increase of penetration with acoustic drive is clearly shown by replotting this data at constant X/D in Figure 5.32. The abscissa $(U_e/U_j)^2$ has been used because it is proportional to driving power and to the momentum ratio of the pulsed jet to the steady jet. Immediately it is seen that the increase of penetration saturates by about $(U_e/U_j)^2 = 1.5$ (about 75 Watts), $X/D = 1.5$ and 3.0 , and from this point of view little further is gained by increasing the excitation. At these locations penetration is unaffected by the proximity of the tunnel ceiling. The maximum increase of penetration is therefore about

67% at $X/D = 3.0$. This behaviour is consistent with the findings of Refs. (1,2) which speculated that the saturation may be due to the excitation of the toroidal vibration mode of the toroidal vortices.

From the jet penetration data the effect of Strouhal number may be deduced by plotting the fractional change of penetration $\Delta Y/Y_0$ versus $(U_e/U_j)^2$ at constant X/D as shown in Figure 5.33. Here the data at $St = 0.22$ forms an upper boundary encompassing all the data from Figures 5.30.1 to 5.30.4. It is possible that more data at other St values, particularly slightly greater or lesser than 0.22, will show that $St = 0.22$ is not an upper boundary, however it does appear that $St = 0.22$ is close to the optimum, agreeing with Refs. (1,2) for a free jet study.

Of importance to combustor designers is the pressure drop ΔP_j across the jet orifice for a particular jet velocity and hence trajectory. The available data has been plotted in Figure 5.34 for stations $X/D = 1.5$ and 3.0 where it will be seen that response lines at constant Strouhal number grow from the jet penetration for "no-drive" conditions. Thus the same "no-drive" penetration at a velocity ratio of 3.34 can be obtained at the optimum Strouhal number (lower $U_j/U_\infty = 1.93$) for a lower ΔP_j for a modest acoustic excitation power or U_e/U_j . Or put another way a jet with less momentum, when excited, can achieve the same penetration as a more energetic jet, and for a lower ΔP_j .

The fluctuating velocity or turbulence measurements of

Figures 5.11 to 5.14, and Figures 5.28.1 to 5.28.8 may be presented in an overall way by calculating the average or overall turbulence, U_{rms}^0 , for a given turbulence profile. This was done for profiles with and without acoustic excitation, and then the "no-drive" value was subtracted from the "with-drive" value to define ΔU_{rms}^0 . Thus this parameter represents the average or overall increase in turbulence due to acoustic excitation. Also the turbulence of the crossflow is eliminated. Figure 5.36 presents this information in dimensionless form over the experimental St range and for specific values of pulsation strength. Figure 5.37 completes the data by showing the effect of U_e/U_j at the optimum Strouhal number. Figure 5.35 also plots the "no-drive" data, where it will be observed that there is some similarity and the data passes through a maximum at about $X/D = 1.5$. The attainment of a maxima is due to the interaction of the jet and cross-stream producing a combined maximum effect near $X/D = 1.5$ and decaying thereafter. As the jet bends, becoming more parallel to the crossflow, the wake shedding processes weaken and hence the turbulence level reduces.

Acoustic excitation increases U_{rms}^0 by more than three times at $X/D = 1.5$, discounting the greater change at $X/D = 0.0$ since this is largely pseudo-turbulence. ΔU_{rms}^0 represents greater mixing, due to acoustic excitation, over the downstream range, and therefore the length to achieve a given state is shortened by excitation. The decay of ΔU_{rms}^0 indicates that U_{rms}^0

decays faster (with X/D) when excited than for "no-drive". Thus the greater turbulence momentum due to excitation decays faster than for the "no-drive" case. This must indicate that mixing with the lower momentum crossflow has been increased, with increase of entrainment mass flow rate in agreement with Ref. (1), ie, mixing has been improved by acoustic excitation. Strouhal number effect may be deduced from ΔU_{rms}^0 , as shown in Figure 5.38, where $\Delta U_{rms}^0/U_j$ has been plotted against U_e/U_j for $X/D = 3.0$ the location where jet response should be well established. Again the curve for $St = 0.22$ forms an upper boundary for the available data and strongly suggests that this is closely the optimum condition. Crow and Champagne (46) used a similar method for a free jet study except that they used the centre-line turbulence of the jet to deduce an optimum Strouhal number of 0.30. This was not used here, largely because of the uncertainty in defining the jet axis, and because the combined response of the jet-crossflow interaction from a mixing viewpoint was the main interest. It is of interest to notice that ΔU_{rms}^0 , and also U_{rms}^0 , only begin to saturate with increase of pulsation strength, $U_e/U_j > 1.2$, and therefore turbulence may still be increased further (hence mixing) by increasing U_e/U_j even though penetration ceases to increase. Vermeulen, et. al., (1) found a similar situation for the increase in entrainment mass flow rate. The optimum response at 0.22 Strouhal number has now been determined from jet penetration and overall turbulence and is in agreement with that found for the

optimum entrainment rate and mixing by a free jet study (1,2).

The effect of acoustic excitation on the maximum velocity of the mean velocity profiles may be conveniently summarised by defining the velocity traverse quality Q_u at a particular downstream location X :

$$Q_u = \frac{U_{\max} - U_m}{U_m}$$

where U_{\max} is the velocity maximum of the mean velocity profiles, and U_m is the mean velocity calculated from the total mass flow rate of jet and crossflow at the test section exit plane, ie., at $X/D = 12.0$. Measurements showed that the temperature was uniform across the exit plane (within 1°C), also there was negligible difference between the temperatures and static pressures at the entry and exit planes of the test section. Therefore, for convenience, U_m was based on the inlet plane density. Q_u has therefore been plotted against X/D for all the tests as shown by Figures 5.39 and 5.40. Because of the ambiguous nature of the measurements at $X/D = 0.0$, and since this profile is not a true jet-transverse profile, these data points have been rejected. Provided U_e/U_j is strong enough Q_u is increased by acoustic drive ie., the velocity maximum is increased, but the rate of decay of Q_u is also increased. Thus the greater momentum indicated by Q_u decays faster than for the "no-drive" case. Again this must mean that mixing with the lower momentum crossflow has been increased

by acoustic excitation, and the mixing length shortened to achieve a desired state.

Z/D = -3.1
HOLE (5)

Z/D = 0.0
HOLE (9)

Z/D = +3.1
HOLE (13)

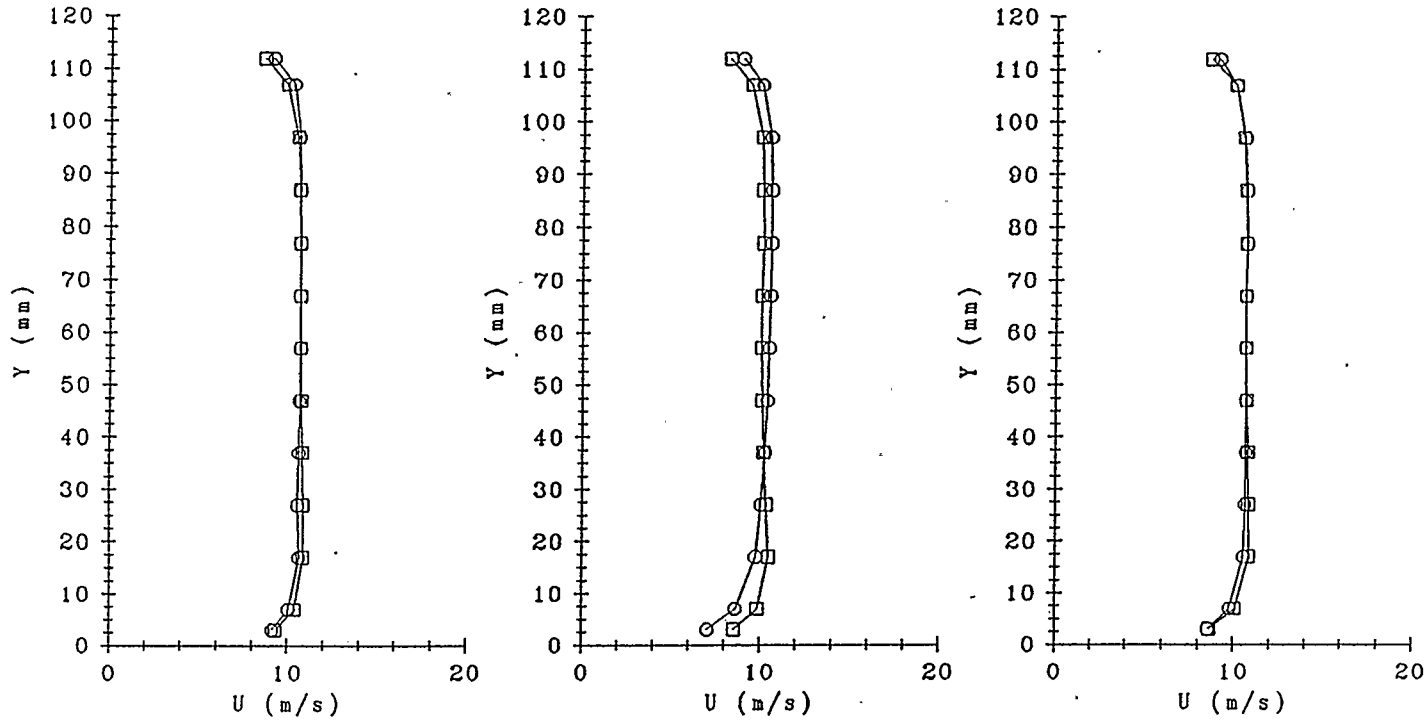


FIGURE 5.1 MEAN VELOCITY PROFILES ACROSS ENTRANCE PLANE FOR 19.93 mm JET DIAMETER AT X/D = -1.5.

$U_j = 10.37 \text{ m/s}$

$U_\infty = 10.32 \text{ m/s}$

○ : "NO-DRIVE"

□ : "WITH-DRIVE", 160 Watts, 208 Hz

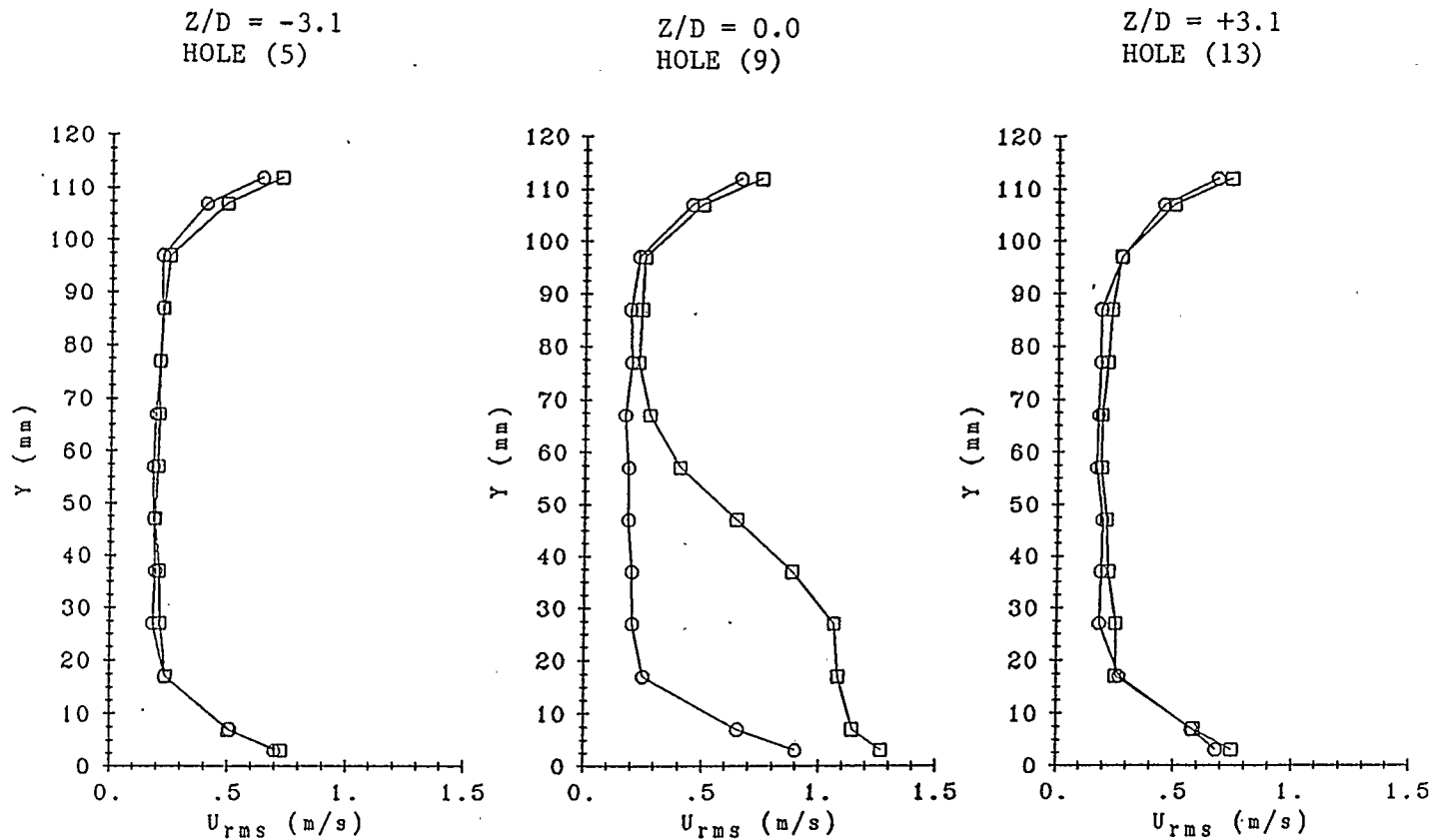


FIGURE 5.2 U_{rms} VELOCITY PROFILES ACROSS ENTRANCE PLANE FOR 19.93 mm JET DIAMETER AT $X/D = -1.5$.

$U_j = 10.37 \text{ m/s}$

$U_\infty = 10.32 \text{ m/s}$

○ : "NO-DRIVE"

□ : "WITH-DRIVE", 160 Watts, 208 Hz

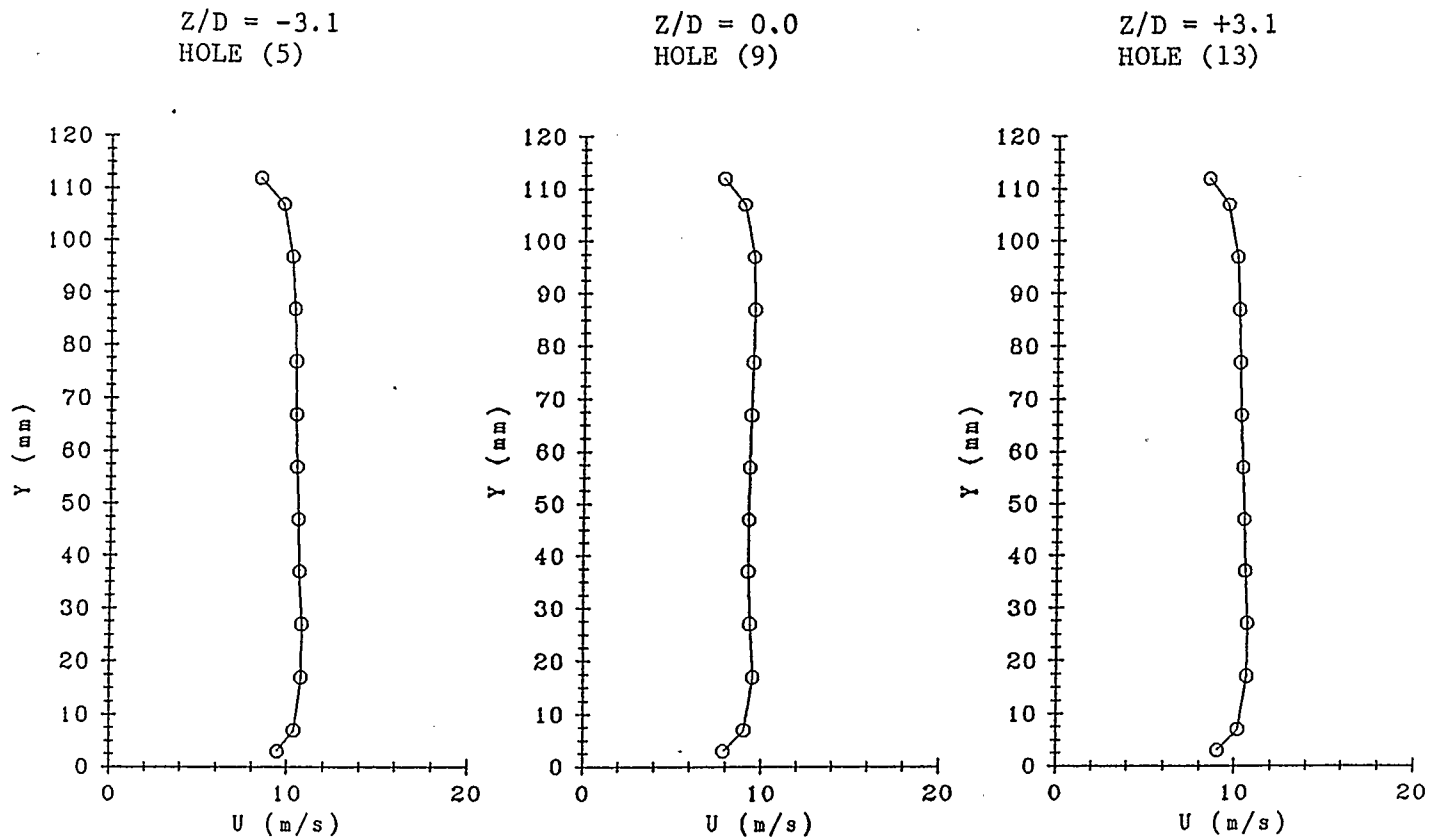


FIGURE 5.3 MEAN VELOCITY PROFILES ACROSS ENTRANCE PLANE FOR 19.93 mm JET DIAMETER AT X/D = -1.5.

$U_j = 42.04 \text{ m/s}$ $U_\infty = 10.32 \text{ m/s}$

o : "NO-DRIVE"

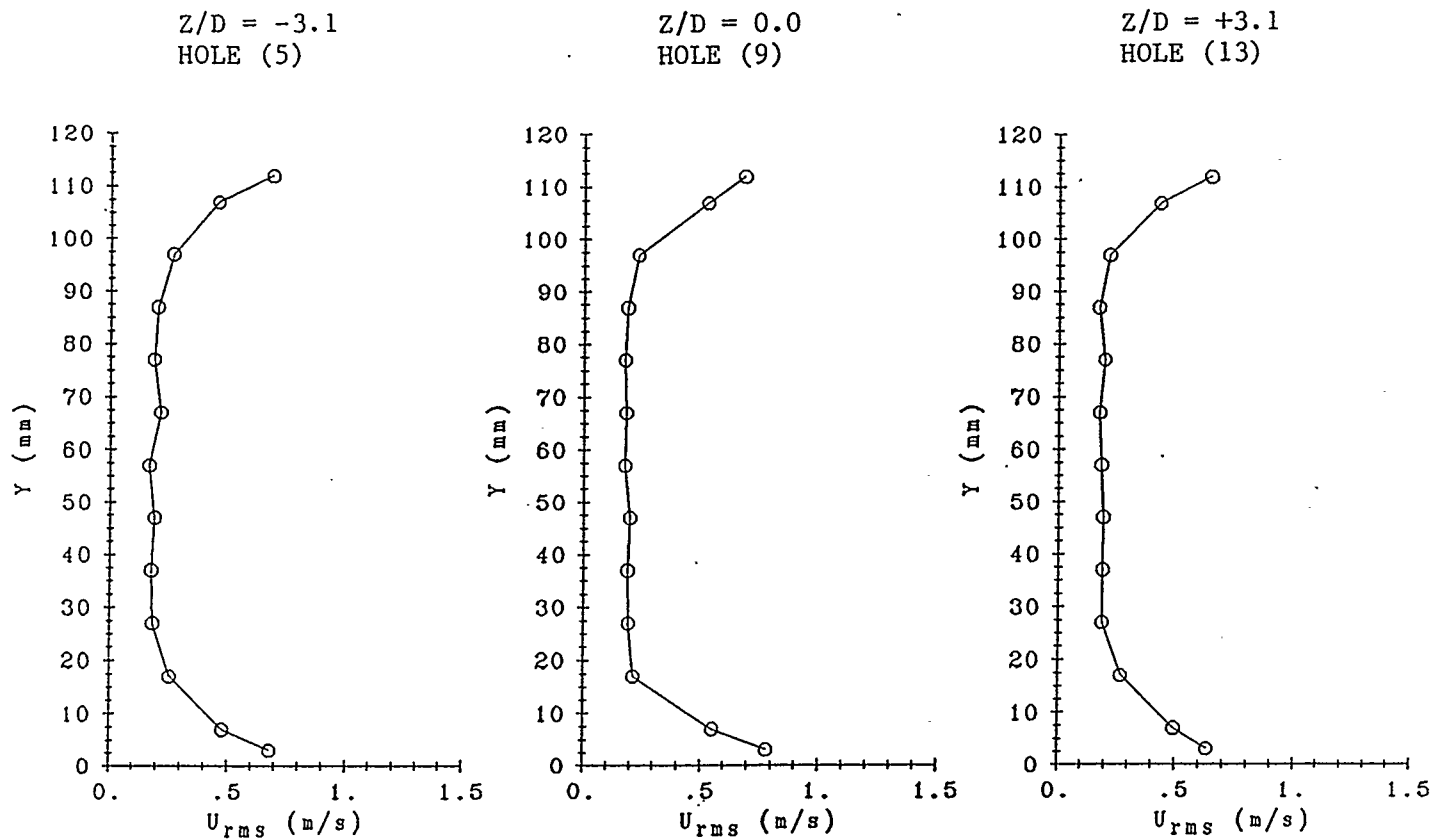


FIGURE 5.4 U_{rms} VELOCITY PROFILES ACROSS ENTRANCE PLANE FOR 19.93 mm JET DIAMETER AT $X/D = -1.5$.

$U_j = 42.04 \text{ m/s}$ $U_\infty = 10.32 \text{ m/s}$

o : "NO-DRIVE"

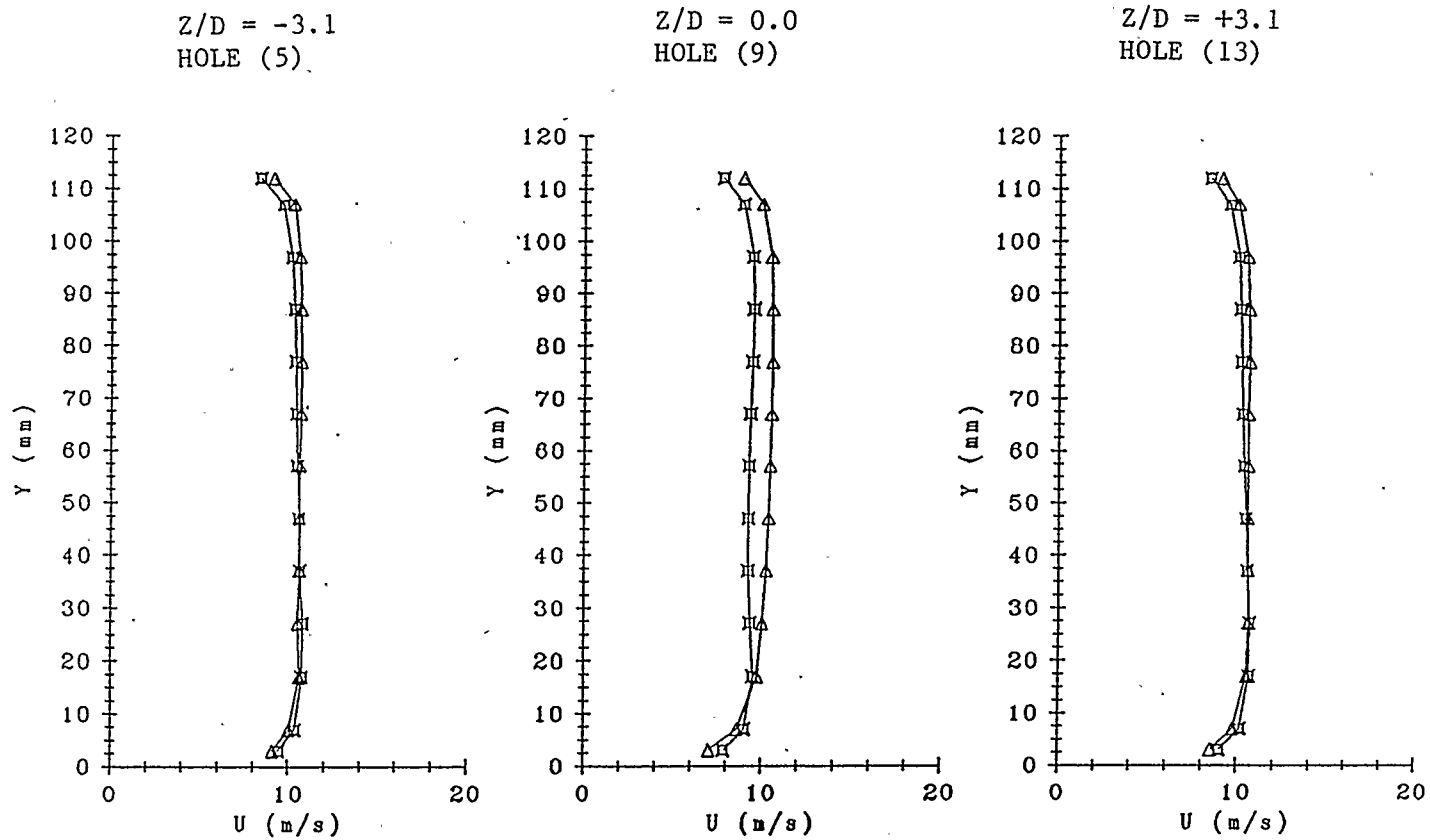


FIGURE 5.5 THE BLOCKAGE EFFECT COMPARISON OF MEAN VELOCITY PROFILES ACROSS ENTRANCE PLANE FOR 19.93 mm JET DIAMETER AT X/D = -1.5.

Δ : $U_j = 10.37$ m/s $U_\infty = 10.32$ m/s
 \square : $U_j = 42.04$ m/s $U_\infty = 10.32$ m/s

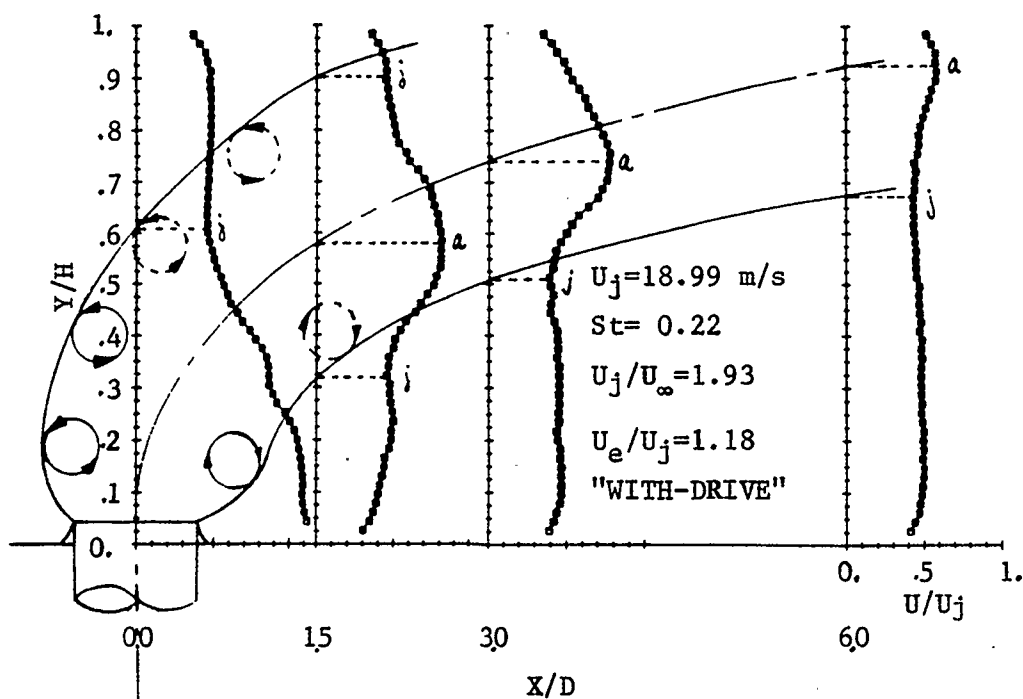
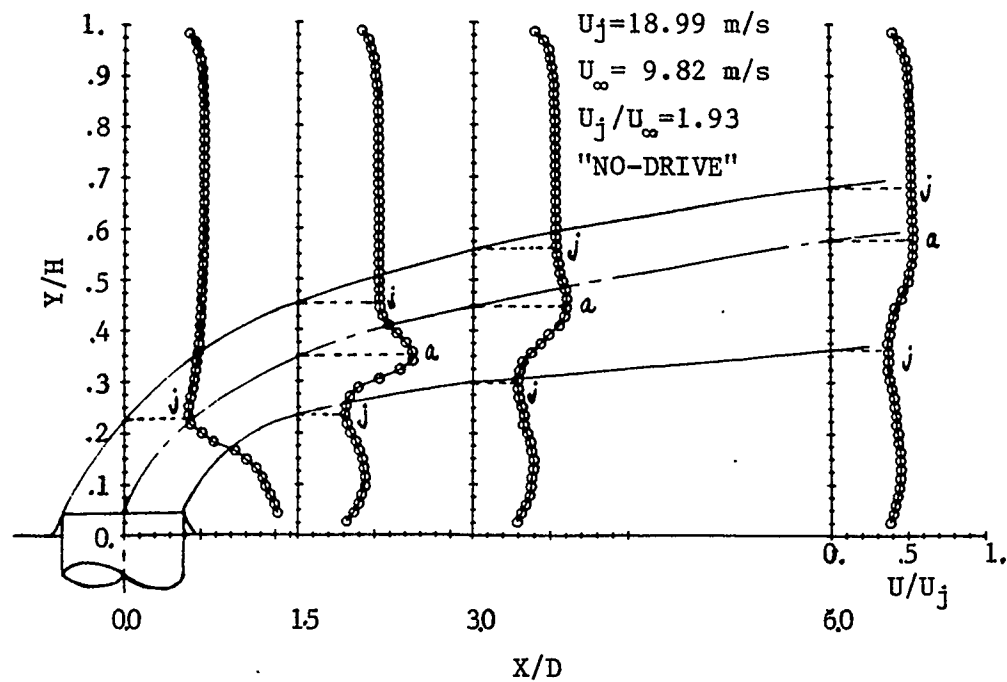


FIGURE 5.6 STRUCTURE OF JET CONSTRUCTED FROM ACTUAL VELOCITY PROFILES FROM FIGURE 5.28.5. VORTICES ARE DIAGRAMATIC ONLY SINCE HORIZONTAL SCALE IS DIFFERENT TO VERTICAL SCALE.

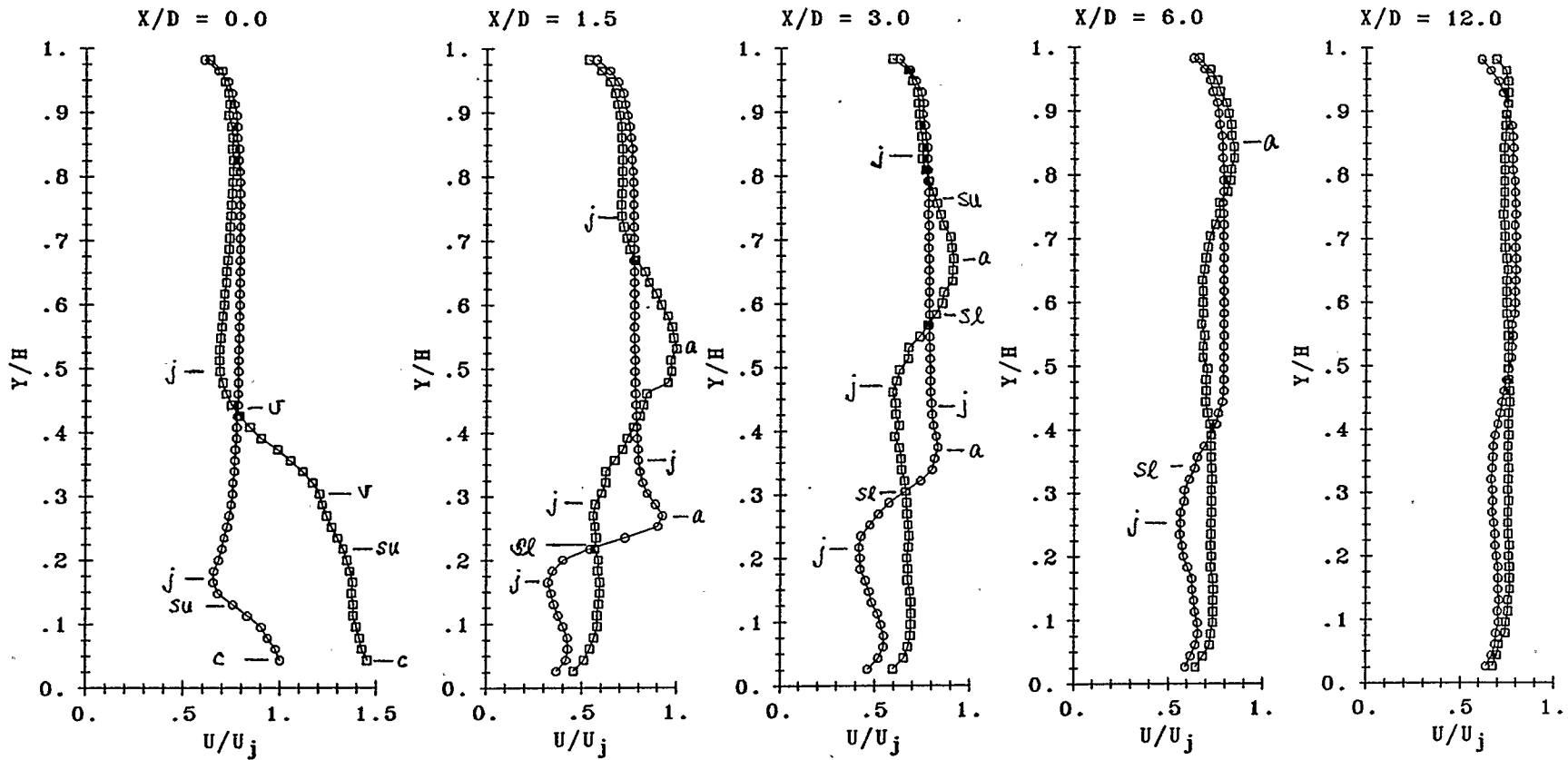


FIGURE 5.7 MEAN VELOCITY PROFILES ON CENTRE PLANE FOR JET ORIFICE 19.93 mm DIAMETER.

$U_j = 13.20$ m/s	$U_\infty = 10.06$ m/s	$U_j/U_\infty = 1.31$
$\dot{W} = 52.80$ W	$St = 0.31$	$U_e/U_j = 1.67$
$f = 208.0$ Hz	$U_e = 22.00$ m/s	o : "NO-DRIVE"
$Re_j = 13878$	$Re_\infty = 83343$	□ : "WITH-DRIVE"
$\rho_j = 0.9912$ kg/m ³	$\rho_\infty = 0.9444$ kg/m ³	

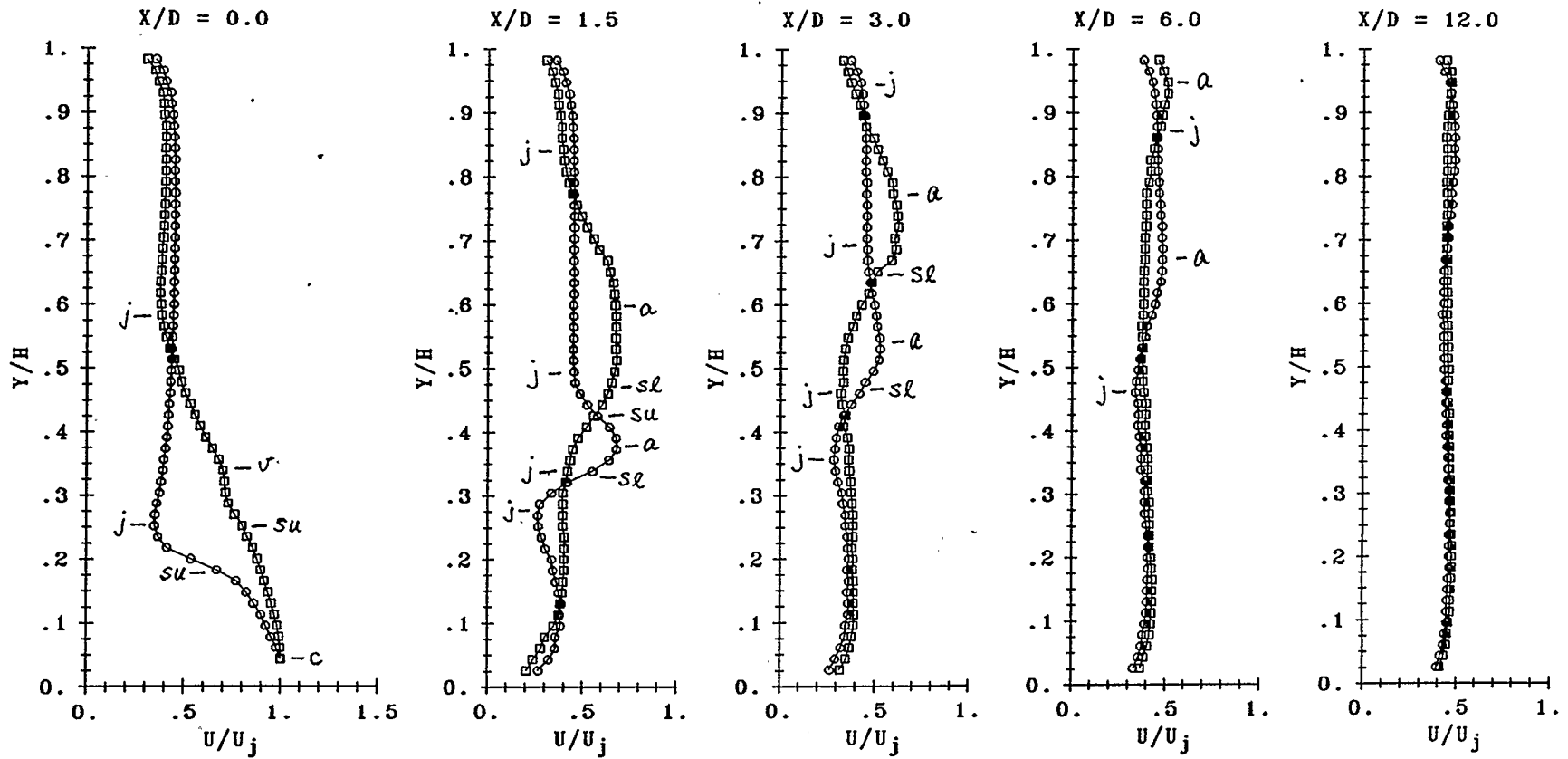


FIGURE 5.8 MEAN VELOCITY PROFILES ON CENTRE PLANE FOR JET ORIFICE 19.93 mm DIAMETER.

$U_j = 23.27 \text{ m/s}$	$U_\infty = 10.27 \text{ m/s}$	$U_j/U_\infty = 2.26$
$\dot{W} = 52.80 \text{ W}$	$St = 0.18$	$U_e/U_j = 0.86$
$f = 208.0 \text{ Hz}$	$U_e = 20.00 \text{ m/s}$	$\circ : \text{ "NO-DRIVE"}$
$Re_j = 24463$	$Re_\infty = 86138$	$\square : \text{ "WITH-DRIVE"}$
$\rho_j = 0.9945 \text{ kg/m}^3$	$\rho_\infty = 0.9540 \text{ kg/m}^3$	

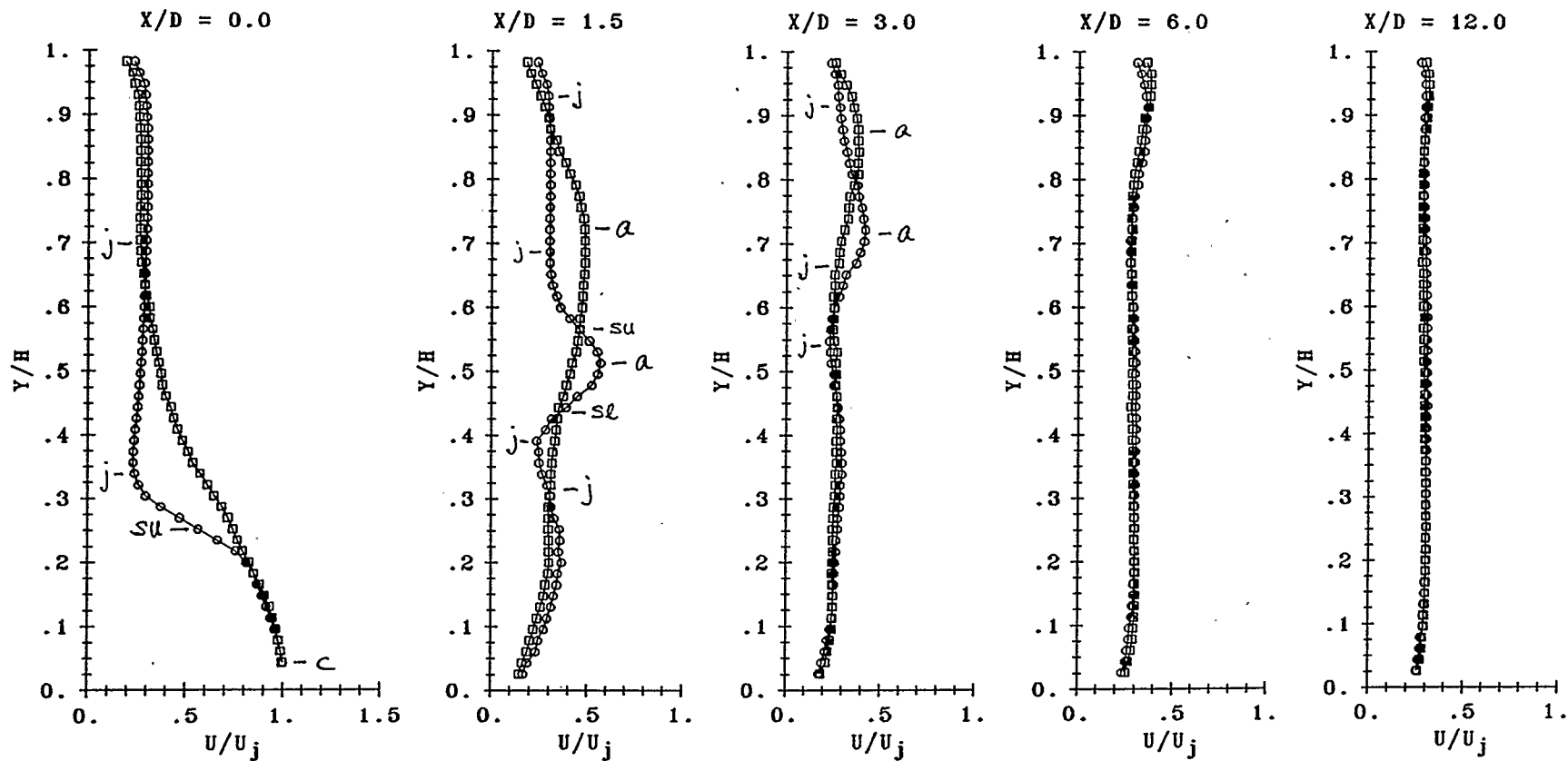


FIGURE 5.9 MEAN VELOCITY PROFILES ON CENTRE PLANE FOR JET ORIFICE 19.93 mm DIAMETER.

$U_j = 34.30 \text{ m/s}$	$U_\infty = 10.27 \text{ m/s}$	$U_j/U_\infty = 3.34$
$\dot{W} = 50.00 \text{ W}$	$St = 0.12$	$U_e/U_j = 0.54$
$f = 208.0 \text{ Hz}$	$U_e = 18.50 \text{ m/s}$	$\circ : \text{"NO-DRIVE"}$
$Re_j = 35581$	$Re_\infty = 87198$	$\square : \text{"WITH-DRIVE"}$
$\rho_j = 0.9905 \text{ kg/m}^3$	$\rho_\infty = 0.9643 \text{ kg/m}^3$	

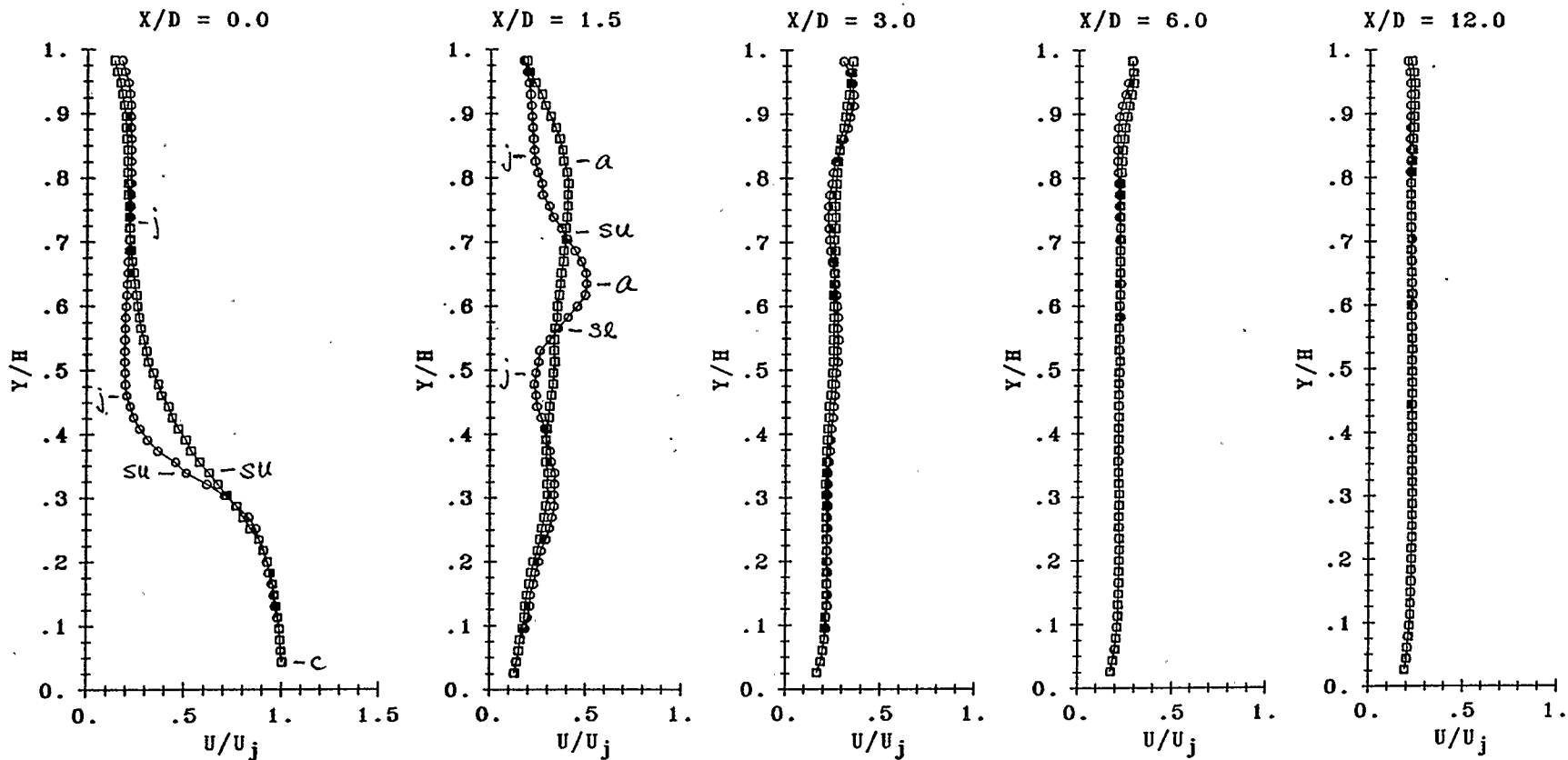


FIGURE 5.10 MEAN VELOCITY PROFILES ON CENTRE PLANE FOR JET ORIFICE 19.93 mm DIAMETER.

$$U_j = 46.22 \text{ m/s}$$

$$\dot{W} = 51.20 \text{ W}$$

$$f = 208.0 \text{ Hz}$$

$$Re_j = 47443$$

$$\rho_j = 0.9842 \text{ kg/m}^3$$

$$U_\infty = 10.13 \text{ m/s}$$

$$St = 0.09$$

$$U_e = 14.00 \text{ m/s}$$

$$Re_\infty = 84954$$

$$\rho_\infty = 0.9575 \text{ kg/m}^3$$

$$U_j/U_\infty = 4.56$$

$$U_e/U_j = 0.30$$

○ : "NO-DRIVE"

□ : "WITH-DRIVE"

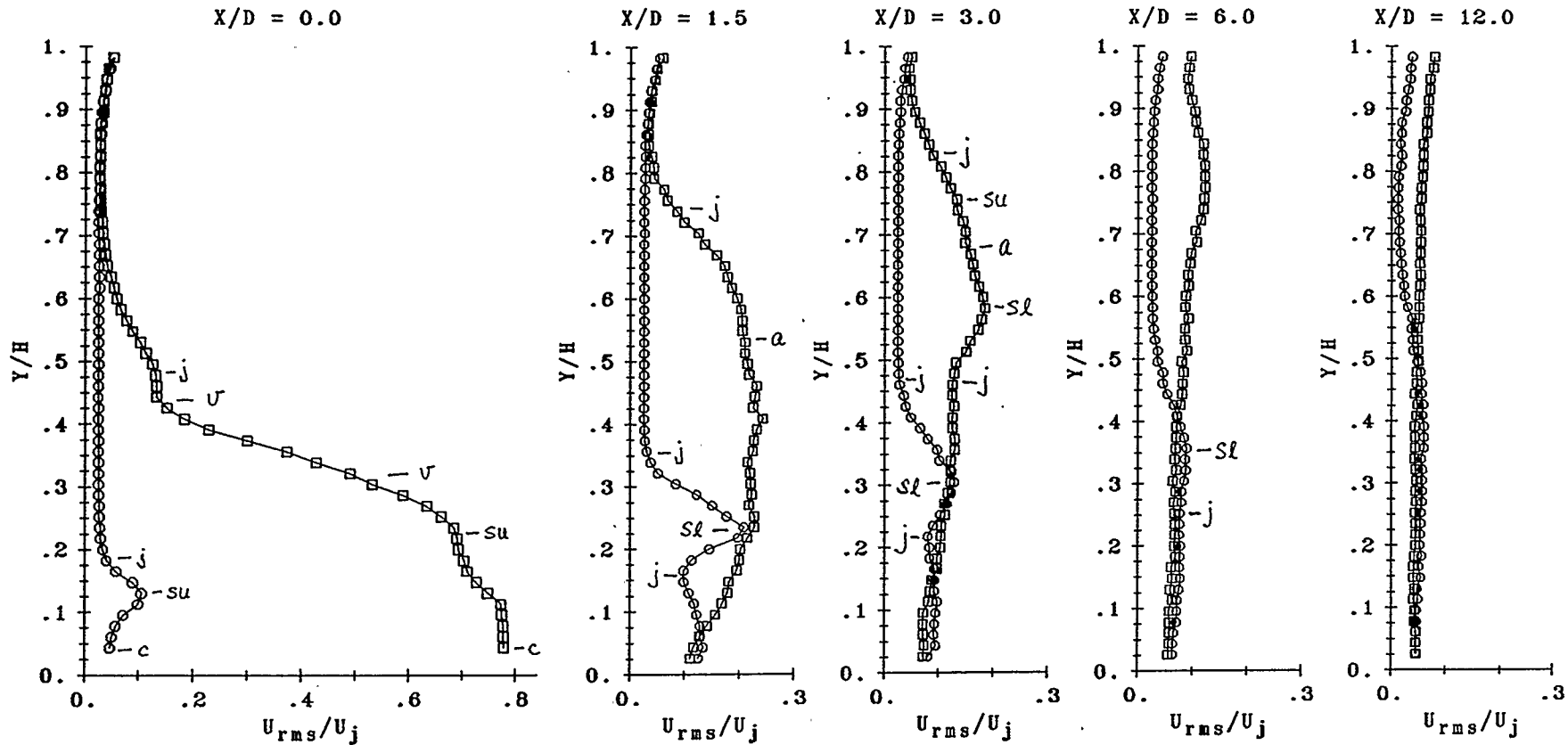


FIGURE 5.11 U_{rms} TURBULENCE PROFILES ON CENTRE PLANE FOR JET ORIFICE 19.93 mm DIAMETER.

$U_j = 13.20$ m/s	$U_\infty = 10.06$ m/s	$U_j/U_\infty = 1.31$
$\dot{W} = 52.80$ W	$St = 0.31$	$U_e/U_j = 1.67$
$f = 208.0$ Hz	$U_e = 22.00$ m/s	o : "NO-DRIVE"
$Re_j = 13878$	$Re_\infty = 83343$	□ : "WITH-DRIVE"
$\rho_j = 0.9912$ kg/m ³	$\rho_\infty = 0.9444$ kg/m ³	

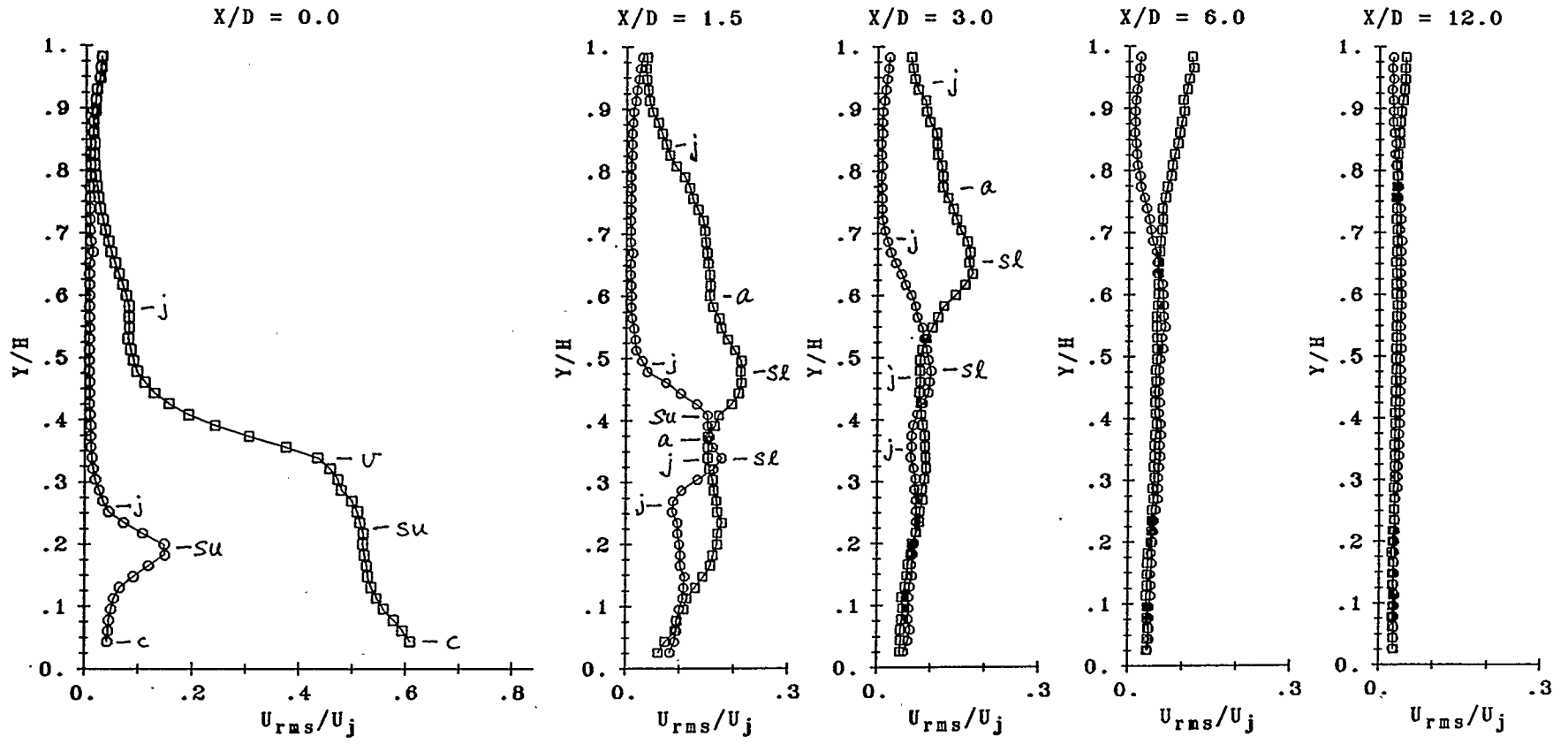


FIGURE 5.12 U_{rms} TURBULENCE PROFILES ON CENTRE PLANE FOR JET ORIFICE 19.93 mm DIAMETER.

$U_j = 23.27$ m/s	$U_\infty = 10.27$ m/s	$U_j/U_\infty = 2.26$
$\dot{W} = 52.80$ W	$St = 0.18$	$U_e/U_j = 0.86$
$f = 208.0$ Hz	$U_e = 20.00$ m/s	o : "NO-DRIVE"
$Re_j = 24463$	$Re_\infty = 86138$	□ : "WITH-DRIVE"
$\rho_j = 0.9945$ kg/m ³	$\rho_\infty = 0.9540$ kg/m ³	

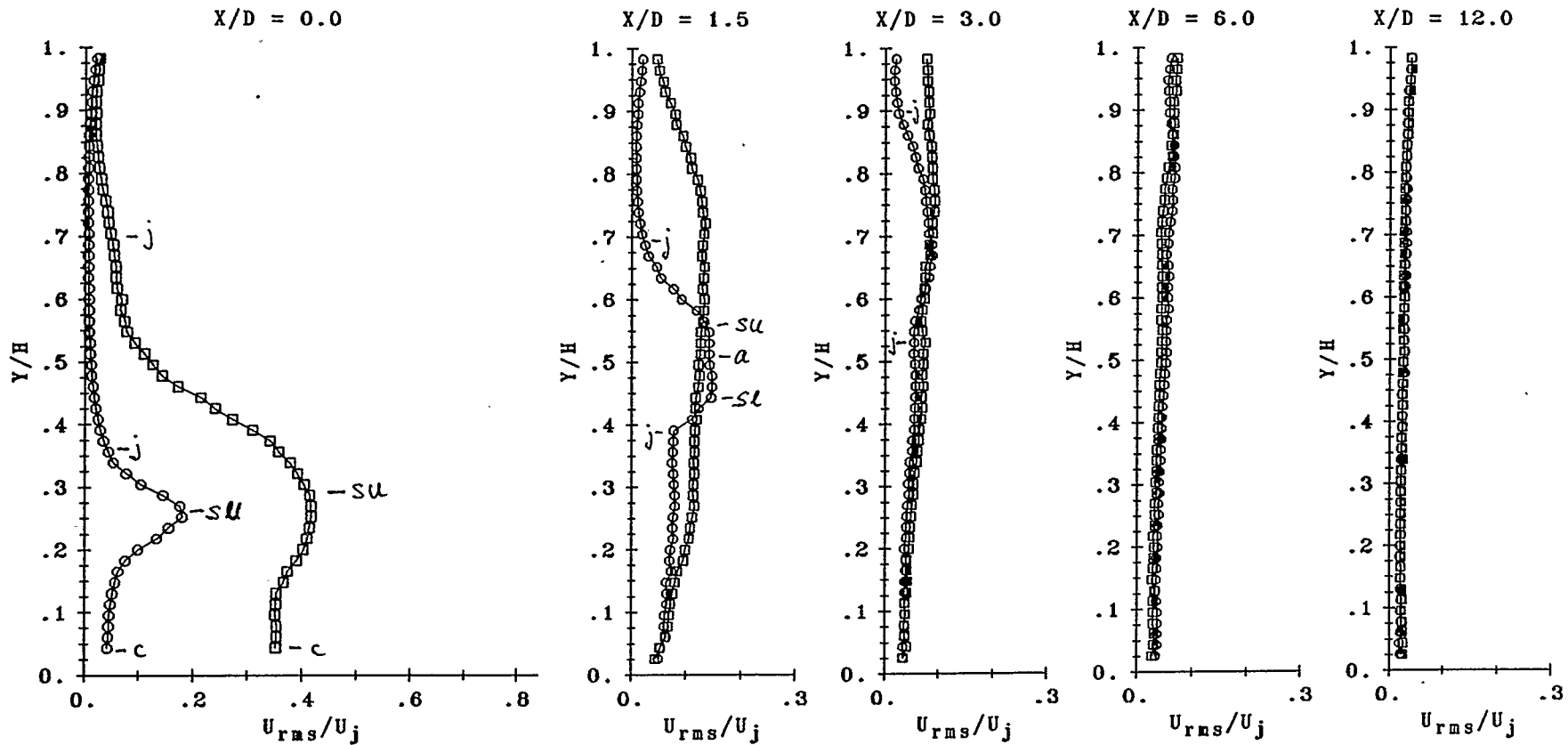


FIGURE 5.13 U_{rms} TURBULENCE PROFILES ON CENTRE PLANE FOR JET ORIFICE 19.93 mm DIAMETER.

$U_j = 34.30$ m/s	$U_\infty = 10.27$ m/s	$U_j/U_\infty = 3.34$
$\dot{W} = 52.00$ W	$St = 0.12$	$U_e/U_j = 0.54$
$f = 208.0$ Hz	$U_e = 18.50$ m/s	o : "NO-DRIVE"
$Re_j = 35581$	$Re_\infty = 87198$	□ : "WITH-DRIVE"
$\rho_j = 0.9905$ kg/m ³	$\rho_\infty = 0.9643$ kg/m ³	

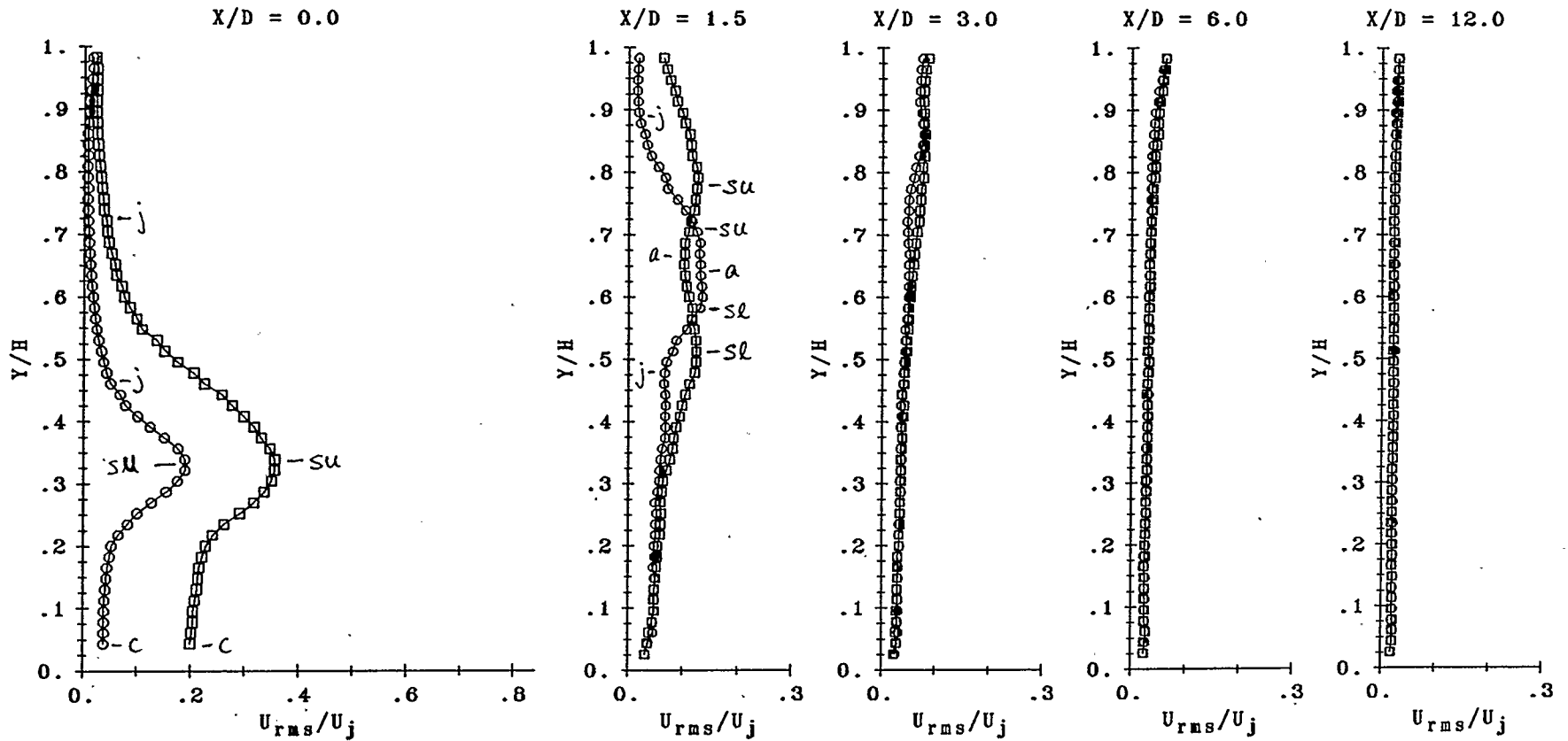


FIGURE 5.14 U_{rms} TURBULENCE PROFILES ON CENTRE PLANE FOR JET ORIFICE 19.93 mm DIAMETER.

$U_j = 46.22$ m/s	$U_\infty = 10.13$ m/s	$U_j/U_\infty = 4.56$
$\dot{W} = 51.20$ W	$St = 0.09$	$U_e/U_j = 0.30$
$f = 208.0$ Hz	$U_e = 14.00$ m/s	\circ : "NO-DRIVE"
$Re_j = 47443$	$Re_\infty = 84954$	\square : "WITH-DRIVE"
$\rho_j = 0.9842$ kg/m ³	$\rho_\infty = 0.9575$ kg/m ³	

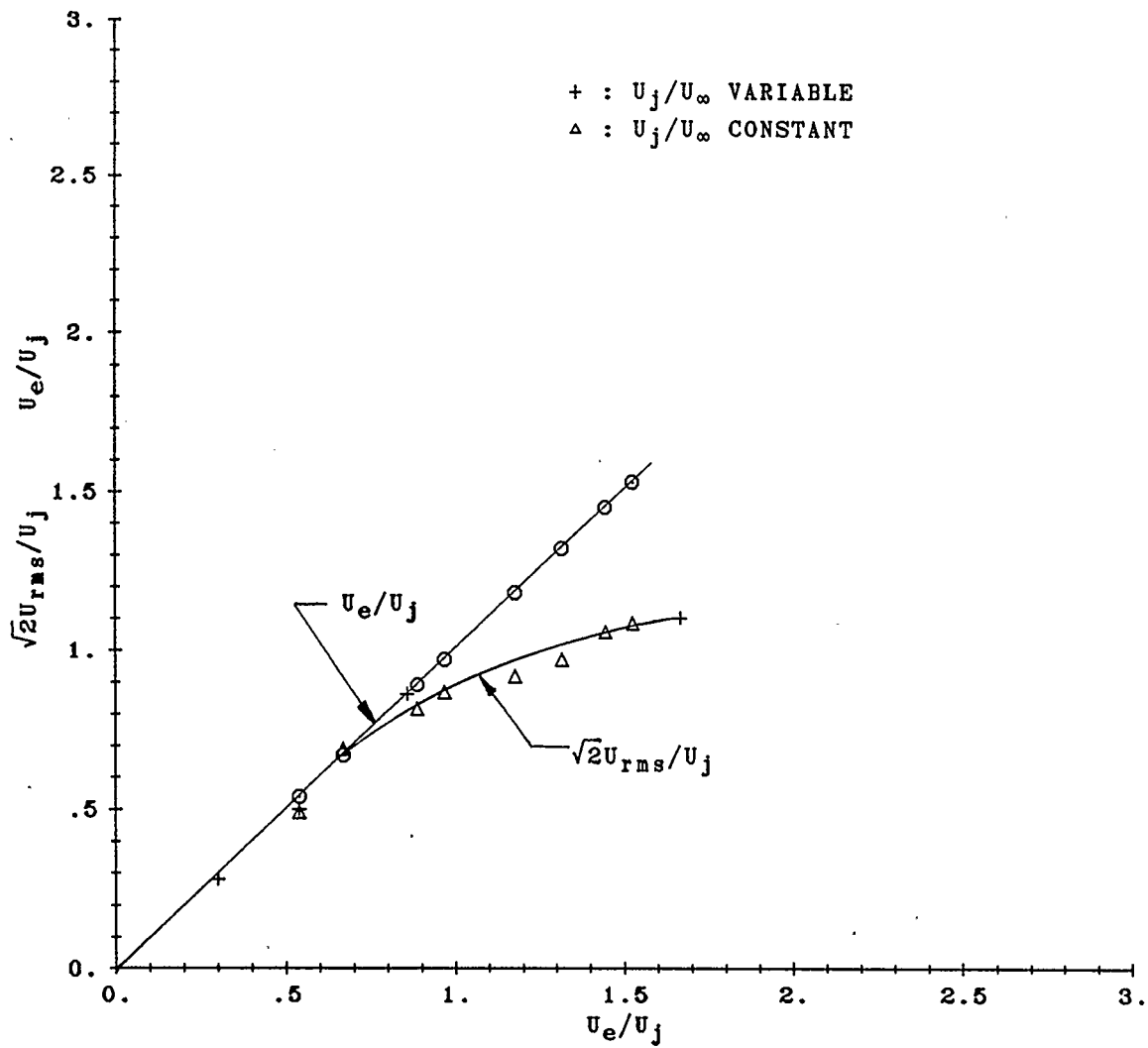


FIGURE 5.15 PEAK VALUE OF TURBULENCE VERSUS RELATIVE PULSATION STRENGTH AT JET CENTRE IN THE ORIFICE EXIT PLANE, $X/D = 0.0$, $Y/D = 0.2$.

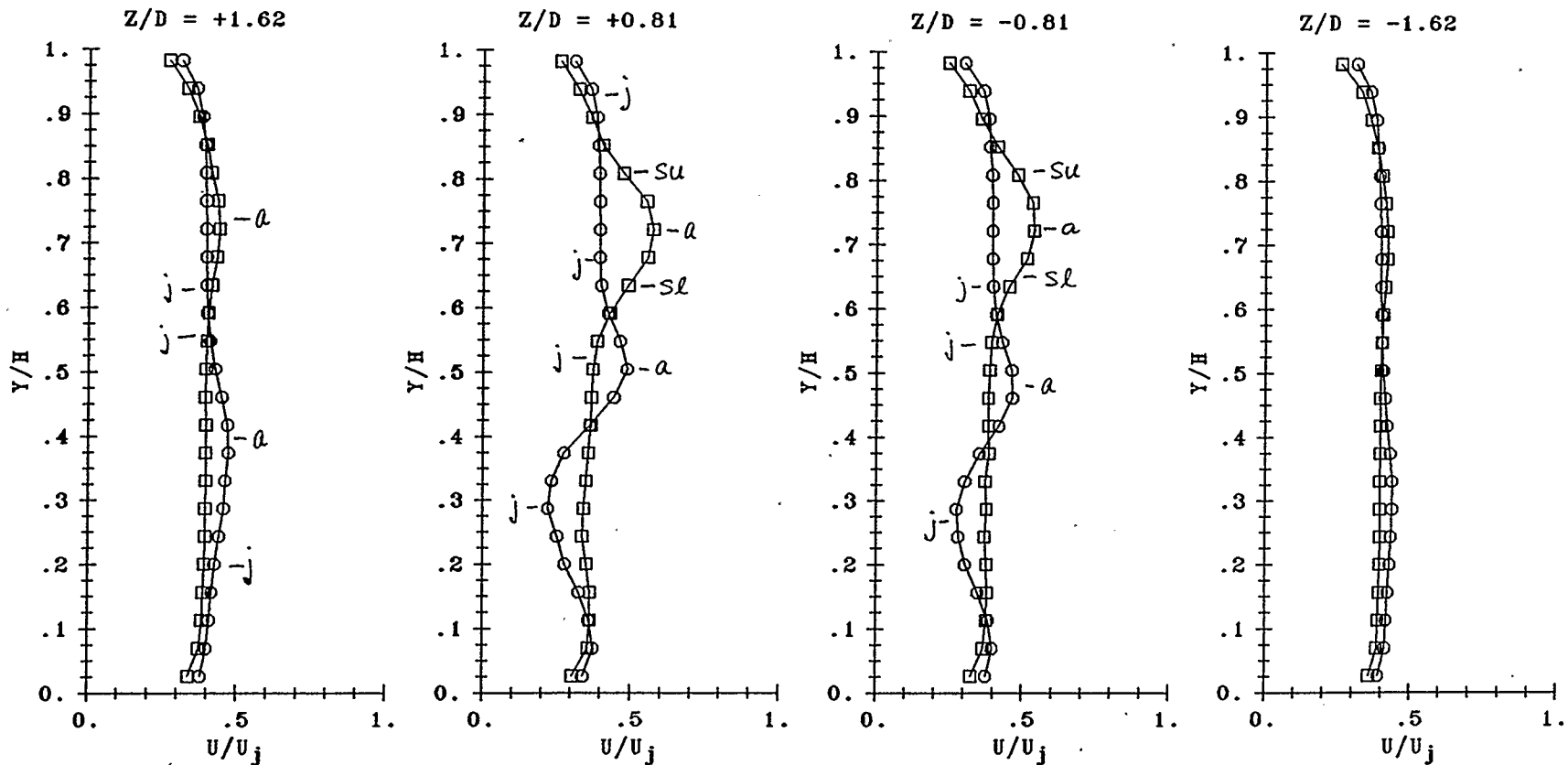


FIGURE 5.16.1 LATERAL MEAN VELOCITY PROFILES FOR JET ORIFICE 19.93 mm DIAMETER, SHOWING SYMMETRY AT $X/D = 3.0$.

$U_j = 25.27$ m/s	$U_\infty = 9.74$ m/s	$U_j/U_\infty = 2.59$
$W = 51.20$ W	$St = 0.16$	$U_e/U_j = 0.61$
$f = 208.0$ Hz	$U_e = 15.50$ m/s	○ : "NO-DRIVE"
$Re_j = 26618$	$Re_\infty = 81730$	□ : "WITH-DRIVE"
$\rho_j = 0.9959$ kg/m ³	$\rho_\infty = 0.9548$ kg/m ³	

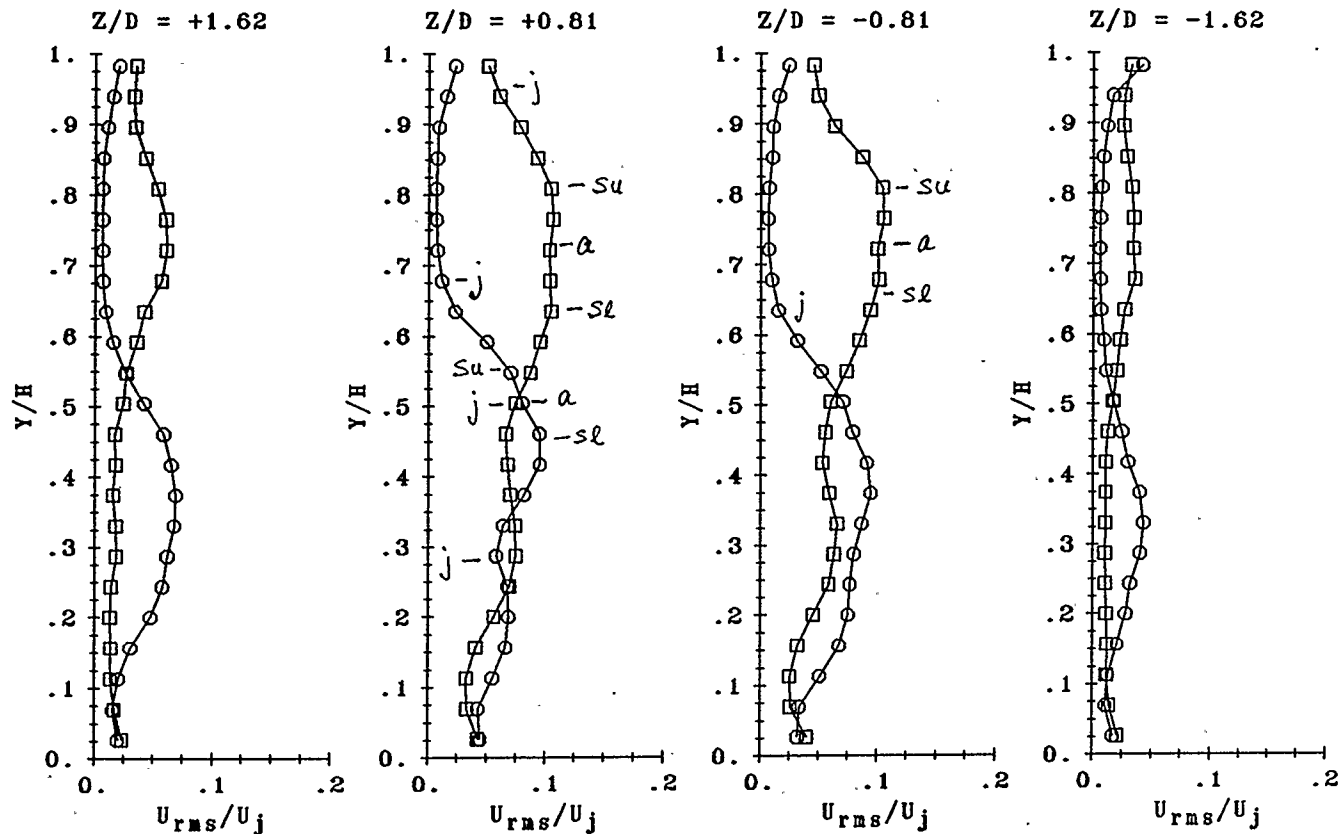


FIGURE 5.16.2. LATERAL U_{rms} TURBULENCE PROFILES FOR JET ORIFICE 19.93 mm DIAMETER, SHOWING SYMMETRY AT $X/D = 3.0$.

(REFER TO FIGURE 5.16.1 FOR OPERATING CONDITIONS)

○ : "NO-DRIVE"

□ : "WITH-DRIVE", 208 Hz

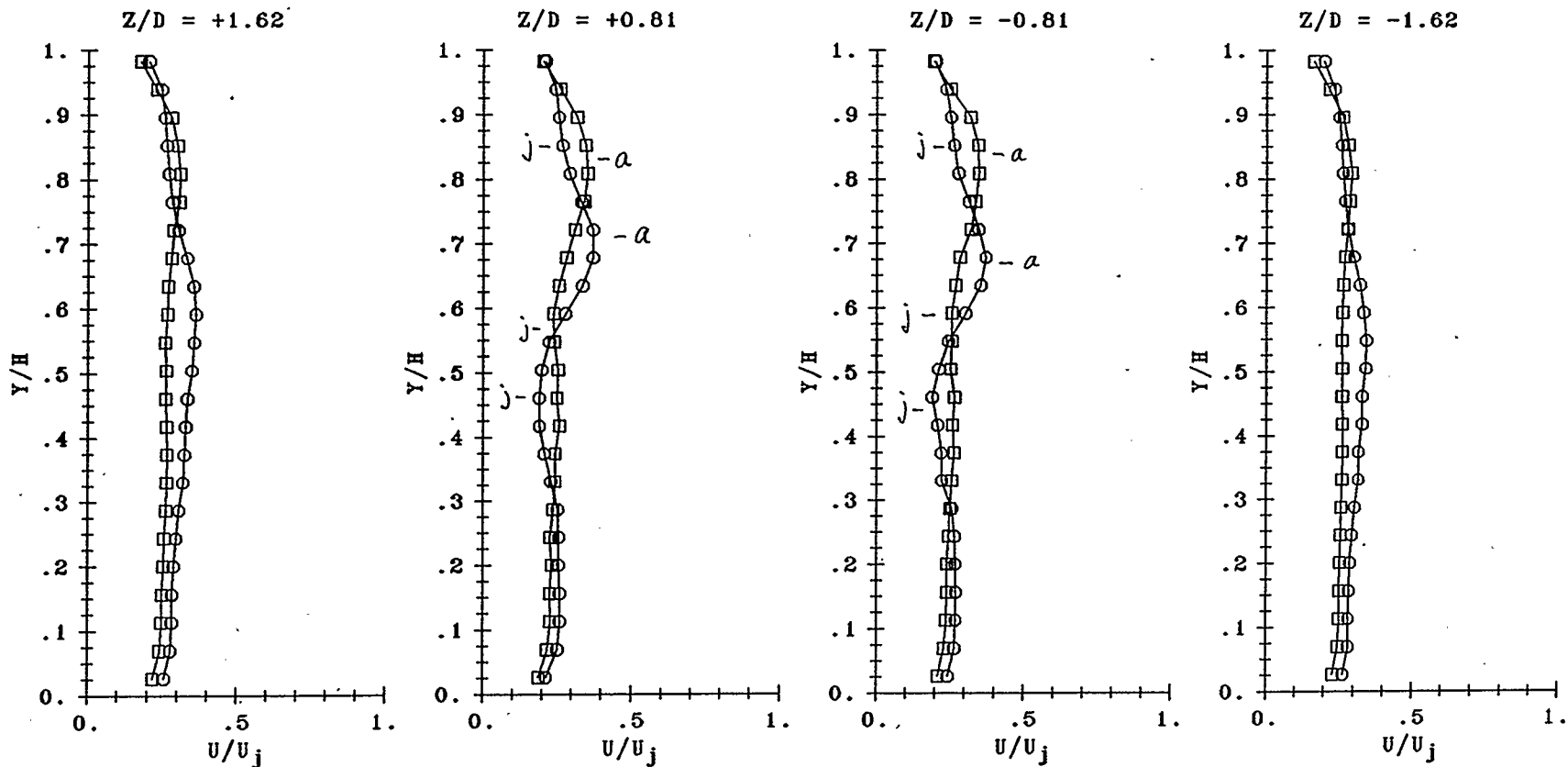


FIGURE 5.17.1 LATERAL MEAN VELOCITY PROFILES FOR JET ORIFICE 19.93 mm DIAMETER. SHOWING SYMMETRY AT $X/D = 3.0$.

$U_j = 37.60$ m/s	$U_\infty = 9.73$ m/s	$U_j/U_\infty = 3.86$
$\dot{W} = 50.40$ W	$St = 0.11$	$U_e/U_j = 0.37$
$f = 208.0$ Hz	$U_e = 14.00$ m/s	\circ : "NO-DRIVE"
$Re_j = 38966$	$Re_\infty = 81699$	\square : "WITH-DRIVE"
$\rho_j = 0.9889$ kg/m ³	$\rho_\infty = 0.9556$ kg/m ³	

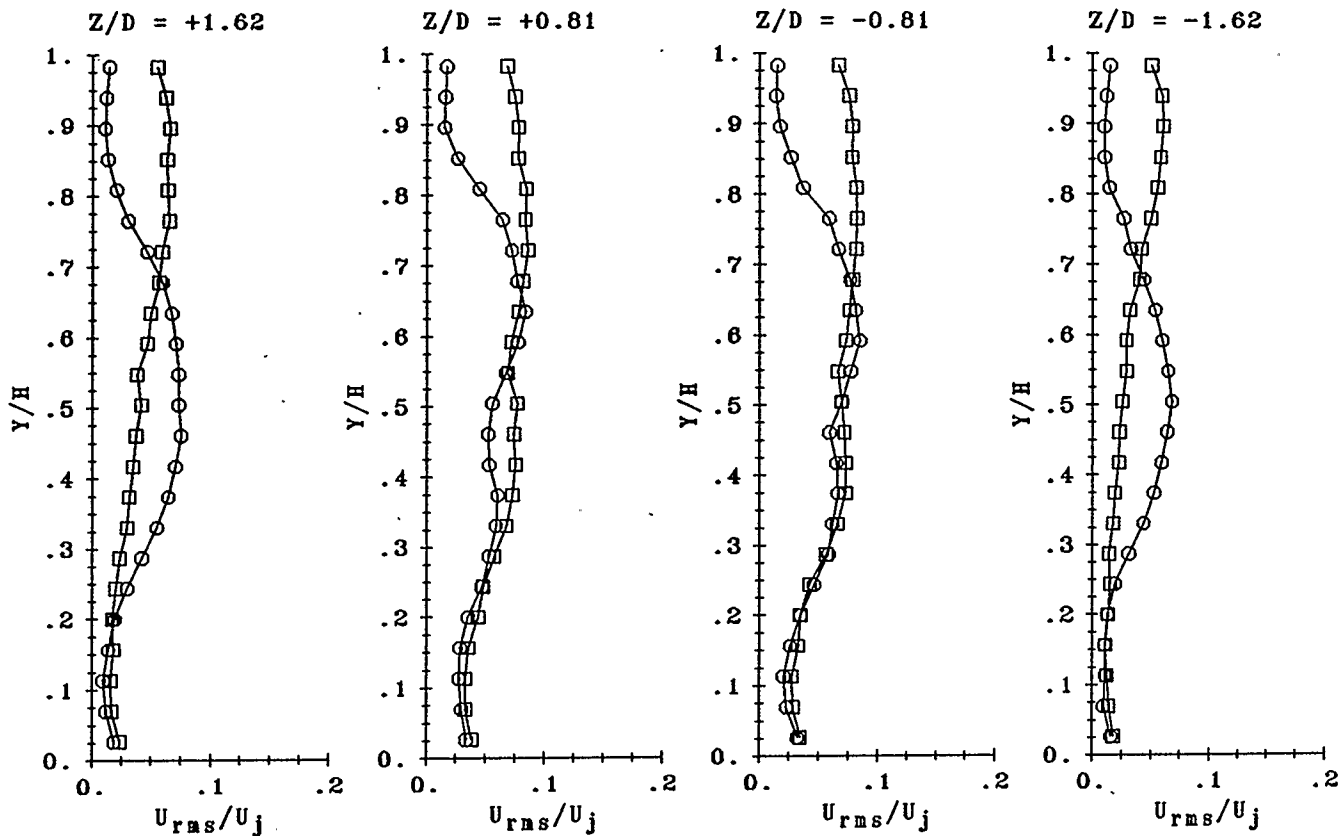


FIGURE 5.17.2 LATERAL U_{rms} TURBULENCE PROFILES FOR JET ORIFICE 19.93 mm DIAMETER, SHOWING SYMMETRY AT $X/D = 3.0$.

(REFER TO FIGURE 5.17.1 FOR OPERATING CONDITIONS)

○ : "NO-DRIVE"

□ : "WITH-DRIVE", 208 Hz

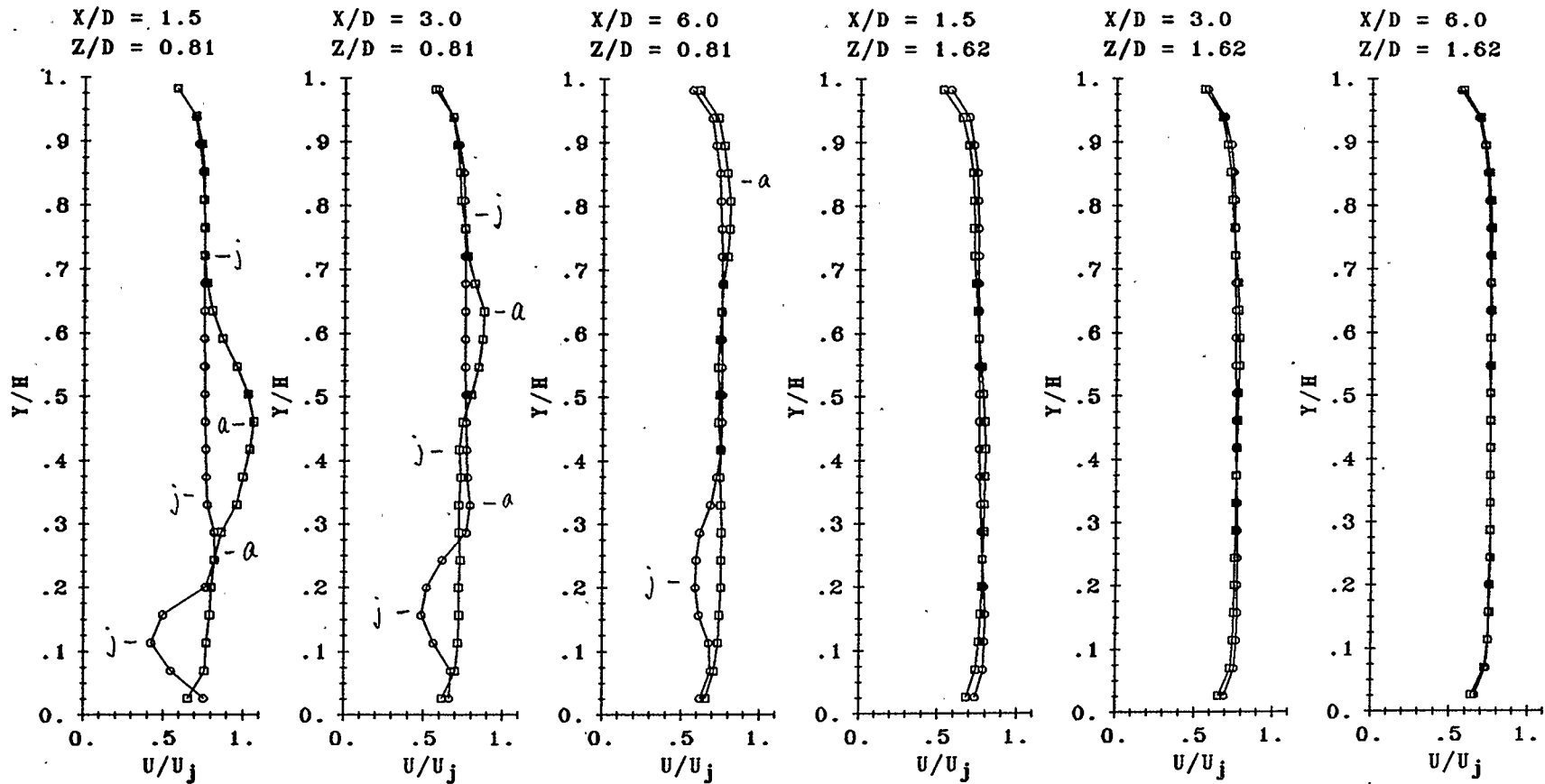


FIGURE 5.18 LATERAL MEAN VELOCITY PROFILES FOR JET ORIFICE 19.93 mm DIAMETER, AT $X/D = 1.5, 3.0, 6.0$. (REFER TO FIGURE 5.7 FOR OTHER OPERATING CONDITIONS)

$U_j = 13.20$ m/s	$U_\infty = 10.06$ m/s	$U_j/U_\infty = 1.31$
$U_e = 22.00$ m/s	$St = 0.31$	$U_e/U_j = 1.67$
$f = 208.0$ Hz	\circ : "NO-DRIVE"	\square : "WITH-DRIVE"

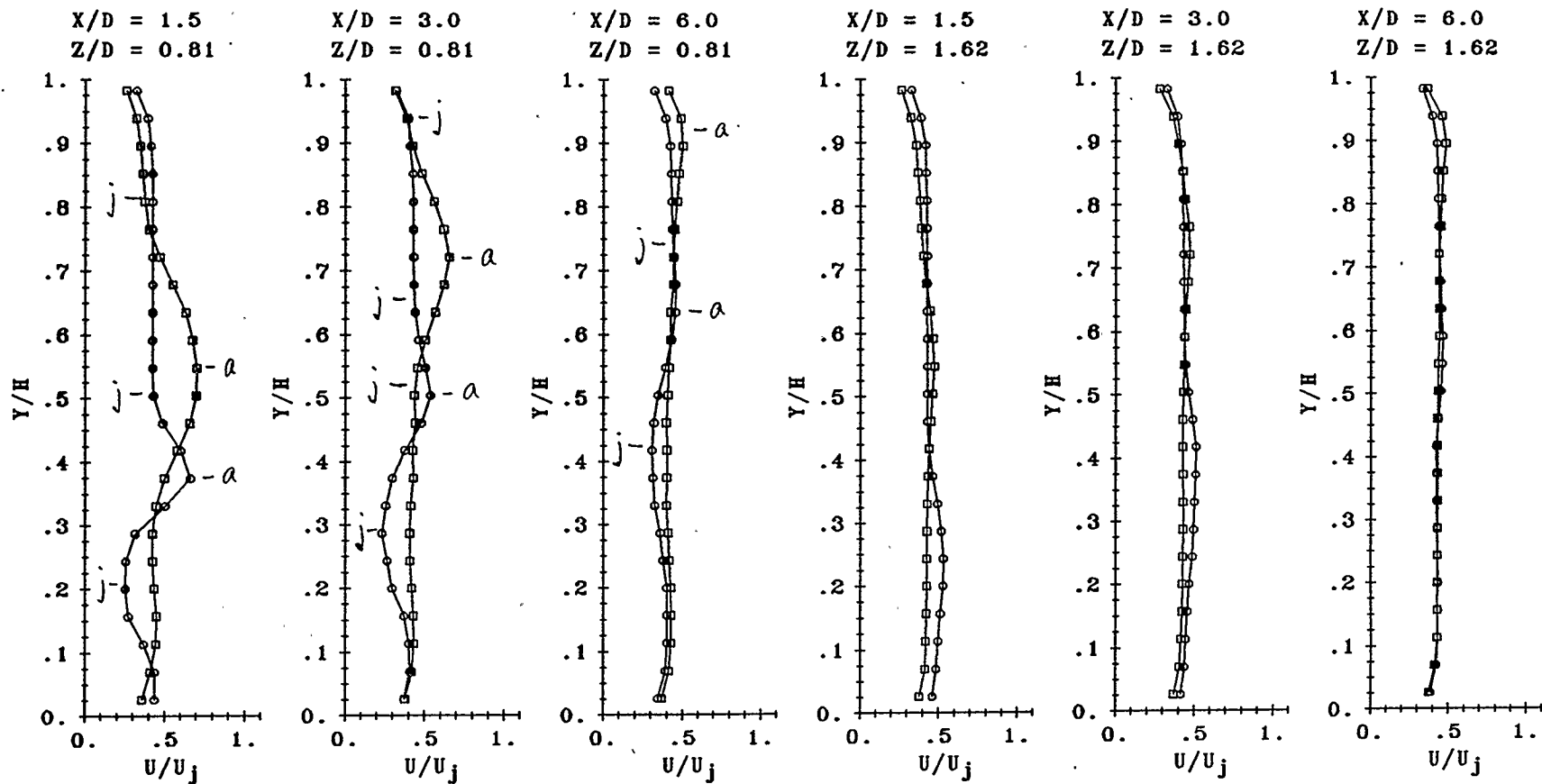


FIGURE 5.19 LATERAL MEAN VELOCITY PROFILES FOR JET ORIFICE 19.93 mm DIAMETER, AT $X/D = 1.5, 3.0, 6.0$.

(REFER TO FIGURE 5.8 FOR OTHER OPERATING CONDITIONS)

$U_j = 23.27$ m/s	$U_\infty = 10.27$ m/s	$U_j/U_\infty = 2.26$
$U_e = 20.00$ m/s	$St = 0.18$	$U_e/U_j = 0.86$
$f = 208.0$ Hz	o : "NO-DRIVE"	□ : "WITH-DRIVE"

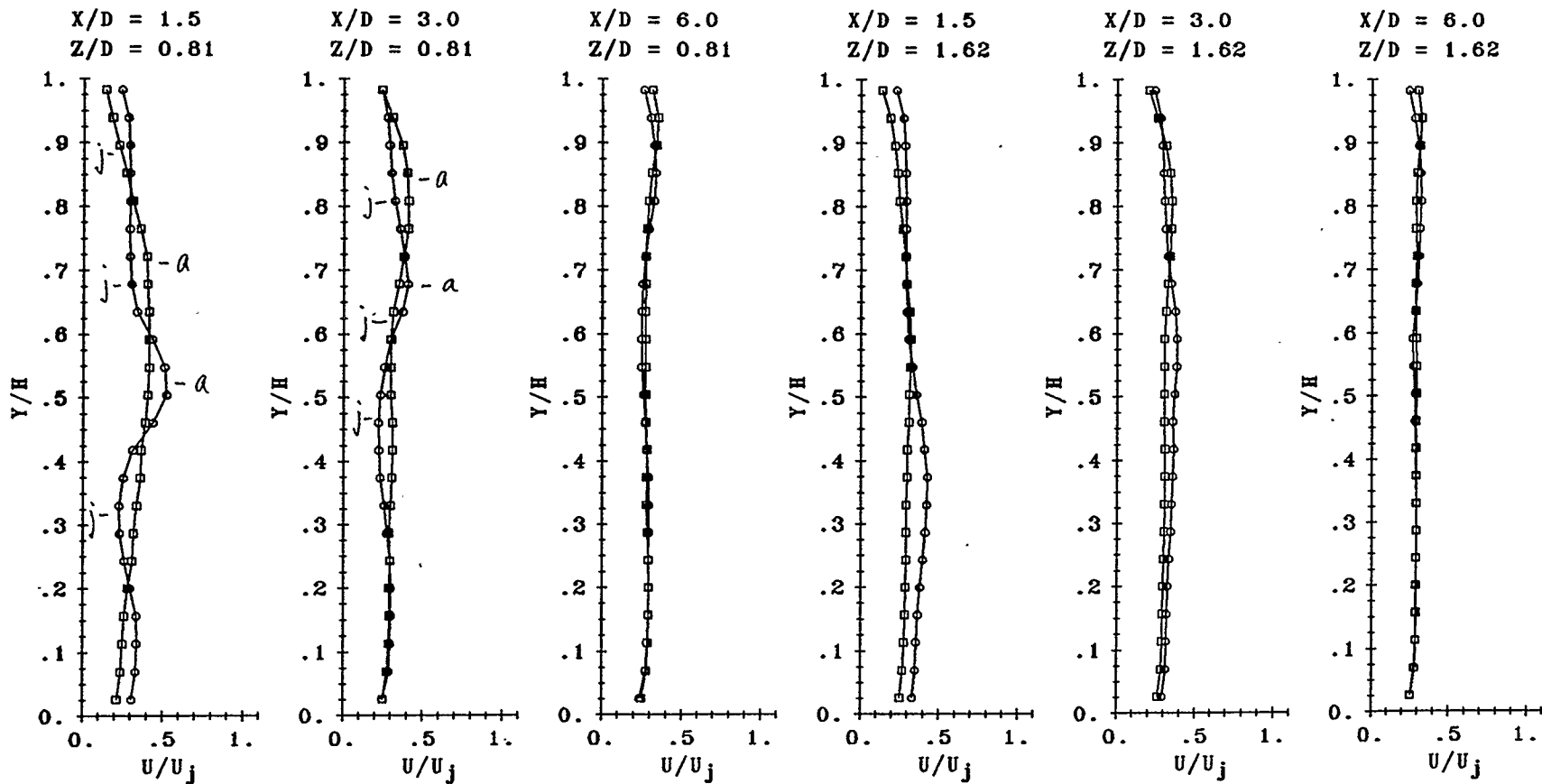


FIGURE 5.20 LATERAL MEAN VELOCITY PROFILES FOR JET ORIFICE 19.93 mm DIAMETER, AT $X/D = 1.5, 3.0, 6.0$.

(REFER TO FIGURE 5.9 FOR OTHER OPERATING CONDITIONS)

$U_j = 34.30$ m/s	$U_\infty = 10.27$ m/s	$U_j/U_\infty = 3.34$
$U_e = 18.50$ m/s	$St = 0.12$	$U_e/U_j = 0.54$
$f = 208.0$ Hz	\circ : "NO-DRIVE"	\square : "WITH-DRIVE"

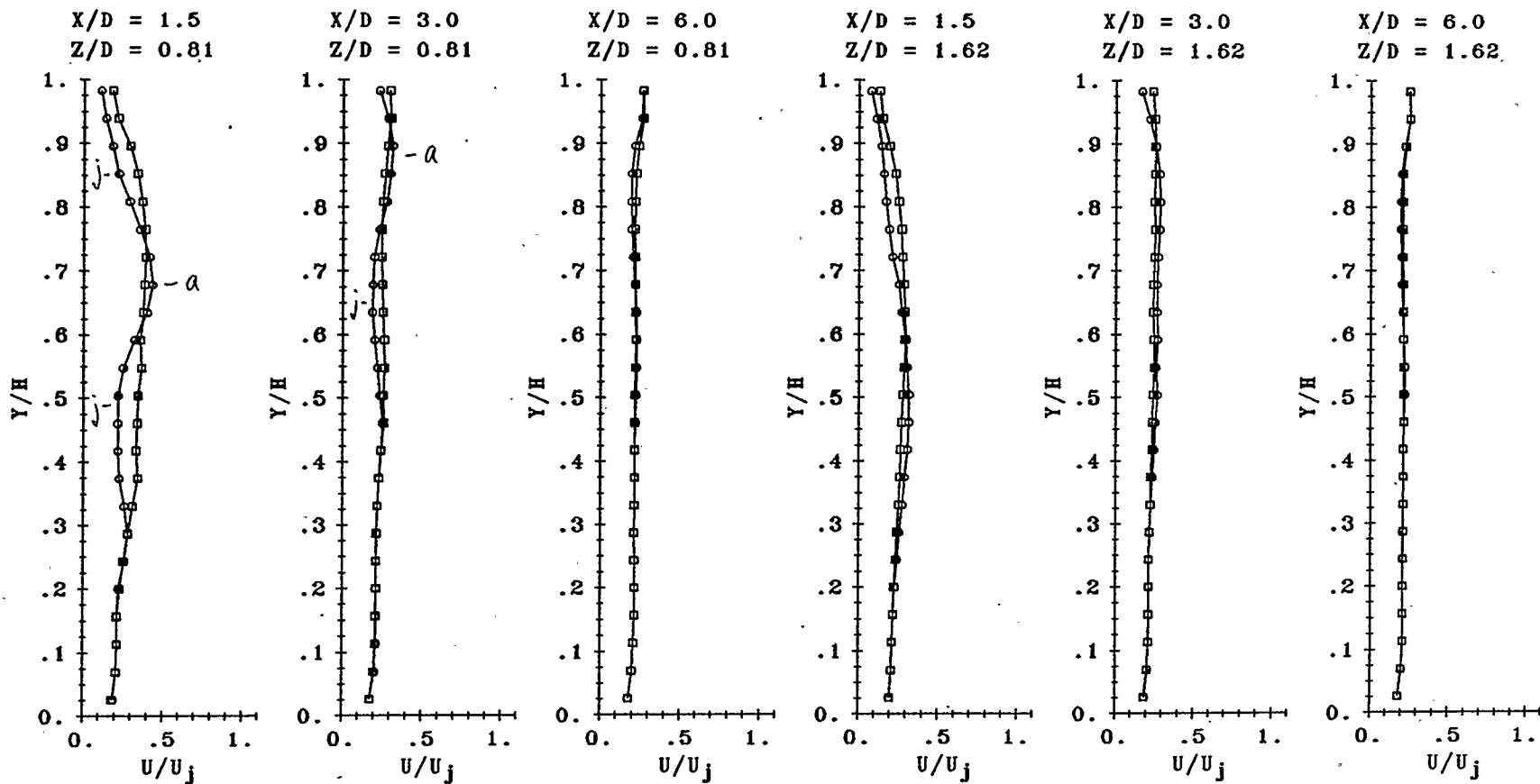


FIGURE 5.21 LATERAL MEAN VELOCITY PROFILES FOR JET ORIFICE 19.93 mm DIAMETER, AT $X/D = 1.5, 3.0, 6.0$.

(REFER TO FIGURE 5.10 FOR OTHER OPERATING CONDITIONS)

$U_j = 46.22 \text{ m/s}$

$U_\infty = 10.13 \text{ m/s}$

$U_j/U_\infty = 4.56$

$U_e = 14.00 \text{ m/s}$

$St = 0.09$

$U_e/U_j = 0.30$

$f = 208.0 \text{ Hz}$

○ : "NO-DRIVE"

□ : "WITH-DRIVE"

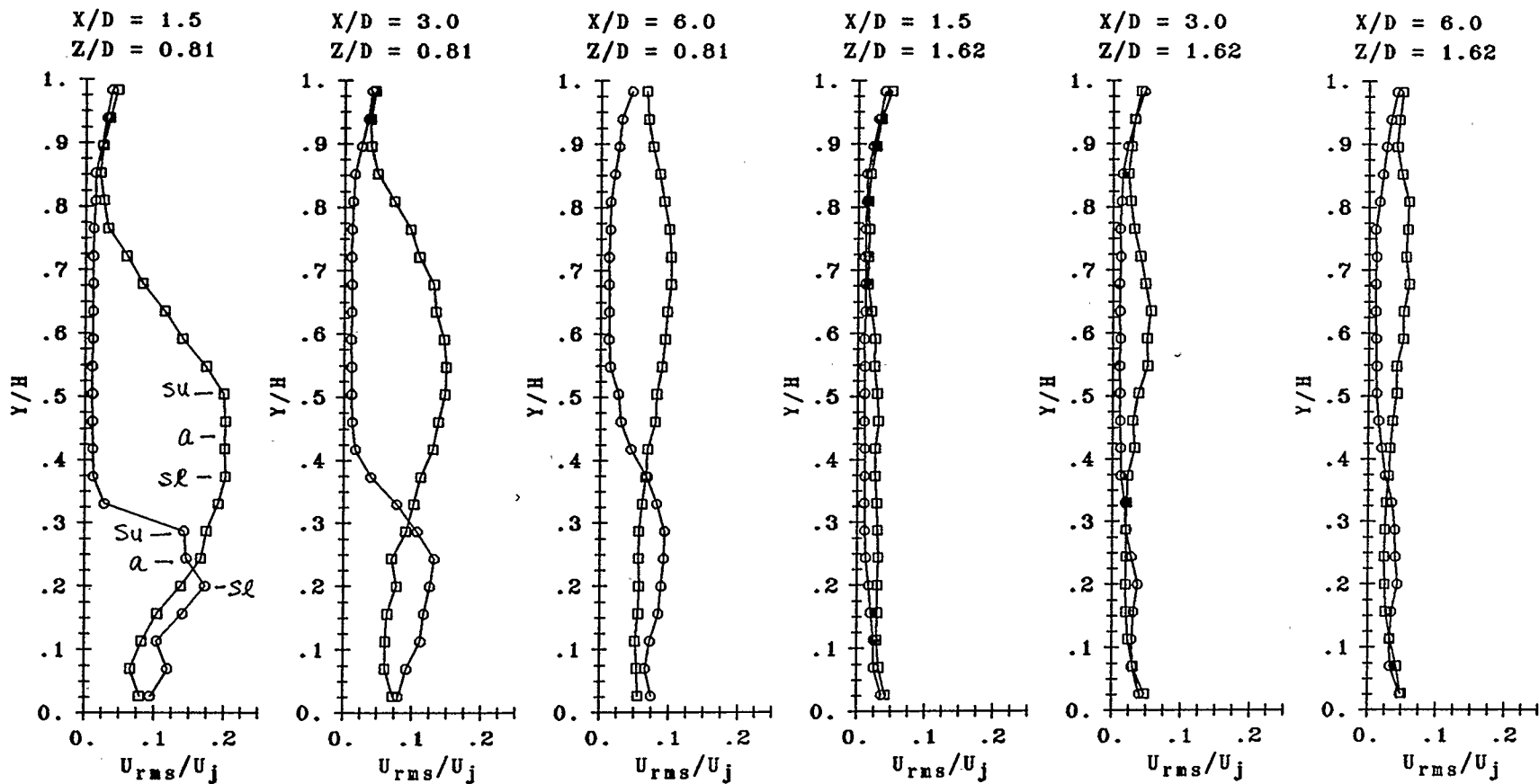


FIGURE 5.22 LATERAL U_{rms} TURBULENCE PROFILES FOR JET ORIFICE 19.93 mm DIAMETER, AT $X/D = 1.5, 3.0, 6.0$. (REFER TO FIGURE 5.7 FOR OTHER OPERATING CONDITIONS)

$U_j = 13.20$ m/s	$U_\infty = 10.06$ m/s	$U_j/U_\infty = 1.31$
$U_e = 22.00$ m/s	$St = 0.31$	$U_e/U_j = 1.67$
$f = 208.0$ Hz	\circ : "NO-DRIVE"	\square : "WITH-DRIVE"

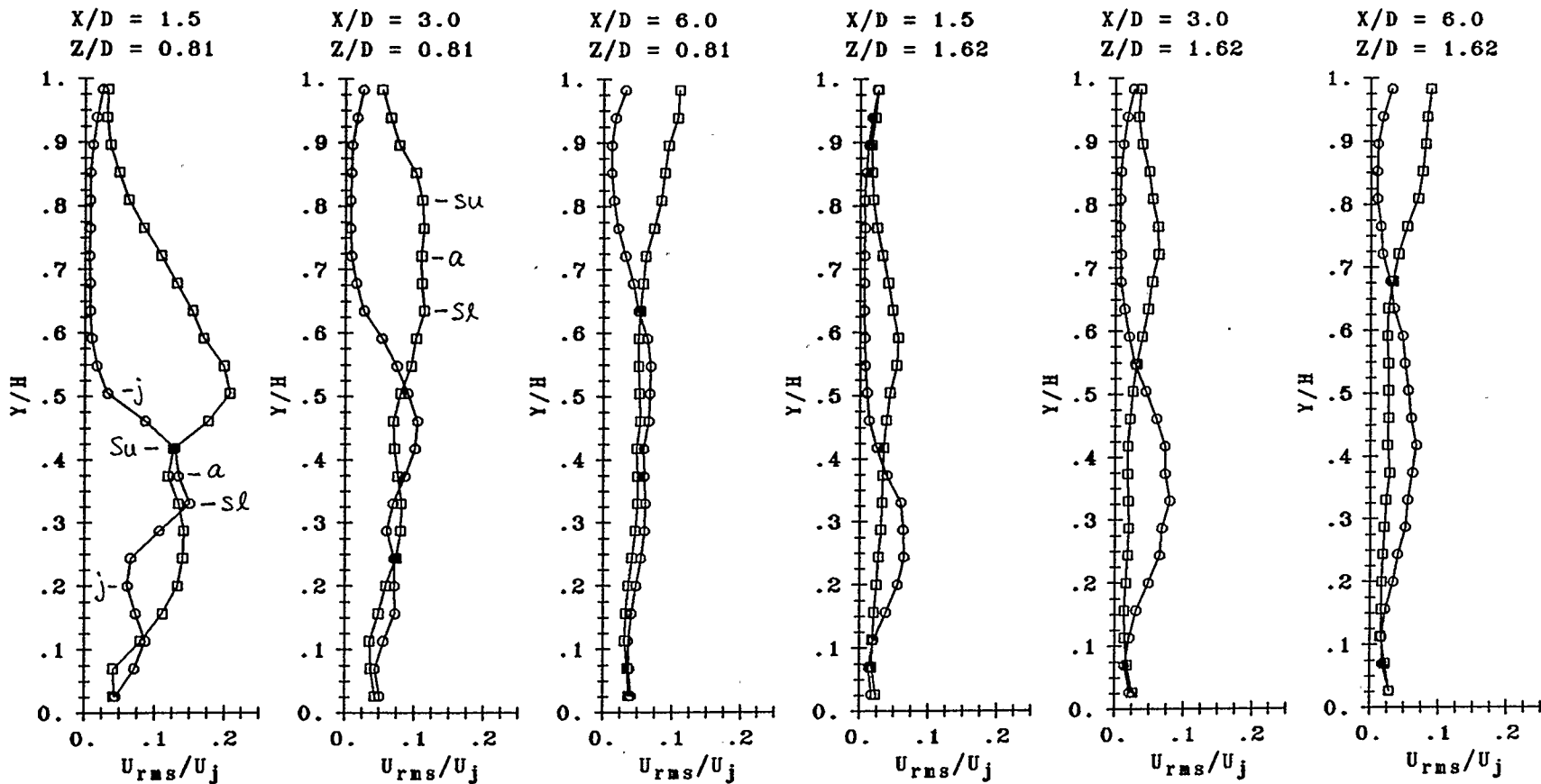


FIGURE 5.23 LATERAL U_{rms} TURBULENCE PROFILES FOR JET ORIFICE 19.93 mm DIAMETER, AT $X/D = 1.5, 3.0, 6.0$. (REFER TO FIGURE 5.8 FOR OTHER OPERATING CONDITIONS)

$U_j = 23.27$ m/s	$U_\infty = 10.27$ m/s	$U_j/U_\infty = 2.26$
$U_e = 20.00$ m/s	$St = 0.18$	$U_e/U_j = 0.86$
$f = 208.0$ Hz	\circ : "NO-DRIVE"	\square : "WITH-DRIVE"

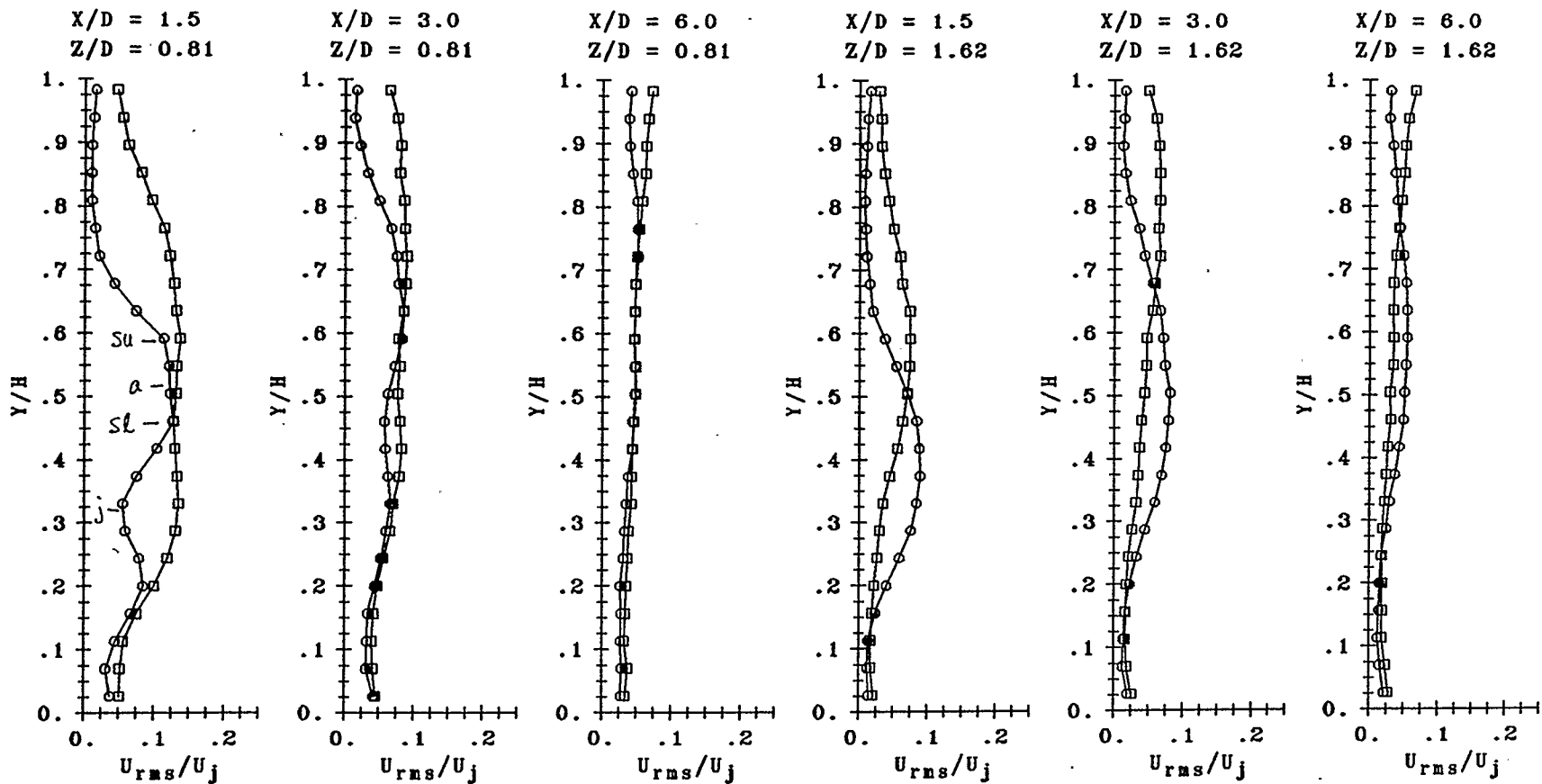


FIGURE 5.24 LATERAL U_{rms} TURBULENCE PROFILES FOR JET ORIFICE 19.93 mm DIAMETER, AT $X/D = 1.5, 3.0, 6.0$.

(REFER TO FIGURE 5.9 FOR OTHER OPERATING CONDITIONS)

$U_j = 34.30$ m/s	$U_\infty = 10.27$ m/s	$U_j/U_\infty = 3.34$
$U_e = 18.50$ m/s	$St = 0.12$	$U_e/U_j = 0.54$
$f = 208.0$ Hz	o : "NO-DRIVE"	□ : "WITH-DRIVE"

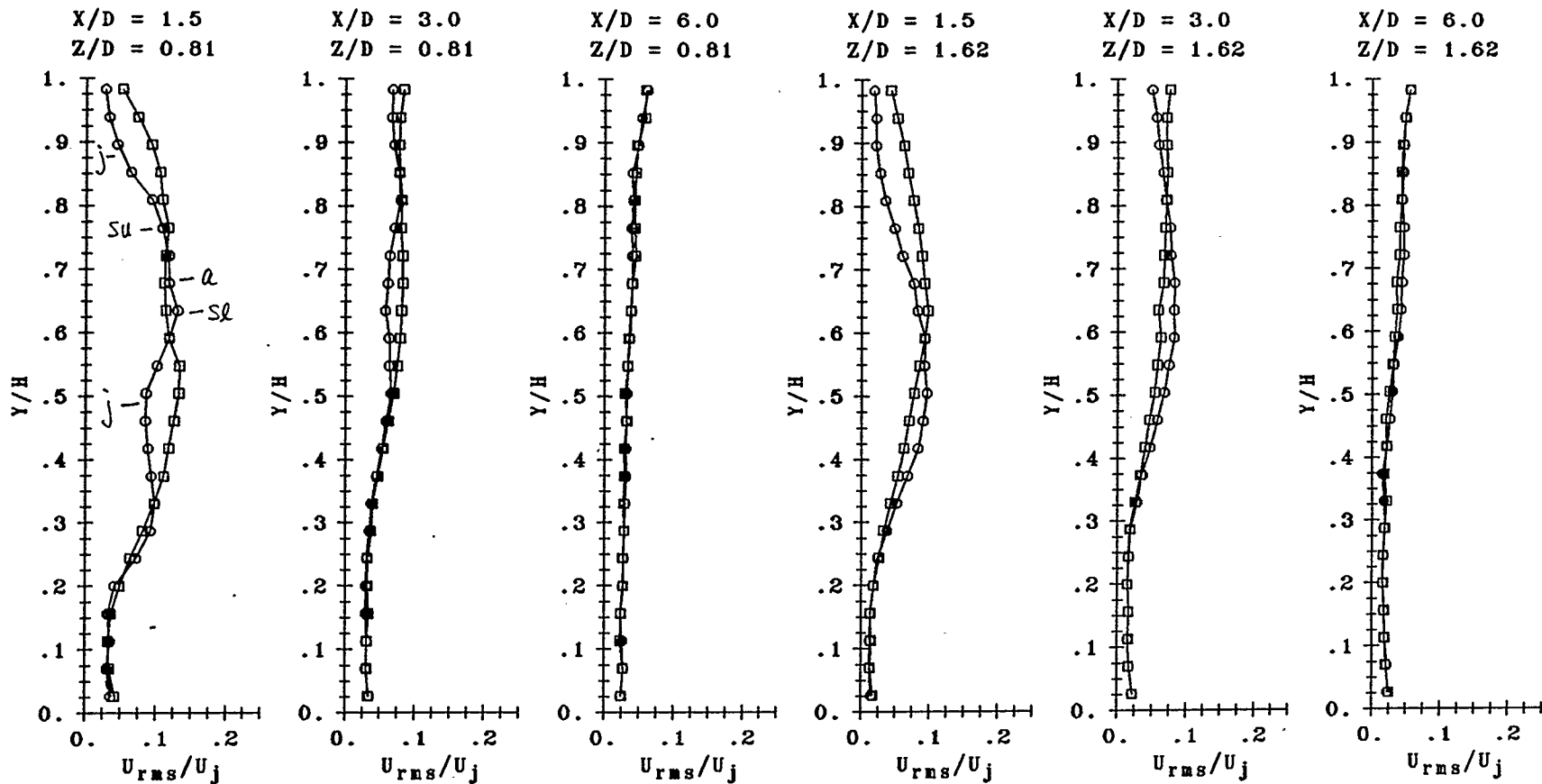


FIGURE 5.25 LATERAL U_{rms} TURBULENCE PROFILES FOR JET ORIFICE 19.93 mm DIAMETER, AT $X/D = 1.5, 3.0, 6.0$.

(REFER TO FIGURE 5.10 FOR OTHER OPERATING CONDITIONS)

$U_j = 46.22$ m/s

$U_\infty = 10.13$ m/s

$U_j/U_\infty = 4.56$

$U_e = 14.00$ m/s

$St = 0.09$

$U_e/U_j = 0.30$

$f = 208.0$ Hz

o : "NO-DRIVE"

□ : "WITH-DRIVE"

$U_j = 13.20 \text{ m/s}$
 $U_j/U_\infty = 1.31$

$U_j = 23.27 \text{ m/s}$
 $U_j/U_\infty = 2.26$

$U_j = 34.30 \text{ m/s}$
 $U_j/U_\infty = 3.34$

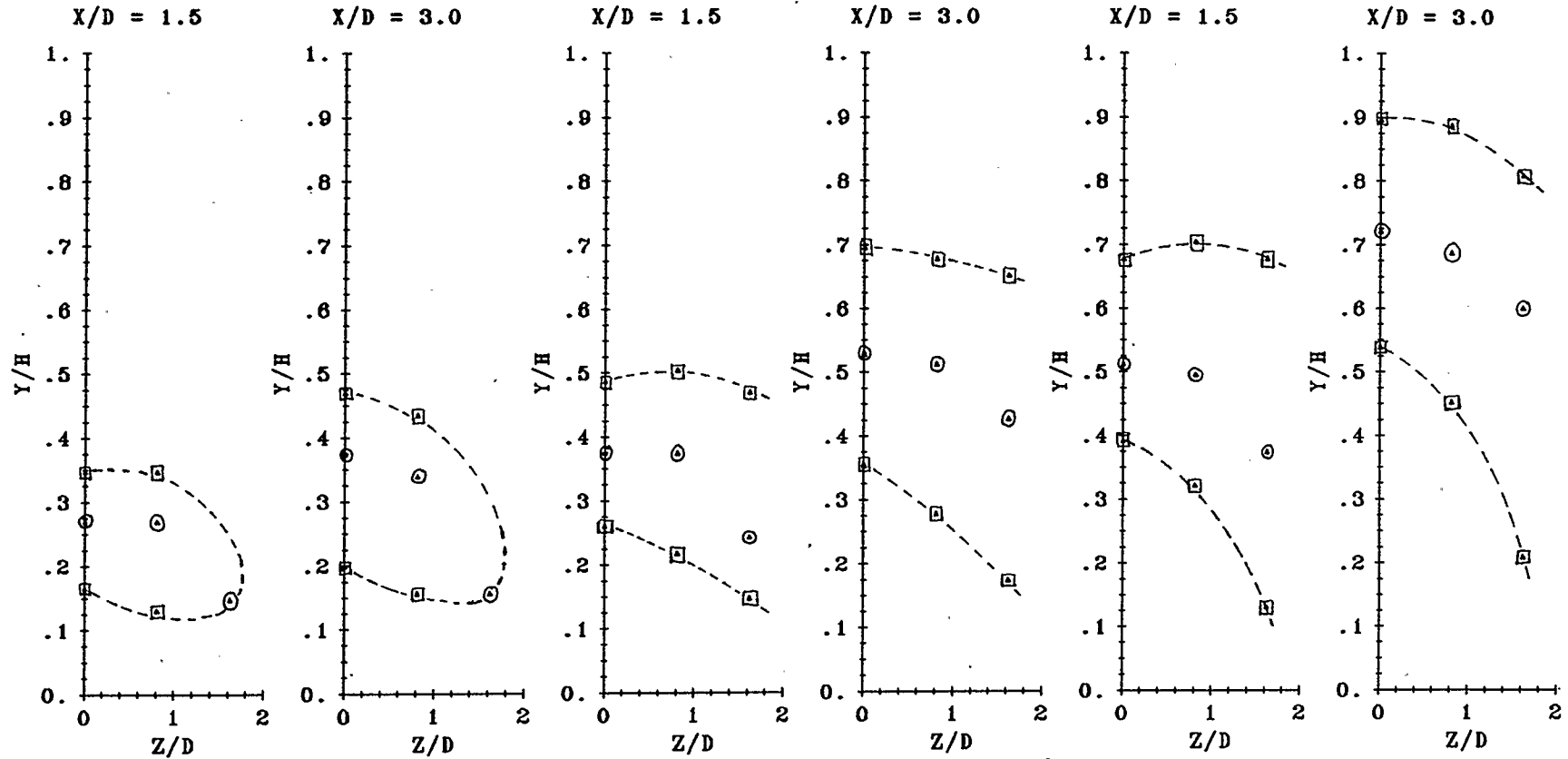


FIGURE 5.26.1 JET BOUNDARY CONTOUR FOR VARIOUS VELOCITY RATIOS "NO-DRIVE",
 FOR JET ORIFICE 19.93 mm DIAMETER.

$U_j = 13.20 \text{ m/s}$
 $St = 0.31$
 $U_j/U_\infty = 1.31$
 $U_e/U_j = 1.67$

$U_j = 23.27 \text{ m/s}$
 $St = 0.18$
 $U_j/U_\infty = 2.26$
 $U_e/U_j = 0.86$

$U_j = 34.30 \text{ m/s}$
 $St = 0.12$
 $U_j/U_\infty = 3.34$
 $U_e/U_j = 0.54$

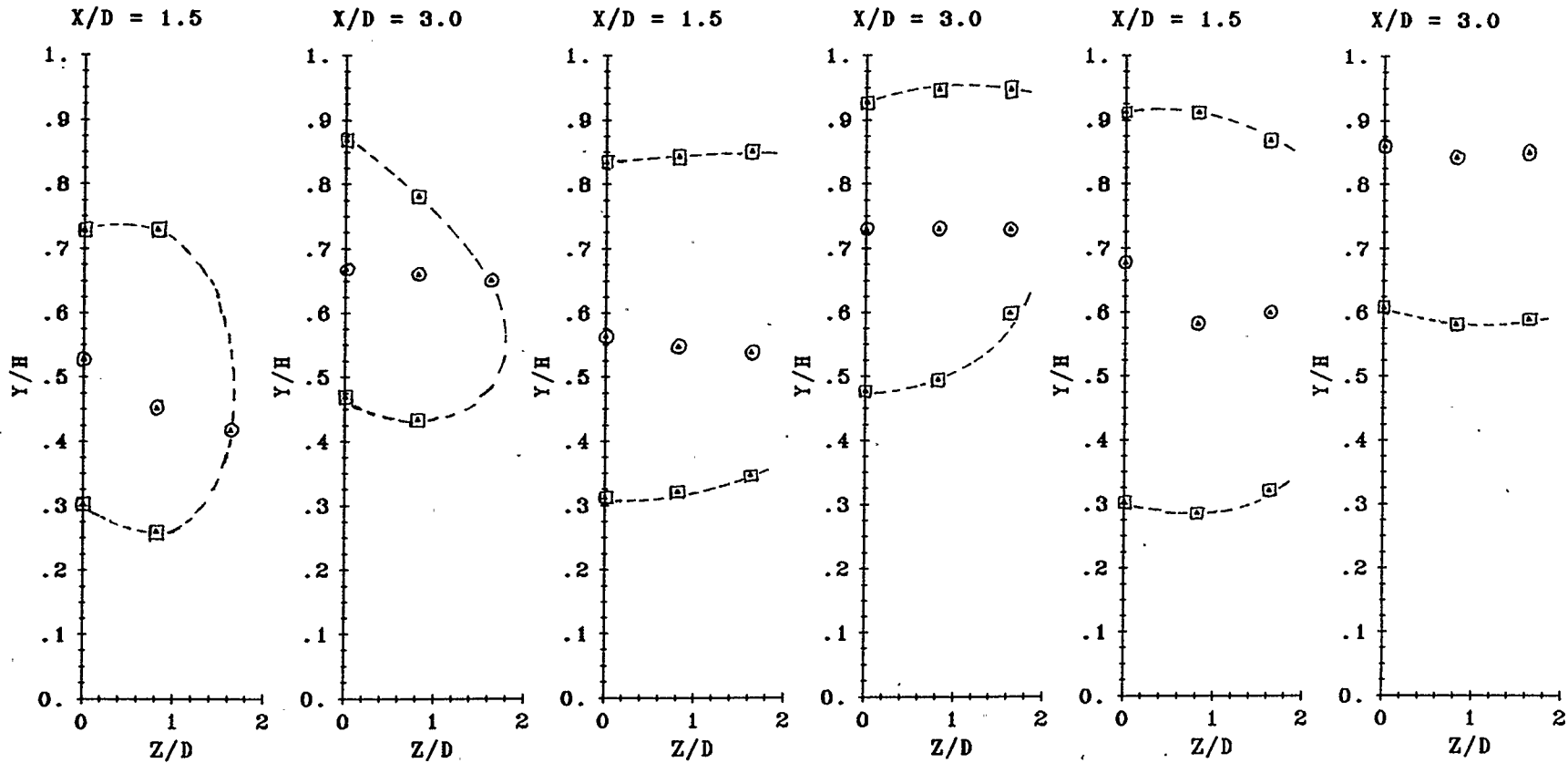


FIGURE 5.26.2 JET BOUNDARY CONTOUR FOR VARIOUS VELOCITY RATIOS "WITH-DRIVE"
 AT 208 Hz, FOR JET ORIFICE 19.93 mm DIAMETER.

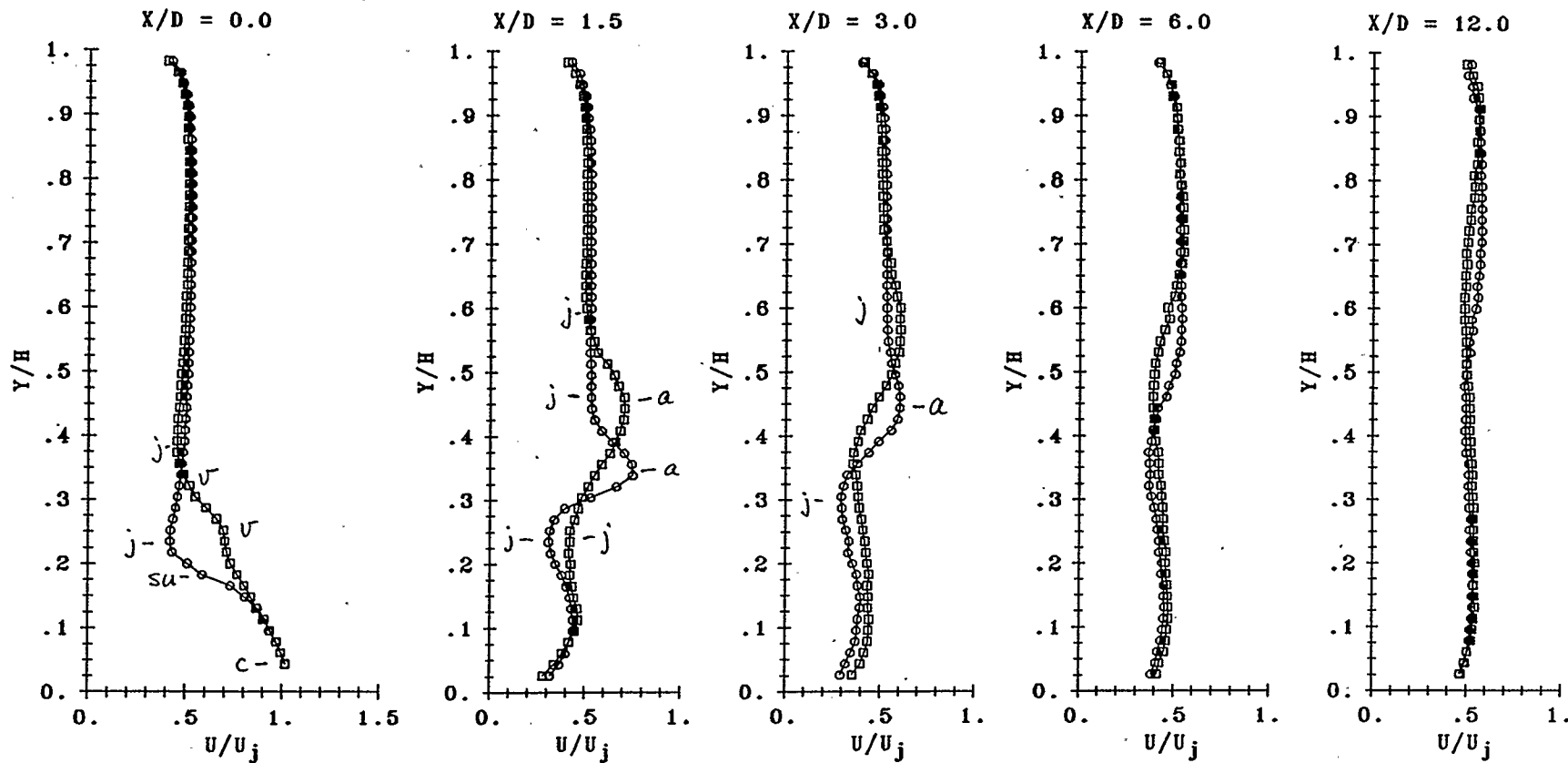


FIGURE 5.27.1 MEAN VELOCITY PROFILES ON CENTRE PLANE FOR JET ORIFICE 19.93 mm DIAMETER, AT CONSTANT STROUHAL NUMBER.

$U_j = 18.99$ m/s	$U_\infty = 9.82$ m/s	$U_j/U_\infty = 1.93$
$\dot{W} = 15.24$ W	$St = 0.22$	$U_e/U_j = 0.54$
$f = 208.0$ Hz	$U_e = 10.25$ m/s	\circ : "NO-DRIVE"
$Re_j = 20294$	$Re_\infty = 83567$	\square : "WITH-DRIVE"
$\rho_j = 1.0081$ kg/m ³	$\rho_\infty = 0.9660$ kg/m ³	

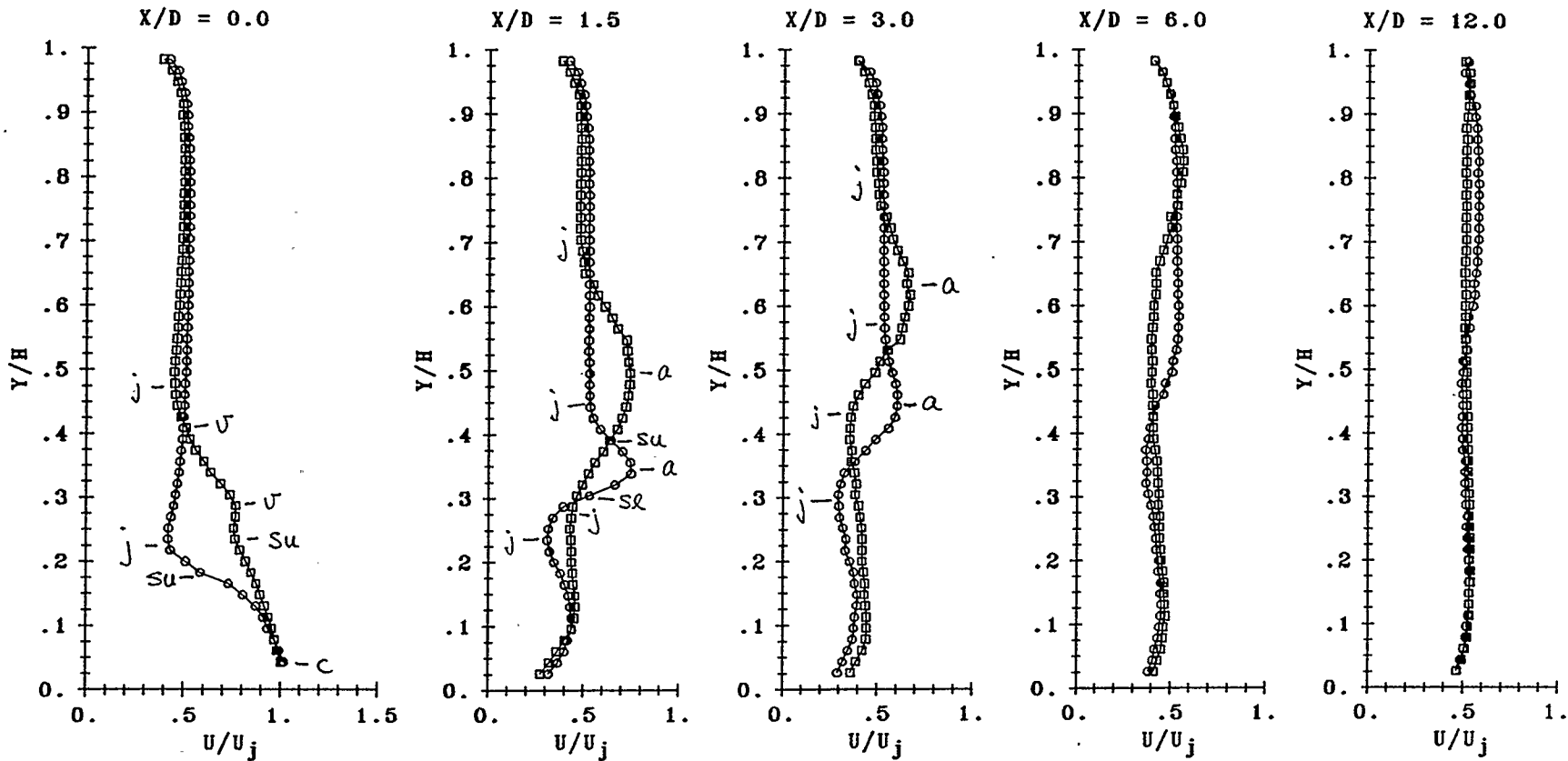


FIGURE 5.27.2 MEAN VELOCITY PROFILES ON CENTRE PLANE FOR JET ORIFICE 19.93 mm DIAMETER, AT CONSTANT STROUHAL NUMBER.

$U_j = 18.99$ m/s	$U_\infty = 9.82$ m/s	$U_j/U_\infty = 1.93$
$\dot{W} = 31.00$ W	$St = 0.22$	$U_e/U_j = 0.67$
$f = 208.0$ Hz	$U_e = 12.75$ m/s	\circ : "NO-DRIVE"
$Re_j = 20294$	$Re_\infty = 83567$	\square : "WITH-DRIVE"
$\rho_j = 1.0081$ kg/m ³	$\rho_\infty = 0.9660$ kg/m ³	

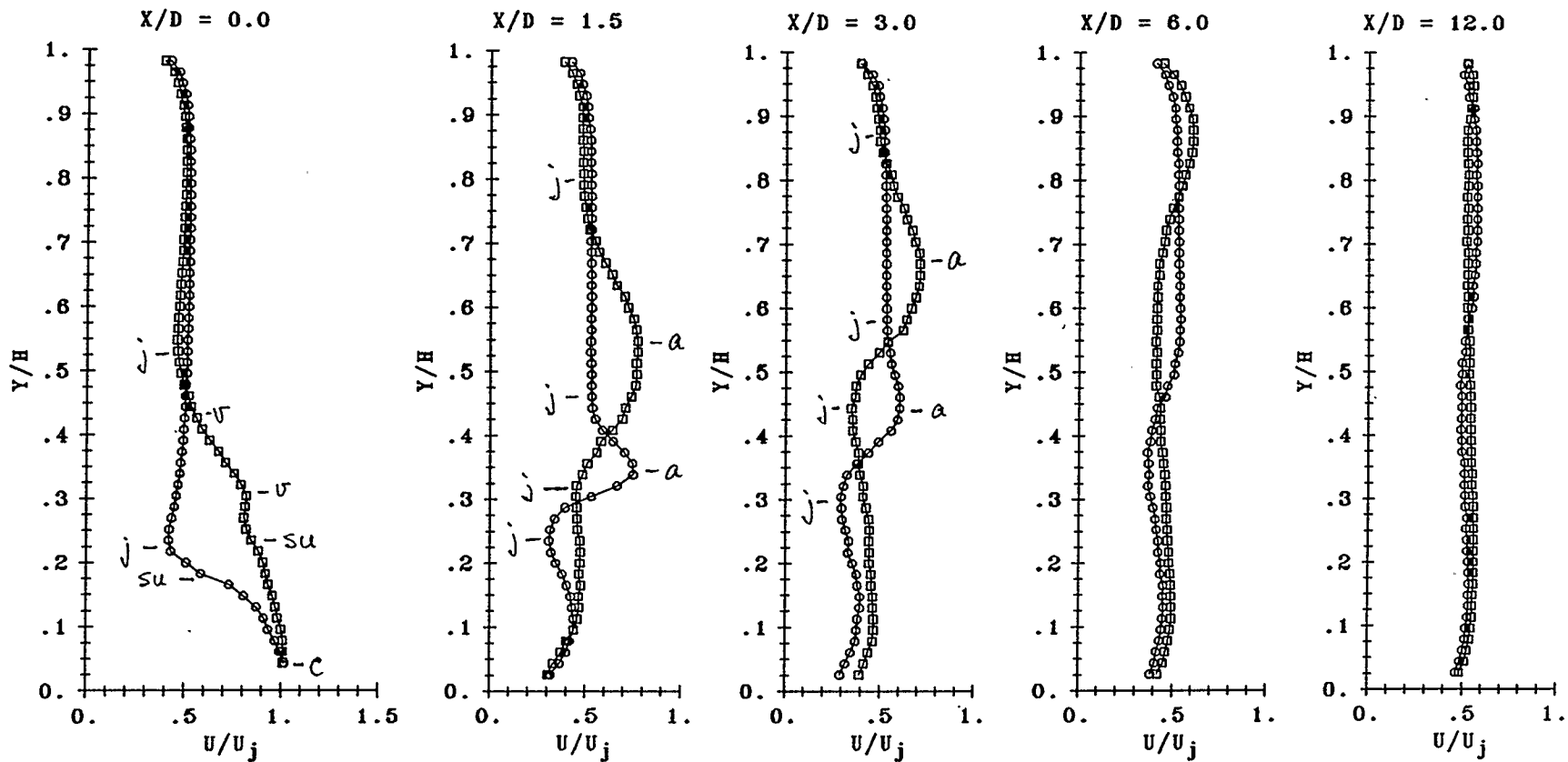


FIGURE 5.27.3 MEAN VELOCITY PROFILES ON CENTRE PLANE FOR JET ORIFICE 19.93 mm DIAMETER, AT CONSTANT STROUHAL NUMBER.

$U_j = 18.99$ m/s	$U_\infty = 9.82$ m/s	$U_j/U_\infty = 1.93$
$\dot{W} = 46.89$ W	$St = 0.22$	$U_e/U_j = 0.89$
$f = 208.0$ Hz	$U_e = 17.00$ m/s	\circ : "NO-DRIVE"
$Re_j = 20294$	$Re_\infty = 83567$	\square : "WITH-DRIVE"
$\rho_j = 1.0081$ kg/m ³	$\rho_\infty = 0.9660$ kg/m ³	

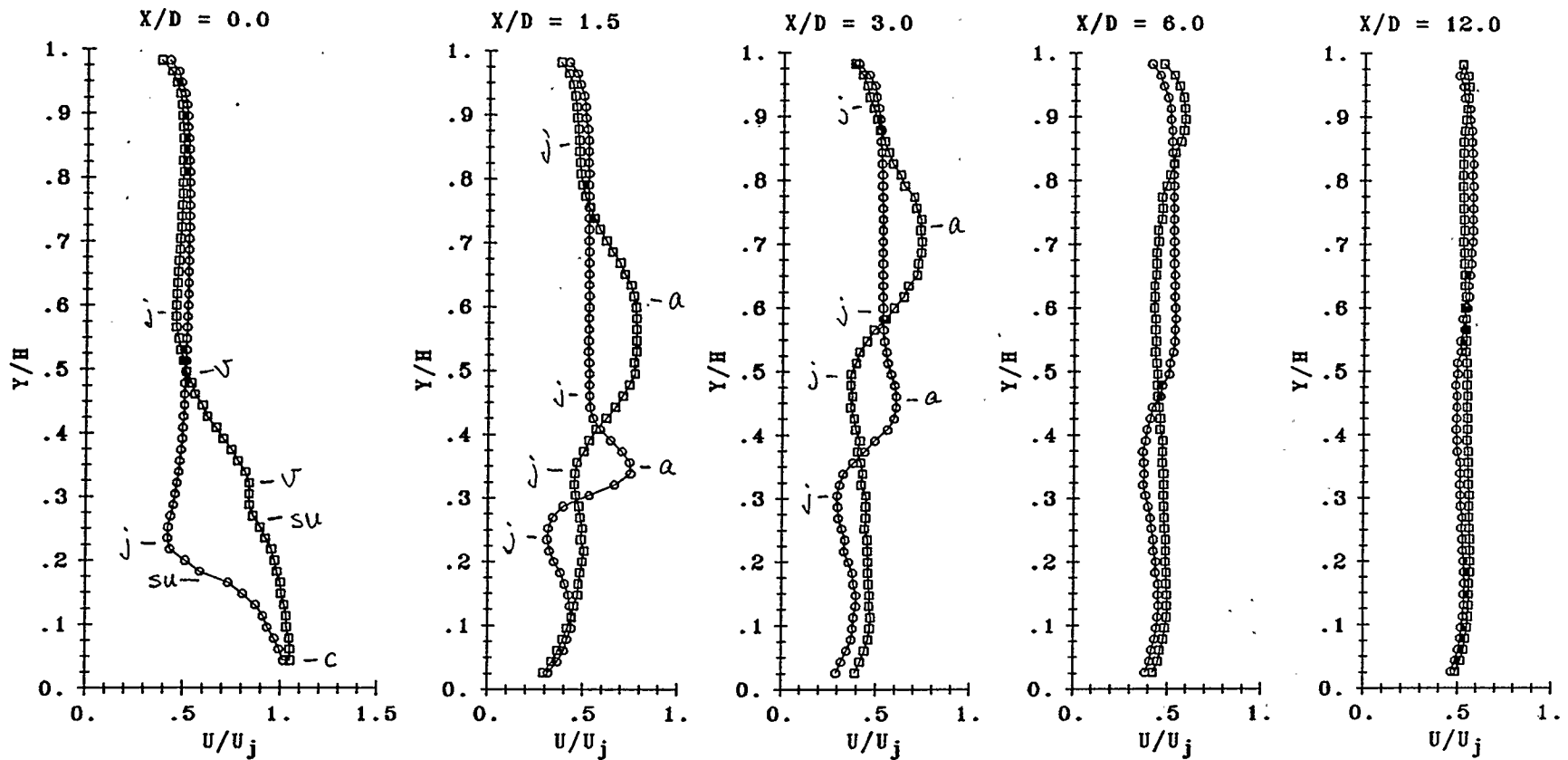


FIGURE 5.27.4 MEAN VELOCITY PROFILES ON CENTRE PLANE FOR JET ORIFICE 19.93 mm DIAMETER, AT CONSTANT STROUHAL NUMBER.

$$U_j = 18.99 \text{ m/s}$$

$$U_\infty = 9.82 \text{ m/s}$$

$$U_j/U_\infty = 1.93$$

$$W = 60.20 \text{ W}$$

$$St = 0.22$$

$$U_e/U_j = 0.97$$

$$f = 208.0 \text{ Hz}$$

$$U_e = 18.50 \text{ m/s}$$

○ : "NO-DRIVE"

$$Re_j = 20294$$

$$Re_\infty = 83567$$

□ : "WITH-DRIVE"

$$\rho_j = 1.0081 \text{ kg/m}^3$$

$$\rho_\infty = 0.9660 \text{ kg/m}^3$$

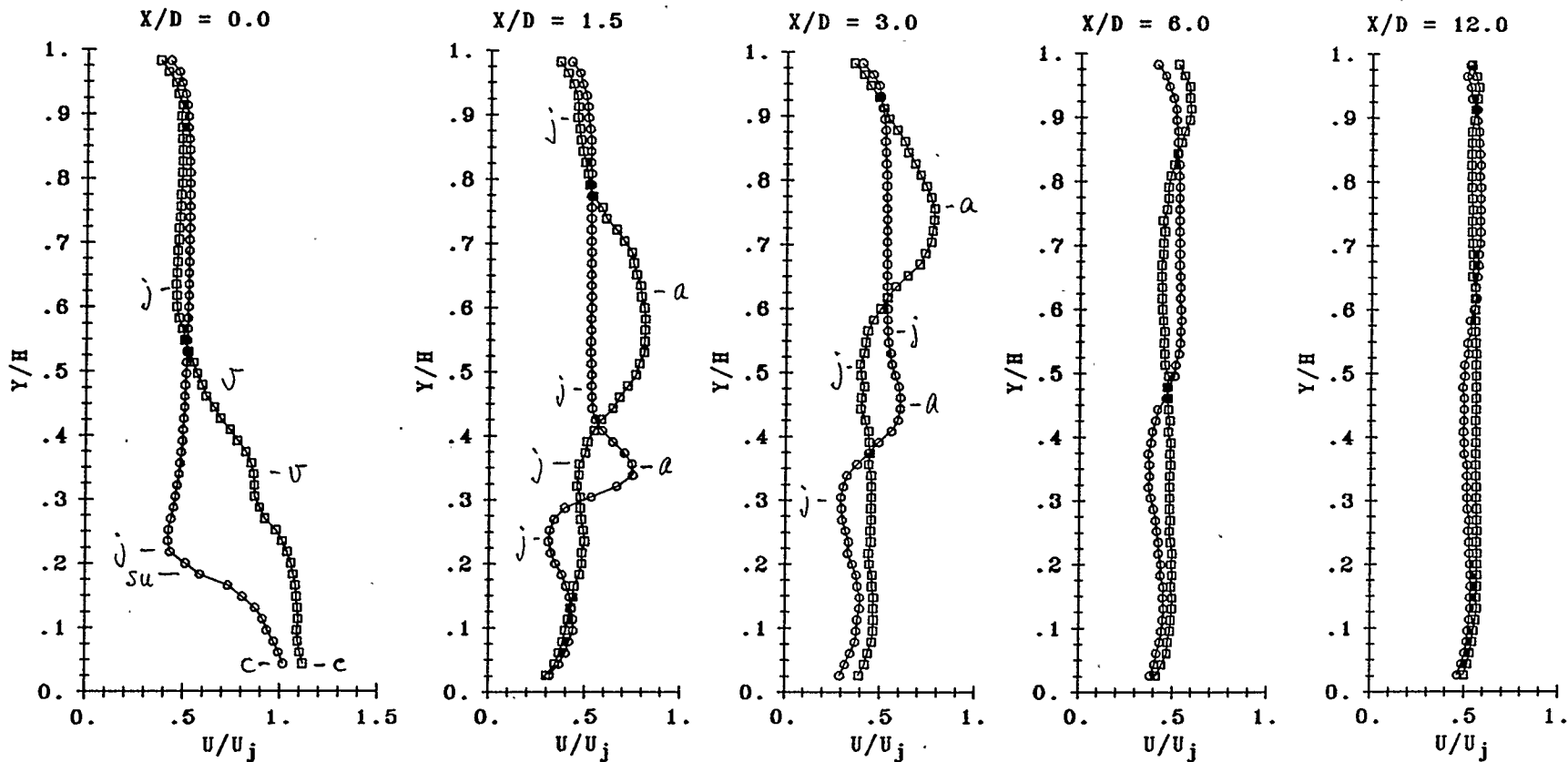


FIGURE 5.27.5 MEAN VELOCITY PROFILES ON CENTRE PLANE FOR JET ORIFICE 19.93 mm DIAMETER, AT CONSTANT STROUHAL NUMBER.

$U_j = 18.99$ m/s	$U_\infty = 9.82$ m/s	$U_j/U_\infty = 1.93$
$\dot{W} = 75.26$ W	$St = 0.22$	$U_e/U_j = 1.18$
$f = 208.0$ Hz	$U_e = 22.50$ m/s	\circ : "NO-DRIVE"
$Re_j = 20294$	$Re_\infty = 83567$	\square : "WITH-DRIVE"
$\rho_j = 1.0081$ kg/m ³	$\rho_\infty = 0.9660$ kg/m ³	

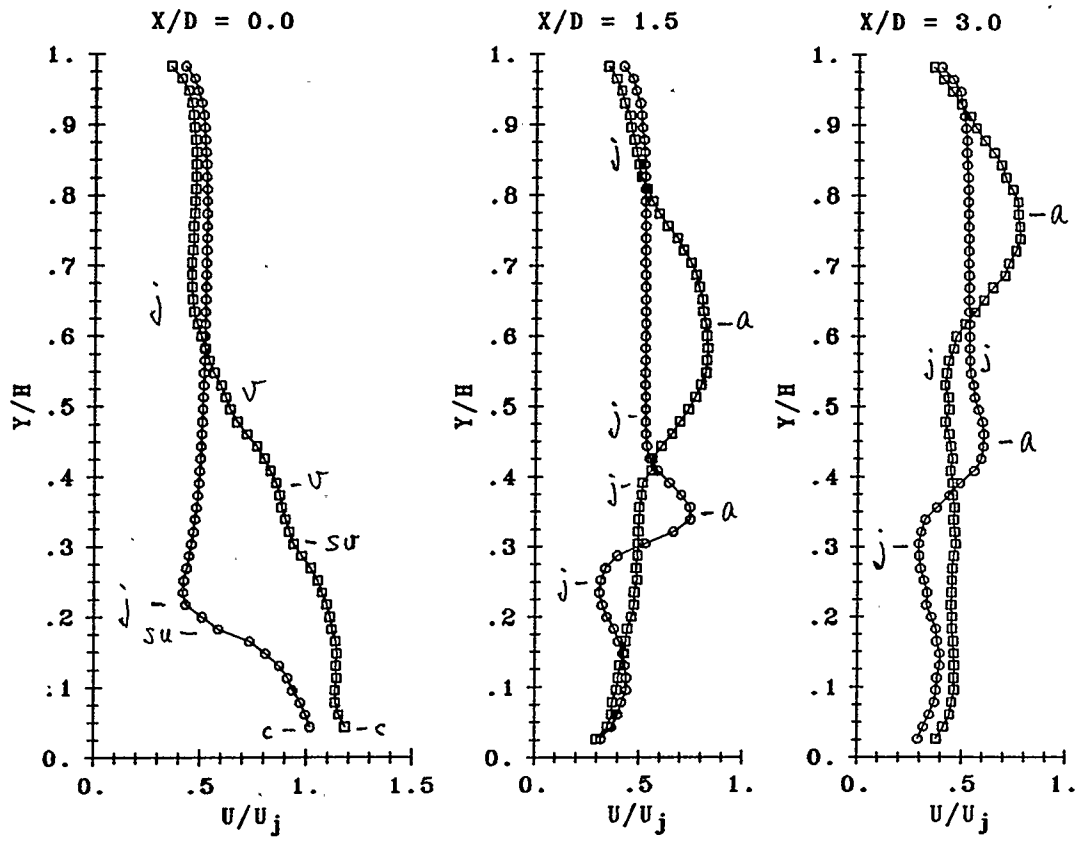


FIGURE 5.27.6 MEAN VELOCITY PROFILES ON CENTRE PLANE FOR JET ORIFICE 19.93 mm DIAMETER, AT CONSTANT STROUHAL NUMBER.

$U_j = 18.99 \text{ m/s}$	$U_\infty = 9.82 \text{ m/s}$	$U_j/U_\infty = 1.93$
$\dot{W} = 90.90 \text{ W}$	$St = 0.22$	$U_e/U_j = 1.32$
$f = 208.0 \text{ Hz}$	$U_e = 25.00 \text{ m/s}$	$\circ : \text{ "NO-DRIVE"}$
$Re_j = 20294$	$Re_\infty = 83567$	$\square : \text{ "WITH-DRIVE"}$
$\rho_j = 1.0081 \text{ kg/m}^3$	$\rho_\infty = 0.9660 \text{ kg/m}^3$	

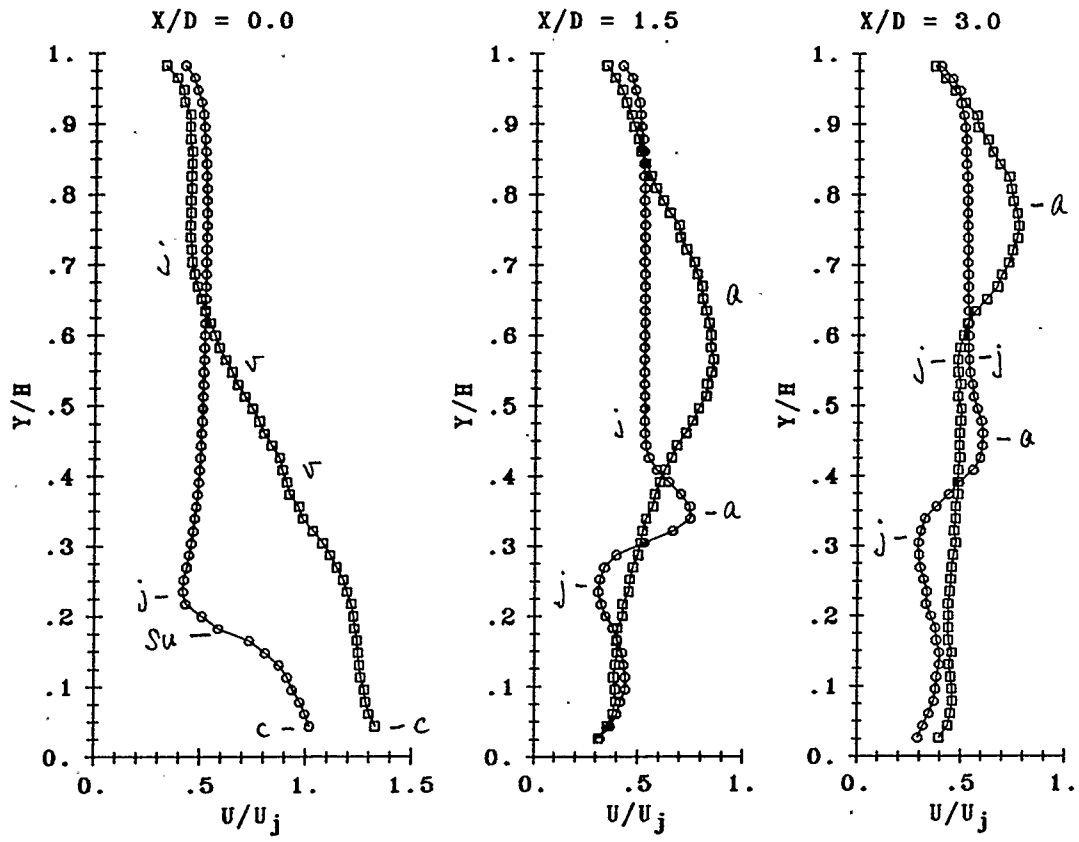


FIGURE 5.27.7 MEAN VELOCITY PROFILES ON CENTRE PLANE FOR JET ORIFICE 19.93 mm DIAMETER, AT CONSTANT STROUHAL NUMBER.

$U_j = 18.99 \text{ m/s}$	$U_\infty = 9.82 \text{ m/s}$	$U_j/U_\infty = 1.93$
$\dot{W} = 141.0 \text{ W}$	$St = 0.22$	$U_e/U_j = 1.45$
$f = 208.0 \text{ Hz}$	$U_e = 27.50 \text{ m/s}$	$\circ : \text{ "NO-DRIVE"}$
$Re_j = 20294$	$Re_\infty = 83567$	$\square : \text{ "WITH-DRIVE"}$
$\rho_j = 1.0081 \text{ kg/m}^3$	$\rho_\infty = 0.9660 \text{ kg/m}^3$	

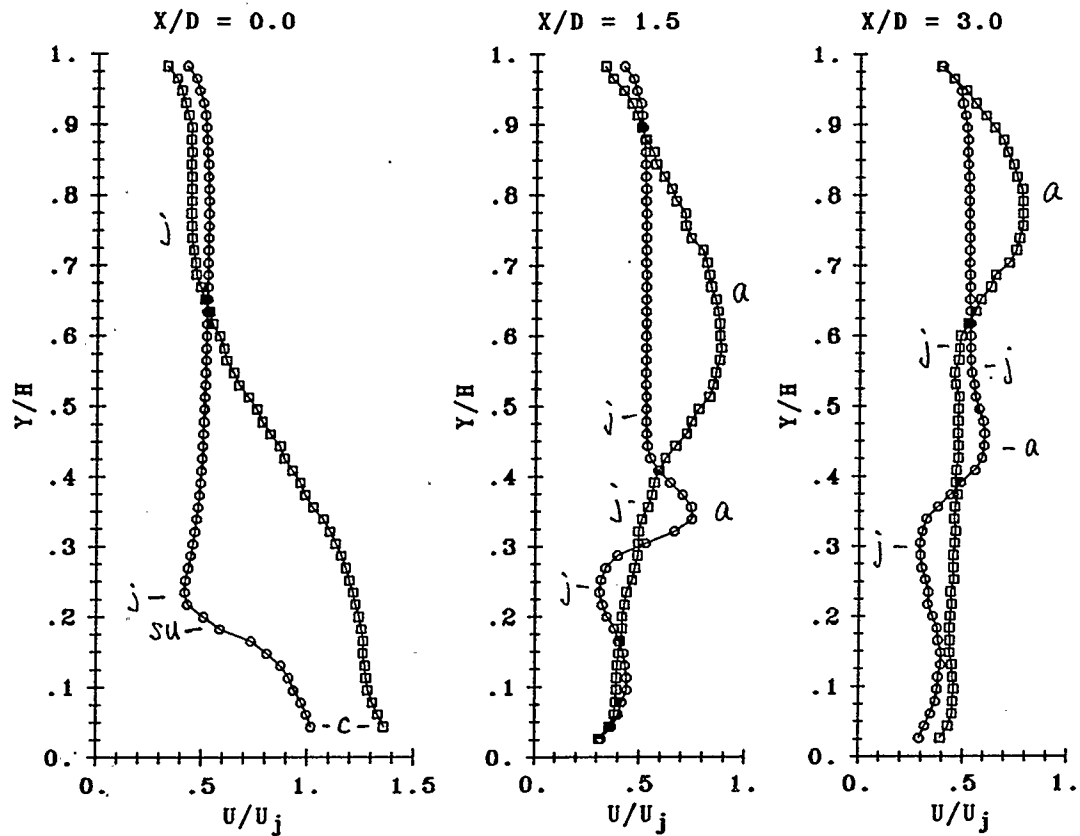


FIGURE 5.27.8 MEAN VELOCITY PROFILES ON CENTRE PLANE FOR JET ORIFICE 19.93 mm DIAMETER, AT CONSTANT STROUHAL NUMBER.

$U_j = 18.99$ m/s	$U_\infty = 9.82$ m/s	$U_j/U_\infty = 1.93$
$\dot{W} = 190.2$ W	$St = 0.22$	$U_e/U_j = 1.53$
$f = 208.0$ Hz	$U_e = 29.00$ m/s	\circ : "NO-DRIVE"
$Re_j = 20294$	$Re_\infty = 83567$	\square : "WITH-DRIVE"
$\rho_j = 1.0081$ kg/m ³	$\rho_\infty = 0.9660$ kg/m ³	

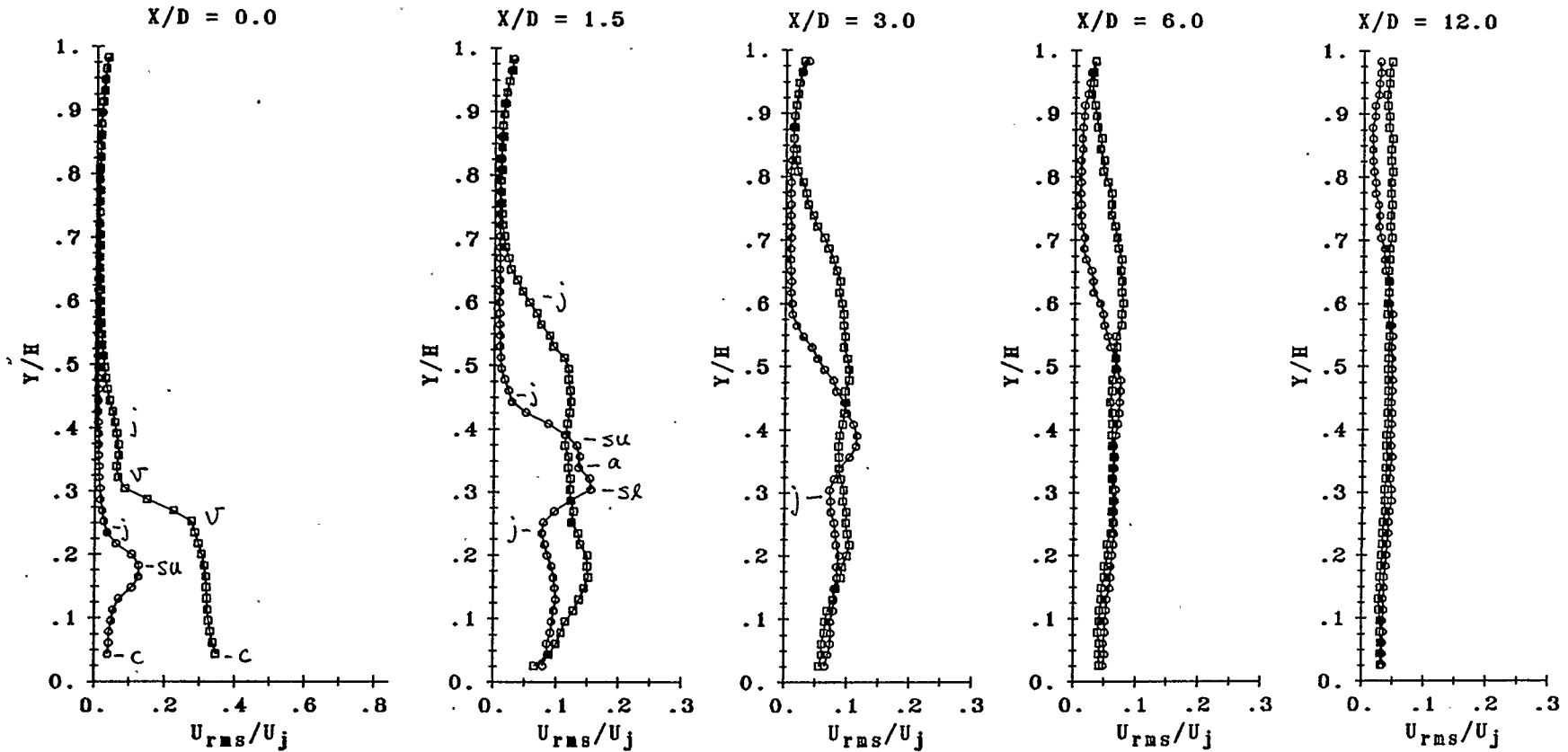


FIGURE 5.28.1 U_{rms} TURBULENCE PROFILES ON CENTRE PLANE FOR JET ORIFICE 19.93 mm DIAMETER, AT CONSTANT STROUHAL NUMBER.

$U_j = 18.99$ m/s	$U_\infty = 9.82$ m/s	$U_j/U_\infty = 1.93$
$W = 15.24$ W	$St = 0.22$	$U_e/U_j = 0.54$
$f = 208.0$ Hz	$U_e = 10.25$ m/s	\circ : "NO-DRIVE"
$Re_j = 20294$	$Re_\infty = 83567$	\square : "WITH-DRIVE"
$\rho_j = 1.0081$ kg/m ³	$\rho_\infty = 0.9660$ kg/m ³	

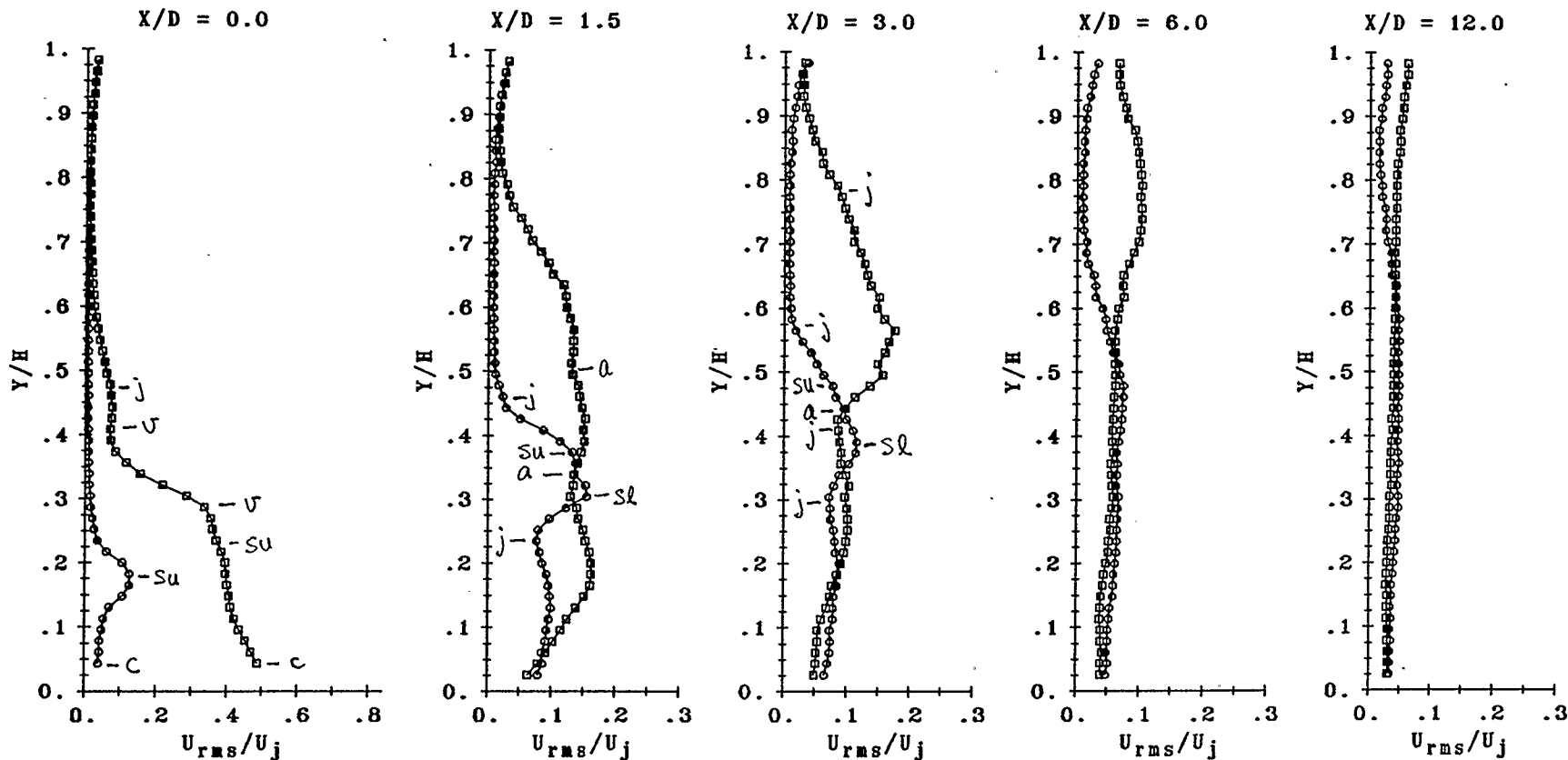


FIGURE 5.28.2 U_{rms} TURBULENCE PROFILES ON CENTRE PLANE FOR JET ORIFICE 19.93 mm DIAMETER, AT CONSTANT STROUHAL NUMBER.

$U_j = 18.99$ m/s	$U_\infty = 9.82$ m/s	$U_j/U_\infty = 1.93$
$\dot{W} = 31.00$ W	$St = 0.22$	$U_e/U_j = 0.67$
$f = 208.0$ Hz	$U_e = 12.75$ m/s	○ : "NO-DRIVE"
$Re_j = 20294$	$Re_\infty = 83567$	□ : "WITH-DRIVE"
$\rho_j = 1.0081$ kg/m ³	$\rho_\infty = 0.9660$ kg/m ³	

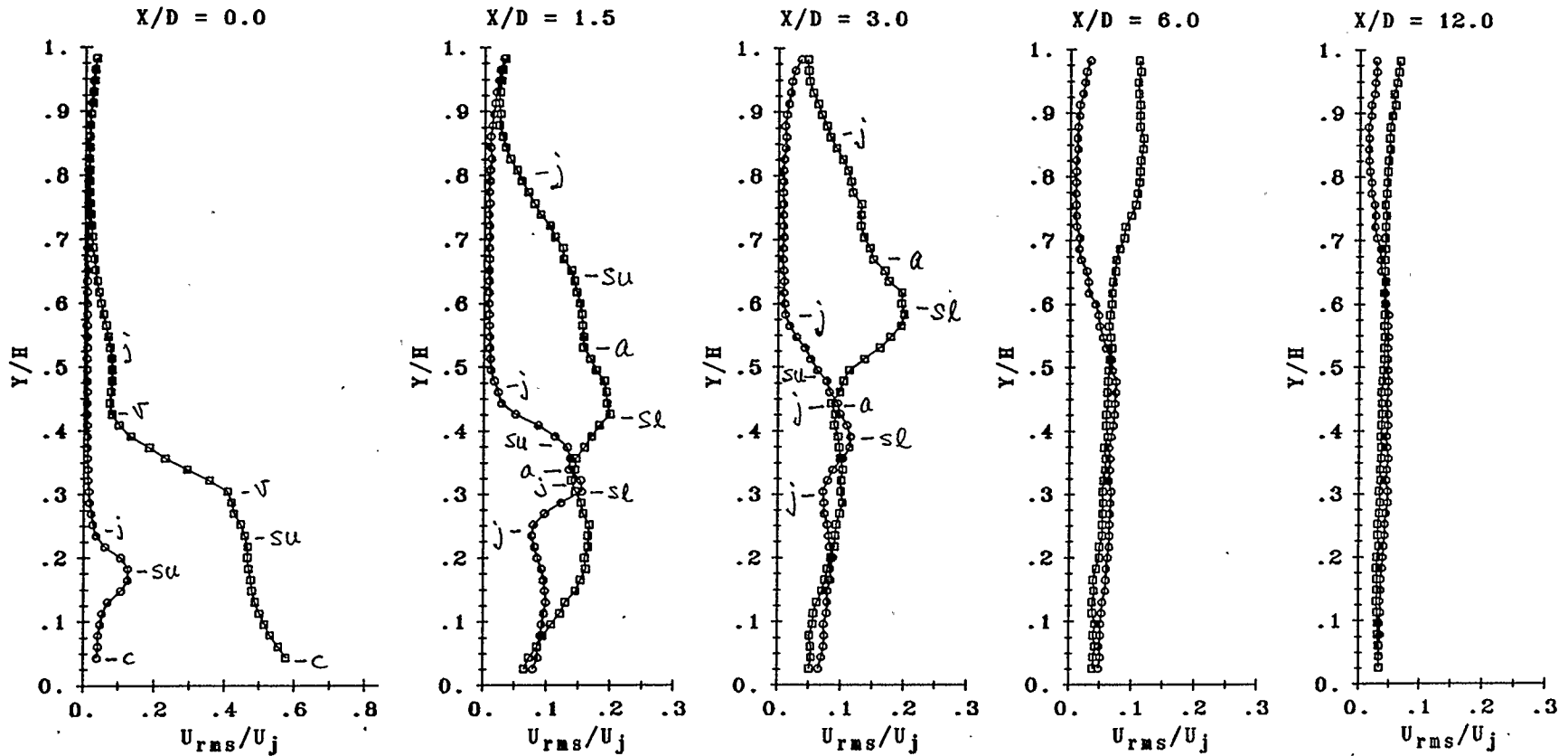


FIGURE 5.28.3 U_{rms} TURBULENCE PROFILES ON CENTRE PLANE FOR JET ORIFICE 19.93 mm DIAMETER, AT CONSTANT STROUHAL NUMBER.

$U_j = 18.99$ m/s	$U_\infty = 9.82$ m/s	$U_j/U_\infty = 1.93$
$\dot{W} = 46.89$ W	$St = 0.22$	$U_e/U_j = 0.89$
$f = 208.0$ Hz	$U_e = 17.00$ m/s	o : "NO-DRIVE"
$Re_j = 20294$	$Re_\infty = 83567$	□ : "WITH-DRIVE"
$\rho_j = 1.0081$ kg/m ³	$\rho_\infty = 0.9660$ kg/m ³	

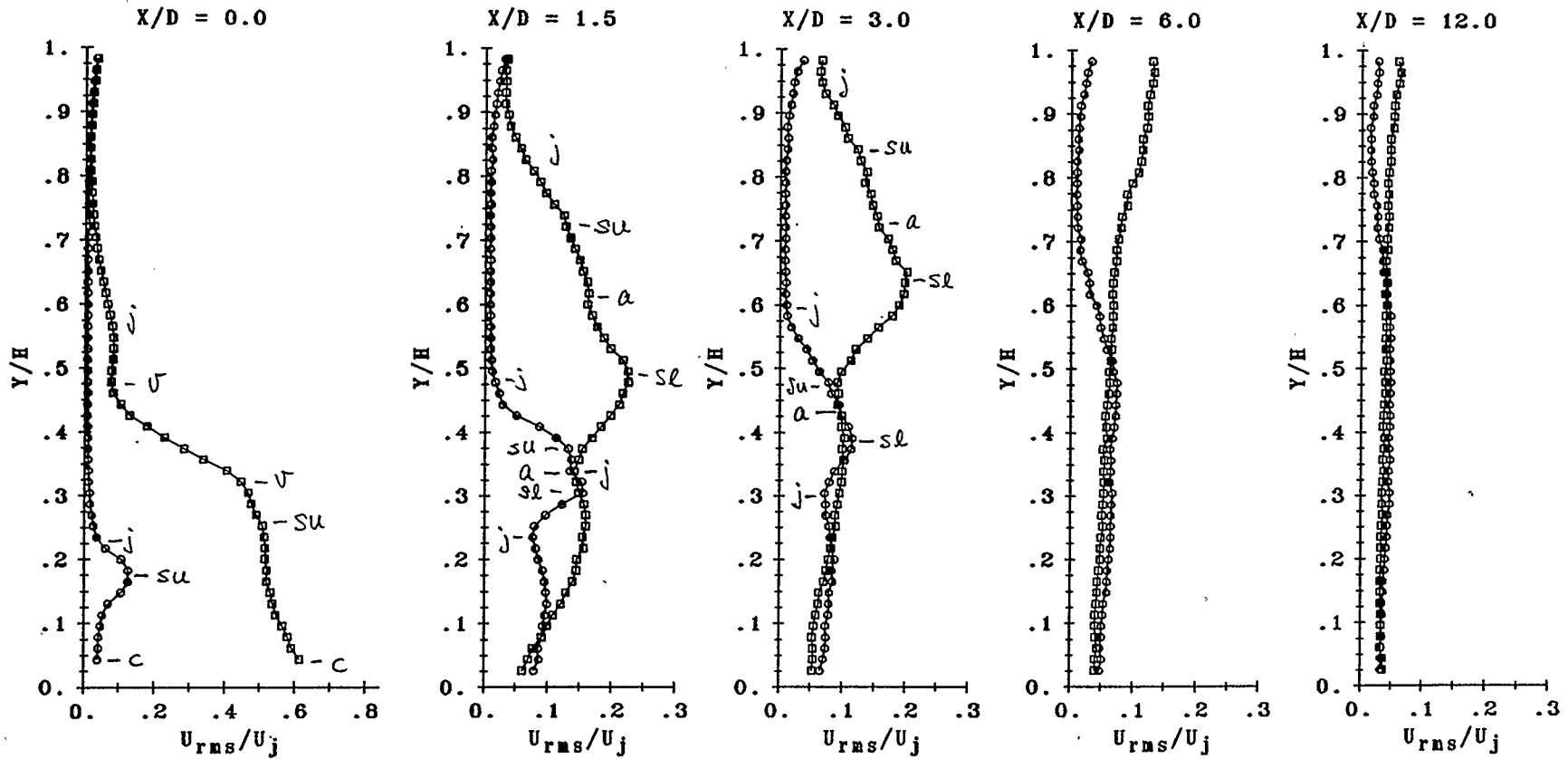


FIGURE 5.28.4 U_{rms} TURBULENCE PROFILES ON CENTRE PLANE FOR JET ORIFICE 19.93 mm DIAMETER, AT CONSTANT STROUHAL NUMBER.

$U_j = 18.99$ m/s	$U_\infty = 9.82$ m/s	$U_j/U_\infty = 1.93$
$\dot{W} = 60.20$ W	$St = 0.22$	$U_e/U_j = 0.97$
$f = 208.0$ Hz	$U_e = 18.50$ m/s	o : "NO-DRIVE"
$Re_j = 20294$	$Re_\infty = 83567$	□ : "WITH-DRIVE"
$\rho_j = 1.0081$ kg/m ³	$\rho_\infty = 0.9660$ kg/m ³	

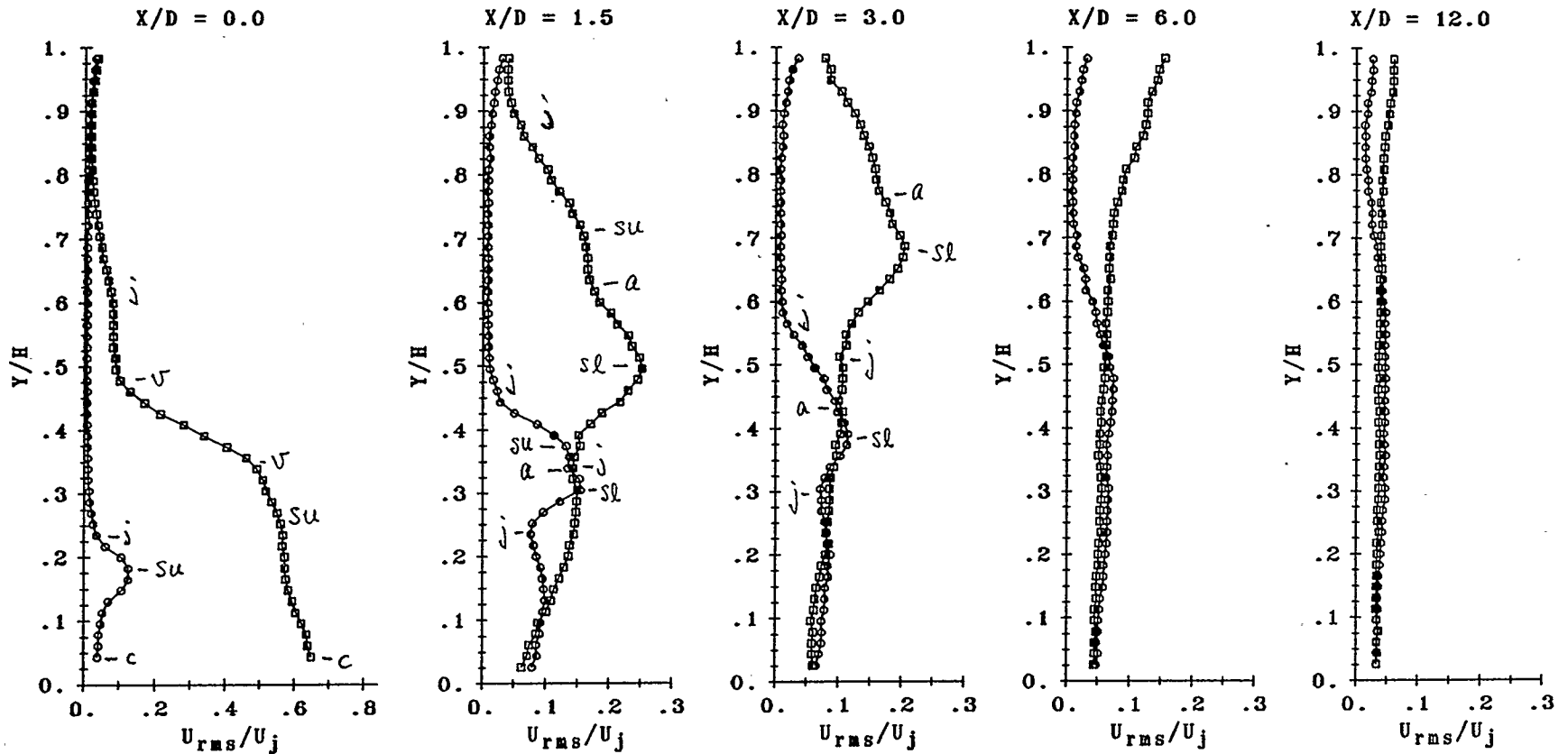


FIGURE 5.28.5 U_{rms} TURBULENCE PROFILES ON CENTRE PLANE FOR JET ORIFICE 19.93 mm DIAMETER, AT CONSTANT STROUHAL NUMBER.

$U_j = 18.99$ m/s	$U_\infty = 9.82$ m/s	$U_j/U_\infty = 1.93$
$\dot{W} = 75.26$ W	$St = 0.22$	$U_e/U_j = 1.18$
$f = 208.0$ Hz	$U_e = 22.50$ m/s	o : "NO-DRIVE"
$Re_j = 20294$	$Re_\infty = 83567$	□ : "WITH-DRIVE"
$\rho_j = 1.0081$ kg/m ³	$\rho_\infty = 0.9660$ kg/m ³	

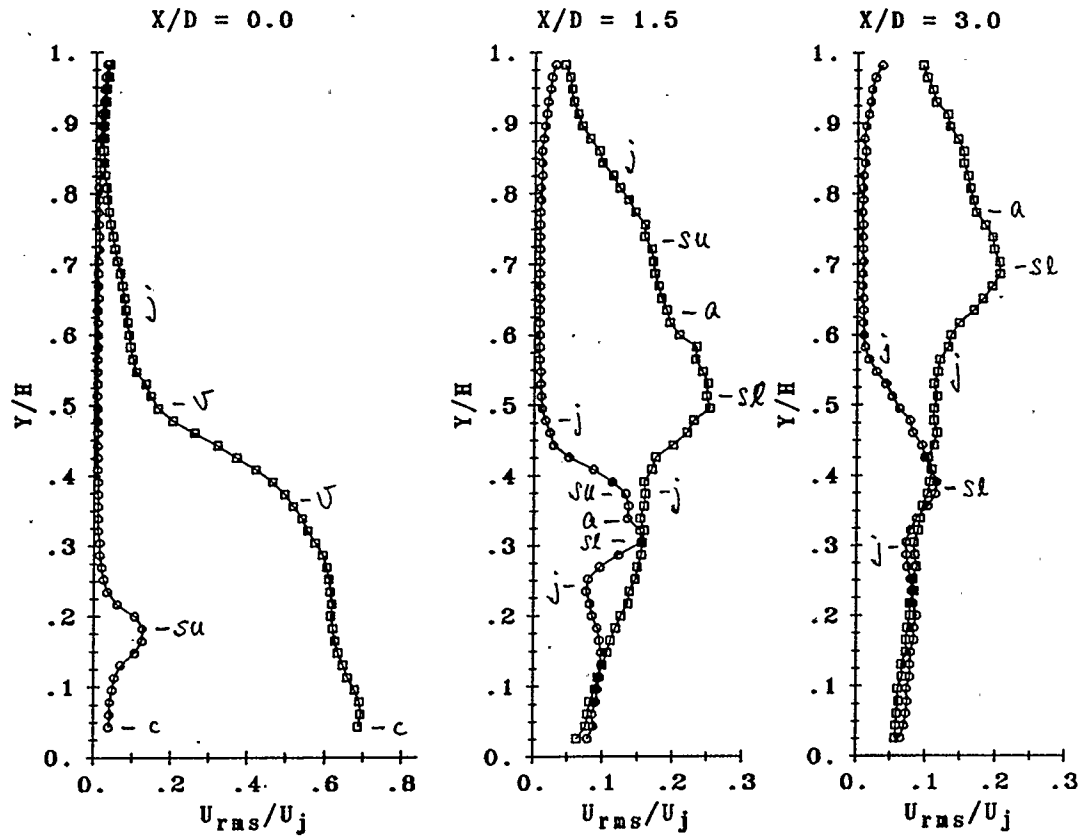


FIGURE 5.28.6 U_{rms} TURBULENCE PROFILES ON CENTRE PLANE FOR JET ORIFICE 19.93 mm DIAMETER, AT CONSTANT STROUHAL NUMBER.

$U_j = 18.99$ m/s	$U_\infty = 9.82$ m/s	$U_j/U_\infty = 1.93$
$\dot{W} = 90.90$ W	$St = 0.22$	$U_e/U_j = 1.32$
$f = 208.0$ Hz	$U_e = 25.00$ m/s	o : "NO-DRIVE"
$Re_j = 20294$	$Re_\infty = 83567$	□ : "WITH-DRIVE"
$\rho_j = 1.0081$ kg/m ³	$\rho_\infty = 0.9680$ kg/m ³	

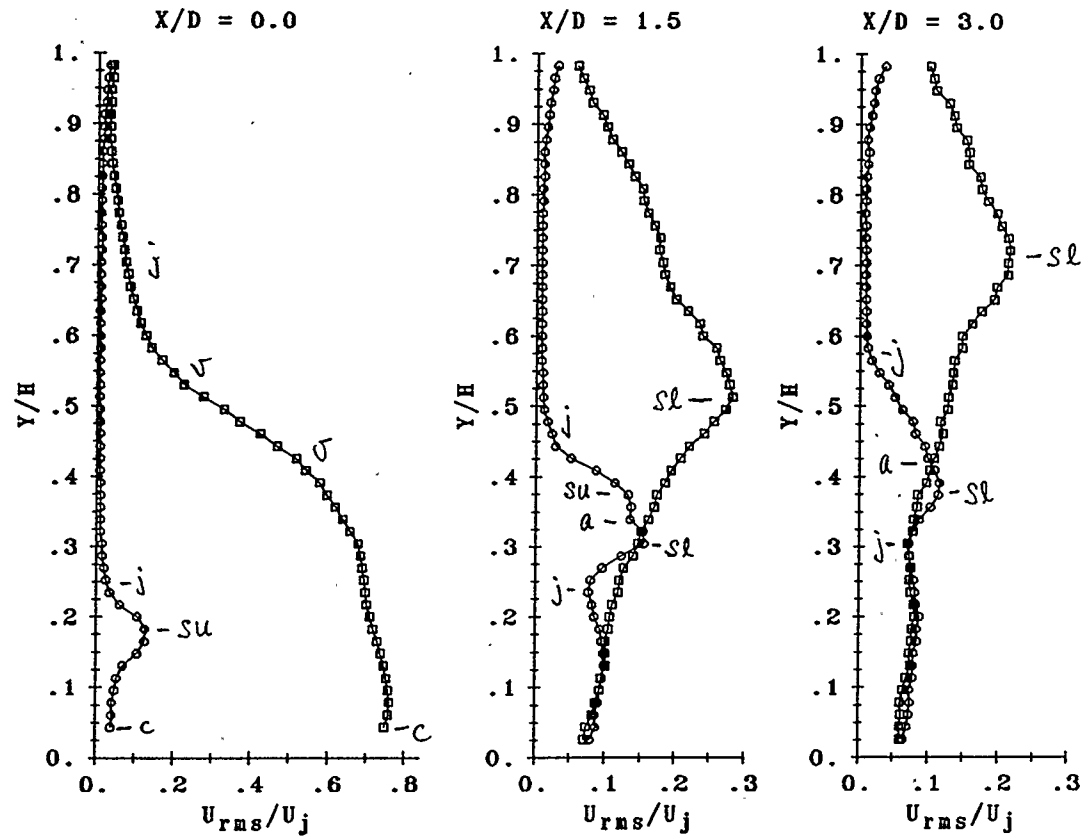


FIGURE 5.28.7 U_{rms} TURBULENCE PROFILES ON CENTRE PLANE FOR JET ORIFICE 19.93 mm DIAMETER, AT CONSTANT STROUHAL NUMBER.

$U_j = 18.99$ m/s	$U_\infty = 9.82$ m/s	$U_j/U_\infty = 1.93$
$\dot{W} = 141.0$ W	$St = 0.22$	$U_e/U_j = 1.45$
$f = 208.0$ Hz	$U_e = 27.50$ m/s	\circ : "NO-DRIVE"
$Re_j = 20294$	$Re_\infty = 83567$	\square : "WITH-DRIVE"
$\rho_j = 1.0081$ kg/m ³	$\rho_\infty = 0.9660$ kg/m ³	

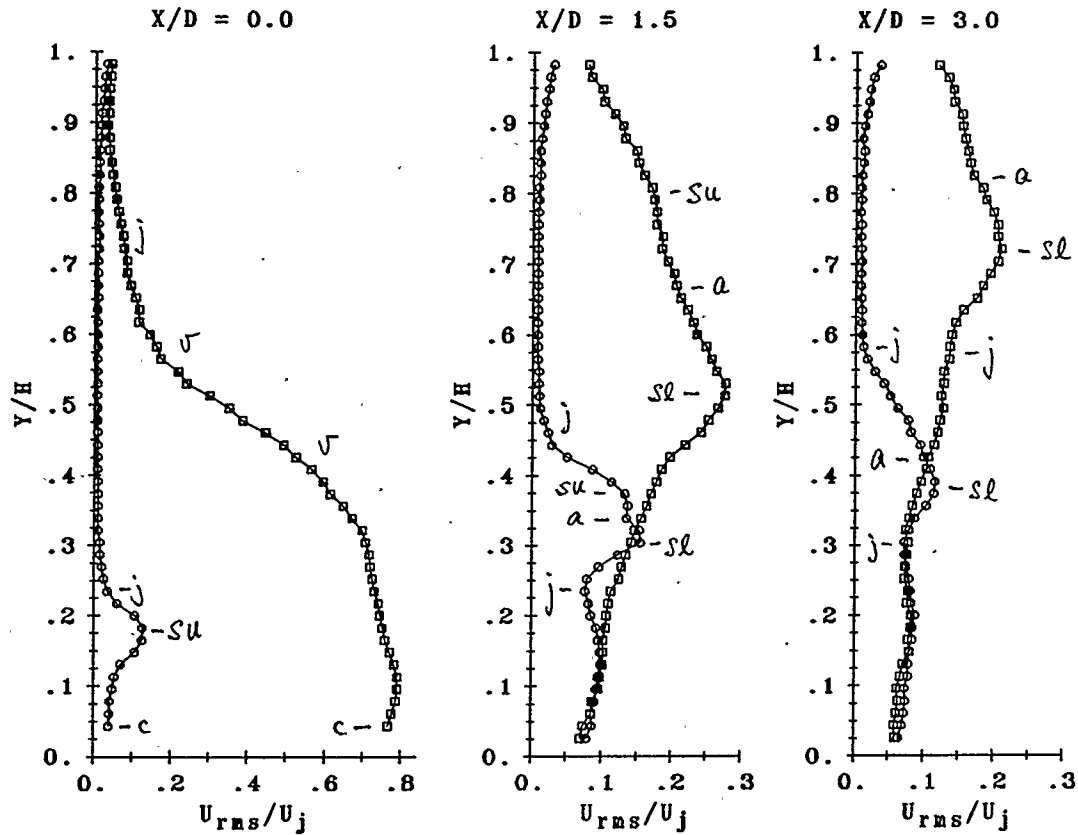


FIGURE 5.28.8 U_{rms} TURBULENCE PROFILES ON CENTRE PLANE FOR JET ORIFICE 19.93 mm DIAMETER, AT CONSTANT STROUHAL NUMBER.

$U_j = 18.99$ m/s	$U_\infty = 9.82$ m/s	$U_j/U_\infty = 1.93$
$\dot{W} = 190.2$ W	$St = 0.22$	$U_e/U_j = 1.53$
$f = 208.0$ Hz	$U_e = 29.00$ m/s	o : "NO-DRIVE"
$Re_j = 20294$	$Re_\infty = 83567$	□ : "WITH-DRIVE"
$\rho_j = 1.0081$ kg/m ³	$\rho_\infty = 0.9660$ kg/m ³	

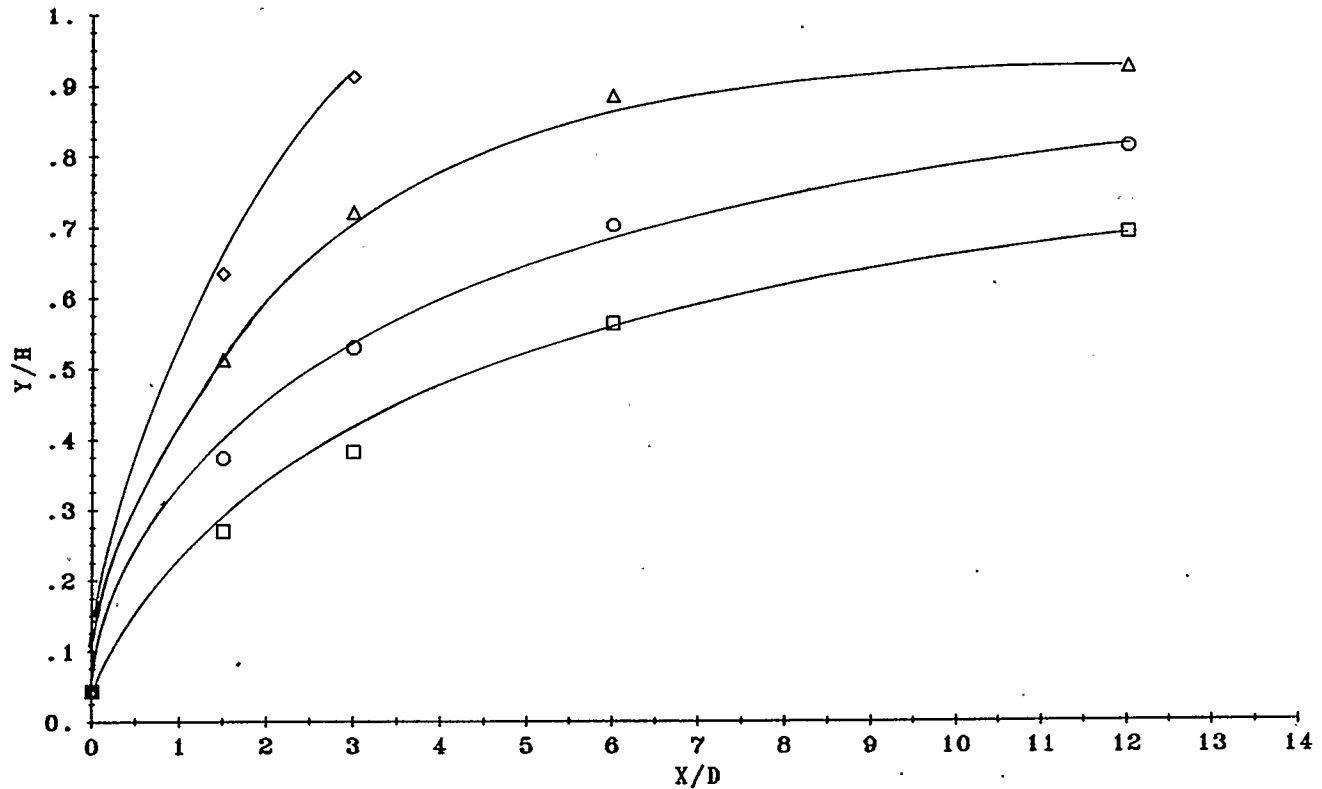


FIGURE 5.29 COMPARATIVE CENTRE PLANE VELOCITY-AXIS TRAJECTORY FOR STEADY JETS AT DIFFERENT DOWNSTREAM X/D LOCATIONS. (REFER FIGURES 5.7 - 5.10 FOR OTHER OPERATING CONDITIONS.)

□	: $U_j = 13.20 \text{ m/s}$	$U_\infty = 10.06 \text{ m/s}$	$U_j/U_\infty = 1.31$
○	: $U_j = 23.27 \text{ m/s}$	$U_\infty = 10.27 \text{ m/s}$	$U_j/U_\infty = 2.26$
△	: $U_j = 34.30 \text{ m/s}$	$U_\infty = 10.27 \text{ m/s}$	$U_j/U_\infty = 3.34$
◇	: $U_j = 46.22 \text{ m/s}$	$U_\infty = 10.13 \text{ m/s}$	$U_j/U_\infty = 4.56$

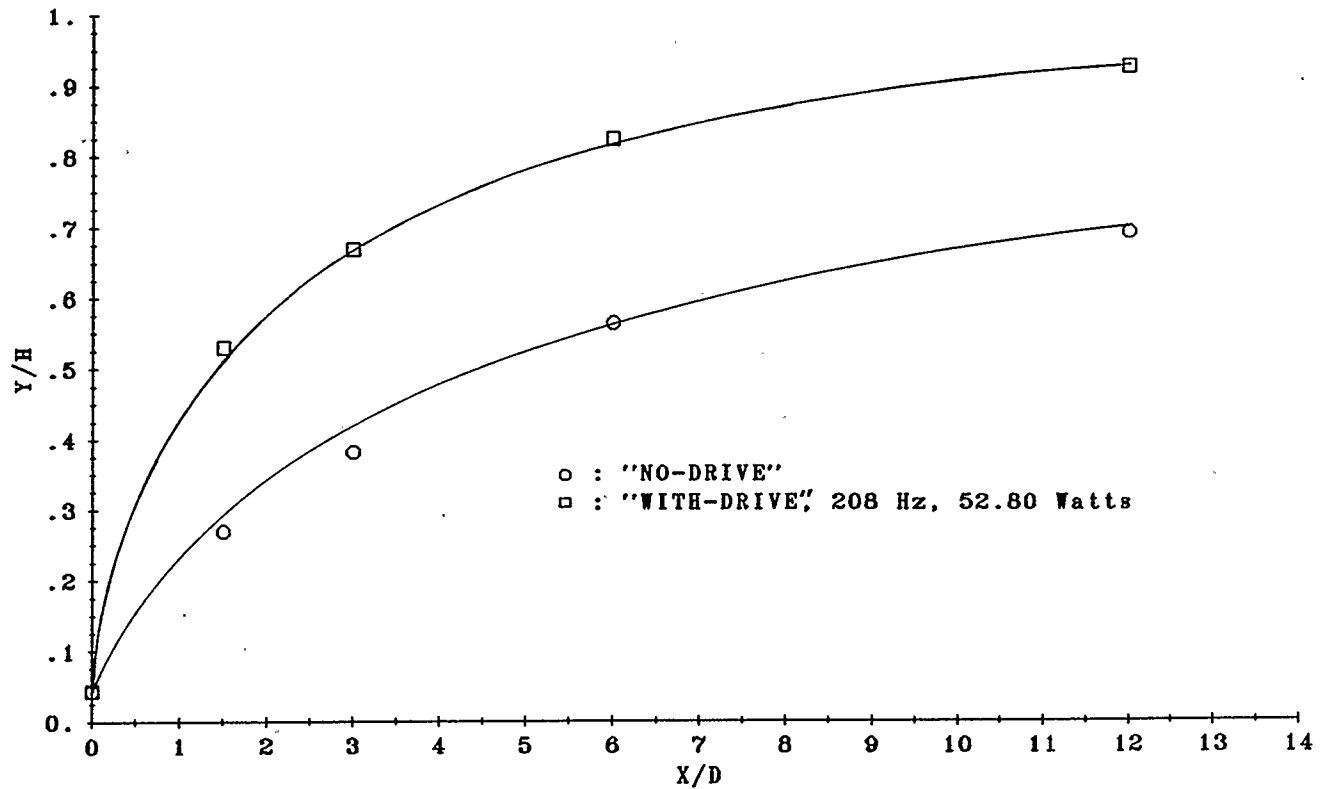


FIGURE 5.30.1 COMPARATIVE CENTRE PLANE VELOCITY-AXIS TRAJECTORY FOR STEADY JET AND UNSTEADY JET AT DIFFERENT DOWNSTREAM X/D LOCATIONS. (REFER FIGURE 5.7 FOR OTHER OPERATING CONDITIONS.)

$U_j = 13.20 \text{ m/s}$	$U_\infty = 10.06 \text{ m/s}$	$U_j/U_\infty = 1.31$
$U_e = 22.00 \text{ m/s}$	$St = 0.31$	$U_e/U_j = 1.67$

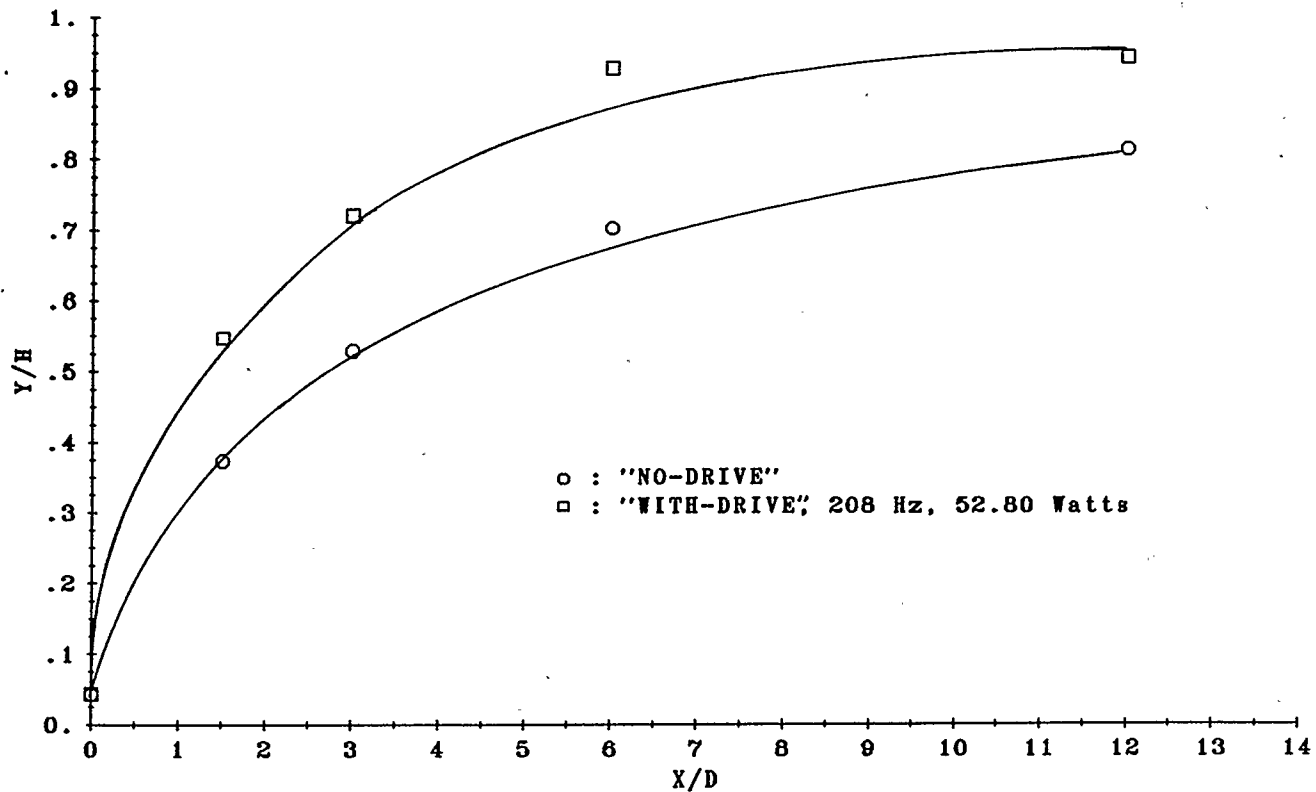


FIGURE 5.30.2 COMPARATIVE CENTRE PLANE VELOCITY-AXIS TRAJECTORY FOR STEADY JET AND UNSTEADY JET AT DIFFERENT DOWNSTREAM X/D LOCATIONS. (REFER FIGURE 5.8 FOR OTHER OPERATING CONDITIONS.)

$U_j = 23.27 \text{ m/s}$	$U_\infty = 10.27 \text{ m/s}$	$U_j/U_\infty = 2.26$
$U_e = 20.00 \text{ m/s}$	$St = 0.18$	$U_e/U_j = 0.86$

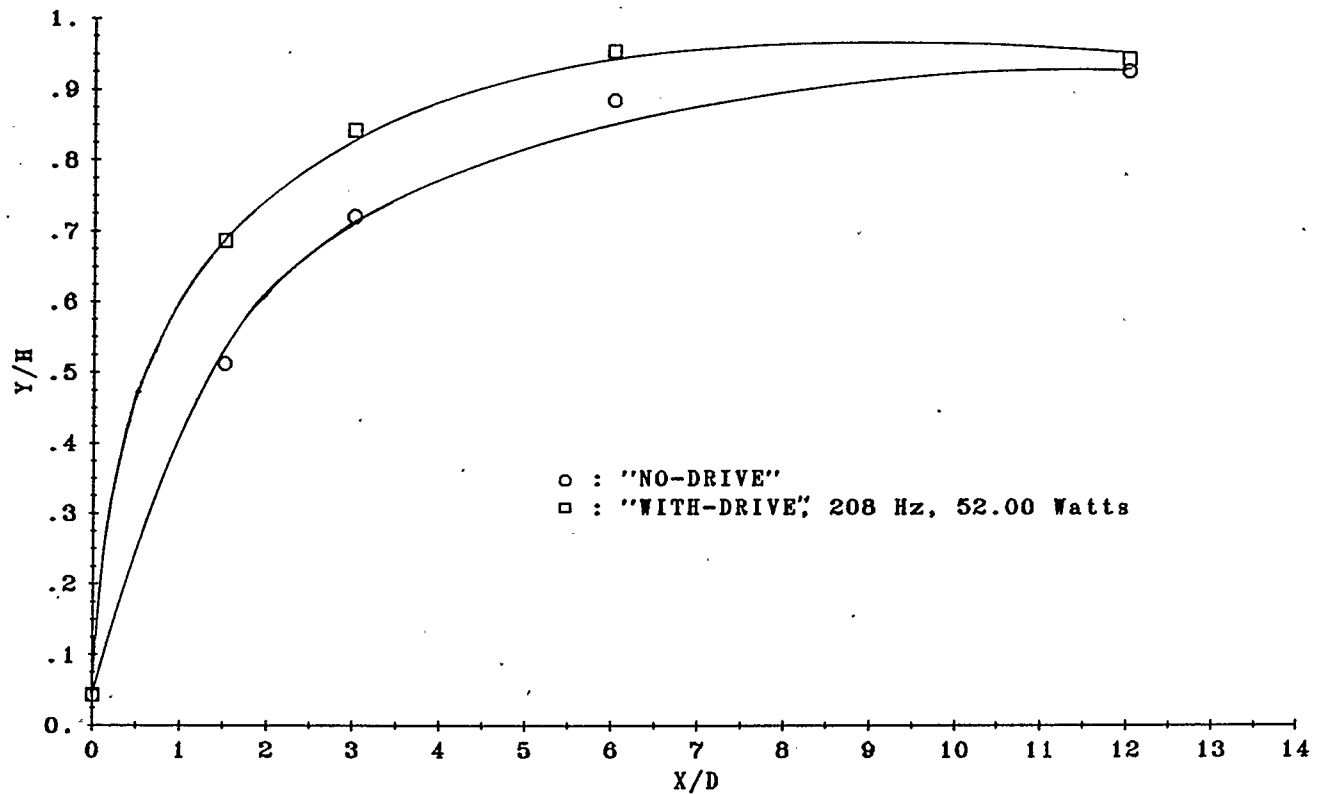


FIGURE 5.30.3 COMPARATIVE CENTRE PLANE VELOCITY-AXIS TRAJECTORY FOR STEADY JET AND UNSTEADY JET AT DIFFERENT DOWNSTREAM X/D LOCATIONS. (REFER FIGURE 5.9 FOR OTHER OPERATING CONDITIONS.)

$U_j = 34.30 \text{ m/s}$	$U_\infty = 10.27 \text{ m/s}$	$U_j/U_\infty = 3.34$
$U_e = 18.50 \text{ m/s}$	$St = 0.12$	$U_e/U_j = 0.54$

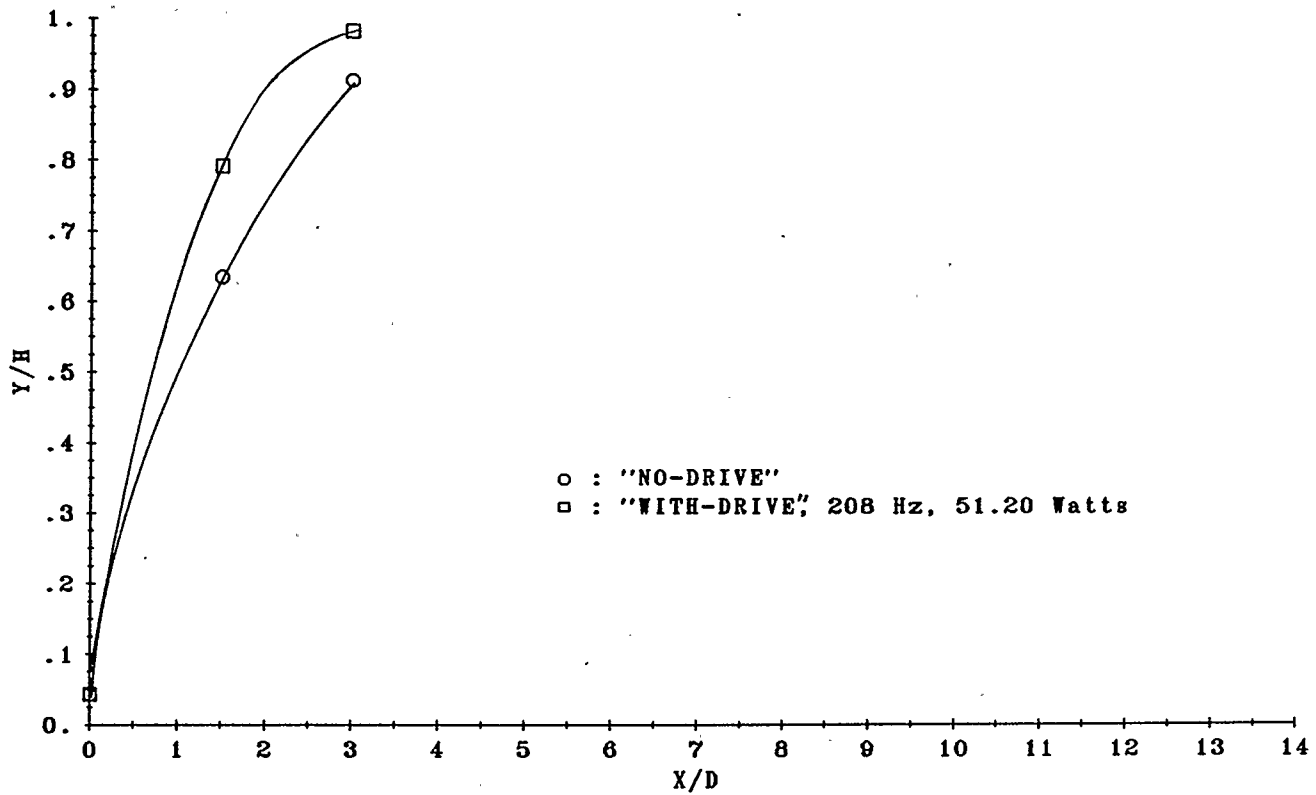


FIGURE 5.30.4 COMPARATIVE CENTRE PLANE VELOCITY-AXIS TRAJECTORY FOR STEADY JET AND UNSTEADY JET AT DIFFERENT DOWNSTREAM X/D LOCATIONS. (REFER FIGURE 5.10 FOR OTHER OPERATING CONDITIONS.)

$U_j = 46.22$ m/s	$U_\infty = 10.13$ m/s	$U_j/U_\infty = 4.56$
$U_e = 14.00$ m/s	$St = 0.09$	$U_e/U_j = 0.30$

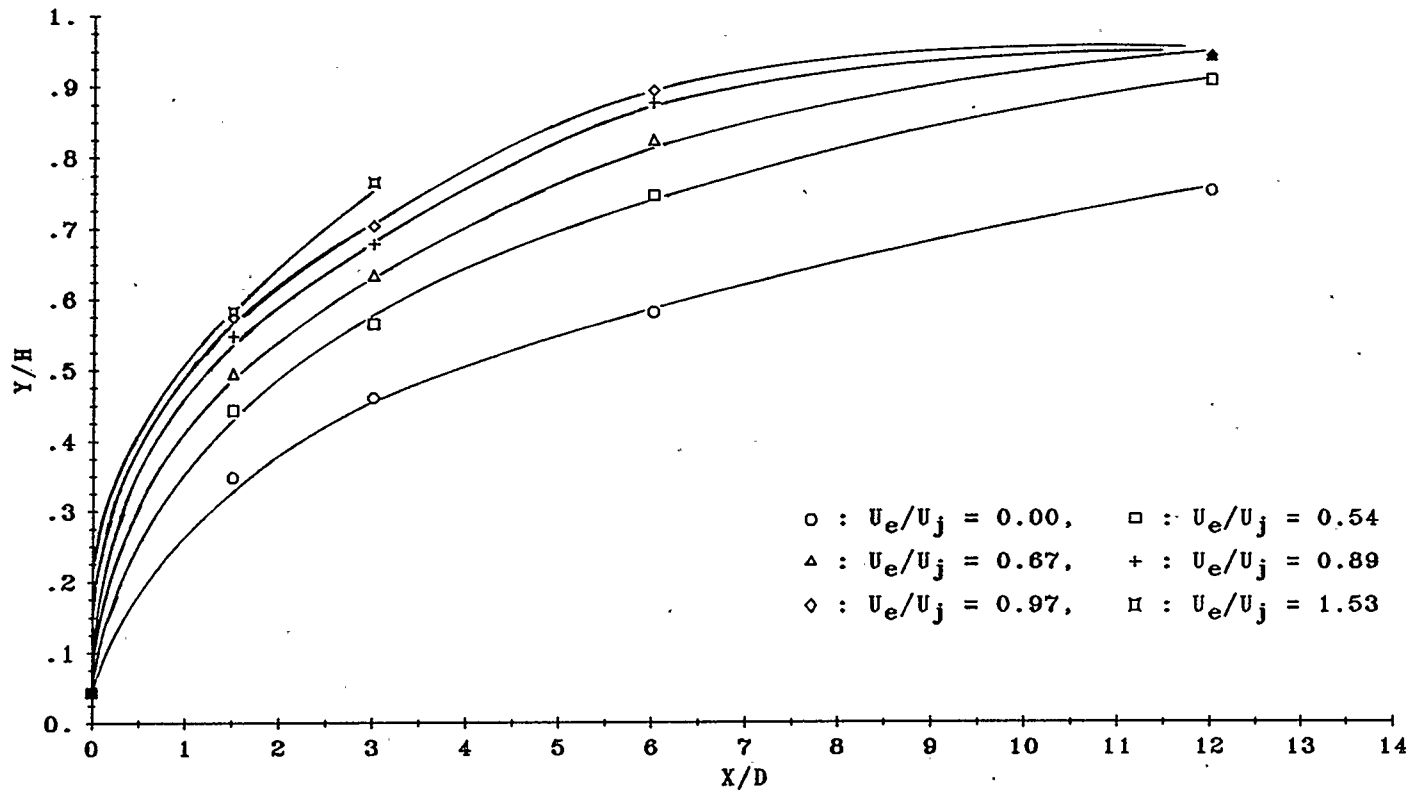


FIGURE 5.31 PENETRATION TRAJECTORY FOR DIFFERENT DRIVING POWER CONDITIONS ON CENTRE PLANE AT CONSTANT STROUHAL NUMBER FOR JET ORIFICE 19.93 mm DIAMETER.

$U_j = 18.99$ m/s	$U_\infty = 9.82$ m/s	$U_j/U_\infty = 1.93$
$f = 208.0$ Hz	$St = 0.22$	
$Re_j = 20294$	$Re_\infty = 83567$	
$\rho_j = 1.0081$ kg/m ³	$\rho_\infty = 0.9660$ kg/m ³	

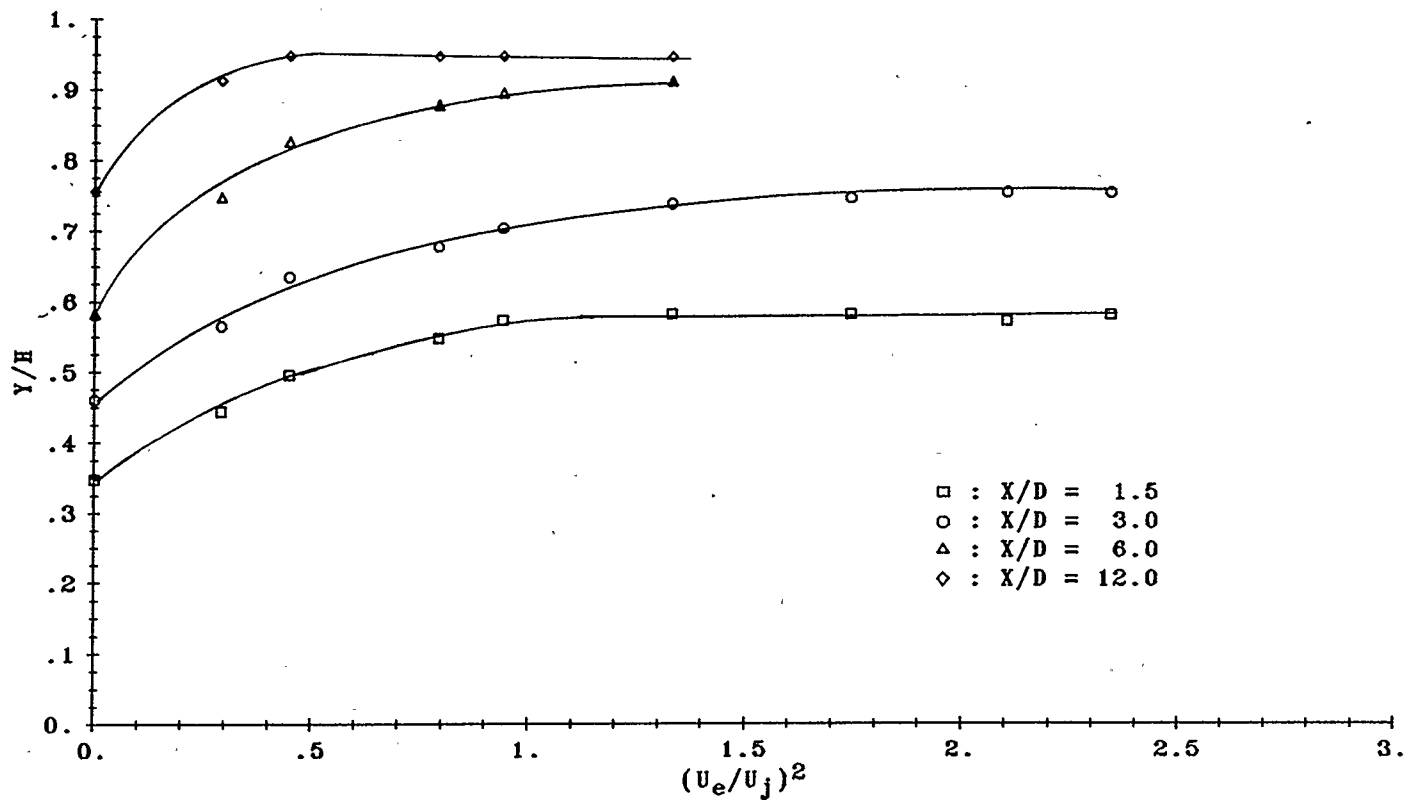


FIGURE 5.32 CENTRE PLANE PENETRATION TRAJECTORY VERSUS RELATIVE PULSATION STRENGTH, AT CONSTANT STROUHAL NUMBER FOR JET ORIFICE 19.93 mm DIAMETER.

$U_j = 18.99 \text{ m/s}$	$U_\infty = 9.82 \text{ m/s}$	$U_j/U_\infty = 1.93$
$f = 208.0 \text{ Hz}$	$St = 0.22$	
$Re_j = 20294$	$Re_\infty = 83567$	
$\rho_j = 1.0081 \text{ kg/m}^3$	$\rho_\infty = 0.9660 \text{ kg/m}^3$	

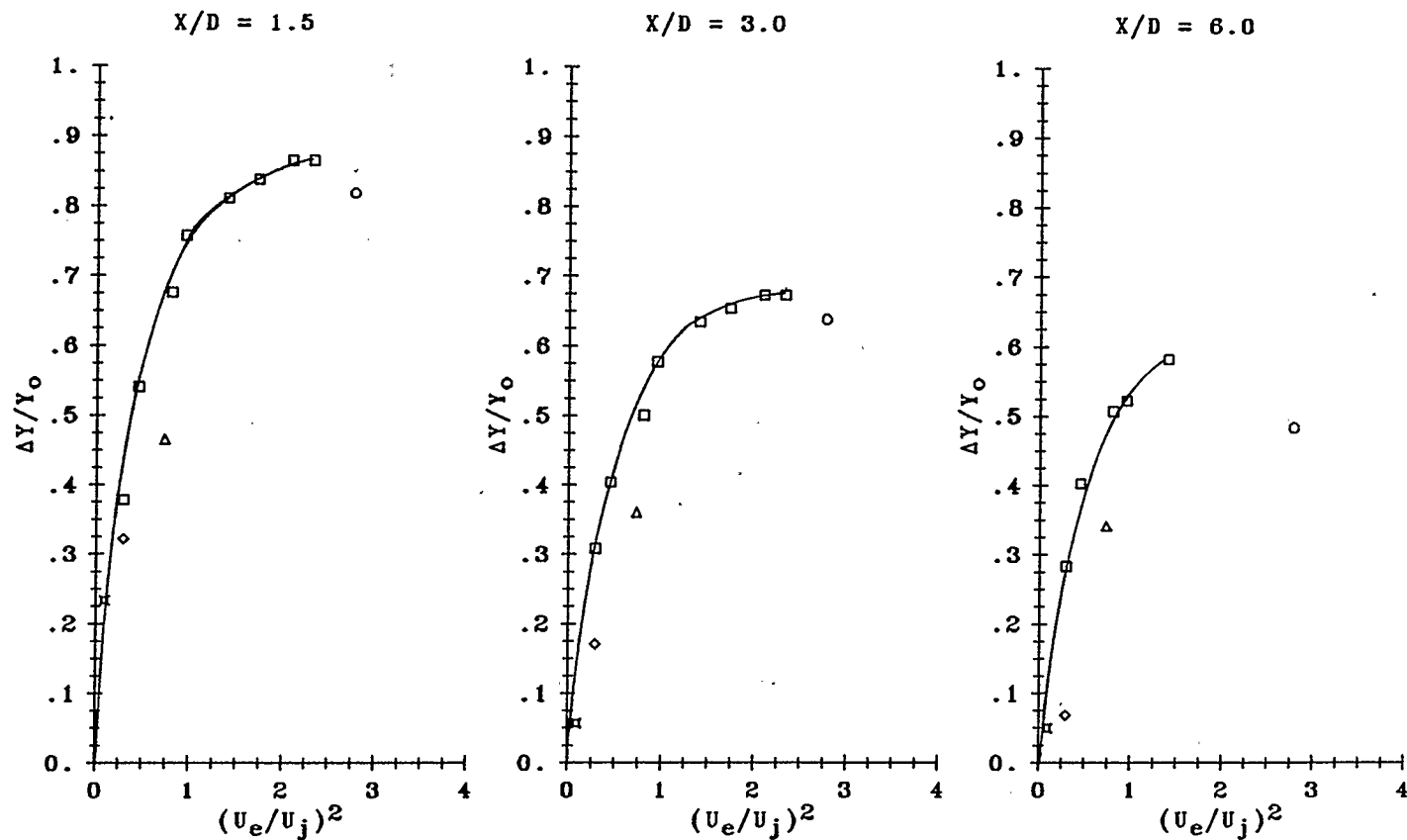


FIGURE 5.33 THE VARIATION OF JET PENETRATION WITH PULSATION STRENGTH AT DIFFERENT DOWNSTREAM LOCATIONS FOR 19.93 mm. DIA. JET ORIFICE, 208 Hz, SHOWING STROUHAL NUMBER EFFECT.

WHERE :-

□ : $St=0.22$
 ◇ : $St=0.12$

○ : $St=0.31$
 ◻ : $St=0.09$

△ : $St=0.18$

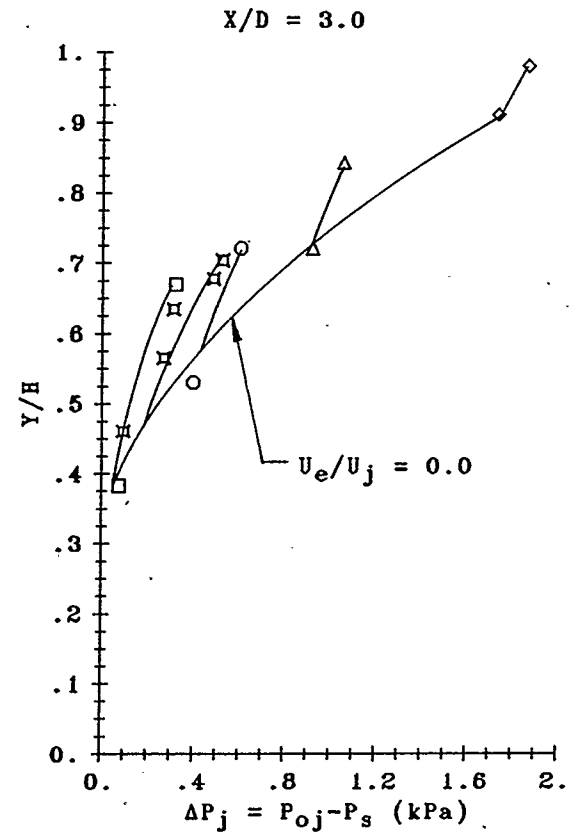
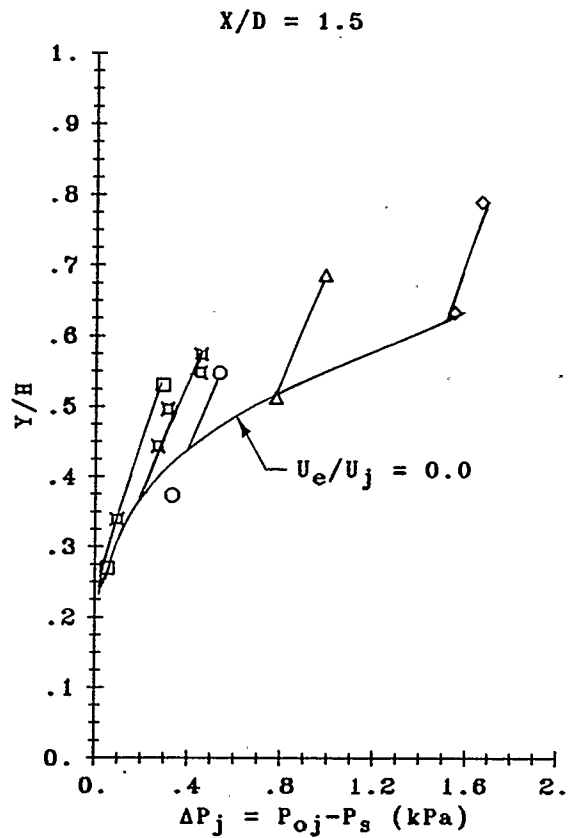


FIGURE 5.34 JET PENETRATION VERSUS PRESSURE DROPPED ACROSS JET ORIFICE AT CONSTANT STROUHAL NUMBER.

- : $U_j/U_\infty = 1.31$, $St = 0.31$, $U_e/U_j = 1.67$
- : $U_j/U_\infty = 2.26$, $St = 0.18$, $U_e/U_j = 0.86$
- △ : $U_j/U_\infty = 3.34$, $St = 0.12$, $U_e/U_j = 0.54$
- ◇ : $U_j/U_\infty = 4.56$, $St = 0.09$, $U_e/U_j = 0.30$
- ⊠ : $U_j/U_\infty = 1.93$, $St = 0.22$, $U_e/U_j = 0.54-1.53$

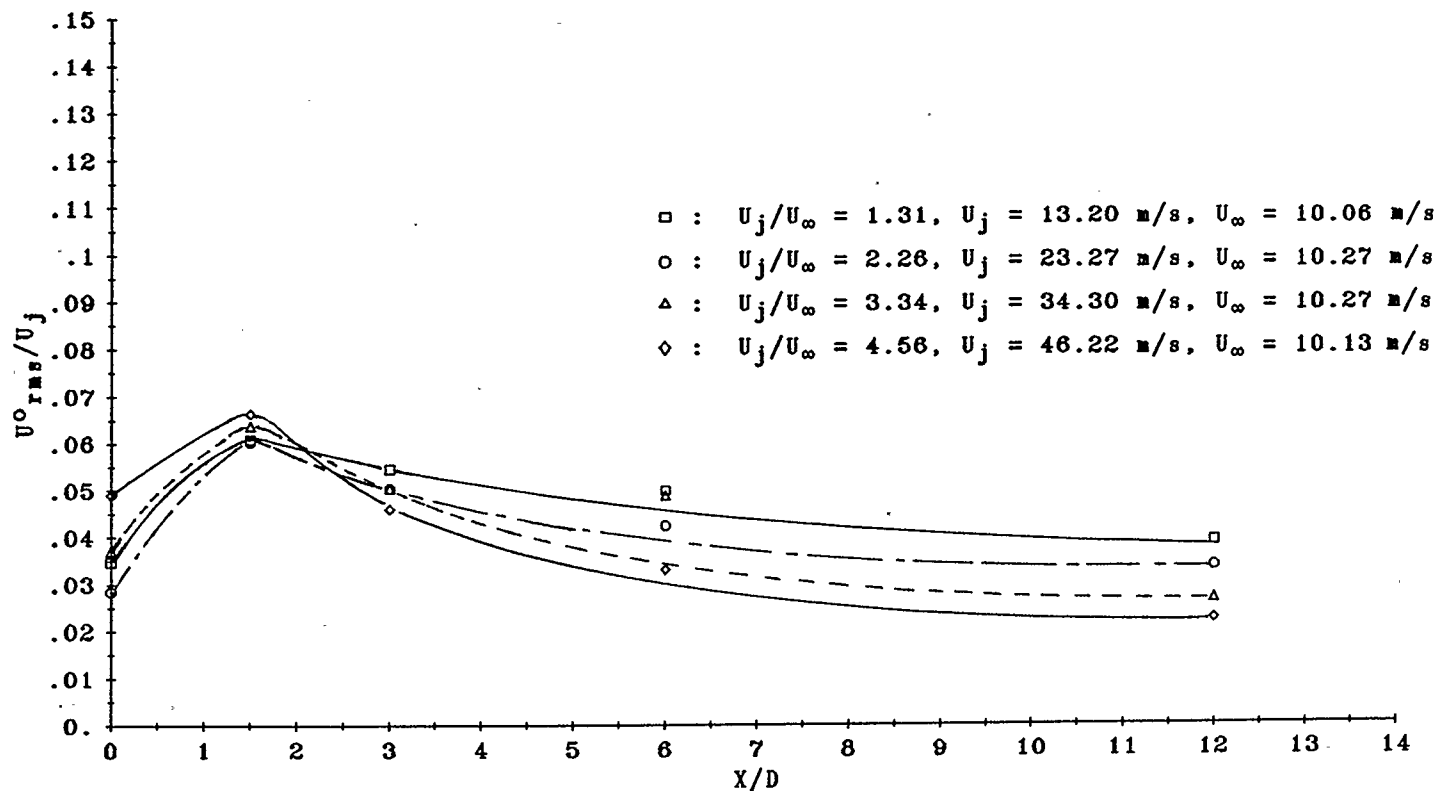


FIGURE 5.35 OVERALL TURBULENCE FOR STEADY JET AT DIFFERENT DOWNSTREAM (X/D) LOCATIONS, FOR 19.93 mm. DIA. JET ORIFICE. (REFER TO FIGURES 5.7 - 5.10 FOR OTHER OPERATING CONDITIONS)

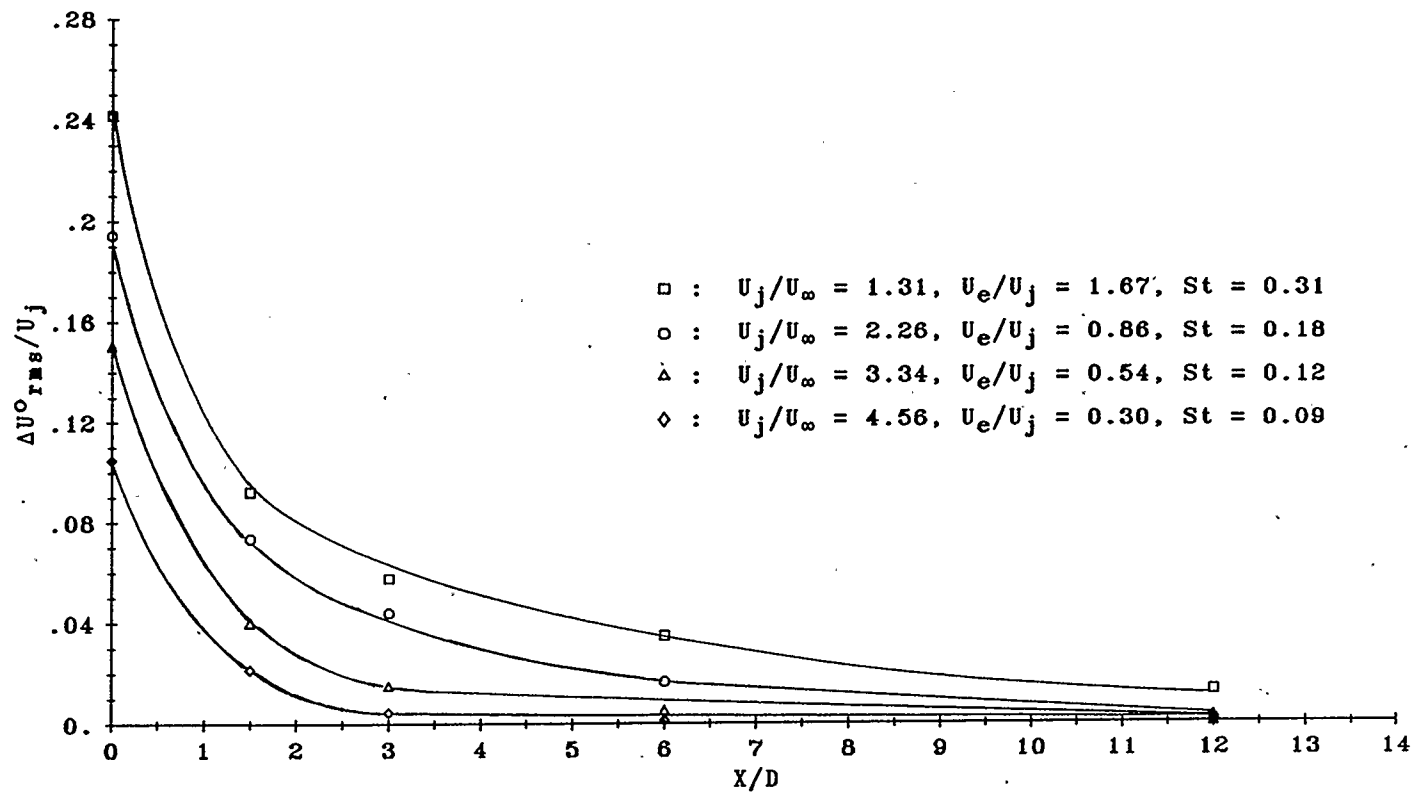


FIGURE 5.36 OVERALL CHANGE IN TURBULENCE AT DIFFERENT DOWNSTREAM (X/D) LOCATIONS, FOR 19.93 mm. DIA. JET ORIFICE AT 208 Hz. (REFER TO FIGURES 5.7 - 5.10 FOR OTHER OPERATING CONDITIONS)

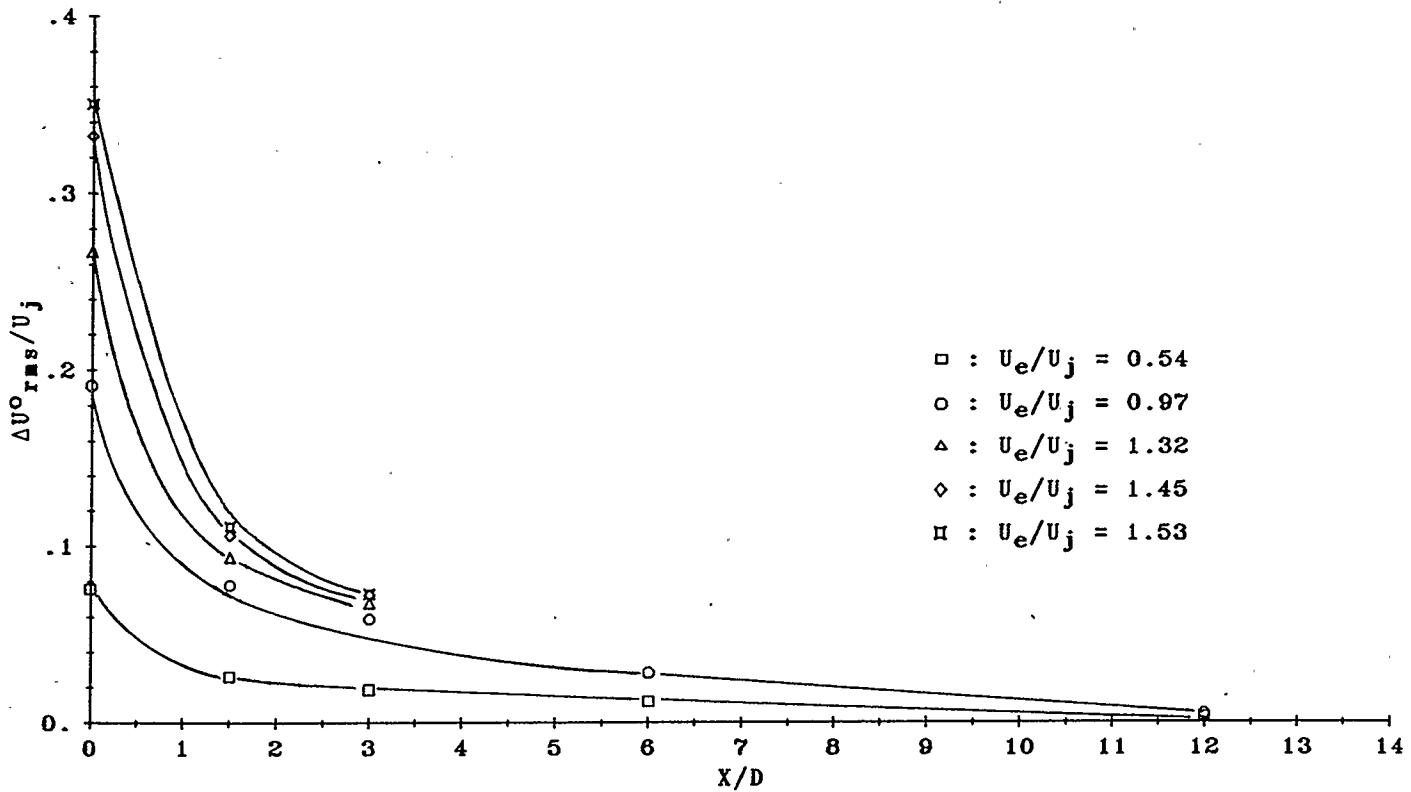


FIGURE 5.37 CHANGE OF U^0_{rms} FOR EACH X/D PLANE VERSUS RELATIVE PULSATION STRENGTH, AT CONSTANT STROUHAL NUMBER FOR JET ORIFICE 19.93 mm DIAMETER.

$U_j = 18.99$ m/s	$U_\infty = 9.82$ m/s	$U_j/U_\infty = 1.93$
$f = 208.0$ Hz	$St = 0.22$	
$Re_j = 20294$	$Re_\infty = 83567$	
$\rho_j = 1.0081$ kg/m ³	$\rho_\infty = 0.9660$ kg/m ³	

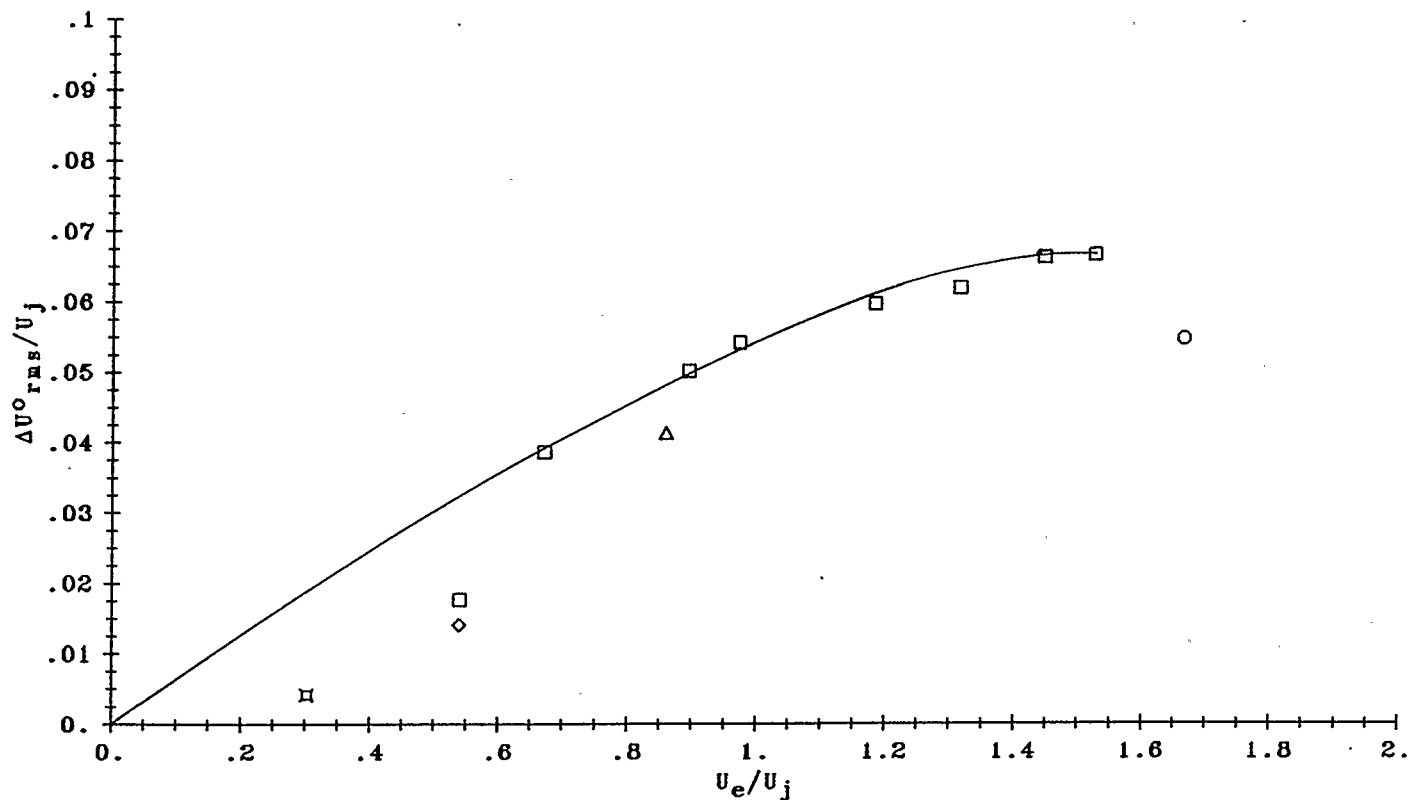


FIGURE 5.38 THE CHANGE OF U^0_{rms} WITH RELATIVE PULSATION STRENGTH AT $X/D = 3.0$, FOR 19.93 mm. DIA. JET ORIFICE AT 208 Hz, SHOWING STROUHAL NUMBER EFFECT.

WHERE :-

□ : St=0.22
 ◇ : St=0.12

○ : St=0.31
 □ : St=0.09

△ : St=0.18

○ : "NO-DRIVE"
 □ : "WITH-DRIVE", 208 Hz

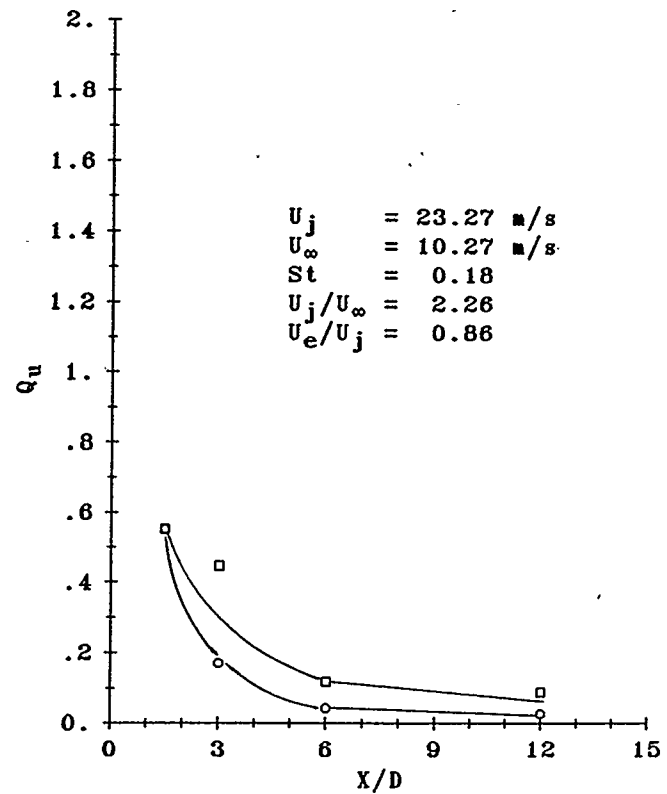
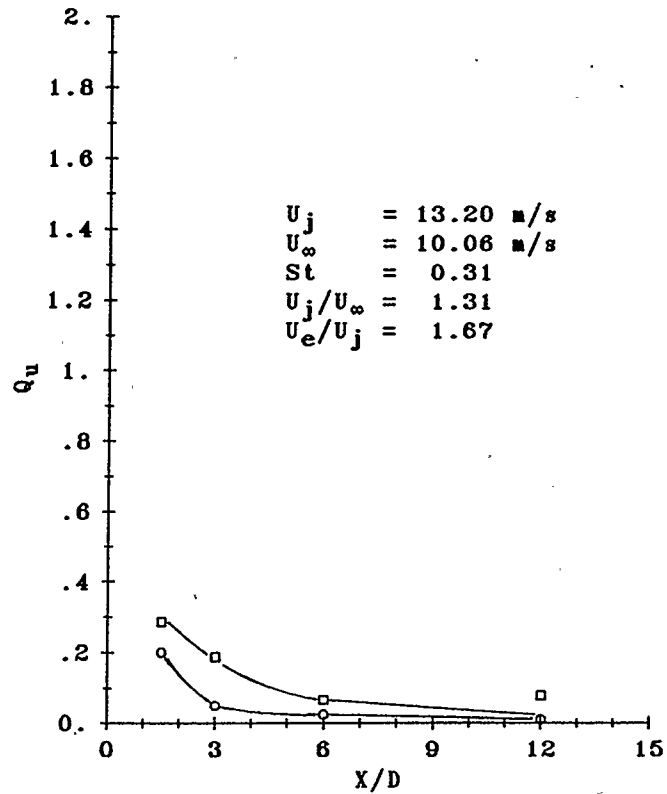


FIGURE 5.39 VELOCITY TRAVERSE QUALITY AT DIFFERENT DOWNSTREAM LOCATIONS.
 (REFER FIGURES 5.7 - 5.10 FOR OPERATING CONDITIONS.)

○ : "NO-DRIVE"
 □ : "WITH-DRIVE", 208 Hz

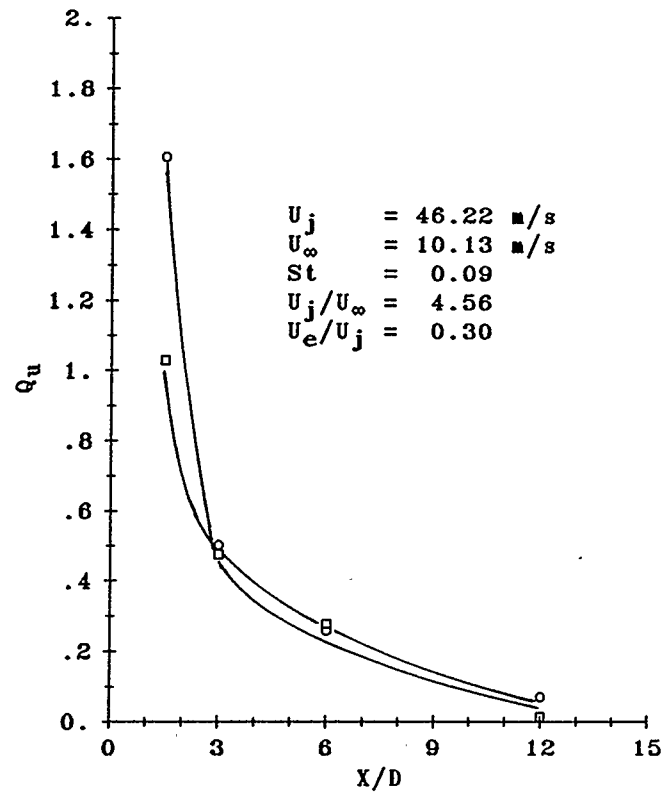
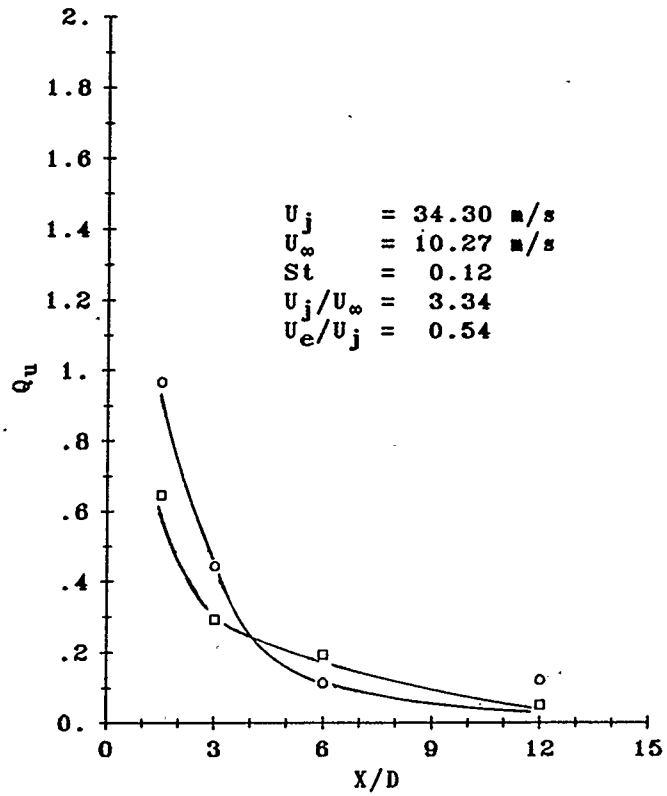


FIGURE 5.39 CONTINUED.

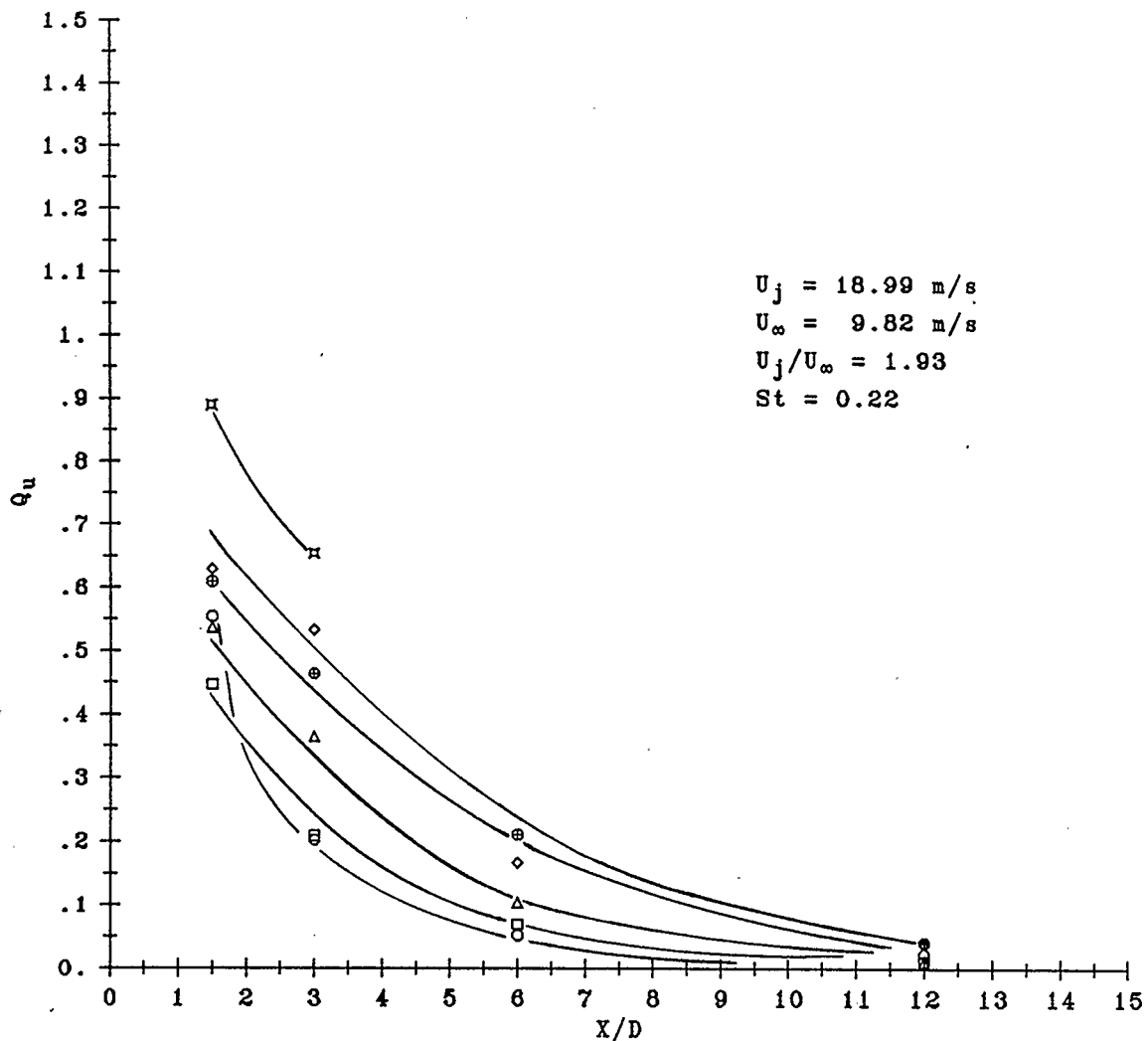


FIGURE 5.40 VELOCITY TRAVERSE QUALITY AT DOWNSTREAM LOCATIONS AT CONSTANT STROUHAL NUMBER. (REFER FIGURE 5.27 FOR OTHER OPERATING CONDITIONS.)

○ : $U_e/U_j = 0.00$, □ : $U_e/U_j = 0.54$
 △ : $U_e/U_j = 0.67$, ⊕ : $U_e/U_j = 0.89$
 ◇ : $U_e/U_j = 0.97$, ⊠ : $U_e/U_j = 1.53$

CHAPTER 6

CONCLUSIONS AND RECOMMENDATIONS

6.1 Conclusions

Development of the experimental apparatus has been completed, resulting in a significant increase in the air mass flow rate through the test section. Flow conditions are now such that a full range of jet velocities and crossflow velocities are available for experimentation. The test section velocity and turbulence profiles were of a quality entirely satisfactory for the work of this thesis and should be adequate for future test programmes.

The strength of the acoustic excitation of the jet flows was increased by means of shorter driver tubes and the installation of more powerful loudspeakers. The strongest response was found to be at about 208 Hz. The measured response of the driver system suggests that a detailed analysis may point to beneficial design changes, however, this was considered to be beyond the scope of this study particularly since the system was adequate for the test programme. The improved system allowed calibration of pulsation strength over a greater power range than that of previous work, and indicated that pulsation strength will have an upper limit

which so far has not been reached.

The "no-drive" experimental results were in good agreement with the reported nature of a steady jet in a crossflow, however, the jet trajectory could not be completely correlated due to tunnel wall effect. Thus test section conditions were normal and hence changes produced under "with-drive" conditions could be properly attributed to the effects of acoustic excitation.

Acoustic excitation was shown to produce strong changes in the mean velocity and turbulence profiles, and indicates considerable improvement in the entrainment and mixing by the jet. Toroidal vortices were shown to be shedding from the jet orifice and produced profound changes in the jet structure. In particular the jet cross-sectional area was increased, the wake region was strongly modified and the typical kidney shaped cross-section ("no-drive") was appreciably flattened. This suggests that a flow visualisation study should be undertaken. The experimental data also showed that the mixing length was significantly shortened. The effects increased with power, and overall it may be concluded that the jet mixing processes are significantly improved, in a controllable fashion, by pulsating the jet flow.

The acoustic drive increased the jet penetration by as much as 67%, measured at three diameters downstream of the jet orifice ($X/D = 3.0$). However, the penetration became limited before maximum power was reached, whereas the turbulence data showed that turbulence may be increased (hence mixing) beyond this point, by

further increase of acoustic excitation, up to the maximum power used (160 Watts). The pressure drop across the jet orifice to achieve a particular trajectory was also beneficially affected by acoustic excitation. Thus a "no-drive" penetration of 53% at $X/D = 3.0$ can be achieved by 41% less pressure drop by acoustic excitation of 75 Watts.

The effect of Strouhal Number was deduced from the jet penetration and turbulence data and was found to be optimum at about $St = 0.22$. This is in agreement with that found by other workers for the optimum entrainment rate and mixing by a free jet.

Overall it may be concluded that a good understanding of the mixing behaviour of an acoustically excited jet with a confined crossflow has been obtained. The effects are beneficial, controllable, and application of the technique will contribute to the development of improved combustors.

6.2 Recommendations for Future Work

This work has satisfied some of the recommendations by Yu (3), however, some remain and new ones have appeared. They are summarised as follows :

(1) Develop a flow visualisation technique, particularly to explore the toroidal vortex shedding and interactions near the jet orifice.

(2) In conjunction with Ref. (1), make detailed measurements on the properties of the toroidal vortices near the jet orifice

(over about the first ten orifice diameters) for a free jet, and for a jet in crossflow.

(3) Carry out a detailed theoretical and experimental investigation of the driver system in order to optimise the jet excitation.

(4) Since characterising jet excitation by pulsation strength is rather crude, effort should be expanded to develop a measurement technique for the energy actually pulsating the jet flow.

(5) Evaluate the mixing effectiveness of pulsating jet/s in a hot confined crossflow by means of temperature profile measurements.

(6) Study the effect of vortex interaction in the longitudinal direction for opposed excited jets, and lateral vortex interaction in a row of excited jets with the influence of jet spacing.

REFERENCES

1. Vermeulen, P.J., Ramesh, V., and Yu, W.K., "Measurements of Entrainment by Acoustically Pulsed Axisymmetric Air Jets", *J. of Engineering for Gas Turbine and Power*, Trans. ASME., Vol. 108, No. 3, July 1986, pp. 479-484.
2. Vermeulen, P.J., and Yu, W.K., "An Experimental Study of the Mixing by an Acoustically Pulsed Axisymmetrical Air Jet", ASME 30th International Gas Turbine Conference and Exhibit, Houston, Texas, Paper 85-GT-49, March 18-21, 1985, pp. 1-10.
3. Yu, W.K., "An Experimental Study of the Mixing Behaviour of Acoustically Pulsed Air Jets", M.Sc. Thesis, University of Calgary, Department of Mechanical Engineering, July 1985.
4. Andreopoulos, J., "On the Structure of Jets in a Crossflow", *J. of Fluid Mechanics*, Vol. 157, 1985, pp. 163-197.
5. Shemer, L., Wagnanski, I., and Kit, E., "Pulsating Flow in a Pipe", *J. of Fluid Mechanics*, Vol. 153, 1985, pp. 313-337.
6. Zaman, K.B.M.Q., "Far-Field Noise of a Subsonic Jet under Controlled Excitation", *J. of Fluid Mechanics*, Vol. 152, 1985, pp. 83-111.
7. Fiedler, H.E., and Mensing, P., "The Plane Turbulent Shear Layer with Periodic Excitation", *J. of Fluid Mechanics*, Vol. 150, 1985, pp. 281-309.
8. Lepicovsky, J., Ahuja, K.K., and Burrin, R.H., "Tone Excited Jets, Part 3 : Flow Measurements", *J. of Sound and Vibration*, Vol. 102, 1985, pp. 71-91.

9. Vermeulen, P.J., Odgers, J., and Ramesh, V., "Full load Operation of a Gas Turbine Combustor with Acoustically Controlled Dilution-Air Mixing", ASME 29th International Gas Turbine Conference, Amsterdam, The Netherlands, Paper No. 84-GT-106, June 3-7, 1984, pp. 1-8.
10. Stone, J.R., and Mckinzie, D.J. Jr., "Acoustic Excitation - A promising New Means of Controlling Shear Layers", ASME Applied Mechanics Division Summer Meeting, San Antonio, Texas, NASA TM-83772, June 17-21, 1984.
11. Andreopoulos, J., and Rodi, W., "Experimental Investigation of Jets in a Crossflow", J. of Fluid Mechanics , Vol. 138, 1984, pp. 93-127.
12. Charwat, A.F., and Walker, B.E., "The Velocity Perturbations above the Orifice of an Acoustically Excited Cavity in Grazing Flow", J. of Fluid Mechanics, Vol. 128, 1983, pp. 413 - 426.
13. Thomas, F.O., and Goldschmidt, V.W., "Interaction of an Acoustic Disturbance and a Two-Dimensional Turbulent Jet : Experimental Data', J. of Fluids Engineering, Trans. ASME., Vol. 105, 1983, pp. 134-139.
14. Lefebvre, A.W., Gas Turbine Combustion, Chapter 4, McGraw-Hill, New York, 1983, pp. 117-126.
15. Vermeulen, P.J., Odgers, J., and Ramesh, V., "Acoustic Control of Dilution-Air Mixing in a Gas Turbine Combustor", J. of Engineering for Power, Trans. ASME., Vol. 104, 1982, pp. 844-852.

16. Ho, C.M., and Huang, L.S., "Subharmonics and Vortex Merging in Mixing Layers", J. of Fluid Mechanics, Vol. 119, 1982, pp. 443-473.
17. Parikh, P.G., and Moffat, R.J., "Resonant Entrainment of a Confined Pulsed Jet", J. of Fluids Engineering, Trans. ASME., Vol. 104, 1982, pp. 482-488.
18. Hasan, M.A.Z., and Hussan, A.K.M.F., "The Self-Excited Axisymmetric Jet", J. of Fluid Mechanics, Vol. 115, 1982, pp. 59-89.
19. Andreopoulos, J., "Measurements in a Jet Pipe Flow Issuing Perpendicularly into a Cross Stream", J. of Fluids Engineering, Trans. ASME., Vol. 104, 1982, pp. 493-499.
20. Zaman, K.B.M.Q., and Hussan, A.K.M.F., "Turbulence Suppression in Free Shear Flows by Controlled Excitation", J. of Fluid Mechanics, Vol. 103, 1981, pp. 133-159.
21. Crabb, D., Durao, D.F.G., and Whitelaw, J.H., "A Round Jet Normal to a Cross Flow", J. of Fluids Engineering, Trans. ASME., Vol. 103, 1981, pp. 142-153.
22. Heavens, S.N., "Visualization of the Acoustic Excitation of a Subsonic Jet", J. of Fluid Mechanics, Vol. 100, 1980, pp. 185 - 192.
23. Disselhorst, J.H.M., and Wijngaarden, L., "Flow in the Exit of Open Pipes during Acoustic Resonance", J. of Fluid Mechanics, Vol. 99, 1980, pp. 293-319.

24. Kibens, V., "Discrete Noise Spectrum Generated by an Acoustically Excited Jet", AIAA. Journal, Vol. 18, 1980, pp. 434-441.
25. Kirmse, R.E., "Investigation of Pulsating Turbulent Pipe Flow", J. of Fluids Engineering, Trans. ASME., Vol. 101, 1979, pp. 436-442.
26. Vermeulen, P.J., Odgers, J., and Ramesh, V., "Acoustic Control of the Exit Plane Thermodynamics State of a Combustor", ASME 24th Gas Turbine Conference and Exhibit, San Diego, Calif., Paper 79-GT-180, March 12-15, 1979, pp. 1-12.
27. Bojic, M.L., and Eskinazi, S., "Two-Dimensional Mathematical Model of a Nonbuoyant Jet in a Cross-Flow", AIAA. Journal, Vol. 17, 1979, pp. 1050-1054.
28. Toshaki, M., and Yoshihiro, M., "Trajectories of Single and Double Jets Injected into a Crossflow of Arbitrary Velocity Distribution", J. of Fluids Engineering, Trans. ASME., Vol. 101, 1979, pp. 217-223.
29. Adler, D., and Baron, A., "Prediction of a Three-Dimensional Circular Turbulent Jet in Crossflow", AIAA. Journal., Vol. 17, 1979, pp. 168-174.
30. Ower, E., and Pankhurst, R.C, The Measurement of Airlflow, 5th Edition (S.I. Metric Units), Ch. 3 and 6, Pergamon Press, 1977.
31. Moussa, Z.M., Trischka, J.W., and Eskinazi, S., "The Near Field in the Mixing of a Round Jet with a Cross Stream", J. of Fluid Mechanics, Vol. 80, 1977, pp. 49-80.

32. Moore, C.J., "The Role of Shear Layer Instability waves in Jet Exhaust Noise", J. of Fluid Mechanics, Vol. 80, 1977, pp. 321-367.
33. Patankar, S.V., Basu, D.K., and Alpay, S.A., "Prediction of the Three-Dimensional Velocity Field of a Deflected Turbulent Jet", J. of Fluids Engineering, Trans. ASME., Vol. 99, 1977, pp. 758-762.
34. Sucec, J., and Bowley, W.W., "Prediction of the Trajectory of a Turbulent Jet Injected into a Crossflowing Stream", J. of Fluids Engineering, Trans. ASME., Vol. 98, 1976, pp. 667-673.
35. Bergeles, G., Gosmann, A.D., and Launder, B.E., "The Near Field Character of Jet Discharged Normal to a Main Stream", J. of Heat Transfer, Trans. ASME., Vol. 98, 1976, pp. 373 - 378.
36. Chan, Y.Y., "Noise Generated Wavelike Eddies in a Turbulent Jet", The 10th Congress of the International Council of Aeronautical Sciences, Ottawa, Ontario, Canada, Oct. 3-8, 1976, ICAS Paper No. 76-42.
37. Vermeulen, P.J., Danilowich, M.S., Heydlauff, E.P., and Price, T.W., "The Acoustically Excited Flame", J. of Engineering for Power, Trans. ASME., Vol. 98, 1976, pp. 147 - 158.
38. Odgers, J., and Wojcikowski, K.A., "Jet Mixing as Defined by Water Models", ASME Winter Annual Meeting, Houston, Texas, Paper 75-WA/GT-2, Nov. 30 - Dec. 4, 1975.

39. Fearn, R., and Weston, R.P., "Vorticity Associated with a Jet in a Cross Flow", AIAA. Journal, Vol.12, 1974, pp. 1666-1671.
40. Chassaing, P., George, J., Claria, A., and Sananes, F., "Physical Characteristics of Subsonic Jets in a Cross Stream", J. of Fluid Mechanics, Vol. 62, 1974, pp. 41-64.
41. Stoy, R.L., and Ben-haim, Y., "Turbulent Jets in a Confined Crossflow", J. of Fluids Engineering, Trans. ASME., Vol. 95, 1973, pp. 551-556.
42. Binder, G., and Favre-Marient, M., "Mixing Improvement in Pulsating Turbulent Jets", ASME Symposium on Fluid Mechanics of Mixing, Georgia Institute of Technology, Atlanta, Georgia, June 20-22, 1973, pp. 167-172.
43. Walker, R.E., and Kors, K.L., "Multiple Jet Study - Final Report", NASA CR-121217, June, 1973.
44. Kamotani, Y., and Greber, I., "Experiments on a Turbulent Jet in a Cross Flow", AIAA. Journal, Vol. 10, 1972, pp. 1425 - 1429.
45. Ramsey, J.W., and Goldstein, R.J., "Interaction of a Heated Jet with a Deflecting Stream", J. of Heat Transfer, Trans. ASME., Vol. 93, 1971, pp. 365-372.
46. Crow, S.C., and Champagne, F.H., "Orderly Structure in Jet Turbulence", J. of Fluid Mechanics, Vol. 48, 1971, pp. 547 - 591.

47. Goldschmidt, V.W., and Kaiser, K.F., "Interaction of an Acoustic Field and a Turbulent plane Jet : Mean Flow Measurements", Chemical Engineering Progress Symposium Series, Vol. 67, No. 109, 1971, pp. 91-98.
48. Simcox, C.D., and Hoglund, R.F., "Acoustic Interactions with Turbulent Jets", J. of Basic Engineering, Trans. ASME., Vol. 93, 1971, pp. 42-46.
49. McMahon, H.M., Hester, D.D., and Palfery, J.G., "Vortex Shedding from a Turbulent Jet in a Cross-wind", J. of Fluid Mechanics, Vol. 48, 1971, pp. 73-80.
50. Hribar, A.E., and Purdy, K.R., "On the Interaction of Intense Acoustic Fields and Viscous Fluid Flows", J. of Basic Engineering, Trans. ASME., Vol. 91, 1969, pp. 74-79.
51. Ingard, U., and Ising, H., "Acoustic Nonlinearity of an Orifice", J. of the Acoustical Society of America, Vol. 42, 1967, pp. 6-17.
52. Keffer, J.F., and Baines, W.D., "The Round Turbulent Jet in a Cross-wind", J. of Fluid Mechanics, Vol. 15, 1965, pp. 481 - 496.
53. British Standards Institution, B.S. No. 1042 : Measurement of Fluid Flow in Pipes, Part 1, Orifice Plates, Nozzles and Venturies, 1964.
54. Abramovich, G.N., The Theory of Turbulent Jets, The M.I.T. Press, Cambridge, Massachusetts, 1963.

55. Anderson, A.B.C., "Vortex-Ring Structure-Transition in a Jet Emitting Discrete Acoustic Frequencies", J. of the Acoustical Society of America, Vol. 28, 1956, pp. 914-921.
56. Anderson, A.B.C. "Structure and Velocity of the Periodic Vortex-Ring Flow Pattern of a Primary Pfeifenton (Pipe Tone) Jet", J. of the Acoustical Society of America, Vol. 27, 1955, pp. 1048-1053.
57. Maxworthy, T., "Some Experimental Studies of Vortex Rings", J. of Fluid Mechanics, Vol. 81, 1977, pp. 465-495.
58. Wood, A.B., "Air Cavities" - A textbook of Sound, G. Bell & Sons Ltd., London, 1964, pp. 179.
59. Holdeman, J.D. and Walker, R.E., "Mixing of a Row of Jets with a Confined Crossflow", AIAA Journal, Vol. 15, 1977, pp. 243-249.

APPENDIX

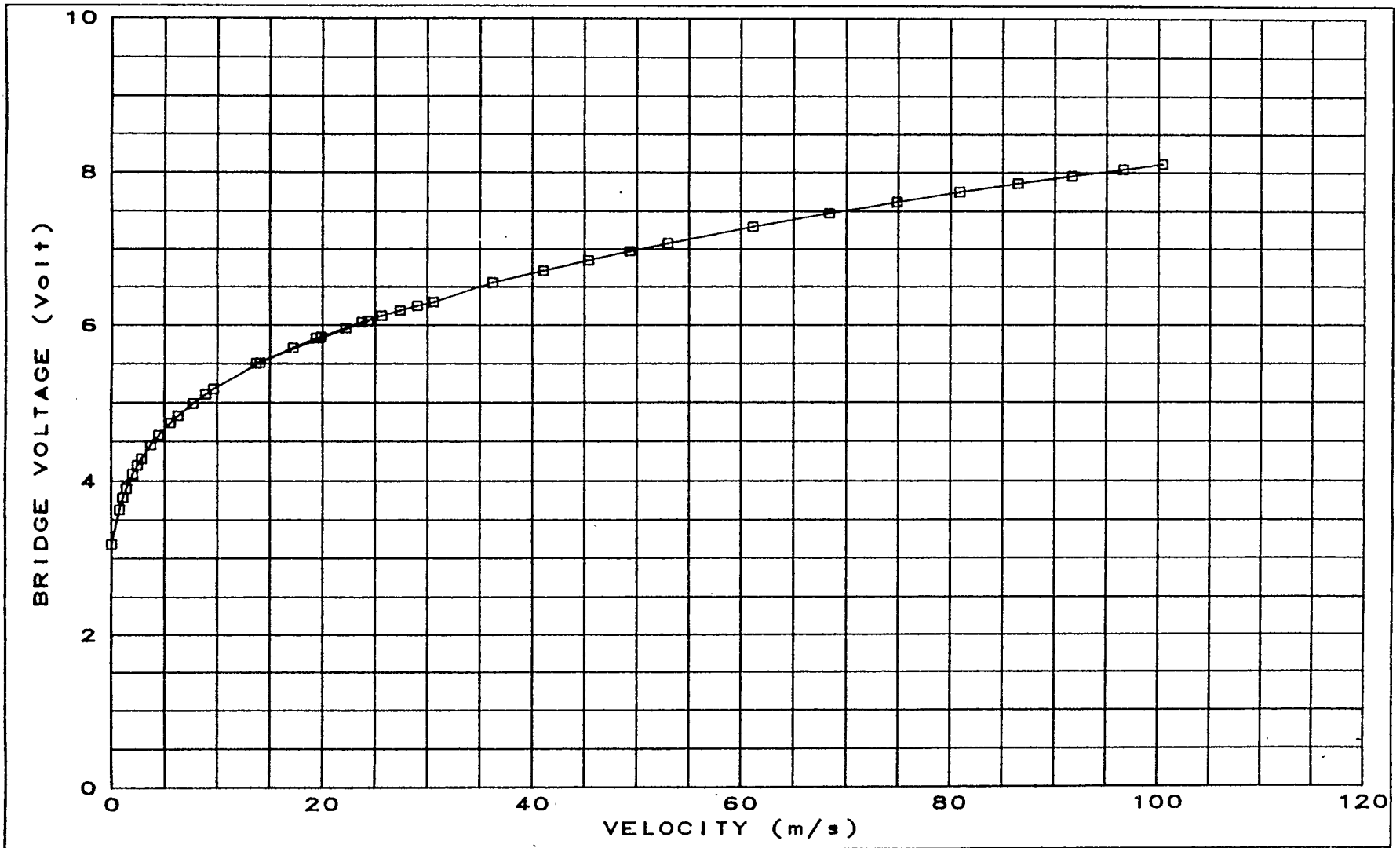


FIGURE A1 CALIBRATION CURVE FOR HOT-FILM SENSOR IN ATMOSPHERIC AIR.
ROOM TEMPERATURE: 26°C, BARO. PRESSURE: 86.95 kPa.